Chip based microelectrode array systems for modelling neurodegenerative diseases: A Multidisciplinary Approach to Model Neurodegenerative Disease

Khan, Muhammad Salman

Publication date:
2020

Document Version
Publisher's PDF, also known as Version of record

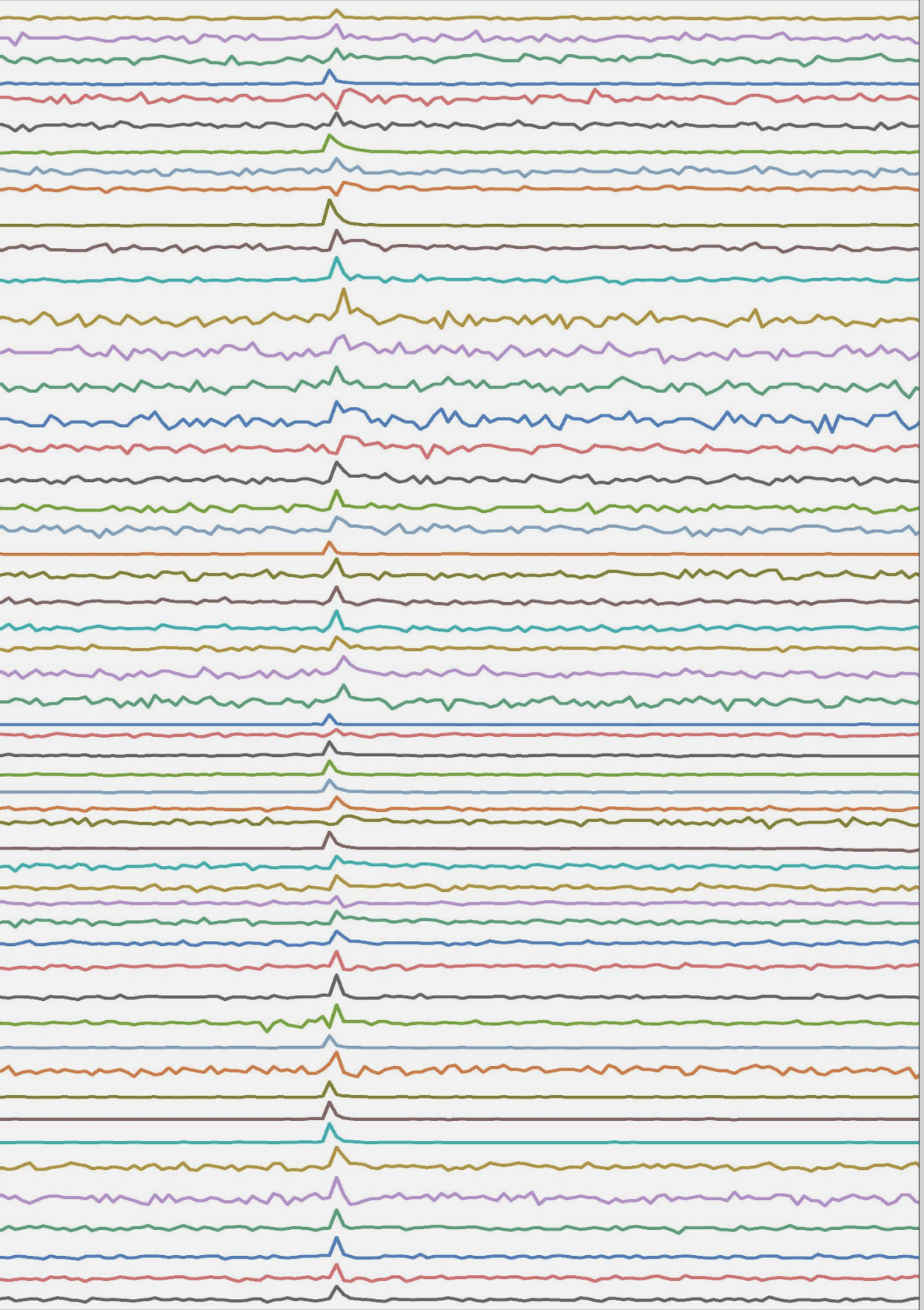

M Salman Khan – PhD Thesis

Chip based microelectrode array systems for modelling neurodegenerative diseases

DTU

Technical University of Denmark

TRAINING4CRM

Chip based microelectrode array systems for modelling neurodegenerative diseases

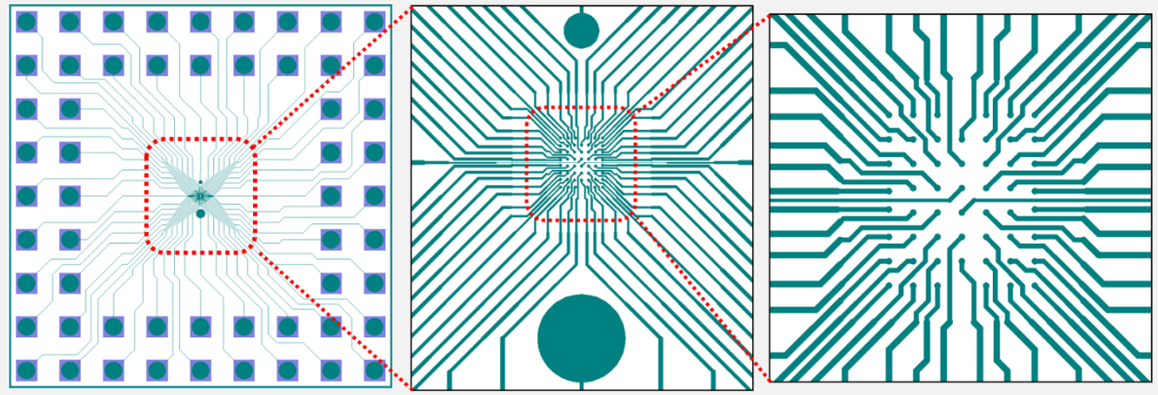

Doctoral Dissertation by

Muhammad Salman Khan

DTU Bioengineering
Department of Biotechnology and Bioengineering

TECHNICAL UNIVERSITY OF DENMARK

TRAINING4CRM

Chip based microelectrode array systems for modelling neurodegenerative diseases

A Multidisciplinary Approach to Model Neurodegenerative Disease

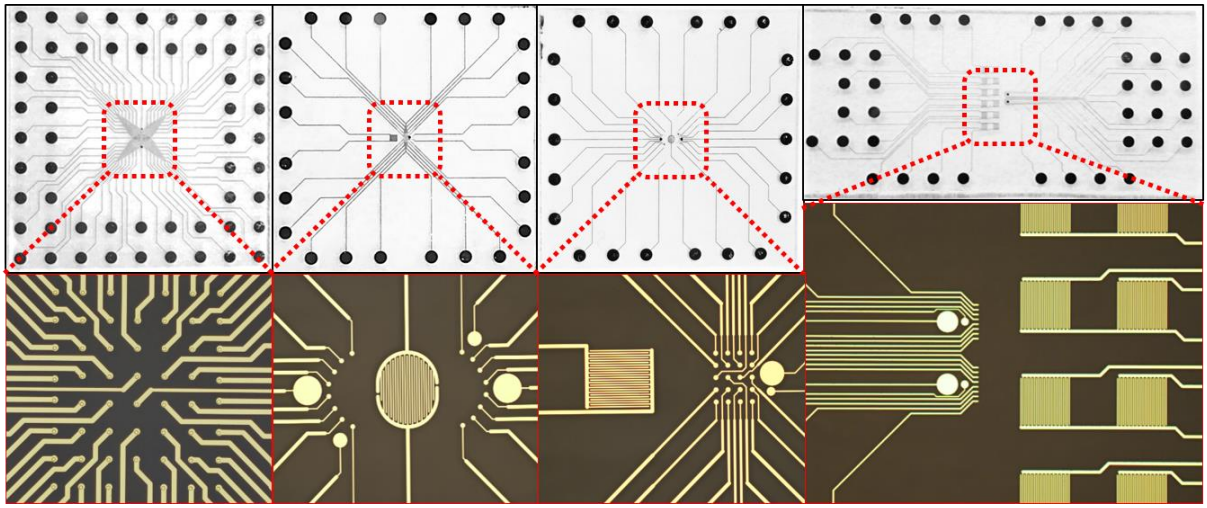

Doctoral Dissertation by

Muhammad Salman Khan

Under supervision of

Prof. Jenny Emnéus

Dr. Arto Heiskanen

DTU Bioengineering | Department of Biotechnology and Bioengineering

Denmark, Copenhagen

September 2020

To my parents

PREFACE

This submitted thesis described the results of a Ph.D. study initiated in June 2017 and finished in September 2020, while working as a Ph.D. student under the Bioanalytics group led by Jenny Emnéus in the Department of Biotechnology and Biomedicine (DTU Bioengineering) at Technical University of Denmark (DTU).

This project was funded by the European Union Horizon 2020 program (H2020-MSCA-ITN-2016) under the Maria Skłodowska-Curie Innovative Training Network with Grant agreement No 722779.

During my Ph.D. study, Jenny Emnéus and Arto Heiskanen from DTU Bioengineering supervised me as the principal supervisor and co-supervisor, respectively.

Salman Khan

October 3, 2020, Copenhagen, Denmark

ACKNOWLEDGEMENT

First of all, I would like to thank my supervisor Jenny Emnéus for providing me the opportunity to join her team and work with diverse disciplines during the project. It was an amazing three years working as part of the professional Bioanalytics group. You gave freedom to work while always being supportive and optimistic. You allowed me a chance to make several mistakes, but that made me grow and learn. Both on and off work, you created a great team spirit among us that ultimately helped to keep the pace.

I would also like to extend my sincere appreciation to my co-supervisor Arto Heiskanen, for the continuous support and in-depth discussion related to fabrication, electrochemistry, micro-milling, and more during my Ph.D. research. His guidance helped while writing the manuscripts and this thesis; it would not be comfortable without his valuable support. Thank you to my office mates and lunch buddies Afia and Hakan for helping me out, and the great time we spend together during three years of studies. Special thanks to the Bioanalytics group member, Mozhdeh, Claudy, and Shashank, for all the laughter and time spent together during breakfast meetings, summer BBQ, and team building events. I wish to thank all my friends, Asli, Nayere, Sina, and Fozia, whose support was a milestone in completing this Ph.D. project. I would like to thank the whole consortium of Training4CRM for their invaluable support and brainstorming session in the meetings and research schools. Special thanks to Marco Sampietro for hosting me in Milan for my external stay. I would also like to mention the contribution of DTU Nanolab employees to my work in the cleanroom.

Finally yet importantly, I would like to thank my family, especially to my brother Nouman Khan, for supporting me spiritually throughout my life and always believing in me.

Salman Khan

October 3, 2020, Copenhagen, Denmark

ABSTRACT

Parkinson's disease (PD) is the second most common progressive degenerative disorder of the central nervous system. It is described as the degeneration of dopaminergic neurons in the substantia nigra, causing a decreased dopamine balance in the striatum, mainly affecting the motor system. There is currently no cure for PD. The available treatments only alleviate the symptoms and do not halt the progression. To understand the physiological and pathological mechanisms of PD, the disease models so far developed include in vitro cell models (2D and 3D systems), animal models, and clinical studies. Nevertheless, the disease models currently developed to understand the complex mechanism underlying the disease fail to reliably mimic the functional and structural complexity of PD found in vivo. Therefore, a novel disease model development is required to overcome the current challenges with the existing PD models.

The research conducted in this thesis presents the new strategies to establish an advanced disease model by integrating state-of-the-art technological advancements in microfabrication, moving from static cell culture platform to flow-based compartmentalized microfluidic cell culture systems, and the advanced design of microelectrode sensors for real-time detection of neurotransmitter release. The development of ultramicroelectrode arrays (UMEA) with 54 individually addressable recording sites on a small footprint (260 µm x 290 µm) enables recording single neuronal activity in a neuronal population to understand the intercellular network communication and detect electrochemically the release of neurotransmitter upon stimulation. The compartmentalized microfluidic chip (CMC) can model the various parts of the brain for constructing the disease model close to the in vivo environment to address PD. The designs include separate compartments connected through microchannels representing the brain's different parts in vivo in the CMC device. To establish more robust in vivo disease models, advanced microelectrode arrays were developed integrated with CMC devices to address individual compartments and manipulate the neuronal activity in one compartment and recording the activity in other compartments. Furthermore, a pyrolyzed 3D carbon scaffold (3D-CS) has been introduced for 3D sensing and characterized electrochemically. Disease modeling was further expanded by performing finite element

simulations to evaluate the electric field behavior of an integrated 3D hydrogel scaffold that mimics brain tissue toward a combination of the 3D-CS and 3D hydrogel scaffold.

RESUMÉ (SUMMARY IN DANISH)

Parkinsons sygdom (PS) er den næst mest forekomne degenerative sygdom i det centrale nervesystem. Den beror på degenerering af dopamin-producerende neuroner i substantia nigra, hvilket forårsager en nedsat dopamin-balance i striatum, der hovedsageligt påvirker motorsystemet. Der eksisterer i øjeblikket ingen helbred for PS. De tilgængelige behandlinger lindrer kun symptomerne men standser ikke progressionen af sygdommen. For at forstå de fysiologiske og patologiske mekanismer af PS er en lang række sygdomsmodeller udviklet, der inkluderer in vitro cellemodeller (2D- og 3D-systemer), dyremodeller og kliniske studier. Disse sygdomsmodellerne klarer dog ikke af at pålideligt forstå den komplekse mekanisme der ligger til grund for sygdommen, eller at efterligne den funktionelle og strukturelle kompleksitet af PS, der findes in vivo. Derfor kræves helt nye sygdomsmodeller for at overvinde udfordringerne med de eksisterende PS-modeller.

Forskningen der er udført i denne afhandling præsenterer nye strategier til etablering af en avanceret sygdomsmodel ved at integrere avancerede teknologiske fremskridt inden for mikrofabrikation, som strækker sig fra en traditionel statisk cellekulturplatform til en rumopdelte mikrofluide baseret cellekulturplatform der inkorporere mikroelektrodearrays til påvisning af frigivelse af neurotransmitter i realtid. For at forstå neuroners netværkskommunikationen med specifik påvisning af neuronernes frigivelse af neurotransmitter, er en ultramikroelektrodearray (UMEA) med 54 individuelt adresserbare registreringssteder på et lille fodaftryk (260 µm x 290 µm) blevet udviklet, der gør det muligt at registrere enkelte cellers neurale aktivitet i en population av neuroner. Den rumopdelte mikrofluidechip kan på den anden side modellere forskellige dele af hjernen til konstruktion af sygdomsmodeller som bedre ligner in vivo situationen. Designen inkluderer separate rum forbundet via mikrokanaler som kan designes for at repræsenterer forskellige dele af hjernen. Avancerede mikroelektrodearrays er blevet udviklet og integreret i disse rumopdelte systemer til at adressere de individuelle rum for at f. ex. manipulere neuron aktivitet i et rum og registrere effekten af dette i et andet rum. Desuden er der udviklet et pyrolyseret ledende 3D-kulbaseret stillads til brug for 3D celle-dyrkning med samtidig mulighed for elektrokemisk måling. Sygdomsmodellering blev yderligere udvidet ved at udføre elementsimuleringer for at

evaluere den elektriske feltadfærd i et 3D hydrogel stillads, der efterligner hjernevæv for fremtidig kombination af 3D-kul- og 3D hydrogel stilladset.

LIST OF CONTRIBUTIONS

The research presented in this thesis are part of the following contributions also available in Appendix A.

I. M Salman Khan, Marco Giacometti, Arto Heiskanen, Afia Asif, Winnie Svendsen, Maria Dimaki, Marco Carminati Giorgio Ferrari, Marco Sampietro, Jenny Emnéus.
Ultramicroelectrode arrays for monitoring dopamine exocytosis from single cells in a cell population.
Paper I

II. Agnieszka Mech-Dorosz, M Salman Khan, Ramona Valentina Mateiu, Claus Hélix-Nielsen, Jenny Emnéus, Arto Heiskanen
Impedance characterization of biocompatible hydrogel suitable for biomimetic lipid membrane applications.
Paper II

Below is a list of conferences I participated in during my PhD:

- 10th International Conference on Impedance Spectroscopy (IWIS), Technische Universität Chemnitz, 25 – 29th September 2017, Poster presentation of research work.
- RegMedForum, Berlin, 6 December 2017.
- I was one of the main responsible for organizing the international Symposium on "Advanced therapies in Neurodegeneration: Bridging Neuroscience, Bioengineering and Optogenetics", originally planned to be held in Lisbon, Portugal on April 29 to May 1, 2020, but the physical meeting had to be cancelled due to COVID-19. Instead we organised it as an online conference on April 29-30, 2020

CONTENTS

Chapter 1

INTRODUCTION

1.1 Perspective of the research

Parkinson´s disease (PD) is currently an incurable disease, and it is not directly possible to study its progression in living humans; the only definitive diagnosis is post-mortem identification of the pathological features. The exact cause and mechanisms underlying PD are still unknown, and the available therapies focus on alleviating symptoms, but which are unable to interrupt or revert the disease progression. Current available techniques to study PD are limited to animal and *in vitro* cellular models. Enormous efforts have been focused on developing different models using experimental animals[1], *ex-vivo* organotypic animal models[2], and *in-vitro* cellular models[3]. Despite initial promising results, animal models often fail to translate into humans physiological data due to inter-species differences[4,5], and *in-vitro* cellular models are unable to reflect the complex physiology of the brain, which altogether leads to challenges to discover new therapeutic agents and insight into PD. No matter how much improvement an individual technology can provide for a better understanding the PD pathology, a substantial advantage would be to combine the evolution of state of the art i.e., human cellular, microfluidic, and sensing tools to create new means that would help to more effectively discover the relevant cellular parameters and study dynamics at the cellular and molecular level related to PD. New hybrid technological solutions have the possibility to address the current challenges and can lead to more physiologically relevant disease models.[6–8].

The motivation behind this doctoral thesis has been stimulated by advancements made in cell culture platforms, moving from current static cell culture systems to flow-based compartmentalised microfluidic cell culture systems[9], compact designs of micro and ultra-microelectrode arrays (MEAs and UMEAs) for specific electrical sensing of neurotransmitters[10,11], computer aided design (CAD)-based computational models for system

design and simulation[12–14], and novel cleanroom microfabrication techniques as well as by using fast prototyping techniques such as micro-milling, 3D printing and soft lithography[15,16].

I have been one of 15 early stage researchers (ESRs) of the Marie Sklodowska Curie Innovative Training Network (MSCA-ITN) called Training4CRM with the role of exploiting the possibility of developing new miniaturised PD disease model systems by using and combing the above-mentioned technologies.

Two basic brain-on-a-chip ideas have been pursued:

1. Fabrication of a static cell culture and electrochemical sensor array platform that could enable to study single neurons in a population of neurons by incorporating individually addressable ultra-microelectrodes in a UMEAs. In this way, when the neuronal population is chemically, electrically or light stimulated, one can study how the individual neurons are responding to the stimulation by electrochemically detecting exocytosis of neurotransmitters (in my case dopamine), arising from the neurons situated on the separate and individually addressable electrodes. The future goal would be to enable stimulation of a single neuron and following the communication with the surrounding neural network by detecting the release of different neurotransmitter (e.g. dopamine, glutamate, GABA) from other neurons in the network.
2. Fabrication of compartmentalized microfluidic chips (CMC), each housing microelectrodes, in which the different compartments are interconnected through microchannel arrays[8]. Different neural phenotypes can then be cultured in the separate compartments and allowed to communicate through the microchannels. In this way, we would be able to study the communication between different neural phenotypes by stimulating one compartment and electrochemically detect the release of different neurotransmitter in the other compartments. This system could be viewed as parallel to *ex-vivo* animal tissue type models, however, here with the possibility to study interaction of human neural cells, which could potentially mirror human physiology better.

These systems have the potential to lead to completely new and more physiologically realistic disease model tools with more complex design than is currently available, potentially providing improved insight into the human PD pathology, moreover applicable to other diseases.

This has been a highly cross-disciplinary project, which has required me to collaborate with some of the other ESRs in Training4CRM across the boundaries of cell biology, micro and nanofabrication, and bioanalytical sensing. My main part has been in the micro and nanofabrication of MEAs/UMEAs, microfluidics systems, their integration and characterisation, following initial biological testing of these systems.

1.2 Objective

The main objectives of the thesis have been to develop:

- ***2D Microelectrodes chips for static culture*** are developed with advanced design to establish the multiple recording sites essential to understand the intercellular communication signalling and detect neurotransmitter release (in our case, dopamine for now) upon electrical, optical, and chemical stimulation through implementing electrochemical techniques. Four micro-electrode array designs were fabricated, each fulfilling a unique purpose for examining neuronal behaviour. Furthermore, these electrode chips were integrated with CMC devices to detect dopamine neurotransmitter release at one container upon exciting the adjacent container connected through axonal projections via microchannels.
- ***2D brain-on-a-chip microfluidic models,*** referring to the construction of the complex neural circuitry network in an advanced in vitro microfluidic model. To achieve this goal, a microfluidic-based multi-compartmentalized device was developed with an innovative fabrication technique that maintains non-identical neurons isolated but promotes the neuronal interaction through the microchannels. The proposed method remarkably simplifies the compartmentalized-microfluidic chip (CMC) device fabrication and design that promotes to model various neural circuitry networks to mimic in vivo model, such as the reconstruction of nigrostriatal pathway for PD disease circuitry model.
- ***Moving from 2D to 3D models.*** Due to the difficulty in mimicking the in vivo microenvironment through 2D cellular culture, the development of a 3D conductive carbon scaffold to be integrated with supported hydrogels for potential 3D cell culture and electrochemical sensing was pursued.

1.3 Thesis outline

The outline of the thesis is described as follow, with a brief introduction of each chapter.

Chapter 2 begins with a brief discussion about Parkinson's Disease (PD), its pathophysiology, symptoms, and available treatments. The second part focuses on current state-of-the-art disease models and their challenges. The last part presents recent advancements using hybrid technological tools for reconstructing improved disease models.

Chapter 3 describes the development process of dense UMEA chips, using direct-write patterning techniques via CAD drawing, through maskless aligner (MLA) technology onto a transparent glass wafer and fabrication characterization. Then, details about the electrochemical characterization of the two UMEAs designs are presented and discussed. This is followed by cell culture and exocytosis experiments using these two UMEAs designs, described in detail in Paper 1 (Appendix).

Chapter 4 focuses on development of neural circuitry network by implementing microfluidic technology. First the fabrication of three new MEA designs, designed to study neural-neural interaction, and their electrochemical characterisation are presented. Next follows a new method to fabricate compartmentalized microfluidic chips (CMCs), representing specialized areas of the brain, and the integration of MEA with the individual compartments of CMC device. Initial cellular experiments were conducted to analyze the CMC-MEAs integrated devices, but due to lack of time, mycoplasma in cell lab, and COVID19 situation, the final experiment could not be concluded.

Chapter 5 introduces a 3D carbon scaffold (3D-CS) fabricated using fast prototyping techniques (3D printing, soft lithography and final pyrolysis), addressing some challenges associated with the fabrication. Lastly, hydrogel scaffold formation and its characterization using impedance spectroscopy and COMSOL multiphysics simulation are discussed, and described in detail in Paper II (Appendix).

Chapter 6 provides the conclusion for the work presented in the thesis and provides future outlook associated with the development of disease models by providing possible improvements for the CMC devices and novel sensor mechanisms to learn more about brain disorders.

Chapter 2

NEURODEGENERATIVE DISEASE MODELS

This chapter briefly familiarizes the reader, firstly, to the pathophysiology of Parkinson's disease (PD), its symptoms and current therapies. Secondly, it describes the current approach to model PD and their challenges. Lastly, it focuses on attempts to model PD with existing technological advancement.

2.1 Parkinson's disease (PD)

PD is an incurable progressive neurodegenerative disease (NDD), primarily caused by the gradual degeneration of dopaminergic neurons (DAn) in Substantia Nigra *pars compacta* (SNpc), and the nigrostriatal pathway, which regulates motor functions. PD is estimated to affect 10-million people globally including approx. 3% of people over the age of 65 years[17,18]. Due to the unavailability of the cure and progressive nature of the disease, the global financial burden of PD has been increased to be approx. 14 billion euros[19,20].

2.1.1 Disease Development

PD was first clinically characterized in 1817, by a British physician named James Parkinson in a monograph entitled as "An Essay of the Shaking Pals" [21,22]. However, the most eminent pathological characteristics of PD were found many years later and were related to the degeneration of SNpc neurons[23–25], and depletion of dopaminergic neurons projections in the dorsal striatum.[26]. Besides the depletion of dopamine levels in the mid-brain, the primary indication includes the formation of cytoplasmic inclusions with misfolded and aggregated α-synuclein, called "Lewy bodies (LB)" which is also considered to cause dementia[27,28]. However, the precise cause and development of PD is still unknown. These disruptions of the dopaminergic pathway are shown in figure. 2.1, which shows the comparison of a healthy brain vs. PD affected brain.

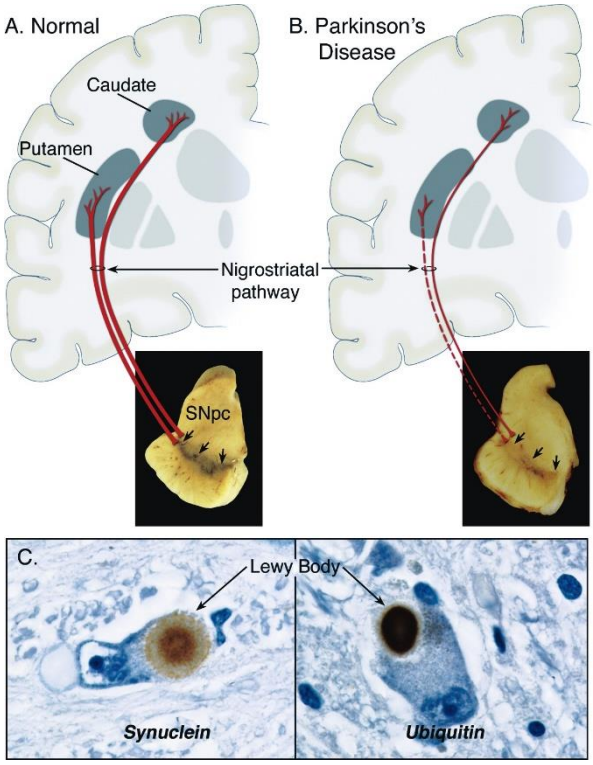

Figure 2.1: Graphical illustration of the nigrostriatal pathway representing dopaminergic projections from SNpc to striatum. a) Thick (solid, red) lines connecting SNpc with striatum (caudate, putamen) representing healthy brain, visible pigmentation in SNpc (black arrows). b) PD diseased nigrostriatal pathway representing loss of dopaminergic projections, from SNpc to striatum (dashed, red), visible depigmentation in SNpc (black arrows). c) Lewy bodies (aggregated α-synuclein & ubiquitin) present in SNpc of PD brain. Represented by immumochistrochemical labeling. Adapted from [29].

2.1.2 Symptoms and Current Therapies

PD is well-known to affect both motor and cognitive functions leading to motor symptoms such as hypokinesia, rigidity, tremor and bradykinesia, and non-motor symptoms like dementia, depression, insomnia, constipation and bladder problems[30,31–35]. These symptoms have a major impact in life thereby emphasizing the immense need for the cure of PD.

Since the exact cause of PD is still undiscovered, the disease has no cure that can halt the progression of disease. The current therapeutic efforts are symptomatic and focus on mitigating the symptoms of disease rather than preventing the disease progression or neurodegeneration. The first therapeutic approach involves drug therapy, that aims to restore dopamine levels through medications such as Levodopa[36] and is to date considered to be the most effective therapeutic approach. However, drug therapies are ineffective due to their

efficacy loss and sever side-effects such as dyskinesia and nausea[37–39]. In later and severe stages of PD, surgical therapy, such as deep brain stimulation (DBS) that involves implantation of electrodes in mid-brain of PD patient, are adopted. Surgical efforts help stimulating and modulating the neuronal activity in the mid-brain resulting in significant suppression of PD tremors[40–42]. However, such surgical treatments are invasive and leads to problems such as multiple seizures, tissue infections, and cognitive impairment[43–46]. One of the current strategies towards curing the disease involves dopamine restoration using regenerative approaches. The initial results of transplanting foetal tissue in striatum for replacing dopaminergic neurons were promising[47]. However, it led to several issues such as graft rejection in the local tissue, the precise number of grafted cells, and ethical issues related to embryonic stem cells. Most recently, the A9 type of SNpc dopaminergic neurons, considered to be lost during neurons degeneration in PD, are developed in-vitro[48–50]. However, challenges are associated with the transplantation process of these neurons, which are related to the need for a reproducible homogenous A9 population in-vitro, improved maturity level of the cells, knowledge of the exact number of neurons to be transplanted, and elimination of risk for tumour formation[51,52]

Although, stem cell based regenerative approaches are at an early stage, their recent advancements include the developments of disease model systems, which involves advanced neural interfaces and sensing platforms that can enable studying modulation of brain activities using real-time monitoring, stimulation, and reading the response of different brain regions.

2.2 Current PD Models

2.2.1 Animal Models

An animal model is a non-human, mostly living and often genetically engineered species, used in medical research to imitate complex aspects of human disease. The reason to employ animal models is to acquire information about the development and progression of the disease, diagnosis, prevention, and treatment by eliminating the risk of harming an actual human being. Due to progressive innovation of animal models, greater understanding has been gained in the molecular and cellular mechanisms that lead to brain cell dysfunction and degeneration. The developed PD phenotype in animal models has allowed us to obtain information about the disease progression and investigate possible treatments for preventions. However, currently,

no animal model has proven to represent a complete phenocopy of the PD disease. Nevertheless, animal models have led to a significant contribution to our knowledge about PD[53]. Multiple animal models are required to replicate PD because of the heterogeneity of the PD pathology[54]. Hence, a variety of animal models have been studied from non-human primates, rodents, to zebrafish and fruit flies[55], where rodent models are the most frequently used.

Two main categories to model PD in experimental animals have been at focus, neurotoxin-induced models and genetic models. The toxin-induced model allows us to reflect midbrain dopaminergic signalling dysfunctions and neurodegeneration resulting from environmental ingredients implicated in PD. Induced-neurotoxins lack the formation of Lewy bodies (LB) but recapitulate the intense and accelerated cell loss in SNpc and evoke motor symptoms that include resting tremor, bradykinesia, and rigidity[56]. Genetic models can induce α-synuclein pathology and LB formation, along with cell loss and motor symptoms. These models can be generated using transgenic animals or by viral transfection through genetic mutations. Neurotoxins-induced models, which administers precursor such as 1-methyl-4-phenyl-1,2,3,6-tetrahydropyridine (MPTP), 6-hydroxydopamine (6-OHDA) and the pesticide rotenone, have extensively refined the therapies used to treat the symptoms of PD[56,57]. Genetic mutation plays a vital role in the PD pathology, as genetic mutations have been identified through linkage analysis in familial PD. SNCA, LRRK2, and PARKIN are the most common mutation in animal models to understand PD's genetics[58].

Although animal models have contributed to develop, elaborate and improve the tested therapies, besides ethical concerns related to animal studies in research, the translatability of animal model to human trials has failed in experimental studies, because of the inter-species differences, hence creating a demand for new rapid and robust research tools in PD[59–63].

2.2.2 In-Vitro Models

The *in-vitro* technique can be described as the study of biological properties performed in a controlled manner within a given environment outside the living organism. PD is a multifactorial and complicated disease in which several factors contribute to the pathogenic process. The idea behind constructing an *in vitro* PD model mainly depends on testing contemporary approaches, able to monitor and manipulate the model quickly and effectively. The choice of the model depends on the characteristics and therapy of PD we want to achieve.

In-vitro models, such as well-established cell lines and primary cell cultures, provides an immense contribution in a controlled favourable environment to explore single pathogenic mechanisms and the genes/proteins involved in PD. Therefore, recapitulating the PD phenotype in cellular model generates the possibility to gain more insight into cellular and molecular mechanisms of the neurodegenerative disorder[64,65]. In contrast to animal models, cellular models involve less ethical concerns, decreased cost, develops the pathology faster, and reduce the overall process duration[3]. Genetic modification are also possible and remains valid, along with large scale testing in a short duration.

The existing *in-vitro* cell systems currently models two main characteristics found in the PD patient's brain: 1) Loss of dopaminergic neurons in the SNpc and, 2) protein aggregates containing α-synuclein[66], (Figure 2.1). To model degeneration of dopaminergic neurons in the SNpc, the extensive use of the neuroblastoma cell line (SH-SY5Y) and the pheochromocytoma cell line (PC12) have been used. These cell lines can produce and release catecholamine's through the cell membrane and has the characteristic to generate neuron-like properties along with cell differentiation to form neurite-like shape and activity upon following specific differentiating protocols. These are outstanding models for studying pharmacological interventions and are more easy to maintain as compared to primary neurons[67–72]. More advance cell lines have been developed and employed to better imitate PD and the degeneration of dopaminergic neurons. i.e., Lund human mesencephalic (LUHMES) cells[73]. Moreover, patient-derived human induced pluripotent stem cells (hiPSCs) differentiated into different neural phenotypes have provided new opportunities to potentially create personalised *in-vitro* disease models[74]. Neurodegeneration and LB formations have all thoroughly been studied in *in vitro* cellular PD models[66].

Physiologically relevant human *in-vitro* cell models may bridge the gap between pre-clinical animal models and humans. However, these cellular models are limited in several aspects, such as lack of sufficient cellular maturation, lack of the complex neural circuitry and vascular components.

2.2.3 Challenges

Research on understanding the physiological and pathological mechanisms of disease includes the use of *in vitro* cell models (both 2D and 3D systems), animal models and clinical

studies. Nevertheless, cell- and animal models face severe limitations. Animal models are crucial, but these models do not provide the human physio-pathological features due to the differences between animal and humans at the molecular and cellular level[75]. Traditional 2D monolayer cell cultures plays a vital role in understanding drug responses, developing therapeutic factors and predicting their side effects[76–78], however they lack the complex neural circuitry and vasculature found *in-vivo*[79], and due to the lack of fully developed pathological conditions and micro surroundings, the overall experiment fails in disease studies[80,81]. 3D cell culture systems, e.g. spheroids, organoids, or 3D organ-on-a-chip systems[82–86] provide more sophistication by recapitulating the *in vivo* microenvironment better than in 2D. Due to varying dimensions and structures, the genetic and biochemical assessment of 3D organoids gets tricky because of the unknown exact location of the seeded cells[87,88]. So far these 3D models are unable to recreate the required *in vivo* microarchitecture, that includes, vascularisation, and cell-cell interaction in complex neural circuitry[89,90].

In order to overcome existing limitations, it is essential to establish even more advanced models, which can be achieved by combining state of the art technologies from physics, biology and chemistry, forming completely new possibilities. Below follows a compilation of some of the strategies conducted to solve some of the above-mentioned challenges.

2.3 Tools used in current diseases model systems

2.3.1 Microfluidics

The fundamental studies of cell biology were performed in classical static 2D cell cultures, in some cases 3D cell cultures, where several cellular behaviours were observed upon external biochemical and biophysical stimuli. However, these systems often lack the basic requirements due to their simplicity and inability to mimic the convoluted biochemical and mechanical microarchitecture. With the advancements in microfabrication techniques, the development of microfluidic technology emerged, and the existing limitation of classical static cell culture models were overcome. Advanced techniques were established to create the characteristics of human & animal tissues and organ structures beyond pure traditional cell cultures[91,92].

Various materials and techniques can be used to create microfluidic platforms for cell studies. They are generally developed using microfabrication techniques such as photolithography, laser printing, contact printing, injection molding, 3D printing, and soft lithography. The materials used include polydimethylsiloxane (PDMS), polycarbonate (PC), Teflon, PMMA, Agarose, etc.[93,94]. The most common microfluidic platforms are still based on PDMS-based soft lithography, due to its transparency, flexibility, oxygen permeability, possibility for high-resolution optical imaging, and simplicity and low cost[95,96,97–99].

Microfluidic cell culture systems can be composed of single or multiple microchannel networks connected via micro-chambers[100–102,103], with the aim to recapitulate the physiological and pathological complexity of the *in-vivo* situation. Such 2D microfluidic systems have been used to study cell differentiation[104,105], neurite extension from neural cells[106–108], cell migration[109] etc., and enabled the generation of chemical concentration gradients. However, 2D microfluidic systems have several limitations due to the inability to form the 3D microenvironment required to mimic the *in-vivo* situation. 3D microfluidic platform has since emerged by incorporating 3D microenvironments through biocompatible hydrogel-based scaffolds, which can provide a well-defined biochemical environment for cells to overcome the limitations available in 2D microfluidic systems[110,111].

Microfluidic platforms have also been designed to incorporate analytical biosensors for the detection of physiological parameters in cell cultures. These biosensors provide fast, rapid and sensitive measurements on small cell population or single cells[91].

2.3.2 Brain-on-a-chip (BOC)

Brain-on-a-chip (BOC) microfluidic model systems, established by any of the above mentioned technologies[112–114], can be designed to provide cells the ability to organize, proliferate, and differentiate inside the chip by delivering the appropriate nutrient, growth factors etc[115]. They can be designed to perform multiple activities by introducing sensors that can be used to evaluate individual cellular behaviour, and various physiological, pharmacological, and biochemical aspects of the cells[116,117]. Several BOC systems have been developed to study e.g., mitochondrial transport mechanisms in dopaminergic neurons[118], stem-cell derived neurons[102,120,121] neurovascularization[122], CNS axon propagation[123], blood–brain barrier (BBB)

function[124–129], brain tumours[130,131], Alzheimer Disease (AD)[132,133], and various neurotransmitter function[134].

Stem cells, which have the ability to self-renew, proliferate, and capability to differentiate into various cell types[135,136], are frequently used in BOC systems. Neural Stem Cells (NSCs), Embryonic Stem Cells (ESCs), and Human Induced Pluripotent Stem Cells (hiPSCs) have been utilized as potential neuro-regenerative cell models[137–140]. The microencapsulation of stem cells was studied in a BOC for localization and delivery of single stem cells to a target site, enhancing cell viability and promoting the exchange of nutrients and waste with the surrounding environment, due to the encapsulation[141,142].

2.3.3 Compartmentalized BOC Systems

Microfluidic technology allows us to reconstruct sophisticated physiological microenvironments to study multicellular phenomena with high complexity and control, along with integration of multiple assay functions on a single compartmentalised microfluidic chip (CMC). This has proven to be a powerful tool to establish and examine neuronal projection and interaction in co-cultures[120].

A CMC consist typically of two main segments: i) two or several separate cell culture compartments that are interconnected through a ii) microchannel array. The microchannel array directs and guides the axonal growth between the separated compartments, without allowing the cell bodies of the neurons to migrate through the channels. The axonal projections from one compartment to the opposite are usually due to associated flow difference and hydrodynamic pressure gradient between the compartments[143,105,144].

Richard B. Campenot designed the first pioneering experiments in 1977[145] to control axonal outgrowth in compartmentalized chambers (Figure 2.2ab). In 2003, the first PDMS-based CMC was fabricated for studying axonal growth through microchannels where the ability to direct the neural attachment site and projection of neurite growth was controlled by micropatterned poly-lysine (PLL)[146]. Figure 2.2cd, shows the typical PDMS CMC device commonly used for co-culture studies[107].

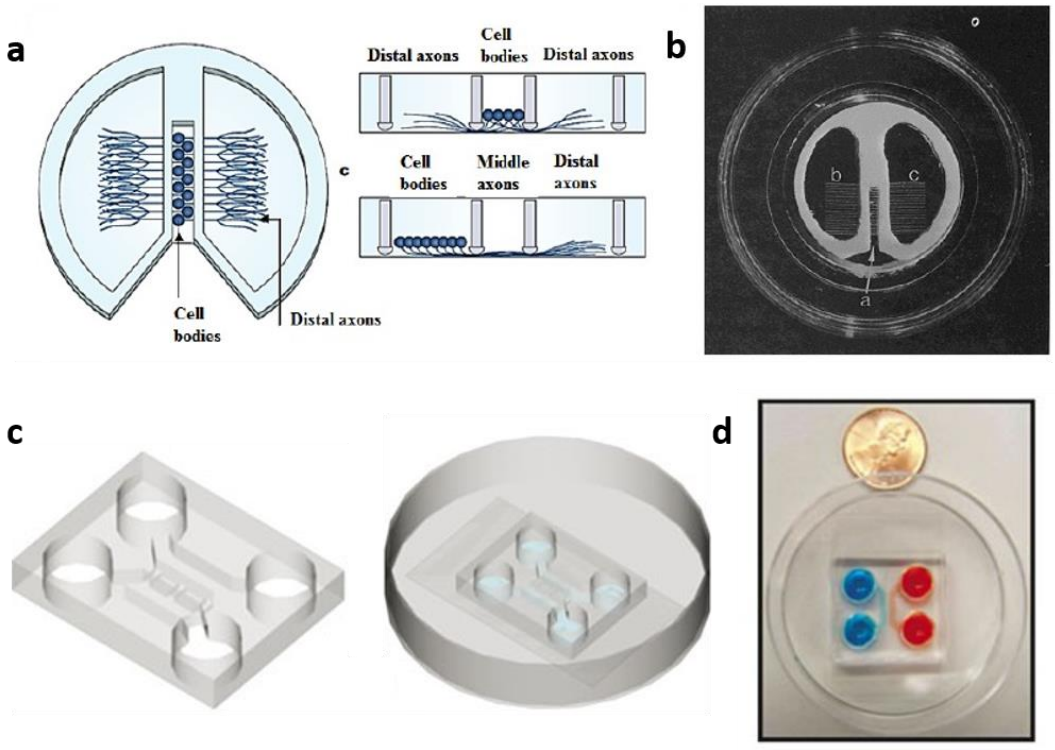

Figure 2.2: Compartmentalized microfluidic chips: a) Schematic representation of Campenot´s CMC device with neurites and cell bodies isolated due to the presence of microchannels[147] and b) the real Campenot prototype[145]. c) Schematic of a PDMS based neuronal culture CMC device with microchannels attached to a glass substrate with the real device shown in d) with fluidic dyes representing microfluidic behavior, adapted from[107].

CMCs have been used to establish and evaluate the neuron-neuron interactions and intra-neuronal signalling, neuron-glial interaction, axon signalling, regenerations and synapse formation and function[148]. A multi-compartment device, where neuronal synapse interaction between two different neural populations was studied (figure 2.3Aa,b), and compartment for microfluidic perfusion was introduced to access and exploit potential synaptic zone inside the microchannels (figure 2.3Ba,b), furthermore the projections and function of axons and dendrites were evaluated using the voltage-clamp technique[149] ,(figure 2.3Ac). Similarly, neuronal and glial cells were co-cultured in separated compartments where neuron-glia synapse formation was confirmed using calcium imaging[150].

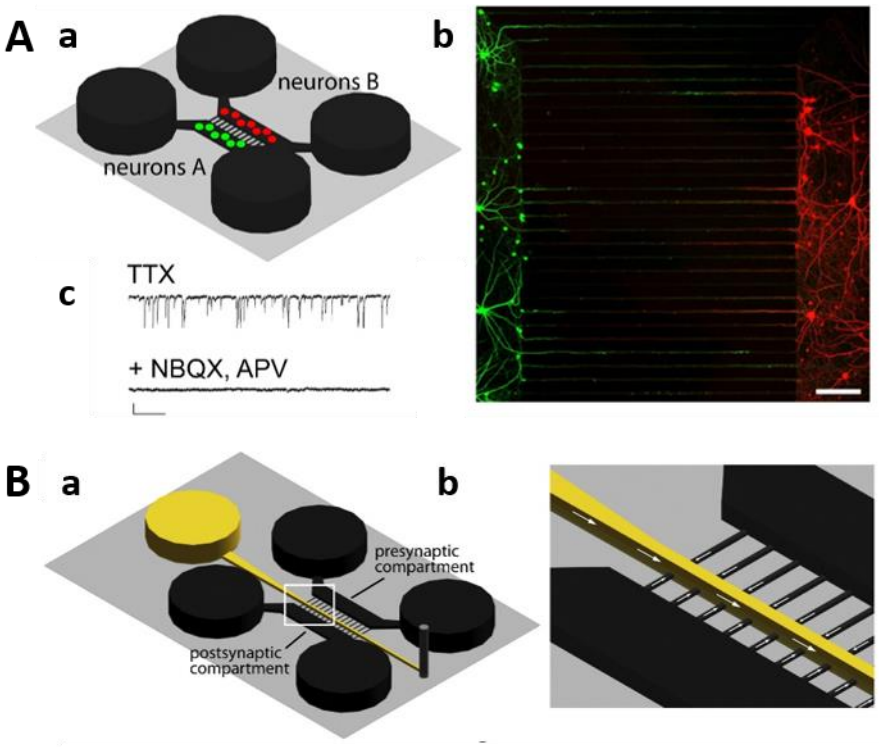

Figure 2.3: Schematic for multi-compartment CMC device. A) PDMS-based 2-compartment device with a) two independent neuronal population synaptically connecting through microchannels (900 μm x 7.5 μm). b) Neurons sending projections and developing connections within the microchannels, GFP (green) and RFP (red), scale bar 150 μm. c) Synaptic activity confirmed using voltage-clap technique. B) PDMS-based 3-compartment device, a) microfluidic perfusion introduced in third compartment (yellow) in the b) direction of arrows (white) to access microchannels, figure adapted from[149]

The part of the brain with unidirectional synaptic connection (e.g., cortex, hippocampus) was constructed to imitate two subpopulations of primary hippocampal neurons with directed connectivity grown in microchannels[6]. The author proposed ten types of microchannels with various shapes and sizes to promote growth dominantly in one direction, see figure 2.4a-b. It was found that the neuronal projections were primarily observed in the desired direction, from the source to the target compartment. While reverse neurite projections were also observed from the target to the source compartment, these projections could not continue and remained trapped due to the triangular trapping segment (Figure 2.4a). Multiple trapping sites were also considered, but one trapping segment was found to be sufficient for unidirectional projection.

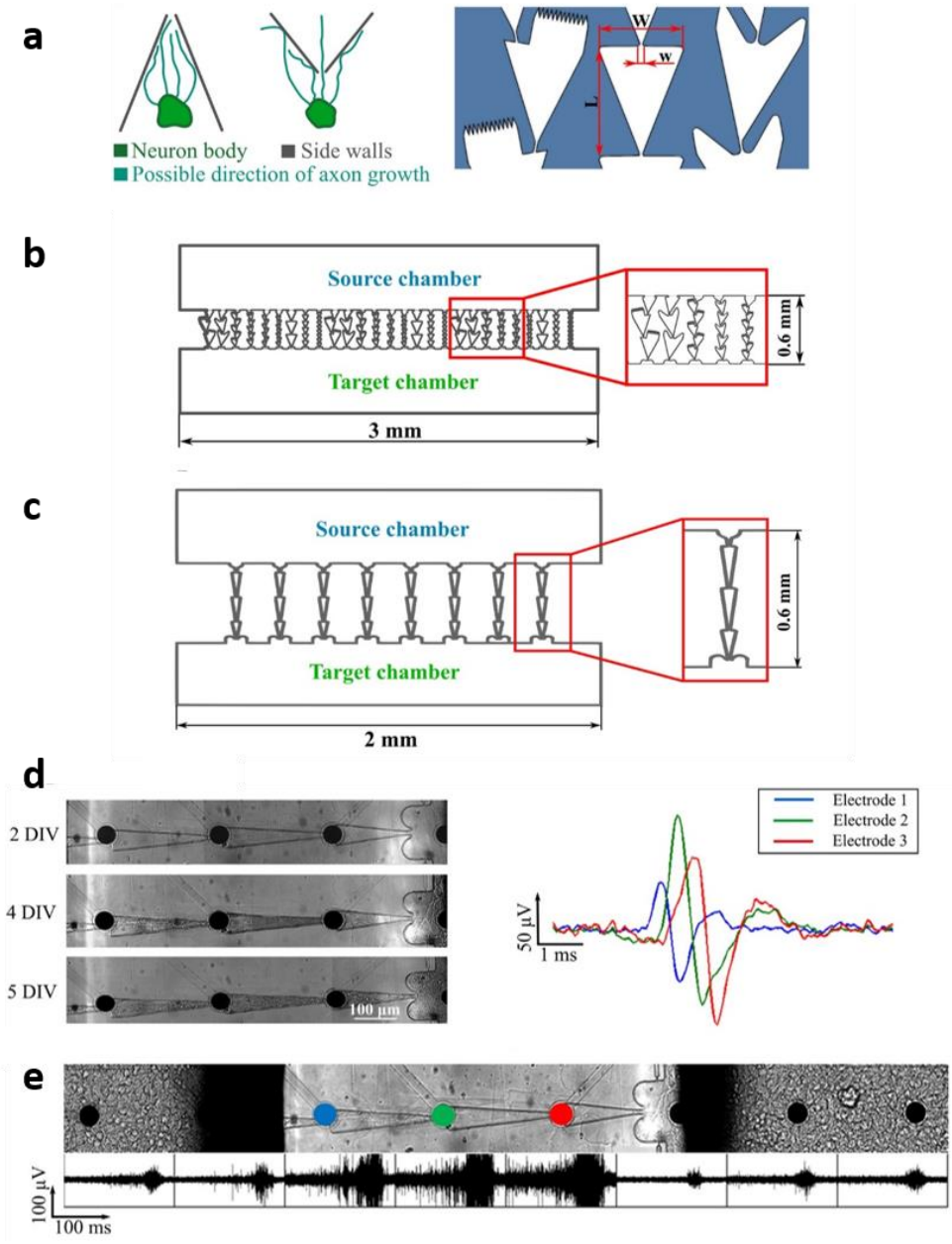

Figure 2.4: Schematic for unidirectional axon growth. a) Schematics of an axon travelling through triangular bottleneck with the width and Length indicated, b) 9 different triangular bottleneck microchannel designs and c) one with only bottleneck design. d) Microelectrode array placed inside the channels with signal recordings from axonal projections at 3 electrodes. e) Higher signal bursting activity recorded inside the channels as compare to electrodes inside the compartments, figure adapted from[6]

A new CMC fabrication technique was recently demonstrated by novel 3D printed-soft lithography, to avoid the manual handling, misalignment errors, low reproducibility and the risk of damaging features during dicing out procedure in conventional PDMS soft lithography. The

new patterning procedure allows fast prototyping, creating micropatterns with high-ratio features, and unfolds the possibility of the prospect materials for soft lithography techniques.

In this study, the open-well compartmentalized device that contribute to the long-term differentiation of sensitive human neuronal stem cells (hNSCs) into healthy neurons and astrocytes has been reported by 3D printed-soft lithography. Furthermore, in-vitro reconstruction of the nigrostriatal pathway, as a proof-of-concept has been developed in the fabricated CFM device[8], see figure 2.5.

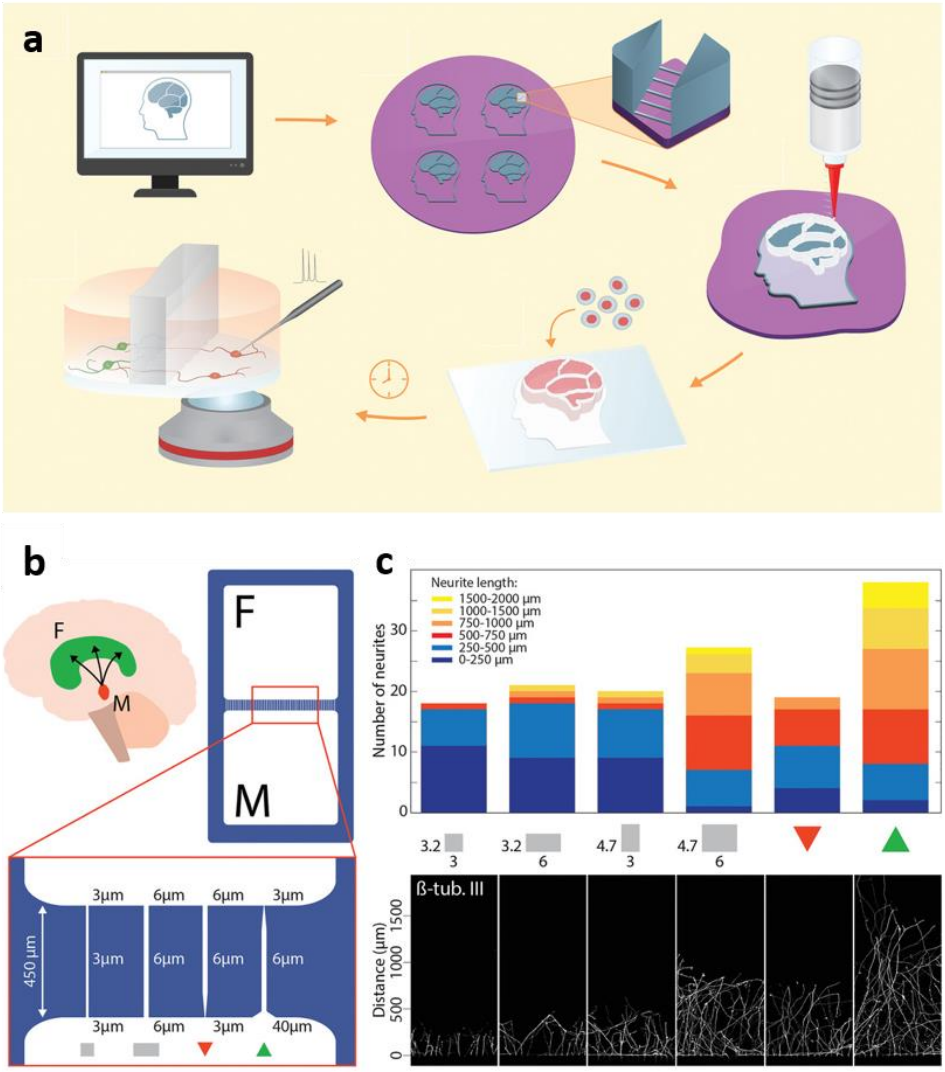

Figure 2.5: Schematic of the 3D printed soft lithography process. a) Design of mask in CAD, fabricating a mold on silicon wafer, direct 3D printing of PDMS on silicon wafer, followed by cell culture studies and optical and physical inspection. b) Schematic of nigrostriatal pathway and a two-compartment CMC (F=forebrain, M=midbrain) with various unidirectional microchannel shapes and dimensions. c) Axonal growth in different channels representing the effect of channel shape and dimension, figure adapted from[8].

Various types of activities have been studied, e.g. synaptic plasticity[151], neural circuit formation[6], axonal growth and regeneration[152], axonal transportation[118] and Huntington´s diseases modelling[153]. In-vitro analysis of neuronal network activity is an essential part of modern brain disease modelling, neuropharmacological trials, and neurotoxicological screening[154,155].

More and more advanced CMCs are emerging allowing the interconnection of multiple compartments to study the interaction between several different neural cells types[156,120] and/or introduction of optical and electrical sensing capabilities[6,8,157] to record neural activity and the communication between different compartments.

2.3.3.1 Electrophysiological sensing

Patch-clamp electrophysiology remains a crucial technique in studying ion current channels and allows high-resolution recording of the ion current flow through a cell's plasma membrane. It was first described by Neher and Sakmann in the 1970s[158]. However, the patch-clamp technique suffer from challenges as the method itself is quite laborious. These challenges include positioning of the patch pipette towards a cell membrane, requires skilful handling, careful electrode fabrication, and to maintain the apparatus with low-noise signal recordings.

An alternative approach has come with the introduction of the microelectrode array (MEA), designed with multiple electrical sensing sites in close proximity on a common substrate. Several studies have been established using MEAs to study neural activities from cultured neurons and axons [159–161]. MEAs have been introduced into CMCs to record the neuronal pathways and their response along the projections of axons in the microchannels, as shown in Figure 2.4c-d[6]. Microchannels incorporating MEAs in CMCs have revealed both transient and slow changes in axonal conduction velocity, which could lead to a new path in stimulation-induced axonal plasticity[162]. hPSC-derived neurons have been cultured in MEA containing microchannels with spontaneous electrical activity recorded in the channels. The study focuses on detecting signal mechanism, facilitated through CMC device among entire hPSC-derived neuronal networks, not only containing axons but also somata and dendrites. In total 8 different microchannels dimensions, with a width of 100, 500, 750, and 1500 μm, along with two different height of 43 μm and 105 μm were tested in combination.

The result shows sufficiently greater percentages of neuronal activities (52–100%) recorded inside the microchannels onto the electrodes compared to the control (27%) with no CMC device. The obtained activities have also been observed that significantly higher peak amplitude and burst counts were acquired from the electrode inside the microchannels. Moreover, neurons with wider channels and lower height represented a higher activity level than the lower width channels. Figure 2.6ab shows the signal comparison of two width dimensions of 100 μm and 1500 μm, respectively. It can be seen that signal frequency and amplitude are recorded higher with 1500 μm width dimensions[7].

In another study, involving activity-dependent myelination with co-cultured neurons and oligodendrocyte, concluded that electrical stimulation through MEAs promotes the generation of myelin segments[157].

Many studies have been performed with MEAs in CMC devices to manipulate the axonal growth, e.g. using high-frequency electrical field applied to the axons in the microchannels[163], with collagen-induced scaffolds[164], and (one-photon & two-photon) optical triggering with electrical recordings into the microchannels[157].

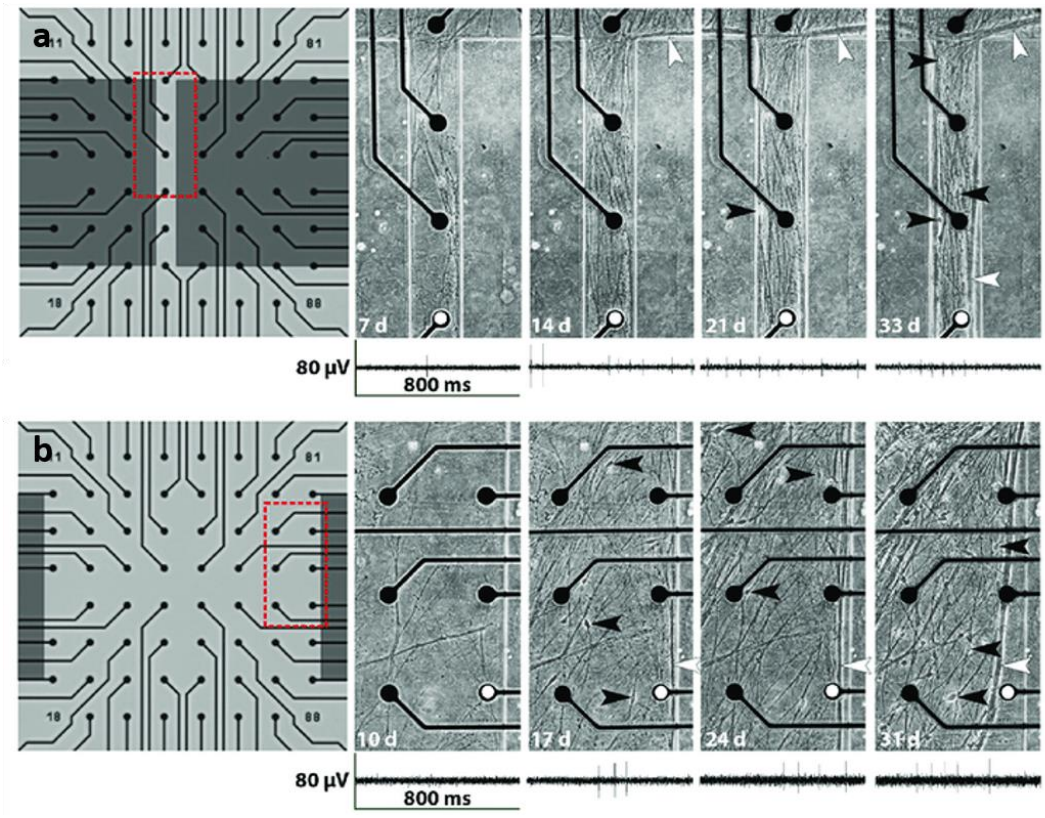

Figure 2.6: Axonal development of hPSC-derived neurons on MEAs. a) Narrow channel region with height (h) = 43 µm and width (w) = 100 µm. b) Broad channel region with h = 43 µm, w = 1500 µm. Signals were recorded (bottom right images of a & b) on different days. Cell bodies (soma) are indicated with black arrows and neurites with white arrows. The highest signals were recorded in the broad region in figure b, figure adapted from[7].

2.3.3.2 Electrochemical sensing

Electrochemical techniques plays a crucial role in the understanding of neuronal cell behaviour and for the detection of neurotransmitters. Electrochemical impedance spectroscopy (EIS), fast scan cyclic voltammetry (FSCV) and chronoamperometry (CA) are techniques that can be used to assess specific responses from neural cells.

EIS provides real-time and non-invasive analysis for the characterization of neuronal cells that includes monitoring of cell adhesion, cell proliferation and differentiation, apoptosis, and degenerative processes[121,165]. CA[166,167] and FSCV[168,169,170] can be used to detect the fast exocytotic release of neurotransmitters like dopamine from neural cells.

The pioneer experiments to detect real-time dopamine exocytosis through electrochemical technique was carried out by Wightman et al.[167] using carbon fiber microelectrodes (CFME). Afterwards, several researcher utilized the CFME technique to acquire vesicular exocytosis from single cells with greater spatial resolution[171–174]. However, due to challenges in CFME technique, such as, recording activity from single cell at a time, difficulty in positioning of the fiber near to cell membrane, targeting at a fraction of cell membrane and time-consuming process, a better approach is required. The challenges associated with CFME has been alleviated by the development in microfabrication lithography techniques[175,176,177].

Recent advancement in fabrication techniques has resulted in MEA designs with promising electrochemical properties, which make them ideal for neural studies, e.g., electrochemical sensing at multiple sites at the same time, and with high spatial resolutions[178–183], along with the flexibility of dimensions and material of interest (e.g., Au, Ti, Carbon)[184–186].

Exocytotic events of the release of dopamine from PC12 cells were recorded by amperometry on MEA chip with 16 independent graphitic-diamond based microelectrodes, each with an active area of ~200 µm^2, fabricated using chemical vapor deposition has been discussed where the signal was recorded only on eight electrodes, see figure 2.7a[184]. In another study, MEA-based 25 gold electrodes of 30 µm each have been fabricated by conventional lithography with an inter-electrode distance of 300 µm to detect dopamine exocytosis from PC12 cells. The

dopamine exocytosis was performed on one or two electrodes at a time, and other microelectrodes were used as counter and reference electrodes on-chip[11], see figure 2.7b. Figure. However, most of the reported applications do not demonstrate simultaneous & individually addressable MEAs with smaller dimensions.

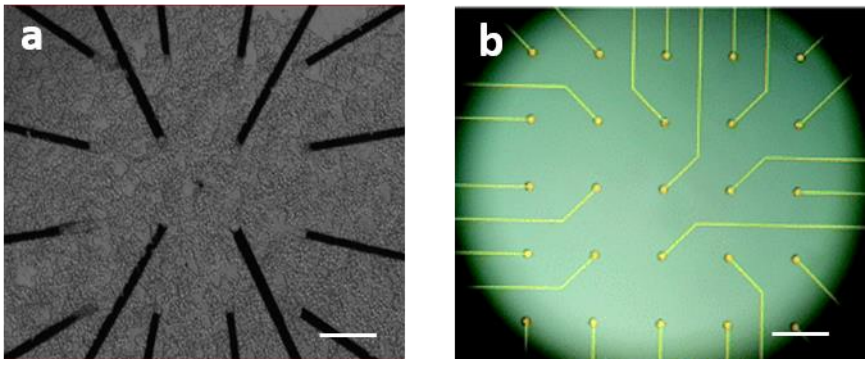

Figure 2.7: Optical images of MEA chips for DA detection: a) 16 graphitic-diamond based microelectrodes, with an active area of approx. 200 μm^2 – fabricated by chemical vapor deposition technique[184], scale bar 200 μm, b) 25 gold microelectrodes - fabricated by conventional lithography with 30 μm diameter electrode and 300 μm interspace between each electrode[11], scale bar 300 μm, figure adopted from[11,184]

With the above mentioned technological advancement in multi-compartment CMC incorporating different sensing approaches, unique methodological perspectives can be foreseen to strengthen future NDD models. In relation to this, my thesis work has focused on fabricated different ultra-microelectrode arrays UMEAs & MEA designs that could be used in various future aspects of NDD modelling, e.g. for electrical stimulation and electrochemical detection of specific neurotransmitters which would be attractive and significantly increase the understanding of neural communication at subcellular scale.

In chapter 3 (paper I), I present a new electrochemical UMEA design. This UMEA chip, incorporates 54 closely spaced individually addressable ultra-microelectrodes UMEs in gold (with either 5 or 10 μm sized electrodes) providing the capability of simultaneous addressing & potentially recording the distributed exocytosis events from a single cell or cell population upon various stimulation mechanism such as electrical, optical or chemical, here with preliminary experiments conducted using PC12 cells.

The current MEA-based studies lack this ability and focuses on larger electrode dimensions and interspaces. So far the idea of individually addressing ultra-microelectrodes in an array,

along with simultaneous recordings of more than 8 to 16 electrodes has not implemented[185,186,11]. The novelty compared to the state of the art is that these UMEA chip designs can provide valuable data statistic of the behaviour of a neuronal population upon electrical, chemical or optical triggering on all 54 UMEs simultaneously. This is not possible in CFME, where the activity at single cell is recorded and only targets a fraction of the cell membrane to record events.

In chapter 4, I present a two-compartment PDMS based CMC, equipped with a specifically designed gold MEAs, that can probe the two different compartments individually; the future aim being to study the communication between different neural phenotypes placed in each compartment by stimulating cells electrically, optically or chemically in one compartment and monitoring the release of neurotransmitter in the other. The mold for the PDMS based CMC was moreover fabricated using a simple micro-milling approach, to avoid expensive cleanroom-based micropatterning techniques.

Additionally, three gold MEA-based chip designs are presented intended for on-chip detection of neural activities. Each MEA chip design incorporates multiple individual addressable electrodes and serves a unique purpose, such as electrical stimulation to guide & enhance neural differentiation, dopamine exocytosis recording upon electrical, optical, or chemical triggering and monitoring cell proliferation and differentiation. These MEA designs consist of individually addressable interdigitated electrodes (IDEs) and microelectrode array (MEAs) arranged in different geometrical formats. The utilization of each MEA chip design is discussed in chapter 4.

Chapter 3

ULTRAMICRO ELECTRODE ARRAYS (UMEA) AND THEIR APPLICATION FOR CELLULAR EXOCYTOSIS STUDIES

This chapter introduces the challenges in fabrication of ultra-microelectrode arrays (UMEA) on a glass substrate, their electrochemical characterization, and application for cell exocytosis measurements.

3.1 Introduction

An ultramicroelectrode (UME) is defined to describe microelectrodes, where at least one dimension is smaller than the diffusion layer thickness of the target analyte[187,188]. The diffusion profile for the transport of electroactive species at planar macro electrodes is usually linear while, on the other hand, the diffusion profile on UMEs is radial or hemispherical. The small dimensions of UMEs play a vital role in, e.g., biochemical, analytical, and environmental applications, as well as capillary chromatography detectors and single-neuron analysis[189–191]. In this scenario, neural studies on arrays of UMEs (UMEAs) provide multi-fold advantages over traditional electrode setups: The ability to 1) record electrophysiological and electrochemical responses for long duration, 2) investigate interactions between neurons as well as neurons and other cells in non-invasive manner, and 3) function as neural interfaces in long-term prosthetics devices[192,193]. Several well-established UME based in vivo and in vitro neuronal studies have been conducted to date by employing planar surface inlaid carbon fibre electrodes [194,195], whereas very few studies have been conducted using UMEAs in both in vitro and in vivo experiments.

We have introduced the concept of dense electrochemical UMEAs with multiple recording sites fabricated using maskless photolithography. At the same time, each site is individually addressable through a connection track between the UME opening and contact pads. The fabrication of UMEAs having UMEs of cellular and subcellular dimensions aimed at the study of

neural responses from single cells in a population. Simultaneous recording of electrochemical responses on each UME was facilitated by 54-channel potentiostat developed through a collaboration in the EU financed FP7 project EXCELL. In this study, UMEAs were used to detect dopamine exocytosis from single rat pheochromocytoma (PC12) cells in a population.

3.1.1 Design of UMEA chips

The fabricated UMEA chips comprised 54 individually addressable disk-shaped UME recording sites (working electrodes, WEs) with dimensions of 5 µm and 10 µm in diameter, connected to 1 mm diameter contact pads via insulated tracks. The chips also had an on-chip counter (CE) and a pseudo-reference electrode (RE) in the proximity of the 54 WEs. In order to avoid fouling and errors in the electrochemical current[196] dynamic electrochemistry, the dimension of the counter electrode and the reference electrode was kept much larger with respect to the WEs, i.e., 250 µm and 100 µm in diameter, respectively. The UMEA chips were fabricated on 4-inch glass wafers by utilizing maskless UV-photolithography, thin-film metal deposition, and deep reactive ion etching (DRIE) in a cleanroom environment. The schematic presentation in figure 3.1 further explains the layout of the UMEA chips.

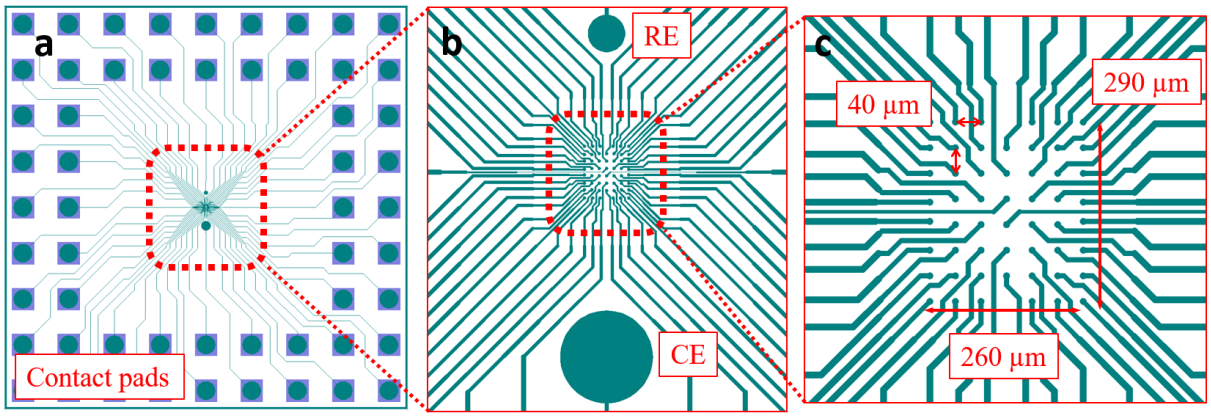

Figure 3.1. CAD design of UMEA chip: a) Layout of a complete UMEA chip (22 x 22 mm^2) with individually addressable contact pads, b) Zoom-in view of the contact tracks from the WEs as well as the CE and RE, and c) a further zoom-in view showing the 54 recording sites tightly packed with interspace of 40 µm and total array area of 260 µm X 290 µm.

3.2 Fabrication of UMEA chips

The UMEA chips were fabricated on 4-inch glass wafers due to their transparency as cell culture analysis would require inspection through an inverted microscope. The conventional fabrication techniques, previously optimized for silicon wafers, were utilized and adapted for

glass wafers. Because of different wafer material, several fabrication processes had to be reoptimized. The concerned parameters and associated challenges are discussed further in detail in section 3.3 below, the process involved in the fabrication of UMEA chips is explained.

1. Because of the particular requirements, the wafers were preheated and subjected to hexamethyldisilazane (HDMS) priming treatment that enhances the adhesion of photoresists on glass substrates (figure3.2a). The negative tone photoresist AZ nLOF 2020 (MicroChemicals GmbH) was spin coated at 5000 rpm for 30 seconds on the glass wafers and baked at 95 °C for 60 seconds to achieve 1.5 µm thickness (see figure 3.2a-b).
2. The traditional UV-lithography exposure was entirely replaced by direct-writing maskless aligner (MLA) system (Heidelberg, MLA 150, Heidelberg, Germany), which defines a pattern through a CAD file without the need of physical photomask production. The exposure doses were optimized and selected for 1.5 µm thick, AZ nLOF 2020 photoresist, which are explained in section 3.3.2. MLA-based UV exposure of a single wafer took 15 min. After the first exposure, the wafers were post backed at 110 °C for 60 seconds and developed with negative developer AZ 726 MIF for 1 min to remove uncross-linked photoresist from the exposed patterns for further processing (see figure 3.2b).
3. Using the developed photoresist as an etching mask, the glass wafers underwent buffered hydrofluoric acid (BHF, 12% HF in ammonium fluoride) wet etching to obtain approximately 220 nm deep grooves with isotropic etching profile to deposit metal layers for the electrodes (WE, CE & RE), connecting tracks and contact pads (see figure 3.2c).
4. The next step involved metal deposition through electron beam (e-beam) evaporation (FerroTec TEMESCAL). The wafers were coated with a 20 nm layer of Ti or Cr followed by 200 nm of Au at the deposition rate of 3 Å/s and 5 Å/s, respectively (see figure 3.2d).
5. The lift-off process was conducted for 1 hr by Remover 1165 (Shipley Co.) in a dedicated ultrasonic bath in order to strip-off the metal coated photoresist, thereby resulting in patterned metal structures. The glass wafers were then rinsed in an ultrasonic bath with isopropyl alcohol (IPA) followed by rinsing with distilled water to remove residual metal and photoresist particles as well as the Remover (see figure 3.2e).

6. To insulate the metal tracks and open active electrode areas and contact pads, two different approaches were tested:
   a. Initially, 500 nm of silicon nitride (Si_3N_4) was deposited through plasma-enhanced chemical vapor deposition (PECVD) followed by a careful second exposure alignment using MLA via a CAD design to define the metal features to be revealed, i.e., the electrodes and contact pads. After the second lithography step, the substrate was developed as in step 2 followed by an anisotropic DRIE process to remove the previously deposited Si_3N_4 layer from the areas where gold was to be exposed,
   b. To deposit a photoresist insulation layer, AZ nLOF 2020 was diluted with propylene glycol methyl ether acetate (PGMEA; 1:1 ratio) and spin coated at 2500 rpm followed by 1 min baking at 110 °C. The second exposure was done similarly as described above followed by development in AZ 726 MIF, (see figure 3.2f-g).

Figure	Process description	Step	Illustration
3.2a	Glass wafer HDMS treated	1	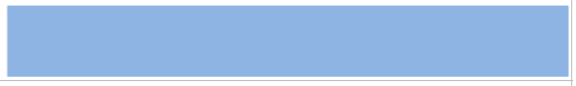
3.2b	After maskless-lithography	2	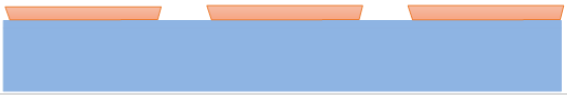
3.2c	After isotropic etch	3	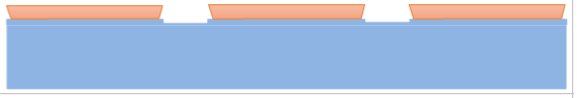
3.2d	After metal deposition	4	
3.2e	After lift off	5	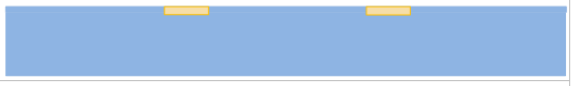
3.2f	After depositing insulation layer	6	
3.2g	After insulation layer opening	7	

Figure 3.2. Fabrication steps involved in fabrication of UMEA chips: Result after a) HDMS pretreatment, b) lithography using MLA, c) BHF etching, d) metal deposition, e) lift-off, f) insulation layer deposition, and g) opening of insulation layer to expose electrode and contact pads.

The electrodes and contact pads were then inspected under an optical microscope to assess whether the patterned openings in Si_3N_4 were properly aligned and Si_3N_4 or photoresist had been completely removed from the 5 µm and 10 µm electrode openings. The two fabricated UMEA designs are shown in figure 3.3.

The second exposure alignment and the reason for replacing the Si_3N_4 insulation layer by diluted AZ nLOF 2020 photoresist is further explained in section 3.3.4.

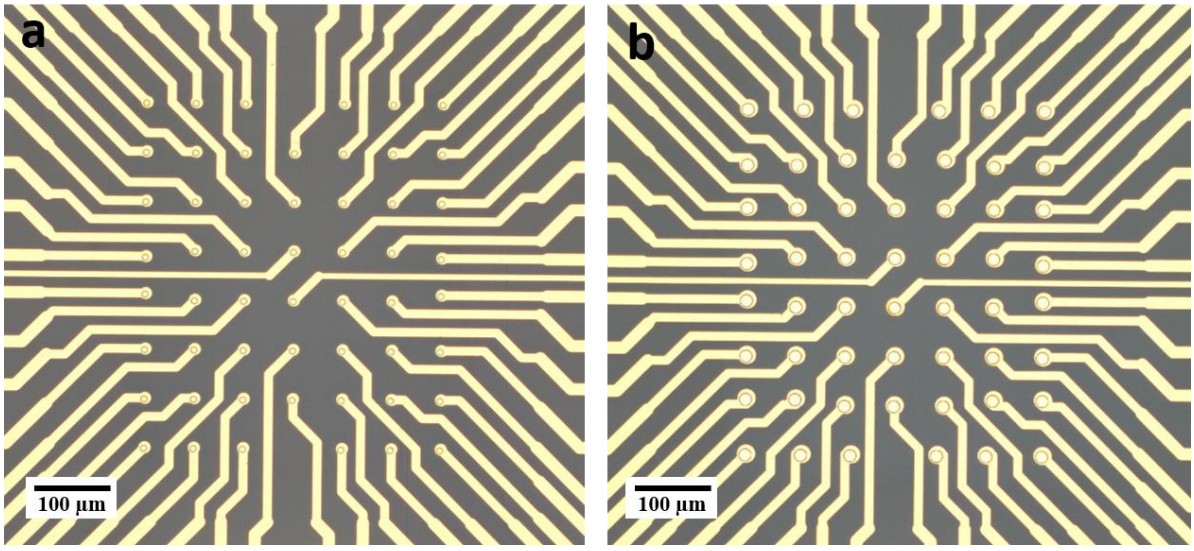

Figure 3.3. UMEA chips after completed fabrication: 54 individually addressable UME recoding sites after dealing with various challenges. A well-aligned insulation layer can be seen for both electrode opening dimensions: a) 5 µm and b) 10 µm in diameter.

3.3 Characterization of UMEA fabrication

3.3.1 Photoresist selection

The negative tone photoresist was chosen in order to minimize the formation of lift-off ears. These are mostly formed when using positive tone photoresists, which lead to the emergence of V-shaped overcut profile after development. As a consequence of this, during metal deposition the upward sloping photoresist side walls are covered by metal that is then partially ripped off during lift-off. The remaining metal sticks to the edges of the lithographically patterned metallized structures, such as connecting tracks and electrodes, resulting in formation of sharp, even hundreds of nanometres long, metallic fringes, lift-off ears, that easily break the insulation layer. This reduces the overall performance of electrodes and, ultimately,

allows electrolyte to access areas that should be insulated, leading to undefined electrode areas and even short circuiting of contact pads. On the other hand, when using a negative tone photoresist, an inverted V-shaped undercut is formed, which allows the photoresist and excess metals to be removed smoothly throughout the wafer during the lift-off process without influencing the patterned metal structures[10,197].

3.3.2 Exposure Dose test with maskless aligner MLA

The features were first tested for the required UV dose to expose a glass substrate with 1.5 µm thick photoresist through a maskless aligner (MLA). A dose test was performed by defining the test feature and testing the dose range along with the depth of focus to pattern with the maximum resolution. The dose and defocuse tests were performed using test features available from the manufacturer of the MLA system. The doses and defocus levels ranged from 100 to 500 mJ/cm^2 with an interval of 100 mJ/cm^2 and -5 to 5 with an interval of 1, respectively. It was observed that 400 mJ/cm^2 with -1 defocus were the most optimal settings. Figure 3.4 a-b show the results for two doses, 100 mJ/ cm^2 and 400 mJ/cm^2, respectively, which clearly show the difference in the effect of the doses. The dose used to expose patterns with MLA was higher as compared to the dose used by conventional mask aligners (MA-6 aligner, Suss Microtec), which is usually 200 mJ/ cm^2 for 1.5 µm thick AZ nLOF 2020 layer. One of the main reasons behind this difference is the UV light source used for exposing patterns, LED laser-diode in MLA and Mercury-Xenon (Hg-Xe) lamp in MA-6 aligner. The MA-6 aligner has an exposure intensity of 11 mW/cm^2 at 365 nm, while MLA uses 375 nm laser diode arrays[198–200].

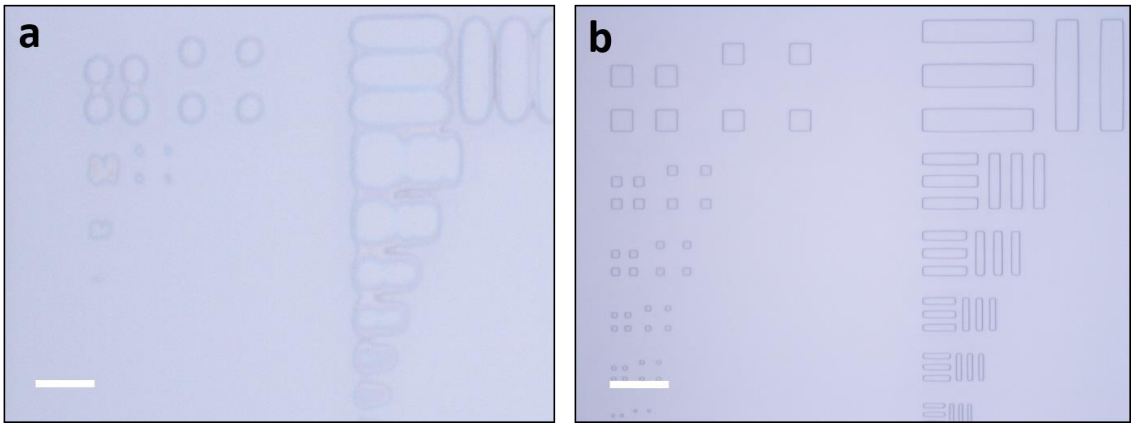

Figure 3.4. MLA dose optimization: For exposing AZ nLOF 2020 negative tone photoresist using a laser diode array, a range of doses were tested. The two most extreme effects are represented by a) 100 mJ/cm^2 and b) 400 mJ/cm^2, latter showing clear test patterns.

3.3.3 BHF Etching (Si vs Glass wafer)

The etching rate of the bath dedicated for BHF etching was approximately 85 nm/s as determined for silicon wafers. Due to fabrication on a different substrate, the etching rate had to be tested for various etching times combined with profilometry characterisation using the Dektek profilometer (Z-axis). After several iterations, the optimised etching rate for glass wafers was approx. 75 nm/min. Hence, to achieve a 220 nm grooves for metal deposition, around 3-min wet etching was performed on glass wafers (See figure 3.5).

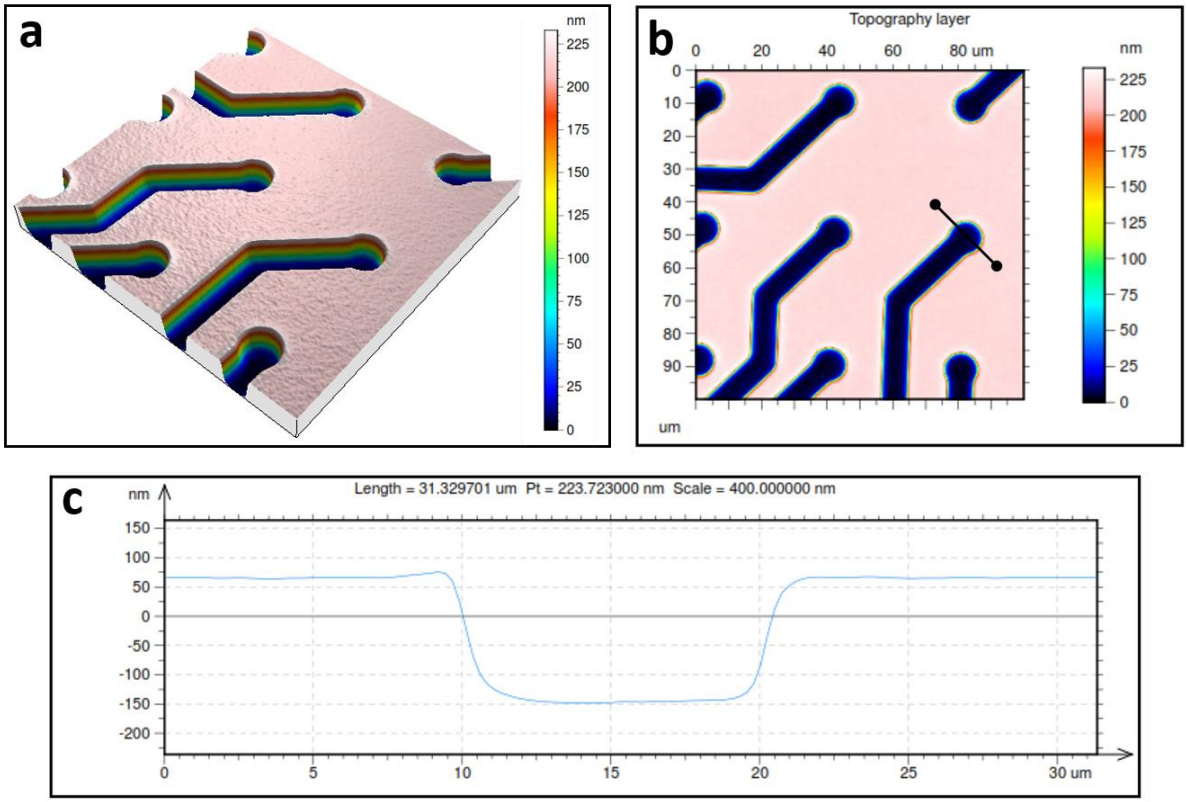

Figure 3.5. BHF isotropic analysis on glass wafer: a) 3D profile obtained using optical 3D imaging of the etched pattern on UMEA chips shown with color profile. b) The top view along with a cross-section line (marked with black) to record the depth. c) Z-axis line graph. The achieved height was approximately 220 nm as desired.

3.3.4 Alignment (Cross Images)

For the second exposure, the simple four crossed shape alignment marks (CSAM) with the coordinate location of [(-40,0)(40,0)(0,40)(0,-40)] on a 4-inch glass wafer were designed with navigation signs in order to alight the patterns correctly as shown in figure 3.6c-d. The alignment for second exposure was critical to the overall chip fabrication process as minor

misalignment could lead to complete failure of the fabrication of the UMEA chips (see figure 3.7a). Initially, square blocks and width of 100 µm CSAM were used as alignments marks, figure 3.6a-b respectively, which resulted in the alignment failure depicted in figure 3.7a. After careful consideration, the CSAM width was decided to be 5 µm as shown in figure 3.6c-d which was the minimum feature size available on the wafer patterns of the second exposure. A successful alignment was achieved after considering the reduced size CSAM. The UMEAs were observed for correct insulation alignment with optical microscopy (Olympus MX40) (see figure 3.7b).

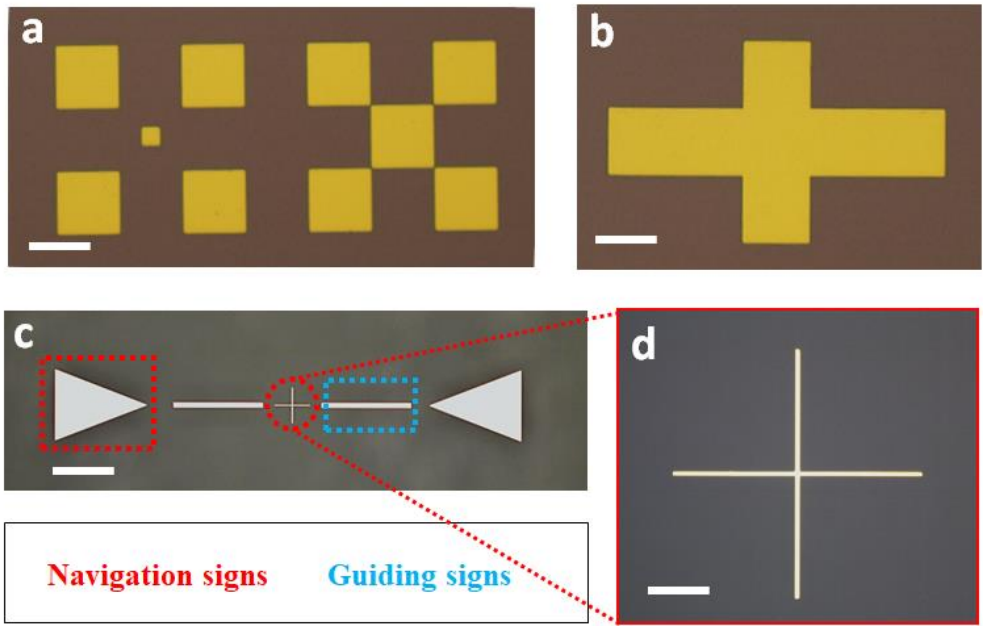

Figure 3.6. Alignment marks used during optimization: a) The very first traditional alignment marks mostly used in chrome masks for multi-layer exposure. b) Simple cross sign with 100 µm width used to expose the insulation layer that resulted in the failed alignment test (scale bar 100 µm). c) The navigation (red) and guiding (blue) marks for locating the alignment marks during the second exposure. d) The final alignment mark with 5 µm width used to achieve successful alignment.

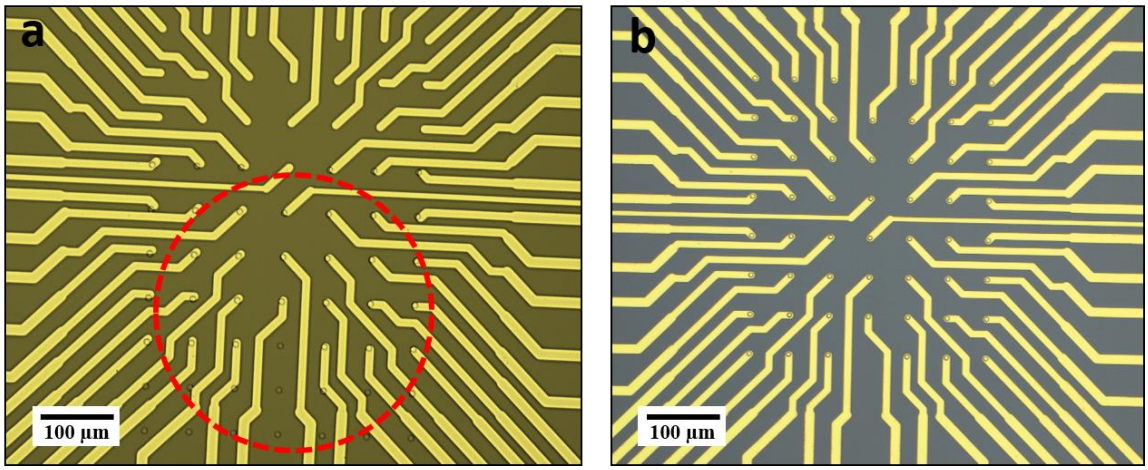

Figure 3.5. Misalignment correction. a) Major misalignment observed during the second exposure because of using traditional alignment marks as well as thick alignment marks in relation to the smallest features, 5 µm, in the design. b) Correct alignment with the smaller dimension of the alignment mark shown in Figure 3.5d.

3.3.5 Etching of insulation layer

The complete opening of all the 54 UMEs was crucial for the UMEA chip design to function correctly, which was a challenge during the advanced silicon etching (ASE) process. After depositing Si_3N_4 and performing the second exposure after careful alignment, the wafer was subjected to anisotropic etching using DRIE process in the advanced silicon etching tool. The anisotropic etching was considered due to the specific opening of 5 µm and 10 µm. On the other hand, isotropic wet etching provides an isotropic profile that would not be suitable for creating precisely 5 µm and 10 µm openings. Anisotropic etching is considered to be uncontrolled. Hence, the effect had to be evaluated. It has been observed that anisotropic etching creates multiple effects, such as rough metal surface, incomplete opening of the areas where gold has to be exposed after etching (e.g. electrodes and contact pads), and over-etching by completely removing the gold from the electrode sites (see figure 3.8a-b). Based on analysis, the observed problems were caused by non-uniformity of the wafer substrate due to the pressure exerted by the chuck holding the wafer.

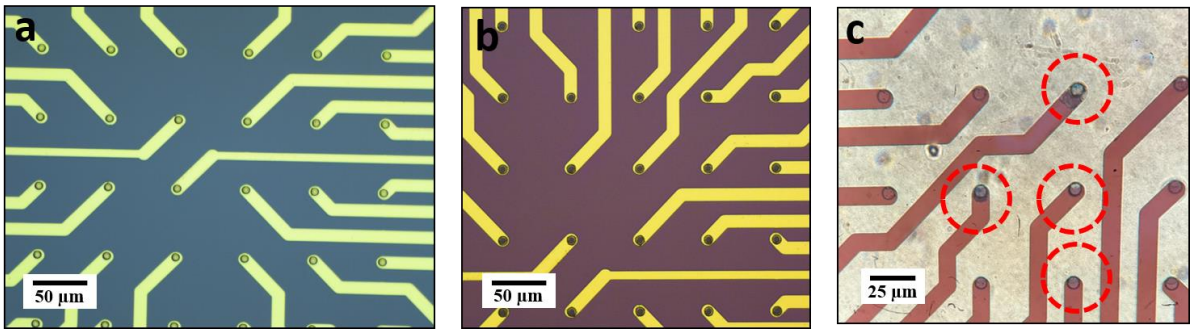

Figure 3.6. Advanced silicon etch optimization: a) Features not completely etched during anisotropic etching due to low etching power (the electrode openings were tested using electrochemistry). b) Over-etching, completely removing the gold from the recording sites aside from the insulation layer. c) Electrodes were corroded and ultimately dissolved during contact with electrolyte and electrochemical measurements due to the smaller side tolerance.

3.3.6 Elimination of electrode corrosion and dissolution

The highly dense UMEAs were designed carefully to accommodate the maximum number of recording sites in a small footprint. Initially, the 5 µm diameter electrode openings at the end of the 7.5 µm connection tracks were used in the design, which also caused low tolerance for misalignment during the second exposure. After successful alignment, the UMEA chips were characterised electrochemically to evaluate their suitability for cell studies to be performed on the chips. During electrochemical characterisation, it was observed that numerous UMEs out of the 54 on a chip, had been corroded and eventually dissolved after acquisition of the first electrochemical measurements, figure 3.8c. The reason was thoroughly investigated on several chips. Due to the low tolerance due to the 7.5 µm connection tracks and 5 µm diameter electrode openings, the only plausible reason was penetration of the electrolyte through the insulation layer into the gap between the deposited metals (Ti or Cr and Au) and the BHF isotropically etched grooves. This may have caused two simultaneous effects: 1) Mechanical detachment of the metals from the substrate, and 2) formation of a galvanic system between the non-noble adhesion metal (Ti or Cr) and Au, leading to partial dissolution of the adhesion metal that further aided the detachment of the metal layers. This issue was solved by the following strategies: 1) A low deposition rate was used for depositing the metals. Previously, the deposition rate was 10 Å/s but after optimisation it was 3 Å/s, which provided more flawless and smoother surface for the deposited metals[201]. 2) Adhesion between the substrate and the insulation layer was enhanced. Initially, we used S_3iN_4 material as the insulation layer.

Generally, S_3iN_4 provides strong adhesion onto silicon wafers and remains intact during experiments[10]. However, due to the different substrate material, the adhesion on glass substrates was not satisfactory for electrochemistry. Hence, the photoresist-based insulation was considered and used for further fabrication. The most promising strategy used was widening of the end of the connecting tracks where the opening was created in the insulation layer for the 5 µm and 10 µm diameter electrodes. It has helped in two primary ways: a) It provided more tolerance for alignment during the second exposure, and b) reduced the possibility for the electrolyte to reach the interspace between deposited metals and the isotropically etched groove (see figure 3.9). Section 3.5 describes the electrochemical techniques utilized and the performed UMEA characterisation to assess their suitability for the intended cell-based experiments.

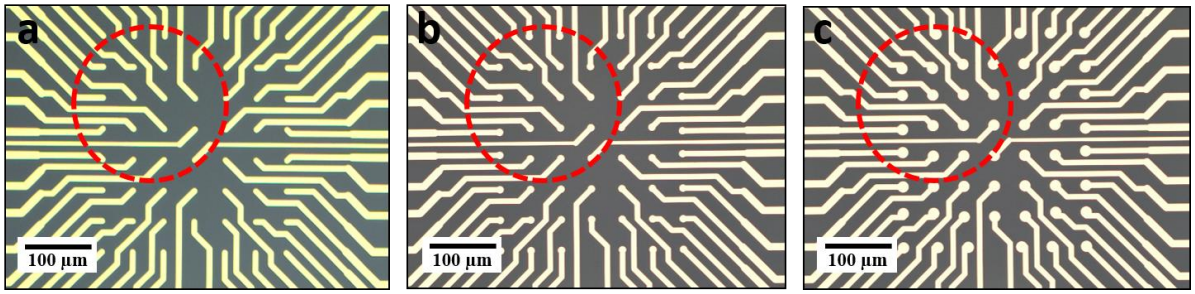

Figure 3.7. Widening of the ends of the connecting tracks. a) Initial design with trach width of 7.5 µm, provides low tolerance for electrode opening. b) Increased area with 10 µm width for 5 µm opening. c) Increased area with 15 µm width for 10 µm opening.

3.4 Micromilling of UMEA chip holder

3.4.1 Fast prototyping by micromilling

With the development of complex microchip and microfluidic technology, there is a demand for rapid prototyping of microchip devices for different applications. Currently, PDMS-based soft lithography is considered to be the universal fast prototyping technique[202,203]. However, this technique is highly dependent on the master mould of microstructures, usually fabricated in the cleanroom to obtain high resolution structures.

Recently, non-lithographic micropatterning techniques have been adapted for fast prototyping of microchip devices, including techniques like laser cutting[204,144,205], 3D printing[206,207,208] and thermal scribing[209,210,211]. These fabrication methods provide several advantages over traditional

cleanroom-based photolithography, such as fast design adaptation, quick prototyping, and cost-effectiveness. However, they often suffer from low resolution, need rigorous optimization, and have limited range of suitable fabrication materials. Micromilling is an alternative prototyping technique to fabricate microchip devices and provides a flexible approach for various design options, low manufacturing cost, time-efficient fabrication with considerable spatial resolution on a variety of materials[212–214]. However, proper handling and procedures are needed to implement the micron dimensions in a more precise, controlled and efficient way.

3.4.2 Chip holder design and fabrication

The chip holder consisted of a bottom and a top plate. The bottom plate has a defined indentation to accommodate an UMEA chip and screw holes for assembly (see figure 3.10a). The top plate has an open window with side shoulders, forming a well to access the UMEA chip and accommodate electrolyte and analyte solutions to perform electrochemistry or cell culture medium to enable cell culture studies (see figure 3.10b). The top plate also contains holes for pins to connect to the contact pads of the UMEA and screw holes for assembly and attachment to the potentiostat. All the polymeric components of the chip holder system were designed using AutoCAD 2015 (Autodesk, Inc., San Rafael, CA, USA) and micromilled using a Mini-Mill/3PRO system (Minitech Machinery Corporation, Norcross, GA, USA). The designs were further converted into a machine-readable format called the G-Code, using a machine-based EZ-CAM17 Express software (EZCAM Solutions, Inc., New York, NY, USA). Figure 3.10c shows the micro-milled and assembled (using 1.5 mm screws) UMEA chip holder to enable electrochemical characterisation of the UMEA chips and to conduct cell-based exocytosis experiments. I have employed this micromilling technique throughout my thesis for fabricating all chip holders and PCBs, but also as a way of fabricating the master-mold for creating a PDMS based CMC device (for further details see Chapter 4).

Milling is performed using a milling machine (Figure 3.10d) with different milling bits depending on the complexity and dimension of the required geometries. The milling substrate, in my case poly (methyl methacrylate) (PMMA), was first fixed onto the milling stage, using double-sided adhesive tape in multiple positions. The required bit was installed to achieve the desired dimension, and the spindle was initiated. A higher spindle rate was used with tools of a smaller

diameter. The first milling step involved shaving out the substrate to a certain depth in order to eliminate any unevenness of the substrate and milling stage. The second step involved milling of the pre-defined microstructures (geometry and holes etc) of the chip holder. The last step involved cutting out the milled structure from the PMMA sheet for further procedures. A compressed air gun was used to cool the workpiece and bit during the milling.

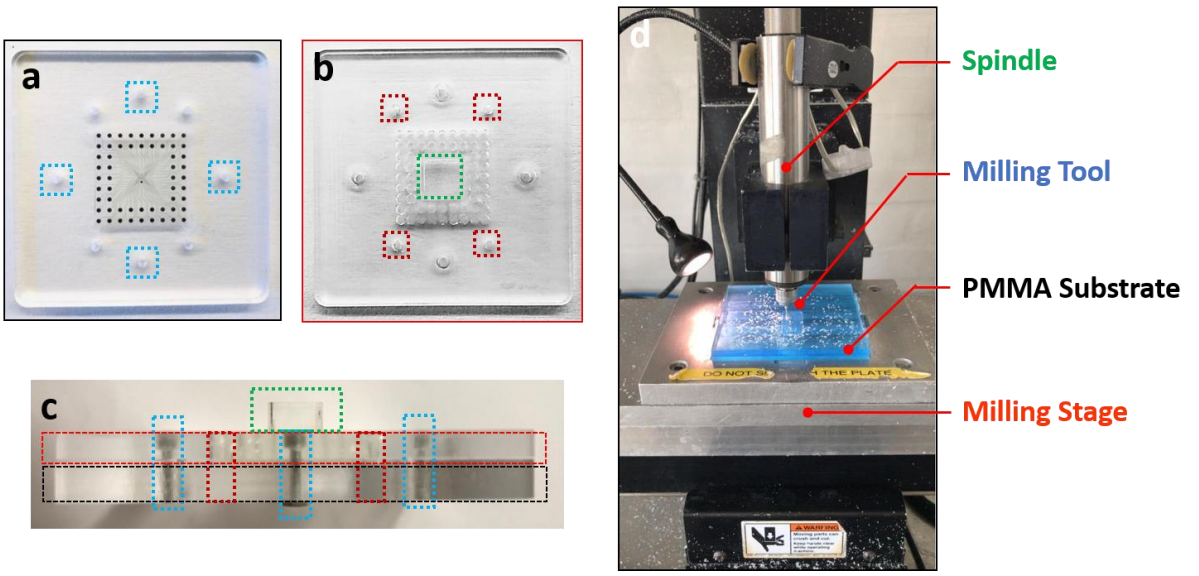

Figure 3.10. Micromilling of a PMMA based UMEA chip holder: a) The bottom PMMA plate with UMEA chip, and 1.5 mm diameter holes (blue) to screw top plate on, b) Top plate along with 1.5 mm diameter holes (dark red) to screw the system inside the potentiostat, open access window (green) for liquid handling, and holes for spring loaded pins for electric interfacing of the UMEA chip to the potentiostat. c) Side view of the assembled chip holder with top (red), bottom (black), screw (blue & dark red) and side shoulders of the access window (green). d) The micro milling machine used to fabricate the chip holders.

3.5 Electrochemical characterization of UMEs

The UMEA chip characterization were performed in the chip holder (Figures 3.10abc and 3.11b-c), while inserted inside a miniaturized custom-made 54-channel PCB-based potentiostat (POLIMI potentiostat)[215] suitable for electrochemical recording of the developed UMEA chips.

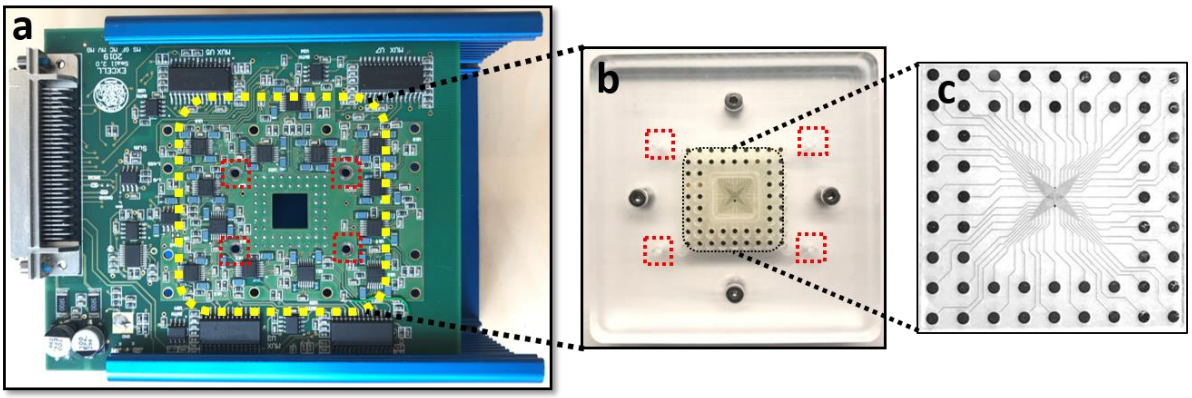

Figure 3.11. Electrochemical setup for recording on UMEA using the POLIMI potentiostat: a) The 54-channel POLIMI potentiostat (developed by Prof. Marco Sampietro´s group at Polytechnic University of Milan (POLIMI), Italy), was designed to individually address and record on all of the 54 UMEs[215]. b) UMEA chip holder for electrochemistry and cellular studies with c) UMEA chip placed inside.

The custom-made POLIMI potentiostat was developed with 54 individually addressable channels to record electrochemical activity using the UMEA chip[215]. The potentiostat is capable of performing cyclic voltammetry and chronoamperometry on the UMEs. The recordings function in serial fashion instead of parallel to make the circuitry design simple, comprehensive and more compact (see figure 3.11). The operational details are explained in a previous publication describing functions of and performance parameters of the circuitry[215].

3.5.1 Cyclic Voltammetry

Cyclic voltammetry is an electrochemical technique that measures the current response of a redox reaction at the working electrode resulting from a linear potential ramp versus time (see figure 3.12a). The potential may be scanned from, for instance, a higher potential toward a lower potential and reversed back. During cyclic voltammetric recordings the current is generally plotted as a function of the applied potential (figure 3.12b). Cyclic voltammetry is usually performed to gain understanding of the electrochemical properties of an electrode in a solution of electroactive species at an electrode surface [216].

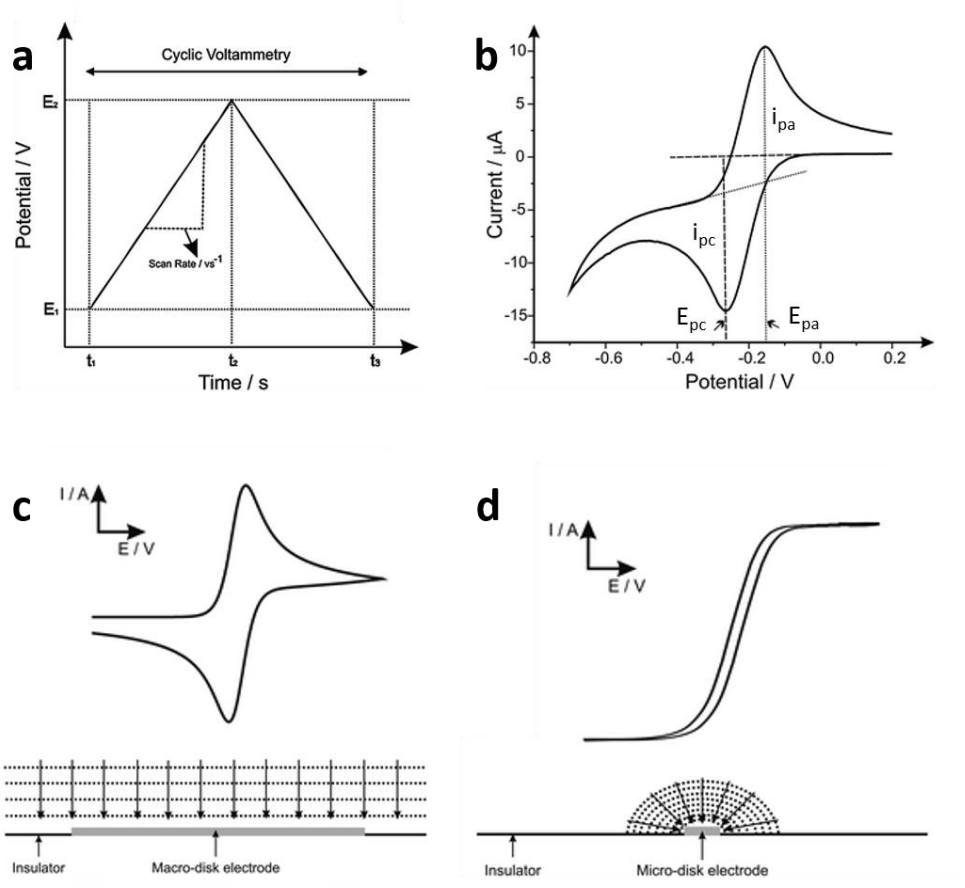

Figure 3.12. Cyclic voltammetry and its behavior on different electrodes: a) Potential sweep from a lower (E_1) to a higher (E_2) potential and back to the lower (E_1) potential as a function of time (t_1-t_2-t_3) generating a cyclic voltammogram (CV). b) A CV illustrating the anodic (oxidation) and cathodic (reduction) peak potentials, E_{pa} and E_{pc}, respectively and the corresponding peak currents, i_{pa} and i_{pc}, respectively. c) A CV for a macroelectrode showing the characteristic planar diffusion profile (bottom), and d) sigmoidal CV recorded for an ultramicroelectrode with the dominating radial diffusion (bottom). The figure is adapted from[217].

The characteristic features of a CV largely depend on the dimension of the electrode. When a macroelectrode is used, the planar diffusion of electroactive species is predominantly observed, resulting in the formation of a current peak due to diffusion limitation (figure 3.12c). On the other hand, at micro- or ultramicroelectrodes radial diffusion of electroactive spices is predominantly observed. As a consequence, the CV has sigmoidal shape, indicating the absence of diffusion limitation (figure 3.12c)[217]. It is crucial to understand the characteristic features of CVs in order to learn about electrode behaviour with an electroactive species.

CVs were acquired on all of the 54 UMEs of both 5 µm and 10 µm in diameter at the scan rate of 50 mVs^{-1} in phosphate buffered saline (PBS, pH 7.4) containing 10 mM of hexacyanoferrate(III/II)

($[Fe(CN)_6]^{3-/4-}$). Due to ultra-micron dimension, the diffusion of the electroactive species followed the radial pattern and hence the sigmodal CV response was observed on all of the 54 electrodes of both 5 µm and 10 µm in diameter. The average anodic and cathodic steady-state current values were (9.0 ± 0.8 nA) and (8.3 ± 0.7 nA), respectively, for the 5 µm diameter electrode opening and (20.8 ± 1.4 nA) and (19.4 ± 1.4 nA), respectively, for 10 µm diameter electrode opening. Further characterization with different scan rates was also conducted to demonstrate that diffusion was the mode of mass transfer at the electrode surface. Detail discussion of UME characterization can be found in Paper I. Figure 3.13a, illustrates the 54 CVs for UMEs of both 5 µm and 10 µm in diameter.

The goal for characterizing the electrochemical response of the 54 UMEs was to learn their fundamental behaviour in order to be able to use for sensing of dopamine (DA) release from neurons or neural stem cells that differentiate into dopaminergic phenotype. The ability of the UMEs to oxidize DA was studied by acquiring CVs at different scan rates in PBS containing dopamine hydrochloride. CVs were acquired on all of the 54 UMEs of both dimensions in solution containing 150 µM DA at the scan rate of 50 mVs^{-1} (see Paper I). The average steady-state oxidation current on the 54 UMEs of 5 µm and 10 µm in diameter was 810 ± 60 pA and 1.55 ± 0.12 nA, respectively. Further, the UMEs were characterized to evaluate the detection sensitivity for DA by acquiring CVs at different DA concentrations. The calculated sensitivity was represented 5.8 ± 0.1 pA/µM and 10.4 ± 0.3 pA/µM for the 5 µm and 10 µm UMEs, respectively. The steady-state oxidation currents showed the proportionality to the increasing concentration. Details of the CVs comparing the individual 5 µm and 10 µm opening electrodes and further DA characterization can be seen in Paper I.

3.5.2 Choronoamperometry (CA)

Due to the electroactive nature of dopamine, it can be electrochemically oxidized to dopamine o-quinone (DQ). This oxidation can be monitored by implementing different electrochemical techniques such as amperometry, differential pulse voltammetry and cyclic voltammetry[218–220]. An elementary definition of choronoamperometry or amperometry could be, a system under a constant potential bias, where the current change is measured over time. This technique is suitable for rapid detection of analyte in a solution for our study due to its sensitivity to measure any instant activity on to the electrode surface. When cultured cells on an UME are triggered to

release dopamine, a sudden change in the dopamine concentration would occur in the close proximity of the electrodes. The released dopamine would then be oxidized at each of the UMEs having a cell residing on it, giving rise to a current peak, and followed by a peak decay.

For the detection of real-time dopamine release, the 54 UMEs should be sensitive and fast enough to register simultaneously the instantaneous and random change in analyte concentration. Amperometry records the faradic current response generated in a system by oxidation or reduction of electroactive spices at an electrode surface over time. A DA solution of 150 µM was prepared in purged PBS, and a volume of 200 µl was pipetted onto chip surface after a stable baseline current had been reached. During the experiment, the 54 UMEs were poised at 0.6 V vs. the on-chip RE. Figure 3.13b shows the CA response obtained for a single electrode of 5 µm (red) and 10 µm (blue) in diameter. Details of the simultaneous amperometric recordings at all of the 54 UMEs are shown in Paper I. After thorough electrochemical characterization of the UMEs, the chips were prepared for cell studies by implementing various preparation steps for enhanced and well-established real-time dopamine detection. In the next section, this is discussed in detail.

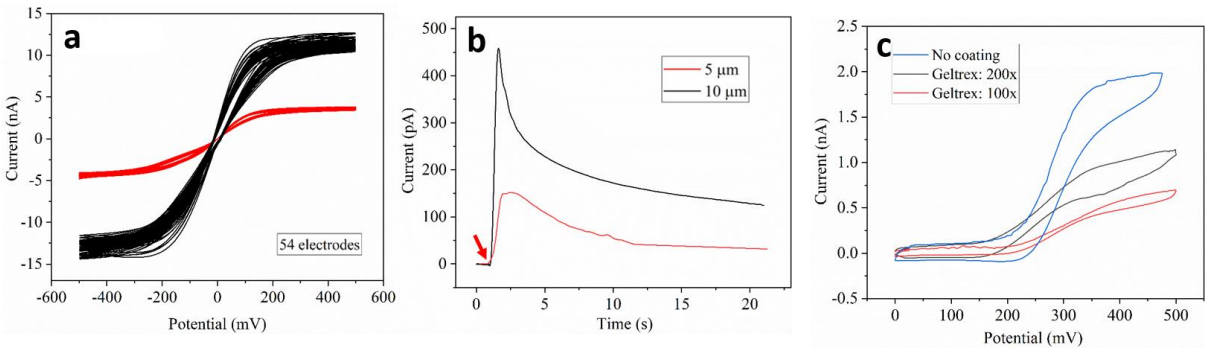

Figure 3.13. Electrochemistry on UMEA chips with both 5 µm and 10 µm UMEs: a) 54 CVs in 10 mM $[Fe(CN)_6]^{3-/4-}$ redox probe solution for 5 µm (red) & 10 µm (black) dimension . b) Choronoamperometry in 150 µM DA solution. c) CVs acquired to assess the influence of different electrode coatings on the electrochemical behavior.

3.5.3 Preparation of UMEA chips for cell studies

Before starting cell studies, UMEA chips were subjected to various required pre-treatment steps to enhance the overall quality of the experiments (as explained below). Below each treatment procedure is explained along with its impact on the UMEs:

1. Due to several lithographic steps inside the cleanroom and in order to improve reproducibility of electrochemical response between the individual electrodes, an

oxygen plasma (total O_2 pressure of 0.6 mbar and power of 50 W) treatment was performed for 1 min to increase overall wettability, to avoid any surface hydrophobicity and increase hydrophilicity to promote strong interaction between electrodes and electrolytes in a region of proximity.

2. DA polymerizes onto Au electrodes, resulting in an overall decrease in the electrochemical sensitivity[221]. To minimise DA polymerization, the UMEs were chemically modified by the weak carboxylic acid terminated mercaptopropionic acid (MPA; 200 mM) for 2 h in cell culture tested water, which has been reported to prevent DA polymerization and enhance DA electrochemistry[222].
3. The batch system and chips had to be sterilised in preparation for cell culture studies. The chip holders were immersed in 96% ethanol (10 min) and 0.5 M NaOH (30 min) followed by rinsing three times with PBS. Before starting the cell studies, an UMEA chip was assembled in each chip holder and sterilised under UV for 30 mins.

To perform a cell-based experiment, the extracellular matrix (ECM) gel (Geltrex) was used to coat the UMEA chips to promote cell adhesion. Based on earlier studies on collagen-coated electrodes, the extracellular matrix protein coating was considered to decrease the efficiency of DA detection. Therefore, UMEA chips were electrochemically characterized before and after Geltrex coating using cyclic voltammetry in DA solution to conclude that the concentration used for coating was suitable. Two coatings were tested for cell experiments, Geltrex diluted in PBS in the ratio a) 1:100 and b) 1:200. Based on the performed electrochemical tests, the conclusion was that Geltrex diluted in the ratio of 1:200 was suitable for DA detection on the UMEAs chips (see figure 3.13c). Further details are discussed in Paper I.

3.6 Real-time DA detection

The cell culturing was carried out in the chip holders inside the cell lab. Then, before exocytosis measurements each chip holder was inserted inside the potentiostat for current recording. Real-time DA detection and the performance of the UMEAs chips in simultaneous recordings is discussed in the sections below.

3.6.1 DA exocytosis by stimulation with high K^+ concentration

The DA exocytosis was monitored on both types of UMEAs chips by culturing PC12 cells for 24 hrs in a CO_2 incubator. K^+-induced DA exocytosis results from the DA containing vesicles bursting out the contents upon fusing with the cell membrane. The released DA is then immediately oxidized at the electrode surface, resulting in the generation of faradic current manifested as a peak-shaped current-time trace during amperometric measurements.

Each chip holder containing an UMEA chip was attached to the potentiostat for recording DA exocytosis upon addition of high-K^+ buffer. The potentiostat was connected to the NI-DAQ data acquisition system for data acquisition and the current recorded during DA exocytosis was stored in a computer. Initially, a baseline was recorded with a low-K^+ buffer which replaced the culture medium. As the stable baseline was achieved, a high-K^+ buffer was introduced to trigger the cells to release DA onto the UMEs. Upon stimulation, the UMEs on both types of chips responded simultaneously. The current-time trace was recorded for 60 seconds in total, and the majority of the electrodes responded to record DA exocytosis event upon stimulation. However, few electrodes registered low DA exocytosis currents. Figure 3.14ab shows the current-time trace response for five of the 5µm and 10 µm UMEs. The current-time trace response on all the UMEAs can be seen in Paper I. A heatmap presentation of the current amplitude on all of the 54 UMEs is shown in figure 3.14cd, where red represents the maximum and white represents the minimum current values. The results indicate successful simultaneous recording of DA exocytosis from individual electrodes of both dimensions. The reason why no exocytosis was recorded on some electrodes may have been caused by either malfunction of the electrodes due to the preparation steps or that there was no cell residing them. The time duration of exocytosis current peaks and total charge generated during DA oxidation, i.e. area under the current peaks, as well as the number of oxidized DA molecules were also calculated for each individual UME. The details are discussed in Paper I (Appendix). To avoid any uncertainty, control experiments were also performed to show that the recorded current peaks were only generated by DA exocytosis and not due to pipetting or other mechanical artefacts (Paper I).

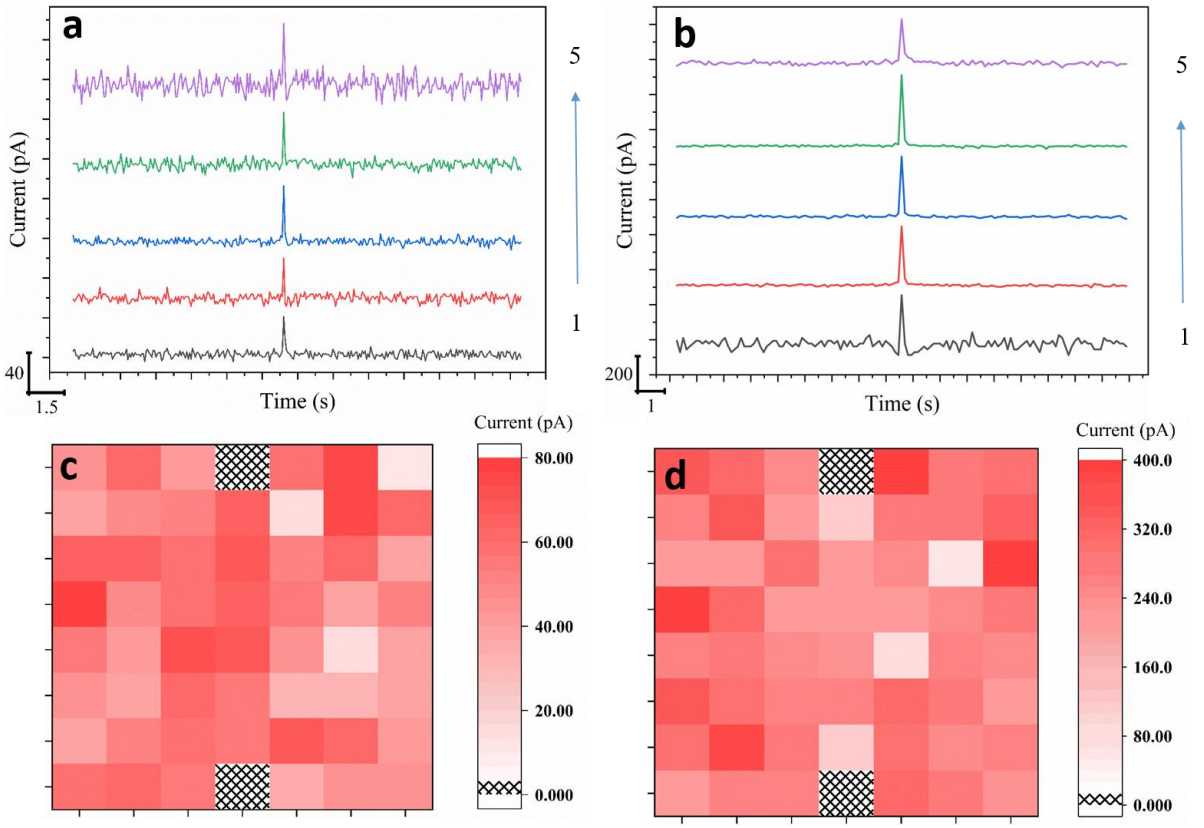

Figure 3.14. Real-time DA response upon stimulation of PC12 cells: Current-time trace recorded during DA exocytosis on five UMEs of a) 5 µm and b) 10 µm in diameter. Heatmap presentation of current amplitude for all the 54 UMEs of c) 5 µm, and d) 10 µm in diameter.

3.6.2 Unique DA response

The simultaneous recordings of the number of vesicles during DA exocytosis on 54 UMEAs from PC12 cells were unique in behaviour since the duration and current amplitude of each exocytosis peak was significantly higher than what is typically recorded during single-cell measurements where each peak corresponds to a release event from a single storage vesicle. The height and duration of the recorded current peaks on the individual electrodes are also significantly different in comparison with cell population based exocytosis measurements[223].

After a thorough analysis, two plausible reasons for the origin of such responses could be: 1) PC12 cells are, on average, 10 µm in diameter. Upon adhesion on the Geltrex coated UMEA chip surface, only one cell could reside on a recessed UME of either 5 µm or 10 µm in diameter, tightly adhering to the electrode opening and acting as a lid. Due to this, one after another, all the vesicles that were able to fuse with the basal cell membrane covering the electrode opening

could directly release DA to the electrode surface. Moreover, due to the release of DA into the confined space defined by the photoresist recession and the covering cell, the DA molecules could not readily diffuse away unlike in traditional single-cell exocytosis measurements, which involve placement of a carbon fibre microelectrode in the vicinity of the cell membrane or placement of a cell on a microfabricated electrode without adhesion. The consequence of this is a fast response that is a sum of several single-vesicle exocytotic events. 2) The ECM gel (Geltrex) coating also enhanced the ability of the basal cell membrane to form multiple focal adhesion points on the UME surface, making the distance between the basal cell membrane, and hence the releasing vesicles, and the UME somewhat constant throughout the surface. In traditional single-cell exocytosis measurements, the distance between individual vesicles and the electrode surface varies due to rounded shape of the non-adhering cells. This could further contribute to the fact that each single-vesicle exocytotic event contributed to a summed response recorded as one peak with significantly higher current amplitude and also slightly longer duration than is customarily observed in single-cell measurements where each peak corresponds to release from a single vesicle.

Based on the two plausible explanations for the observed current responses, as described above, it is also possible to conclude that despite the close proximity of the UMEs in a UMEA (area of approx. 260 µm x 290 µm), the adhering cell forming a lid on the recessed UME could essentially eliminate the possibility that a recorded current peak was contributed to by other surrounding cells. Similar behaviour on UMEs has also been discussed earlier[224]. Further details are available in Paper I (Appendix).

This chapter presented the fabrication of UMEA chips with UMEs of 5 µm and 10 µm in diameter. The UMEs are simultaneously individually addressable. The first part presented the UMEA chip fabrication techniques along with the encountered challenges and how they were solved. The second part discussed about the electrochemical characterization of UMEs using $[Fe(CN)6]^{3-/4-}$ and dopamine . Lastly, PC12 cells were cultured on the UMEA chips and their real-time response was recorded through 54-channel custom-made potentiostat upon stimulation using high-K^+ buffer.

Chapter 4

COMPARTMENTALIZED MICROFLUIDIC CHIPS (CMC) WITH INTEGRATED MICROELECTRODE ARRAYS (MEA)

This chapter focuses on developing compartmentalized microfluidic chips (CMC) with integrated electrochemical microelectrode arrays (MEA) for neurotransmitter (dopamine) detection with the ultimate aim to develop a proof-of-concept nigrostriatal pathway (NSP) on chip. The first part presents the design, fabrication and electrochemical characterization of different MEA chip designs to be integrated with future CMC devices. The second part discusses the fabrication of the CMC device, its characterization, and preliminary cellular studies performed.

4.1 Introduction

The intricate architecture of the human brain undergoes extraordinary self-origination upon various morphological changes that occur during its development. The real-time interconnected neural activity in brain networks is one of the fundamental mechanisms for brain circuitry. In the brain's complex structure neurons grow in well-organized and well-oriented densely packed three-dimensional scaffolds, encouraged by various surrounding cues, such as signaling factors, protein, and supportive neighboring cells. The brain is composed of many specialized areas, typically, neural projected extensions are responsible for creating a deep network to form the connectivity between these areas, which makes in vivo investigation a significant challenge[156].

One of the best approaches for understanding complex neural circuitry is re-engineering the neural pathway in *in-vitro* cultures, which may uncover the neural circuitry's primary mechanism. Compartmentalized microfluidics chips (CMC), described in chapter 2, have become invaluable tools for experimental neuroscientists, capable of organizing neuronal pathways and access their distinct subcellular microenvironment for manipulation and

measurement[225]. These CMC have been used in a broad range of applications to study neural circuit formation[6], axonal injury and transport[118], synaptic plasticity[151], viral infection[226], as well as various disease models[153].

In most of these studies, the master mold for making the CMC are fabricated using traditional cleanroom-based UV-lithography. The mold is usually created on a silicon wafer that contains the inverse structure of the physically separated compartments with the interconnecting microchannels, which subsequently is used to generate the final CMC using PDMS soft-lithography. The PDMS CMC is then bonded on a glass substrate to create a closed fluidic system to enable further neural studies. In most cases where a MEA has been integrated as part of the CMC, the systems have been adapted to fit to already commercially available MEA, and essentially all involve electrophysiological studies of the cells´ electrical behavior[7].

In the following sections, I present my efforts towards the development of a CMC with integrated customized interdigitated electrodes (IDEs) and MEAs, with the future aim being that the MEAs should enable us to:

a. Monitor and specifically detect the delivery of dopamine from midbrain-derived dopaminergic neurons in one compartment (our "SNpc"), which project into another compartment, containing forebrain derived neurons (our "striatum"), which in a real situation would activate these neurons, see also Figure 2.5b.
b. Electrically trigger the dopamine exocytosis release mechanism at one electrode, following dopamine detection on surrounding electrodes. So far triggering of exocytosis have been performed mainly using chemical[227] or optical triggering (optogenetics)[228].
c. Electrically stimulate the differentiation and maturation of the neurons while cultured in the CMC[229,230] and potentially following this process using electrochemical impedance spectroscopy followed by dopamine detection at surrounding electrodes.

My work started with the design, fabrication and characterization of three different gold MEA designs with individually addressable electrodes for the electrochemical detection of dopamine aligned with neurite guidance channels in a CMC (Design 1- Neurite guidance MEA), electrical triggering of exocytosis or stimulation of neuronal differentiation followed by dopamine detection (Design 2-Matrix MEA and Design 3-Radial MEA). Design 1 was then integrated into a previously developed two-compartment CMC for neurite guidance[8], as a proof

of concept NSP and initially tested with PC12 cells. A new CMS fabrication technique was tested, developing a PMMA based CMC, to circumvent challenges encountered when bonding and alignment of the microchannel array on PDMS based CMCs with the individual electrodes in the neurite guidance MEA.

4.2 MEA Design & development

MEAs are widely used for analysing neuronal networks, as discussed in chapter 2. The majority of studies are conducted on commercially MEAs, which have proven invaluable for a range of different investigation[231,232]. However, commercial MEAs have very limited degrees of freedom in respect to dimension and interspace and lack the adaptability to any system for specific analytical purposes.

I have therefore designed, fabricated, and characterized new customised MEAs for our specific purposes. Gold was the chosen material for fabricating all electrodes, connection leads, and contact pads of the MEAs, since it exhibits long-term performance, low impedance, and biocompatibility[233,234].

4.2.1 Neural guidance MEA – Design 1

This neural guidance MEA was customized particularly for the CMC previously developed in our group[8], shown also in Figure 2.5b. The idea behind this MEA was to see if we could monitor dopaminergic neurons, projecting from the midbrain compartment ("SNpc"), synaptically connect with neurons in the forebrain compartment ("striatum") by monitoring the exocytotic release of dopamine on the "striatum-side" when neurons in the "SNpc-side" were stimulated (chemically, electrically, optically). This chip was thus designed to address a few microfluidic channels on the "striatum-side" with microelectrodes that should record the dopamine release. Figure 4.1a shows a schematic of the whole neurite guidance MEA with the centre part highlighted in Figure 4.1b. The right compartment ("striatum") contains the 16 individually addressable electrodes, each with a diameter of 30 µm and an area of 700 μm^2, to be aligned with a few microfluidic channels in the final CMC. The left compartment contains instead 12 semi-individually addressable interdigitated electrodes (IDEs), which can also be addressed in pair of 2 IDEs if required, as one contact pad can address one side fingers of 2 adjacent IDEs. These electrodes can be used, on hand to follow the growth and differentiation of this neural

population using impedance spectroscopy[121], and on the other hand, to measure dopamine release from this same cell population[223- paper I (appendix A)]. Due to the limited area of the chip and the compact network of connecting leads, only 16 microchannels were included. The interspace between the electrodes sets, such that 12-IDEs and 16-MEAs in each compartment side were apart by 450 µm distance, which is the same length of the microfluidic neurite guidance channel array in the CMC to which the MEA will be bonded to.

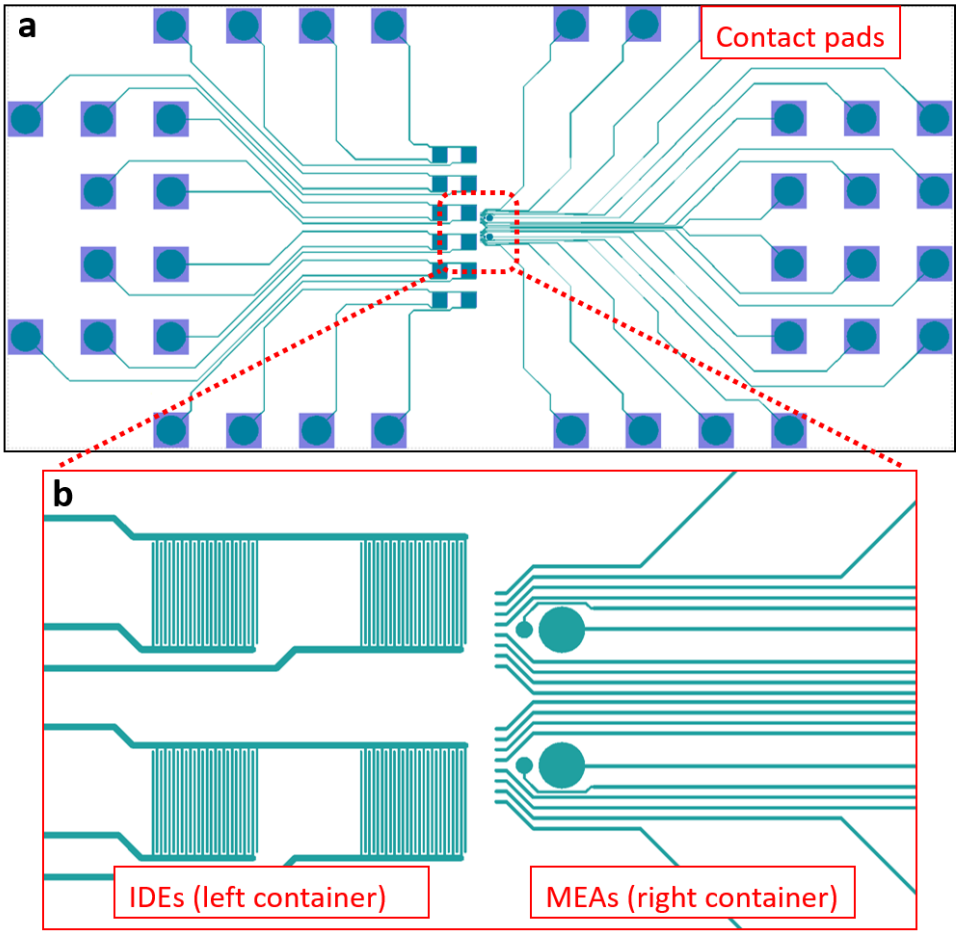

Figure 4.1. Neural guidance MEA – Design 1: a) The complete neural guidance design (16 x 11 mm) with contact pads, tracks for leads, and electrodes, including working, counter and reference electrodes. b) Zoomed image: *Right compartment:* 2 x 8 microelectrode arrays (each with an opening of 30 µm in diameter after passivation) to be aligned with microfluidic channels in a CMC, two circular counter- (200 µm in diameter) and reference (50 µm in diameter) electrodes, addressing each one of the two 8-electrode arrays. *Left compartment:* 12 semi-individually addressable IDEs, with 13 fingers on each side of the IDE (length: 500 µm, width: 10 µm and spacing between fingers: 10 µm) each covering an area of 500 x 500 µm. The IDEs are semi-individually addressable and can also be used in pairs of 2, as each finger side of 2 adjacent IDEs are shorted.

4.2.2 Rectangular MEA - Design 2

The second design was more straightforward compared to Design 1 because it is designed to address more area in forebrain compartment by incorporating 20 microelectrodes of 30 um diameter, spread in an array format to cover a larger area for detecting dopamine exocytosis, unlikely as design1 that only addresses specific number of microfluidic channels, as shown in Figure 4.2. Here, the right compartment was designed with 20 microelectrodes, arranged in a rectangular array of 5 x 4 individually addressable microelectrodes, each with a diameter of 30 µm, along with a large counter- and a small reference electrode. The left-hand side compartment was designed with one IDE, having the same dimensions as in Design 1. The primary purpose of this IDE is to provide electrical stimulation pulses to potentially enhance and promote stem cell differentiation[229,230]. The second reason would be to use them to electrically trigger exocytosis of neurons in this compartment and record the released dopamine from the interconnected neurons in the right opposing compartment. The size of the IDE placed in the centre of the compartments and the interspace between IDE and 20-MEAs in each compartment side were apart by 500 µm distance, which is the same length of the microchannel in the CMC device to which the MEA chip will be attached.

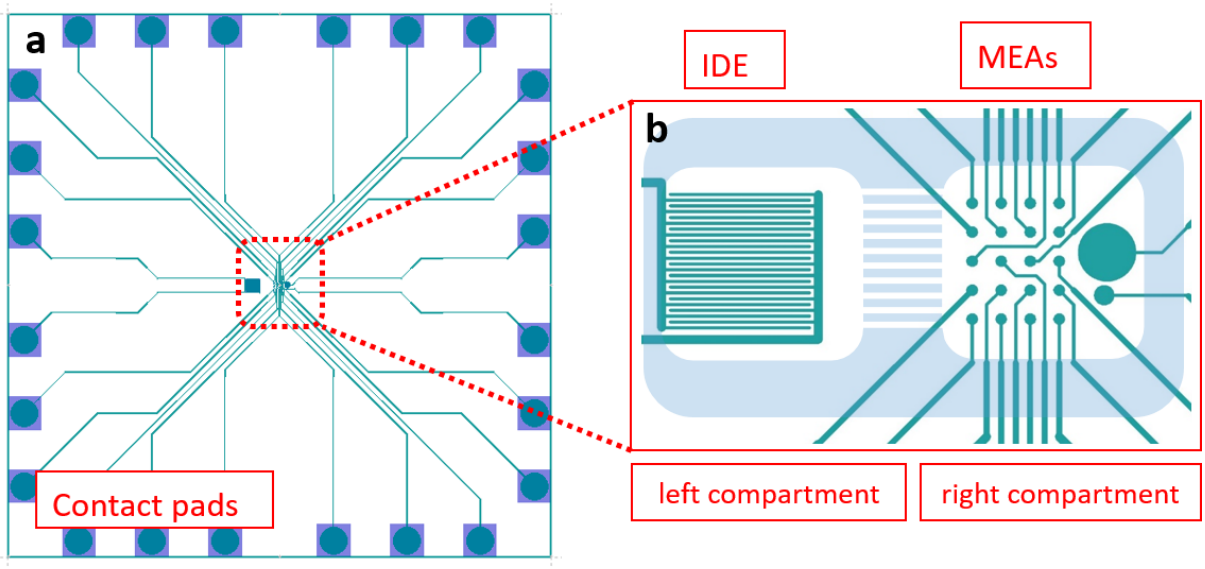

Figure 4.2. Schematics of the rectangular MEA (Design 2): a) The complete rectangular MEA design (21 x 21 mm) with tracks for leads, connection pads and electrodes in both compartments. b) Shaded area (blue) indicates the position of a potential CMC device connected through microchannels (white). *Left compartment:* one IDE (with 13 fingers on each side of the IDE (length: 500 µm, width: 10 µm and spacing between fingers: 10 µm) with a total area of 500 x 500 µm. *Right compartment*: 20 electrodes (5 x 4 electrodes) each with a diameter of 30 µm, one counter (diameter of 200 µm) and one reference (diameter of 50 µm) electrode.

4.2.3 Radial MEA - Design 3

This third radial design was constructed to be integrated into a three-compartment CMC device, and shown in Figure 4.3. This idea behind creating this MEA design addressing 3-compartment CMC device was to construct a detailed neural circuitry pathway, such as in Parkinson's disease (PD) neurodegeneration extends beyond the SNpc region and results in the malfunctioning of interconnected signalling mechanism in the brain. It is reported. that loss of glutamatergic neurons in thalamus[235] and motor cortex[236] has also been observed in PD. To model interconnected cascaded signal mechanism for PD, such CMC devices are formed.

The design is split into three regions, a right, left, and central region. The right and left region consists each of 8 radially arranged microelectrodes (each with a diameter of 30 µm) surrounding the central region, containing one IDE. The sensor functions are similar as discussed in design 2, the difference is in number of compartments and their geometrical arrangements. In this design, neuronal projections are considered omnidirectional, where the projected extensions spanning over a considerable distance all around the compartments.

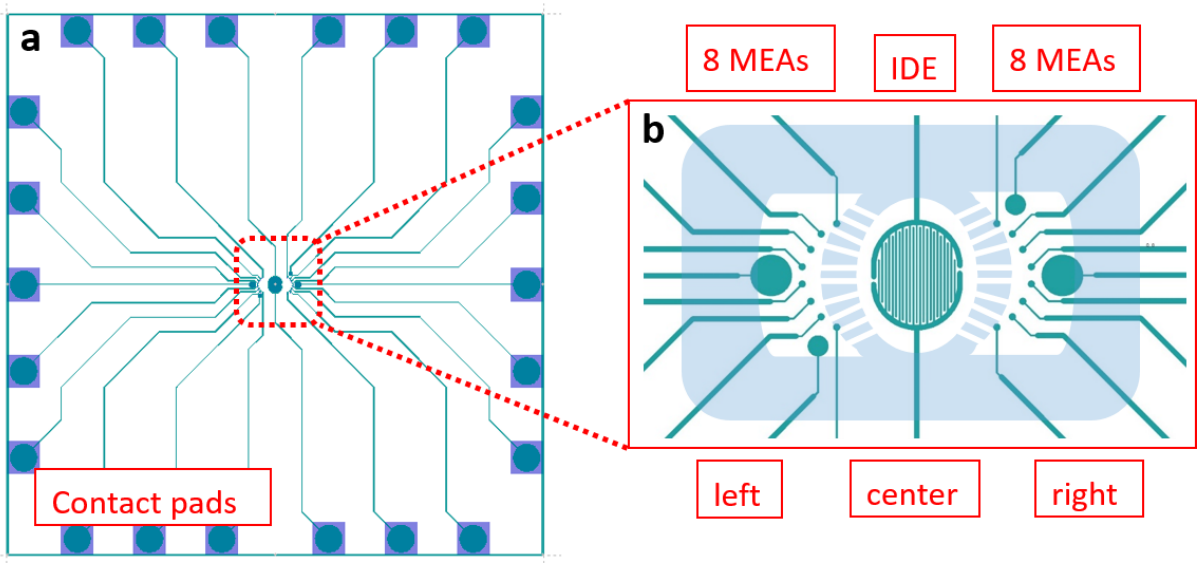

Figure 4.3. Schematics of a radial MEA (Design 3): a) The complete radial MEA design (21 x 21 mm) with tracks for leads, connection pads and electrodes. b) The left and right side, each with 8 radially arranged microelectrodes, a counter- (diameter: 200 µm) and reference electrode (diameter: 50 µm). A centrally placed spherical IDE with a total area of 500 µm^2, having 12 fingers on each side (Length of fingers varying between 200-600 µm, width: 10 µm, spacing between fingers: 10 µm). Shaded area (blue) indicates the position of a potential CMC having microfluidic microchannels arrays connecting the left- and right side compartments with a central compartment.

4.3 Fabrication and electrochemical characterisation of MEAs

4.3.1 Fabrication of MEA chips and chip holders

The fabrication of the three MEA designs followed the same protocol as that described in chapter 3 for the 54 electrode UMEA chip. Briefly, a transparent glass wafer was used as the substrate. Direct writing, using a CAD design file and MLA UV-exposure was performed followed by thin-film metal e-beam deposition of Ti and Au, and reactive ion etching for passivation openings. All fabrication details were discussed in chapter 3. Figure 4.4 shows the three different fabricated MEAs.

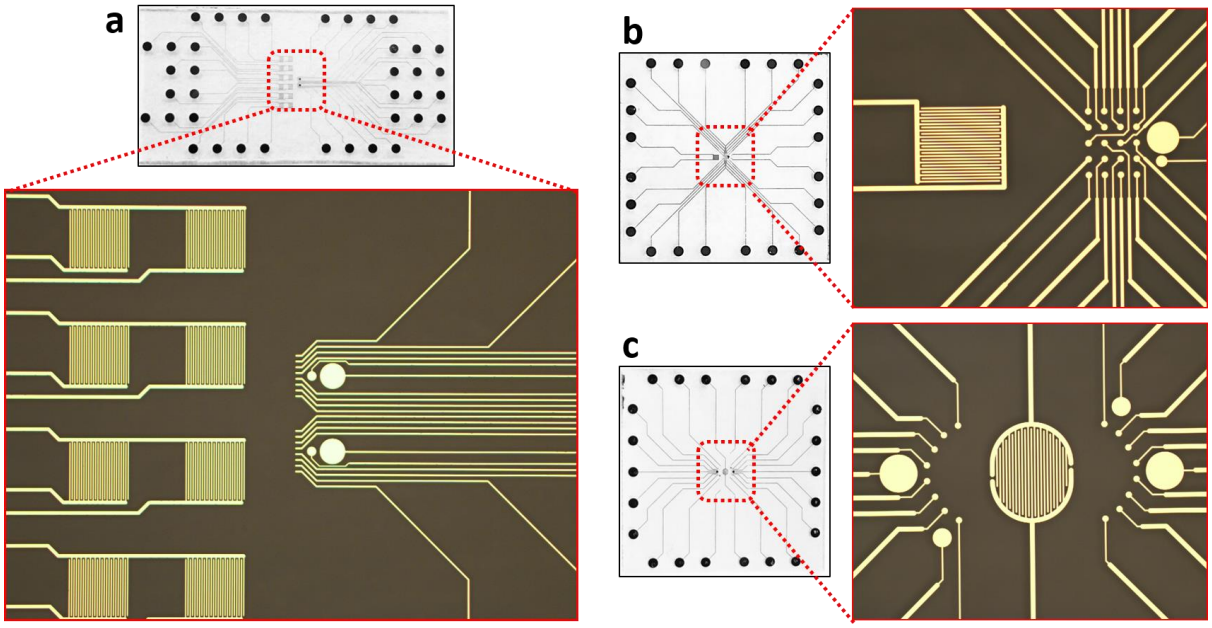

Figure 4.4. Photographs of the three fabricated gold MEA designs: a) Design 1: The fabricated neurite guidance MEA (top) and a zoomed image (bottom), highlighting IDEs on the left-hand side and 2 x 8 microelectrodes with large circular counter and small circular reference electrodes on the right-hand side. b) Design 2: The fabricated rectangular MEA (left) and a zoomed image (right), highlighting the IDE on the left-hand side and the 5 x 4 microelectrodes with a large circular counter and a small circular reference electrode on the right-hand side. c) Design 3: The fabricated radial MEA (left) and a zoomed image (right), showing the radial arrangement of the 2 x 8 microelectrodes around one IDE electrode. For specific MEA dimensions, see Figures 4.1-4.3.

In order to be able to electrochemically characterise the function of the individual electrodes in the three different MEA designs, two batch chip holders were fabricated (as in chapter 3 for the UMEA chip), one for Design 1 and one common for Design 2 and 3. Each holder has a sample compartment well in PMMA attached exposing the area of electrodes to analyte and electrolyte solution. All parts of the chip holders were fabricated using micro-milling, as described in

chapter 3, section 3.4. Figure 4.5 shows the three chip holders with the same three main components: A bottom plate with dedicated space for the MEA chip to hold it in place. A top plate with a sample compartment well to access the electrodes on the MEA. A PCB placed at the top, with an access window with wires and pins that connects the electrodes on the MEA chips with an external potentiostat. All three parts were assembled using 12 mm screws with 2 mm diameter.

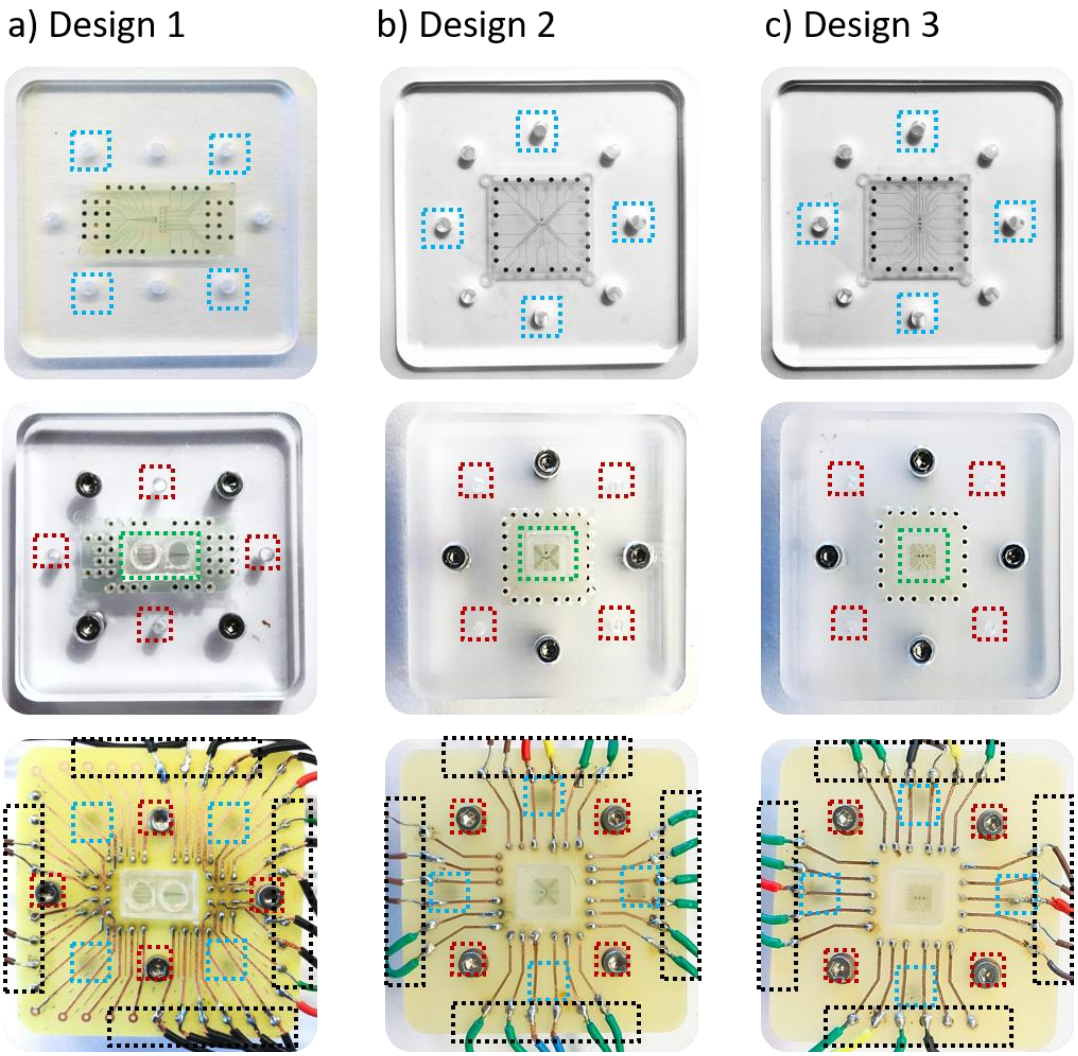

Figure 4.5. Chip holder for electrochemical characterization of individual electrodes: a) MEA Design 1 and (b) MEA Designs 2, and c) MEA Design 3: All images show: a bottom plate (top row images) with dedicated space for placing MEA chips (Design 1: 16 x 11 mm, Design 2&3: 21 x 21 mm), and with 2 mm holes (blue) to attach a top plate (middle row images) where sample compartment wells (Design 1: 14 x 9 mm, height: 10 mm, volume 200 µl), (Design 2&3: 10 x 10 mm, height: 10 mm, volume 200 µl) are present to address electrode in MEAs chip, and hole (red) for attaching PCB. A PCB board (bottom row images) with access window, wires (black), and pins for connection MEA chip with an external potentiostat. All parts were assembled via screws (2 mm bolts).

4.3.2 Electrochemical characterisation

Electrochemical characterization of the individual electrodes of the three MEA designs was done using cyclic voltammetry (CV) with the redox couple $[Fe(CN)_6]^{3-/4}$ (FC/FoC) and dopamine. 16 CVs from 2 x 8 electrodes from MEA Design 1, 20 CVs from 5 x 4 electrodes of MEA Design 2, and 16 CVs from 2 x 8 electrodes of MEA Design 3. Figure 4.6 shows the CVs obtained for each MEA design, indicating that the electrochemical responses are highly reproducible between electrodes within each design, and the nearly sigmoidal shapes of the CVs with limiting oxidation and reduction currents are typical for UME behaviour. The maximum currents obtained for all microelectrodes in the three designs were very similar (average oxidation currents: 78.6 ± 5 nA, 71.3 ± 3 nA, and 76.2 ± 4 nA for Design 1, Design 2, and Design 3, respectively) due to the fact that open accessible electrode areas of all designs were the same (diameter: 30 µm), also indicating highly reproducible fabrication processing.

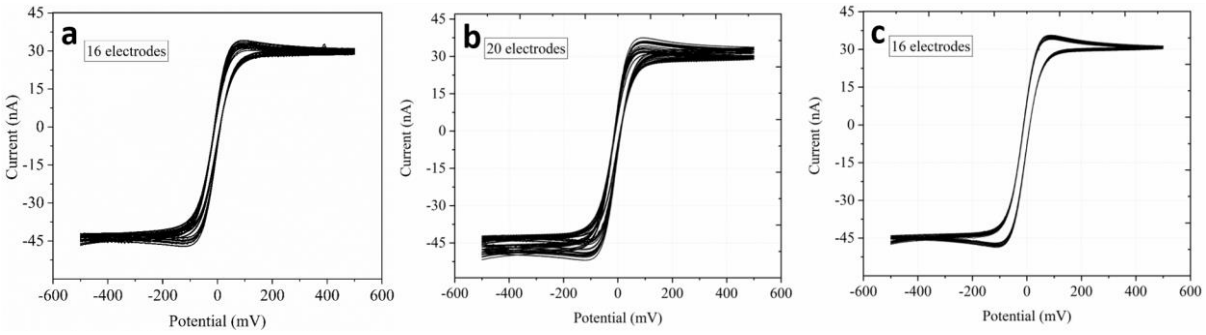

Figure 4.6. CVs obtained in $[Fe(CN)_6]^{3-/4}$ for all microelectrodes in the three MEA designs: a) Design 1 with 16 (2 x 8) microelectrodes, b) Design 2 with 20 (5 x 4) microelectrodes and c) Design 3, with 16 (2 x 8) microelectrodes. Recorded in 10 mM of $[Fe(CN)6]^{3-/4}$ in PBS (pH 7.4) using a scan rate of 50 mV^{-1}, and the on-chip Au counter and reference electrodes in each MEA design.

These MEA designs were further characterized using dopamine, as it is the analyte to be detected in further cell-based exocytosis experiments. Dopamine concentrations ranging from 50 µM to 250 µM were used to acquire CVs from each MEA design. Figure 4.7a-c show CVs from one single microelectrode in each MEA designs, whereas Figure 4.7d shows three calibration graphs, plotting limiting currents obtained from all microelectrodes in each MEA design versus concentration. The sensitivity for dopamine on all microelectrodes in each MEA design[237] were 31.8 ± 2 pA μM^{-1} (Design 1), 32.2 ± 2.5 pA μM^{-1} (Design 2) and 31.2 ± 1.5 pA μM^{-1} (Design 3), again indicating very good reproducibility between microelectrodes within each MEA design.

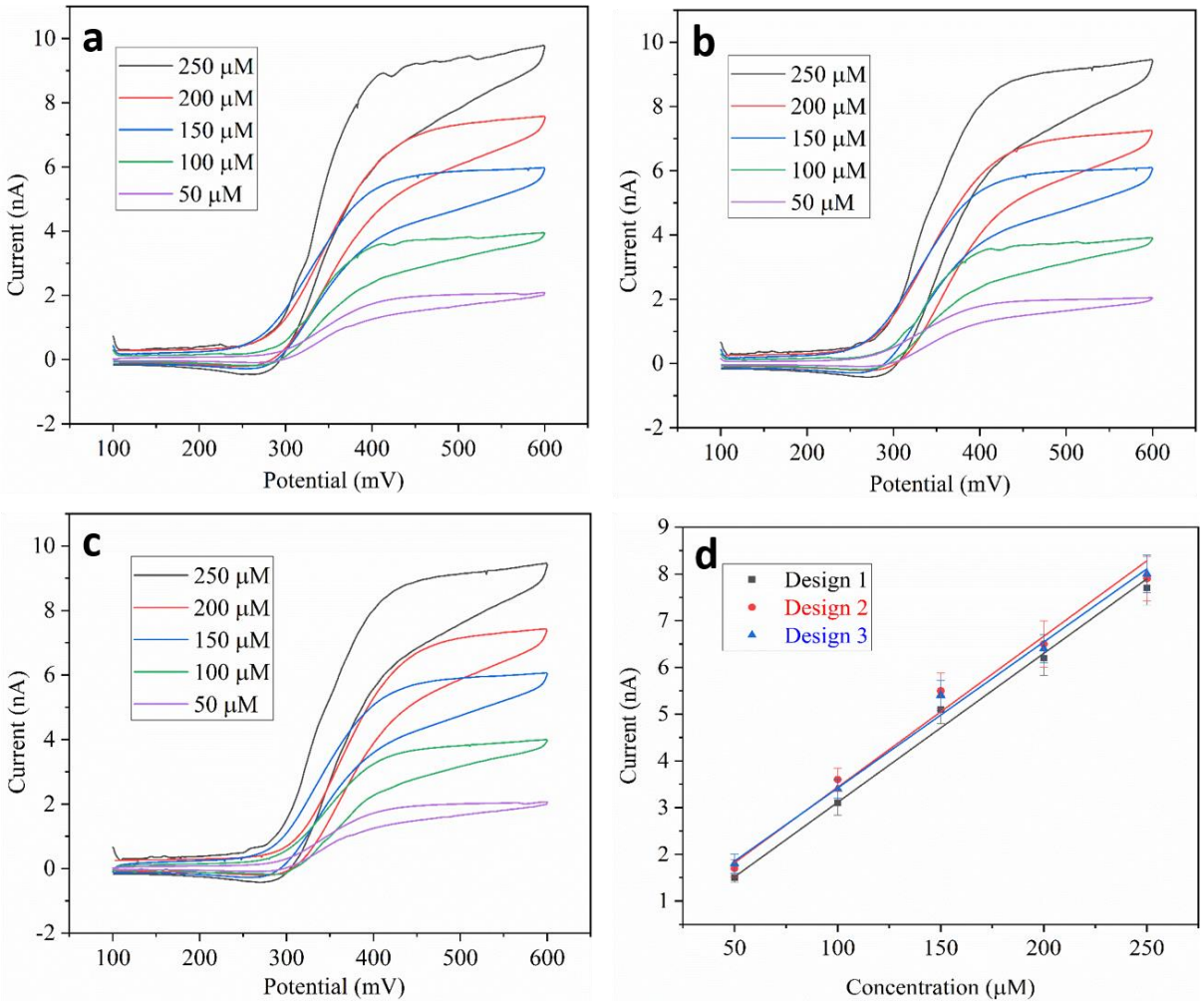

Figure 4.7. CVs and calibration graphs for dopamine on the three MEA designs: CVs for different dopamine concentrations for one single microelectrode in a) Design 1, b) Design 2 and c) on Design 3. d) Calibration curves with limiting currents plotted vs concentration. Recorded at a scan rate of 50 mV/s using the on-chip Au counter and reference electrodes in each MEA design.

4.4 Integration of MEA Design 1 in a two-compartment CMC

4.4.1 Initial CMC-MEA study

A two-compartment PDMS based CMC was recently fabricated in our group, with a new technique that we call 3D printed soft lithography[8]. This technique provides considerable degrees of freedom in device design capability and was found in general to increase the biocompatibility of the device when testing long-term hNSC differentiation as compared when using traditional PDMS based lithography. Here, the idea was to develop a proof-of-concept human *in vitro* model of the NSP[8] (as shown in Figure 2.5) by spatially separating dopaminergic

neurons from midbrain-derived hNSCs ("the SNpc") from neurons and astrocytes from forebrain-derived hNSCs in the other compartment ("the striatum"), while facilitating unidirectional outgrowth of dopaminergic projections through directional microfluidic channels. Further advancement of this model would be to study dopamine signalling along this NSP model. The idea was therefore to implement the neural guidance MEA chip (Design 1) from above, specially designed to fit with this two-compartment CMC with microelectrodes aligned with the microfluidic channels outlets, to enable studying the dopamine release from "the SNpc" compartment to "the striatum" compartment, as shown in Figure 4.8. Figure 4.8e shows how difficult it was to align perfectly the microfluidic channels of the CMC with the microelectrodes in the MEA Design 1 chip. This turned out to be a real challenge even when a micro-manipulator with inspection under the microscope was used. The reason is that the PDMS based CMC is soft and very sticky and as soon as it touches the glass chip surface it is stuck and cannot be removed. In the end we found that a successful alignment was based on pure luck, where Figure 4.8e was the luckiest of our attempts.

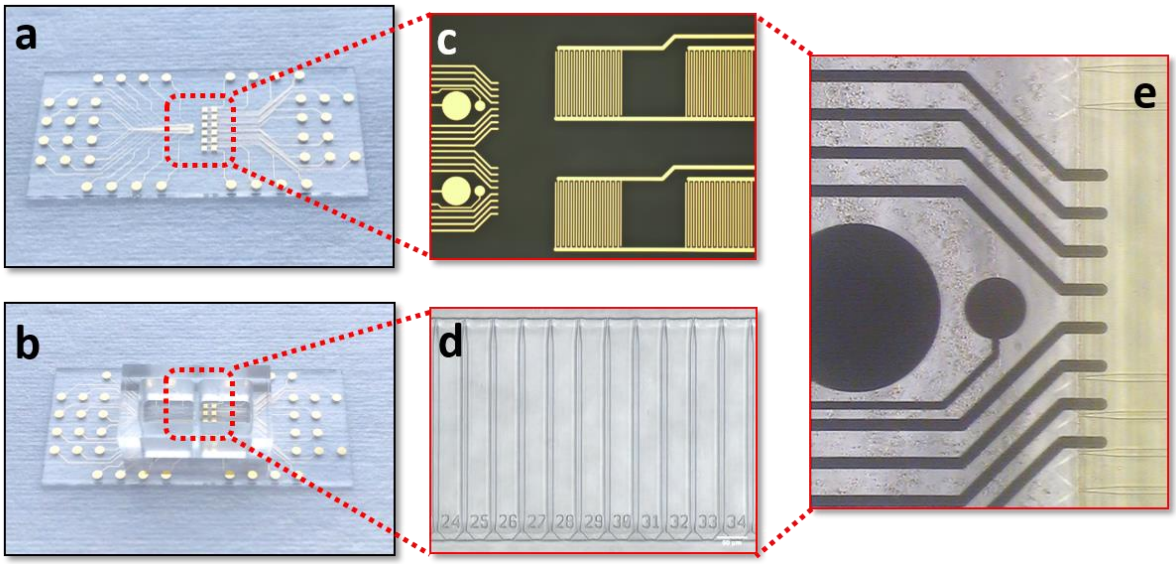

Figure 4.8. Two-compartment CMC integrated with MEA Design 1: Photos of a) MEA Design 1 chip, with b) the CMC bonded on top, and zoomed images of c) MEA Design 1 of figure a, d) microfluidic channel array geometry of figure b (dimensions: Channel length (450 µm), width (6 µm) and 4.7 µm height, with opened tapered inlets and narrow tapered outlets for unidirectional neural guidance), and e) attempt to align the 2 x 8 microelectrode array with the microfluidic channels of the CMC on "the striatum" side.

To circumvent this problem, I decided to make a new CMC with larger microfluidic channel dimensions that would be easier to align to the microelectrode array. However, in the middle of this came the Covid-19 lockdown of DTU, which meant no access at all to the clean-room during and very limited access to wet labs or the cell lab the last half year of my PhD. This meant that there was no way to make a new CMC master mold with larger channels in the clean room. I thus decided to try micro-milling as the method to fabricate a CMC master mold with larger microchannels, in this way avoiding the need for the clean room.

A CMC mold of two compartments and the microfluidic channels in between was micro-milled, which was subsequently followed by traditional PDMS soft lithography to create a final PDMS CMC replica. The mold fabrication and characterization, and finally the bonding of the PDMS CMC replica to a glass slide with an initial PC12 cell study are described in the following sections. The micro-milling technique, procedures involved, and set up is described in Chapter 3 and shown in Figure 3.10b.

4.4.2 CMC mold and PDMS replica and their characterisation

A CAD design was developed for the CMC mold using AutoCAD 2016 with defined dimensions for compartment and microfluidic channels, as shown in Figure 4.9A. These designs were further converted into the machine-readable G-Code format using the machine-based EZ-CAM software. A 3 mm thick PMMA sheet was used as a substrate for micro-milling the CMC mold. Figure 4.9 shows the dimensions of the CMC mold design (A), the fabricated mold (Bac) and resulting PDMS replica CMC in (Bb).

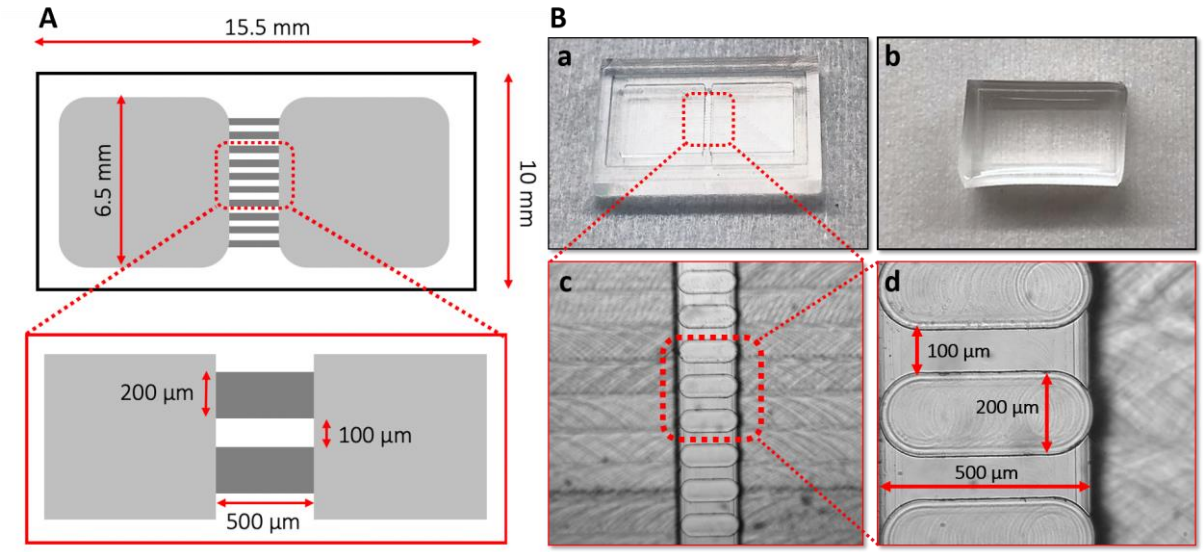

Figure 4.9. CMC mold design, fabricated mold and resulting PDMS replica: A) Schematic and dimensions of the CMC mold design (top) with a zoomed image (bottom) of the microchannel dimensions (white space) between them. B) The fabricated CMC mold (a) with highlighted microchannels in (c-d) and the resulting PDMS replica CMC in (b).

The two compartments were designed with sufficient area (6.5 mm^2) to get access to the MEAs in the bottom to enable electrochemical measurements and culture and differentiate of cells on top of the MEA. The height of the microchannels was set to be 50 µm for initial testing of the milling and tool resolution. Compartments and microchannels were micro-milled, using a 200 µm tool bit diameters with a spindle rpm of 35k and feed rate of 1 mm/s, and took 2 hrs to mill.

Before PDMS soft-lithography, the PMMA based CMC mold was rinsed with isopropyl alcohol and cleaned with a brush to remove residual debris from the microchannels. Figure 4.9Bc shows the inverse microchannels of the mold and Figure 4.9Bd shows the channel width and interspace. One feature is that the edges on each side of the channels are tapered with enlarged opening, which is a problem since guided and unidirectional projections are wanted[6]. This can in principle be dealt with by changing to a smaller milling tool and changing the milling parameters. The dimensions of the CMC mold was characterised using a stylus profilometer (Figure 4.10b), which indicates quite good milling accuracy with channel and interspace widths determined to be 96 µm and 194 µm, respectively, and the channel height measured at 51 um, all in good agreement with the given dimensions of the design (Figure 4.9A).

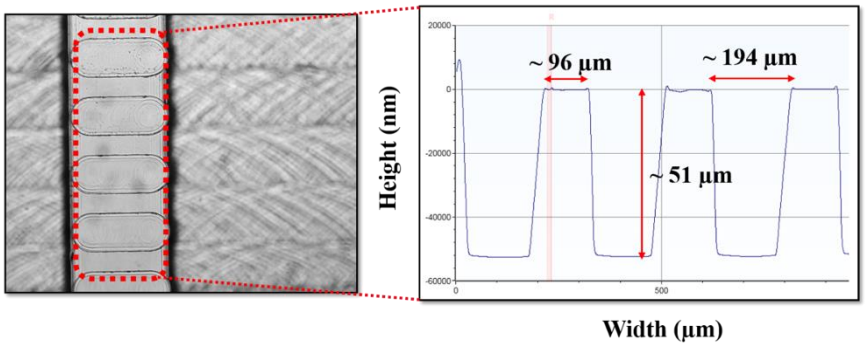

Figure 4.10. Surface profile characterization of milled PMMA CMF mold: *Left:* The PMMA mold with highlighted channels. *Right:* Surface profile obtained using a Dektak profilometer, representing the actual dimensions achieved after milling. Red arrows indicate channel and interspace widths and height of the structure.

A PDMS replica was created by pouring liquid PDMS on the PMMA mold, followed by vacuum desiccation to remove any trapped air bubbles in microchannels, and final curing in an oven for 2 hrs at 60 C, see Figure 4.9Bb. The CMC was created by first removing the PDMS replica from the mould and then forming compartments either by using a biopsy punch or by careful manual dicing out the compartment region, whereas biopsy punch results in safer opening of compartments due to lower chance of destroying the microchannels as compare to manual dicing. Before the PDMS replica was bonded to the glass slide, both were treated with oxygen plasma for 60 seconds to improve the wettability of compartments and microfluidic channels, see system in Figure 11.

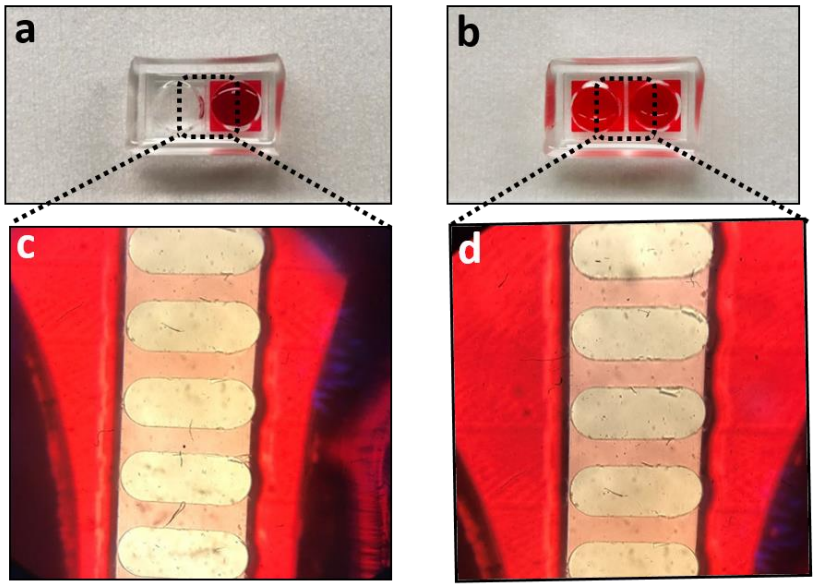

Figure 4.11. Microfluidics in PDMS CMC: a) Top view of PDMS CMC device with one compartment and, b) later in both compartments, filled with red color dye to study the flow in the channels, and c & d) observed from sides for any leakage. e & f) Zoom version shows the filled channels and no leakages observed for long durations.

To see if the system was leak tight and that microfluidic channels were functioning, food colour was added in one of the compartments (Figure 4.11a) to visually observe the colour transport to the other compartment (Figure 4.11b), a transport that took approximately 3 mins, and indicated that the device seemed leak proof.

As indicated above, due to the Covid-19 lockdown, I had no or very little access to wet labs or cell lab, and my PhD time was running out. In the end, I had no time to explore the CMC-MEA integrated chip for the intended experiments, however, a final experiment was conducted to see if we could differentiate PC12 cells (the neural model cell line used in Chapter 3) in the CMC and observe neural projections through the microfluidic channels.

4.4.3 PC12 culture and differentiation in CMC

Before cell culture, the CMC was sterilized using UV light for 30 mins and then coated with Geltrex extracellular matrix for 2 hrs to enable efficient cell adhesion. As surface treatment with oxygen plasma enhances system wettability, two bonded CMC devices were prepared, one with and the other without oxygen plasma treatment before starting the coating process with Geltrex.

PC12 were cultured and prepared at the same conditions as used in chapter 3 (paper I). PC12 cells were seeded in both compartments of the CMC chips with a cell density of 15k cells/cm^2, with the bottom compartment area of 0.6 x 0.6 cm^2. Since the same volume of media has been added to both sides, there should essentially be no flow between the compartments. PC12 cells are quite small (10-12 µm in diameter), which means that we can expect that the cells themselves could migrate into the microfluidic channels (approximately 100 µm width). Figure 4.12 indicates that no or very few cells were present in the channels at the day of seeding, a few can be observed in the oxygen plasma-treated CMC in Figure 4.12b. After 24 hrs of cell culture, the differentiation of PC12 cells was initiated by exchanging the media on both sides with differentiation media containing NGF-β (nerve growth factors-β from rat). Media exchange was conducted every 24 hrs, due to small volume in the compartment and media evaporation. At day 4 of differentiation, the cell lab was completely shut down, due to detection of mycoplasma, and

all cell work had to be terminated. The CMCs were inspected on that final day and can be seen in Figure 4.12c and d. As seen, differentiated PC12 cells with neurite extensions can be observed in both CMCs, however only the oxygen plasma treated CMC (Figure 4.12c) shows cell migration and nerite projections inside the microchannels.

A chip preparation was initiated in parallel on MEAs-CMC device to perform cell studies with PC12 before testing with human neural stem cells (hNSC). Figure 4.13ab show the bonded MEAs-CMC device and well aligned microchannels with more than one electrode occupying the channel, however experiment could not begin due to lab closure, as mentioned above.

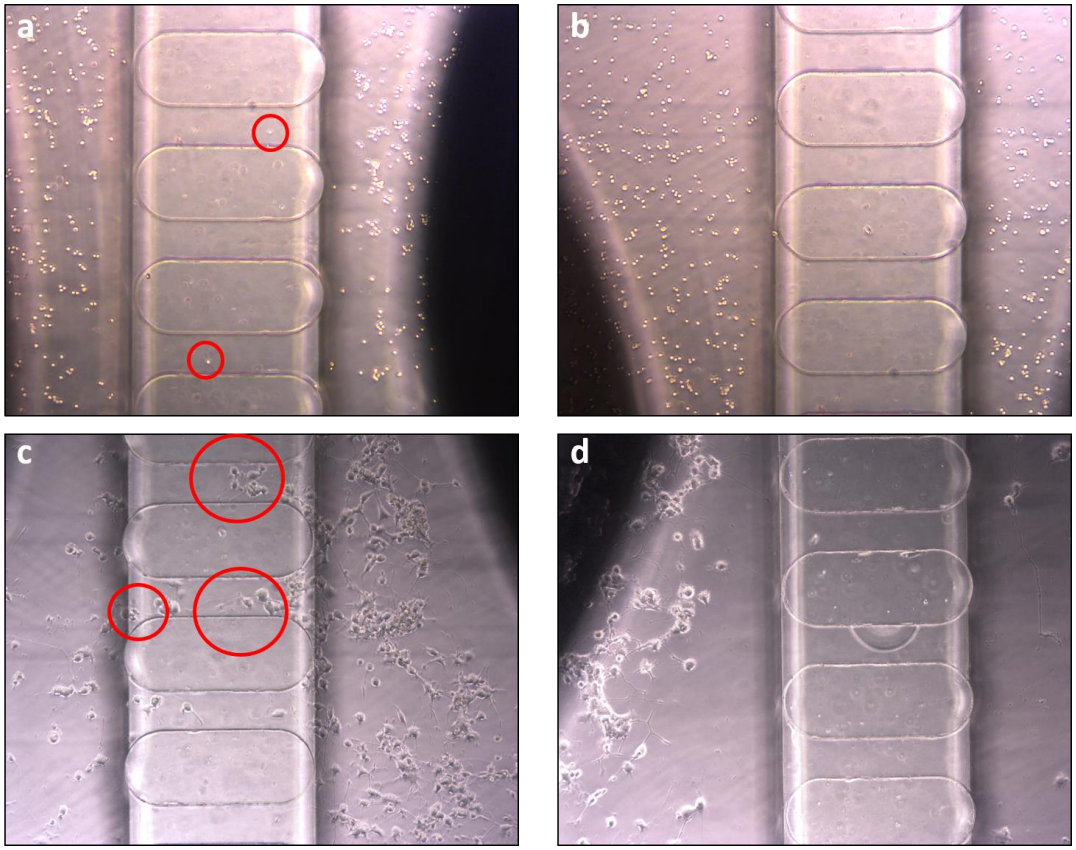

Figure 4.12. PC 12 cells cultured and differentiated in CMCs: a) Oxygen plasma treated CMC at the day of seeding. b) Untreated CMC at the day of seeding. c) Day 4 of differentiation in oxygen plasma treated CMC with cell migration and neural projections observed in microchannels. d) Day 4 of differentiation in untreated CMC with less neurite projections, but none seen inside the microchannels. Conditions: For figures a and b - cell density of 15k cells/cm^2 added to both compartment (area: 0.6 x 0.6 cm^2). For figures c and d - 200 µl differentiation media with NGF added.

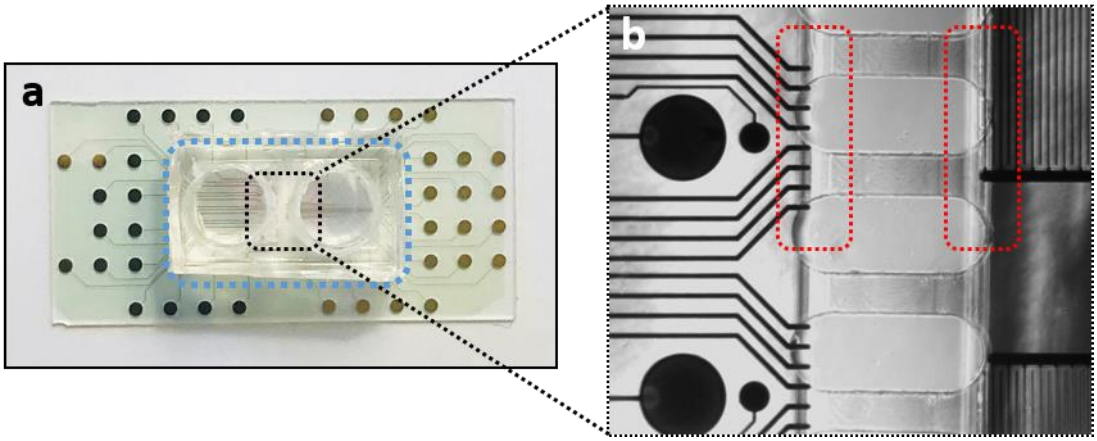

Figure 4.13. MEAs-CMC device: a) PDMS-based CMC device (blue) bonded onto a Design 1-MEA chip with IDEs in left and MEA in right compartments. b) Zoom version IDEs and MEAs where some are aligned with microchannels (red).

This first micro-milling-derived CMC is no way the optimal system we are seeking, especially relating to the future use of hNSC-derived neurons, where cell body migration should be avoided, thus the very narrow channels of 3-6 µm as seen in Figures 2.5 and 4.8[8]. In the available literature on CMCs device, primary neurons are often used, combined with much larger interconnecting microchannels (10-400 µm)[7,156,225], and with focus on creating asymmetric channels and bottle necks to avoid cell body migration[6]. With our micro-milling method, we believe that this in principle can be dealt with by changing to smaller milling tool and adjusting the milling parameters to reduce the height of the microchannels and explore the minimum resolution that can be achieved in the x-y direction as tool vibration is one the possible challenge. Unfortunately, no time was available to pursue this.

Chapter 5

MICRO-STRUCTURED 3D CARBON SCAFFOLDS (3D-CS)

This chapter introduces 3D conductive scaffolds for neural studies. Firstly, the need of a 3D microenvironment is described, followed by a new techniques to fabricate the 3D-CS. It further describes the methodologies to improve the 3D-CS for electrochemical characterization using $[Fe(CN)_6]^{3-/4-}$ redox probe. Lastly, the chapter focuses on the development and finite element (FE) simulation characterization of 3D hydrogel-based microarchitecture to support cell studies.

5.1 Introduction

Although traditional 2D monolayer cell cultures have proven vital as *in-vitro* cellular models, they do not provide the essential cell-cell or cell-matrix interactions, available in the *in vivo* 3D microenvironment[238,239]. To address this issue, 3D *in-vitro* models have been developed to better mimic the complex *in-vivo* architecture and function of the brain to study neural disease[240]. Numerous studies have been conducted that have involved development of 3D scaffolds with distinctive nano/microstructured topographical cues[238,239,241] and conductive scaffolds[242–244] to enhance the growth and differentiation of neurons[245–248]. Conductive scaffolds with micro- and nanopatterns have been utilized as topographical conductive cues for human neural stem cell differentiation[240,243,249,250], but also for sensing of neurotransmitter release from cells residing on the scaffold[223,251].

In this initial study on 3D scaffolds, I have investigated two different aspects:

1. A micro-structured 3D-CS was fabricated from a 3D SU-8 scaffold template, pyrolyzed in a furnace at 900°C and inert environment. The ultimate idea was to see how such relatively large 3D scaffold would behave electrochemically, and to use it as a future conductive scaffold for combined 3D cell culture and sensing.

2. In a second study (Paper II), I was responsible for conducting simulation characterization to evaluate how an electrical field would penetrate through a 3D hydrogel at various frequencies from 1MHz down to 100 mHz. This is important in future 3D hydrogel-based cell culture studies where 3D conductive electrodes would be utilized to manipulate and record neural activities upon electrical, chemical or optical stimulation in 3D microenvironment.

5.2 Fabrication and electrochemistry of 3D-CS

5.2.1 3D-CS fabricated from a sacrificial sugar cube mold

3D-CSs were fabricated by implementing a process similar to soft-lithography, using SU-8 polymer resist, instead of the conventional PDMS elastomer, cast around the mold[248], followed by UV curing and subsequent pyrolysis of the cured 3D SU-8 scaffold. The initial work involved the use of a sacrificial sugar cube as the mold template[246], with the fabrication described in Figure 5.1 with the different steps involved listed below. Figure 5.2 shows images of the different scaffolds generated through these steps.

1. A porous sugar cube was placed inside an empty small petri dish to begin soft-lithography with SU-8.
2. Sufficient amount of SU-8 2035 was poured into the container covering all parts of the sugar cube.
3. The container was placed inside a desiccator and vacuum was applied to remove any air bubbles inside the sugar cube ensuring that all porous parts of the sugar cube structure were filled with SU-8 (Figure 5.2a).
4. The SU-8 sugar cube mixture was then exposed to UV for 5 min, followed by heating at 80 °C inside an oven to cross-link the entire SU-8 polymer, resulting in brown coloured sugar cube structures (Figure 5.2b).
5. The cured SU-8-scaffold structure was diced out from the petri dish and then immersed in warm water (60 °C) under ultrasonication to dissolve the sugar cube completely, resulting in a an SU-8 replica of the sugar cube (Figure 5.2c).
6 The SU-8 sugar cube replica was then pyrolyzed at 900 °C in a furnace in inert nitrogen environment to generate a microporous 3D-CS (Figure 5.2d).

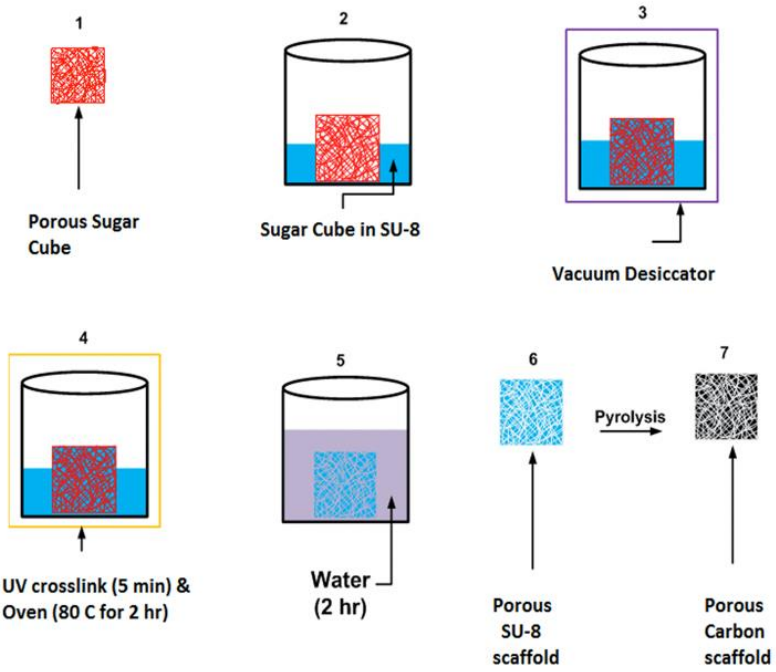

Figure 5.1. Schematics of the fabrication of 3D-CS using a sugar mold template: 1 & 2) Sugar cube placed in a container (petri dish) with SU-8 resist poured over it. 3) Sugar cube with SU-8 placed in a vacuum desiccator to remove air from microporous features in the sugar. 4) UV crosslinking and baking to cure SU-8. 5) Dissolution of sugar cube in warm water. 6 &7) Microporous SU-8 scaffold pyrolyzed to obtain a conductive microporous 3D-CS, similar to PDMS based sugar templating procedure described in our group[248].

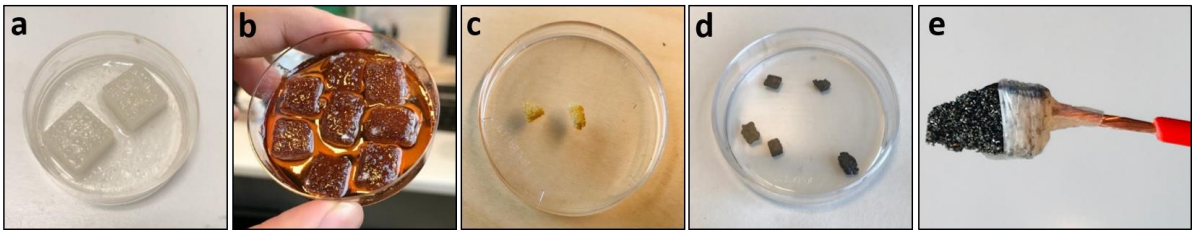

Figure 5.2. Images of scaffolds at different steps of the fabrication: a) Sugar cube with SU-8 poured over the cubes. b) After UV-crosslinking of SU-8 and baking it the oven. The color change indicates cured SU-8. c) SU-8 sugar replica scaffolds were obtained after dissolving the sugar in warm water. d) 3D SU-8 scaffolds pyrolyzed into 3D-CSs. e) 3D-CS attached (wrapping through parafilm around) to copper wire to form a 3D-CS working electrode.

Once the scaffold fabrication was completed, we tried to see if the scaffold could be used as a working electrode for electrochemistry by attaching the 3D-CS to copper wire (Figure 5.2e). However, due to that the 3D scaffold was porous throughout, this turned out to be difficult since the analyte crept inside the 3D structure and came in direct contact with the copper wire, which resulted in unstable and distorted CVs. To address this, we decided to create a 3D-CS equipped

with a non-porous contact handle for electrical connection to the copper wire, by 3D printing a sacrificial mold structure, as previously described[246].

5.2.2 3D-CS fabricated from a 3D printed PVA mold

A sacrificial dissolvable sugar cube holder equipped with a hollow handle was designed and 3D printed (using FelixRobotics 3D filament printer Pro2) in poly vinyl alcohol (PVA, filament from FelixRobotics with diameter of 1.75 mm), as shown in Figure 5.3a. The holder was designed to fit a standard sugar cube, and when SU-8 was poured into the holder the hollow space of the handle was filled with SU-8 to generate a non-porous handle connected to the SU-8 sugar cube replica. The fabrication process thereafter followed the same procedure as in Figure 5.1 with a few modifications, as described below. Figure 5.3 illustrates the fabricated 3D-CS with a non-porous contact lead. The main steps involved in creating the 3D-CS with a built in non-porous contact lead:

1. A CAD design of the sugar cube holder was created in AUTODESK TINKERCAD software and transformed into a SLA file format, readably by the 3D printer, shown in Figure 5.3a.
2. The holder was then 3D printed in PVA, as shown in figure 5.3b.
3. SU-8 photoresist was poured in the holder containing a sugar cube with SU-8 smoothly filling the hollow handle structures, Figure 5.3c.
4. In the same way as shown in Figure 5.1, the PVA holder was placed inside a vacuum desiccator to remove air from the microporous of sugar cube and allow SU-8 to fill all cavities.
5. The PVA-SU-8-sugar structure was then cured, exposing with UV for 5 min from each side due to thick layer of SU-8 throughout the scaffold layer, followed by heating at 80°C inside an oven over night, Figure 5.3d.
6. The PVA-SU-8-sugar structure was immersed in warm water (60 °C) and ultrasonicated to dissolve the sugar and PVA mold to attain the micro-structured SU-8 scaffold with solid SU-8 handle, as shown in Figure 5.3e.
7. The SU-8 scaffold was then pyrolyzed into the corresponding 3D-CS, as shown in Figure 5.3f. The SEM images of the microstructures of the scaffolds before and after pyrolysis are shown in Figure 5.4.

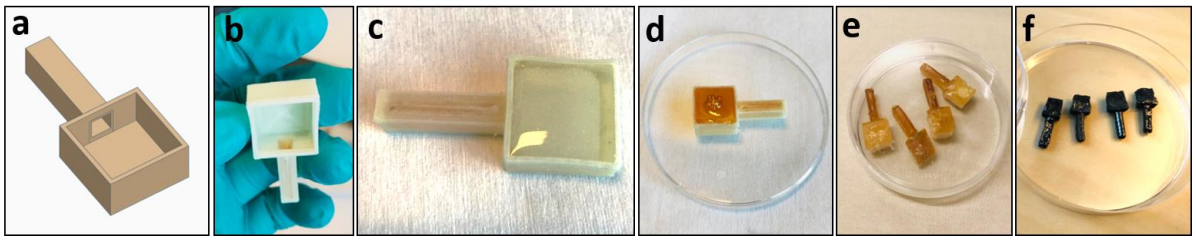

Figure 5.3. Design and fabrication of a 3D-CS with a non-porous handle using 3D printing: a) CAD design of sugar cube holder. b) 3D printed sugar cube holder with a hollow handle. c) The holder with a sugar cube inside filled with SU-8 through-out and d) the UV cured and thermally baked structure. e) Microporous SU-8 scaffold with a solid SU-8 handle after removal of PVA and sugar in warm water using ultra-sonication. e) The resulting 3D-CS scaffold after pyrolysis.

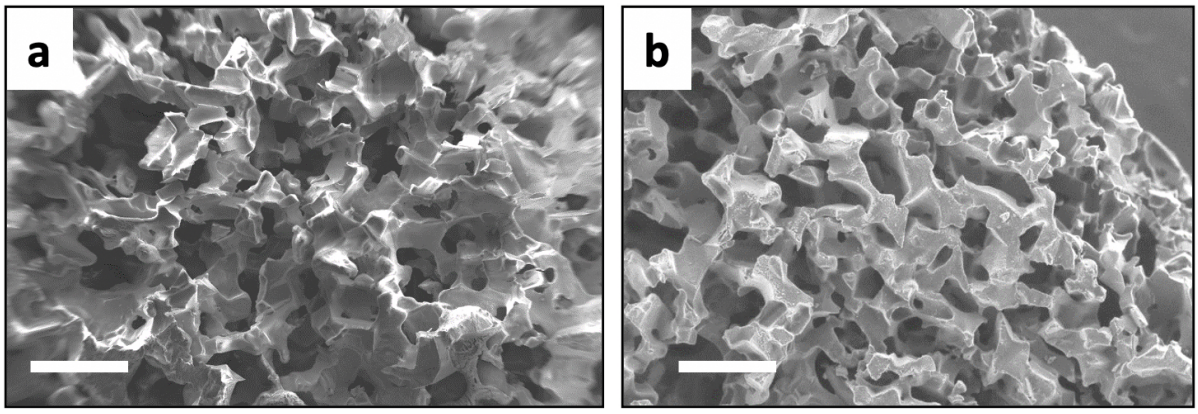

Figure 5.4. SEM images of the microstructure of 3D scaffolds: a) The 3D SU-8 scaffold replica before and b) the corresponding 3D-CS after pyrolysis. Scale bar 500 µm.

5.2.3 Electrochemistry on 3D-CS

The electrochemical set-up, shown in Figure 5.5a, was composed of the oxygen plasma treated (total O_2 pressure of 0.6 mbar and power of 50 W for 60 sec) 3D-CS as a working electrode placed in a beaker with an electrolyte solution. The 3D-CS handle was clamped with a crocodile connector attached to a copper wire. The counter and reference electrodes were made from gold plated silicon wafers diced into relatively large 8 x 20 mm pieces attached on the beaker´s sidewalls and connected through wires. The counter and reference electrode were immersed in the solution at approximately 10 mm depth, while a manual micromanipulator controlled the immersion depth of the working electrode to 1, 2 or 4 mm, exposing more and more of the electrode area to the solution (Figure 5.5b-c). Figure 5.5e shows the obtained CVs for the 3D-CS for increasing electrode area, with a resulting increase in the current, indicating that the 3D-CS electrodes were functional with the contact handle.

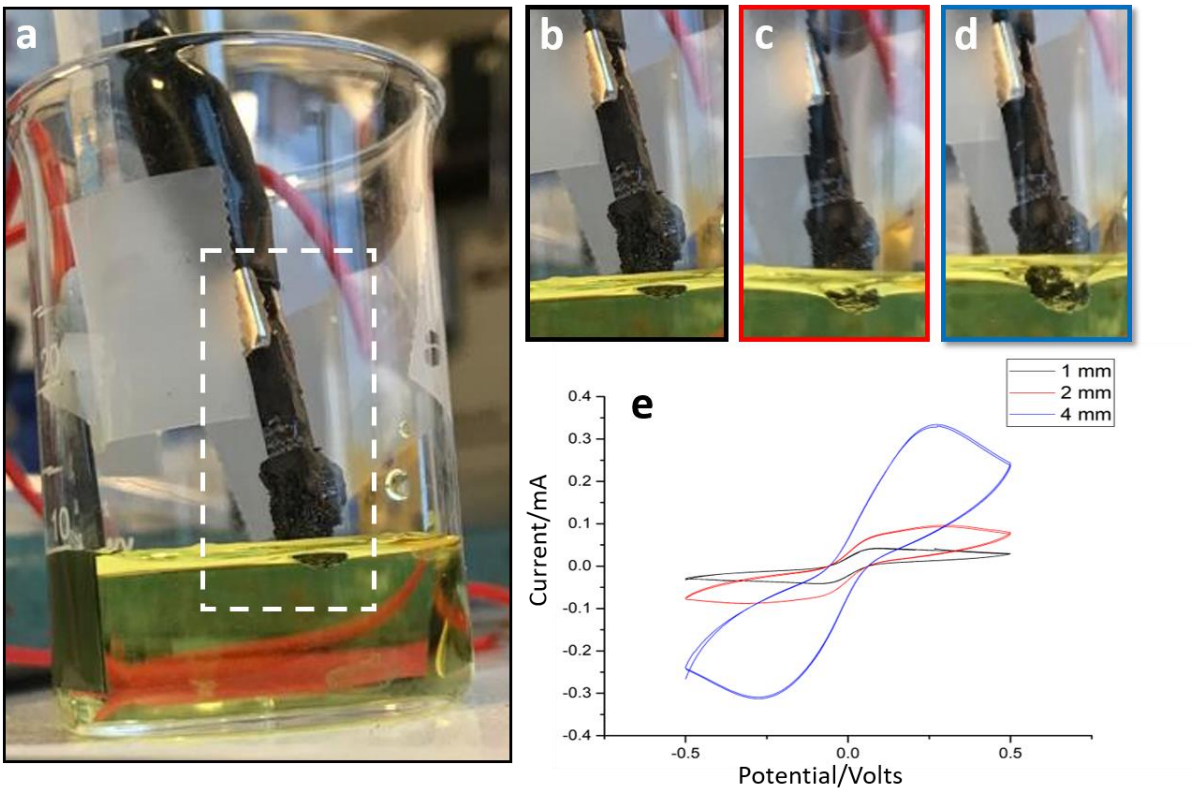

Figure 5.5. Electrochemical setup and CV obtained with the 3D-CS as working electrode immersed in the solution: a) Electrochemical set up with the 3D-SC working electrode highlighted (dotted white rectangle). 3D-CS exposed to solution at different depths, b) 1 mm, c) 2 mm, and d) 4 mm. e) The CVs obtained in 10 mM of $[Fe(CN)_6]^{3-/4}$ in PBS (pH 7.4) at a scan rate of 50 mV/s. Reference and counter electrodes were made from 8 x 20 mm gold plated silicon sheets.

5.3 Hydrogel based 3D scaffold

Brain tissue is one of the softest tissues in the human body with unique intrinsic mechanical properties[252]. To mirror the *in vivo* environment in a 3D cell and tissue culture, the surrounding micro-environment should thus possess a similar elastic modulus (E) as that of brain tissue, i.e., approx. ($E \leq 0.1 - 0.4$ kPa)[253], which can be compared to that of the liver, cartilage and bone of ($E \geq 1$ kPa), ($E \geq 10$ kPa), and ($E \geq 1$ GPa)[254], respectively. Hydrogels are polymeric materials that contain physical and chemical properties that can be used to construct scaffolds as a means to mimic the 3D micro-soft-architecture crucial for cell growth and neural regeneration[255].

The ultimate goal is to provide a 3D environment similar to the elastic modulus of brain tissues to be integrated with 3D electrodes, where the hydrogel mimics the soft 3D micro

microenvironment for cell growth and differentiation, and 3D electrodes are used to explore the neural activity by electrochemical means or for electrical stimulation of cells residing in this 3D environment. My main contribution to this work was to employ the COMSOL multiphysics finite element (FE) software simulation to characterize how electric fields behave and penetrate through such hydrogel environments that is crucial to understand hydrogel characteristics.

The simulations were based on the experimental study found in Paper II (appendix I) where a poly(2-hydroxyethyl methacrylate) (pHEMA) hydrogel, crosslinked to different degrees with poly(ethylene glycol)-dimethacrylate (PEGDMA), was characterized using electrical impedance spectroscopy (EIS) to study the electric field (EF) response in a 3D pHEMA hydrogel. All measurements were conducted using a gold microelectrode chip, having three circular on-chip working electrodes with large common on-chip reference and counter electrode (see Figure 5.6a). The entire working electrode area was covered with a tethered 3D crosslinked hydrogel layer (PEGDMA: pHEMA ratio of 1:100, 1:200, or 1:400) tethered on top of the three working electrodes as seen in Figure 5.6b with a Cryo-SEM image of the 1:200 crosslinked hydrogel in Figure 5.6c.

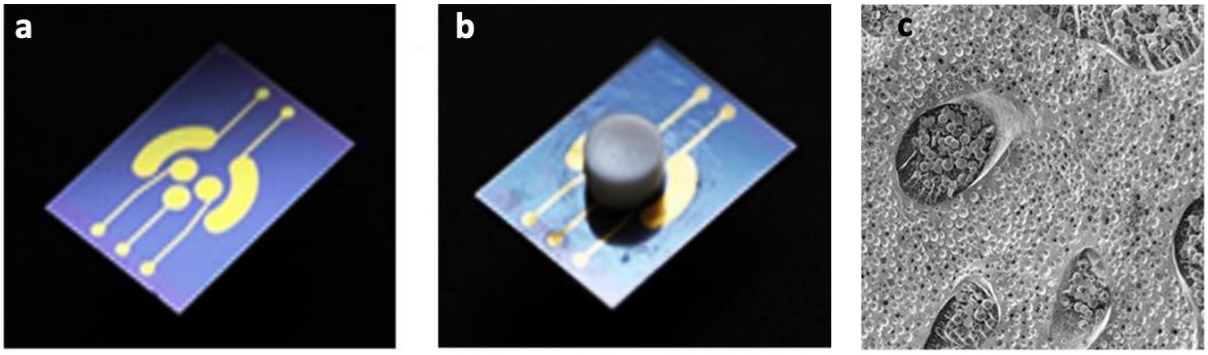

Figure 5.6. Electrode microchip and hydrogel polymerization setup: a) A photo of a gold electrode microchip comprising three circular working electrodes (WE, Ø 1.5 mm) placed in the center, and two larger electrodes used as counter (CE) and reference electrode (RE) during electrochemical characterization. b) A photo of an *in situ* polymerized covalently tethered hydrogel disk (thickness: 1 mm, diameter: 6 mm) on a gold electrode microchip. The hydrogel covered the three WEs and the surrounding silicon nitride insulation layer. c) A cryo-SEM image of the 1:200 crosslinked hydrogel on top of the electrode in b, forming a compact porous matrix (round pores, 2-3 µm in diameter) engulfing large irregular pores.

To explore the EF behaviour when a 3D hydrogel scaffold is tethered on top of the electrodes, EIS characterization at a wide frequency window (100 mHz to 1 MHz) was performed. The premise for the chosen simulation conditions was that EF cannot bypass the hydrogel and

propagate directly from the WE to the CE. In the experimental work presented in Paper II, this condition was met by the performed surface modifications that ensured that the hydrogel was tethered on both the WEs and the surrounding silicon nitride surface. However, in applications, where a hydrogel is either only tethered on the WE or only loosely placed on the used electrode chip, the EIS response primarily depends on the degree of contact between the hydrogel scaffolds and the plain electrode surface. Under such experimental conditions, another complicating factor may be that hydrogel scaffolds usually develop corrugated voids between the scaffold and electrode surface due to a random scaffold structure (Figure 5.6c). These voids promote current leakage, such that the electrical fields avoid the scaffold structure and bypass through the electrolyte, which is not desired in the characterization of the hydrogel scaffolds. This anomaly was previously described by Tully-Dartez et al.[256] in a similar study between chitosan scaffolds with embedded cylindrical electrodes. To determine the EF behaviour (originating here from an applied sinusoidal potential) across the 3D hydrogel scaffold, residing on top of the electrode surface, it must essentially penetrate through the hydrogel during the entire frequency range.

To evaluate the EF penetration through a hydrogel scaffold, COMSOL Multiphysics v5.0 finite element (FE) simulations were carried out at the frequency range 100 mHz to 1 MHz. For simplicity, only a two-electrode setup was considered (Figure 5.7). The 3D hydrogel (pHEMA) and electrolyte (PBS) along with two electrodes (gold) were modelled using two different configurations:

Case 1: The scaffold resides only on top of the working electrode (WE) without covering the counter electrode (CE), which was the used experimental condition in Paper II, see Figure 5.7a.

Case 2: The scaffold resides on top of both the WE and CE, hence entirely covering both electrodes, see Figure 5.7b.

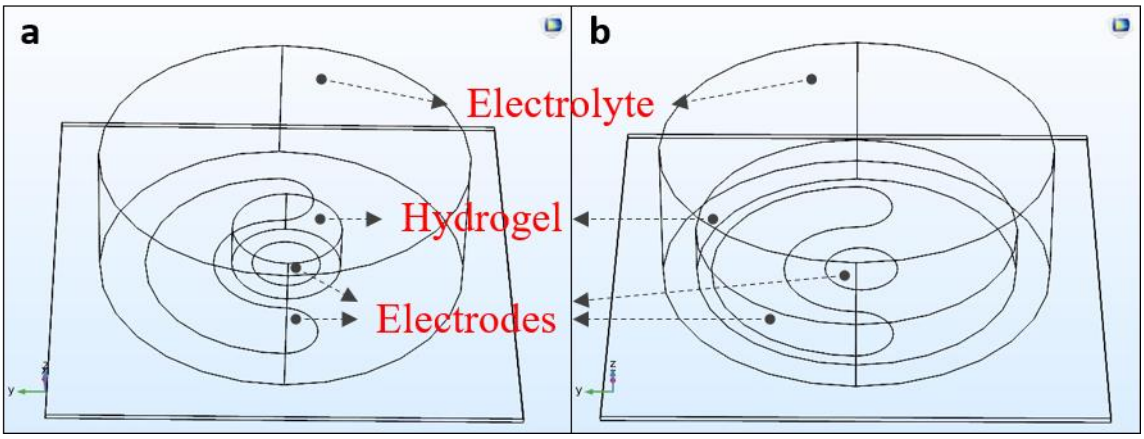

Figure 5.7. 3D modeling in COMSOL multiphysics for studying EF behavior in a 3D hydrogel: a) Case 1: Hydrogel covering only the WE without covering the CE in the presence of electrolyte, b) Case 2: Hydrogel covering both the WE and CE in the presence of electrolyte.

The frequency domain and time-dependent 3D space dimension study, with the AC/DC physics interface, was selected to represent the practical model into finite element simulation. The parameters for each material were defined carefully to model the practical scenario in the simulation. To construct the model, the conductivity of pHEMA hydrogel was set to 3.5 mS/m, and for PBS to 1.6 S/m, based on literature studies[257,258]. A well-defined finite element mesh is crucial to approximate the model, which subdivides the CAD design into smaller domains, known as elements. A set of required equations, according to the selected study (AC/DC in our study), are solved on each element to approximate the practical model. The mesh consisted of tetrahedral elements for both case 1 and 2, with the element parameters tabulated in Table 5.1.

Table. 5.1: Mesh elements for the constructed COMSOL geometry of case 1 and case 2.

Element	Case1	Case2
Domain elements	109519	187687
Boundary elements	26402	38952
Edge elements	1491	1895
Mesh quality	0.91	0.92

The results obtained for case 1 (only WE covered) in Figure 5.8a and c demonstrate that nearly all of the EF lines penetrate through the hydrogel and enter the electrolyte region to reach the

counter electrode. The results for case 2 (both WE and CE covered) in Figure 5.8b and d, show that the majority of the electric field lines penetrate the hydrogel, entering into the electrolyte region, and then re-enter the hydrogel from the top to reach the CE. Figure 5.8 shows the 3D modelled EF simulation of two frequencies for both cases at 100 mHz (Figure 5.8a and b) and 1MHz (Figure 5.8c and d). The complex EF behaviour at various frequencies and potentials is discussed in Paper II (Appendix A).

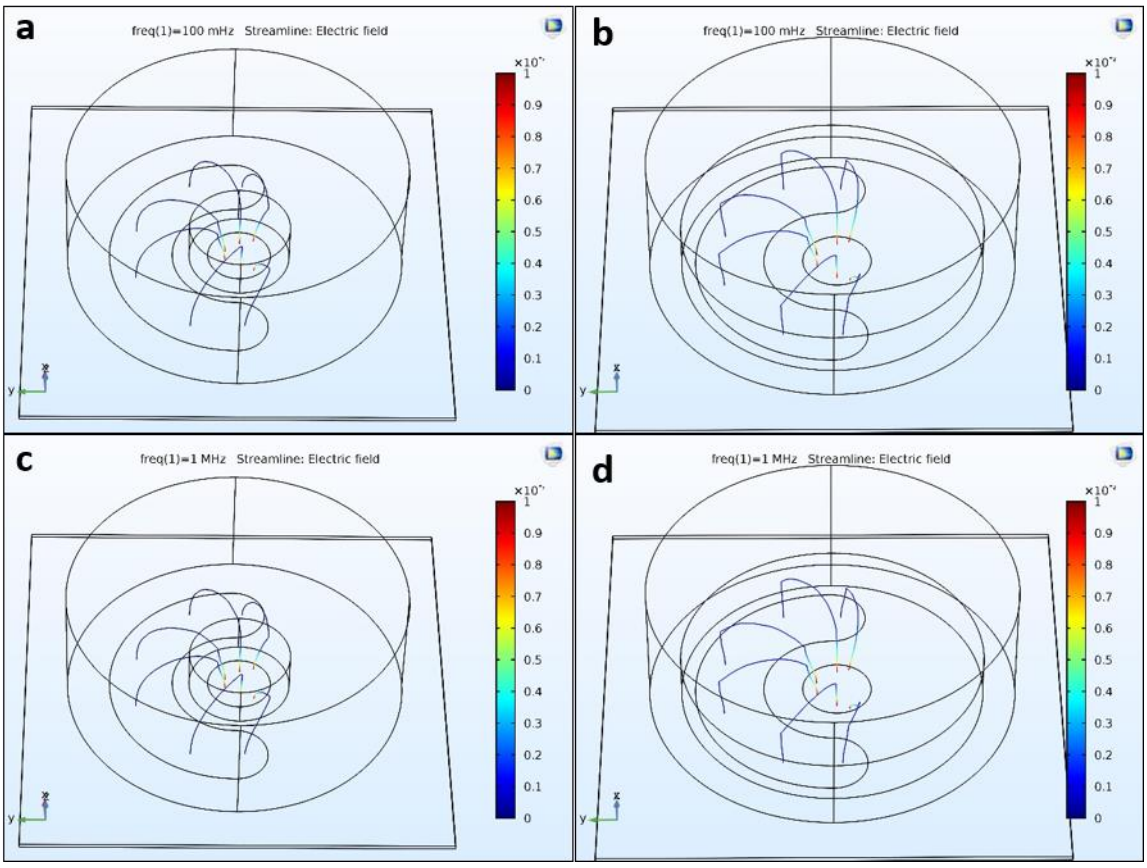

Figure 5.8. 3D modeling for studying EF behavior in hydrogel for the two cases: Case 1 with only WE covered by hydrogel shows EF lines passing through hydrogel reaching the counter electrode at a) a frequency of 100 mHz and c) at 1 MHz. Case 2 with hydrogel on both WE and CE, shows EF lines passing through hydrogel into the electrolyte and then re-entering the hydrogel to reach the CE at c) 100 mHz and d) 1 MHz.

The FE simulation provides detailed spectral information, showing the characteristics of the electrical fields in the hydrogel. The presented 3D model provides a simplification of the experimental frequency range (from 1 MHz down to 100 mHz), which is sufficient to illustrate the EF line behaviour in the xyz plain. However, the simulation lacks the ability to account for the corrugated porous environment and often more complex hydrogel matrix structure in real life,

as exemplified in Figure 5.6c, and is a limitation. These preliminary simulations on EF penetration through a 3D hydrogel show promise for applications relying on electrical/electrochemical measurements in future 3D scaffolds with 2D and 3D electrode dimensions to establish cell studies in such 3D microenvironments.

Chapter 6

CONCLUSION & OUTLOOK

6.1 Conclusion

This thesis presents the development of technological advancements and novel approaches to model brain-on-a-chip systems for the treatment of brain disorders. The described research is multidisciplinary and combines state of the art elements of microfabrication, electrochemistry, additive printing, finite element simulations, and cellular studies. The main focus of the thesis was to produce 2D and 3D microsensors and microfluidic devices and to characterize them with electrochemical methods, and via simulations. Moreover, these devices were further used for the culture and differentiation of cells to demonstrate dopamine detection upon chemical stimulation.

Starting from the development of ultra-microelectrode array (UMEA) chips, we have fabricated 54 ultramicroelectrodes (UMEs) densely packed into a small area with 5 µm and 10 µm diameter openings, each individually addressable with an on-chip counter and pseudo-reference electrodes. These UMEs are simultaneously addressable via a custom-made potentiostat for experimental studies. Since the aim was application for cellular studies, the UMEAs were fabricated on transparent glass substrate that supports imaging during experiments, which required optimization of the conventional silicon wafer-based fabrication protocols.. After successful optimization of the fabrication procedure, the UMEA chips were further characterized using electrochemical techniques, such as cyclic voltammetry and amperometry. The UMEA chips were then integrated into micromilled PMMA chip holders and assembled with the custom-made potentiostat to acquire simultaneously readings on all the 54 UMEs. The UMEA chips were further prepared and treated to enable cellular studies, which included MPA electrode modification, extracellular coating optimization, and sterilization of chip holders. Multiple cellular experiments with PC12 cells cultured on UMEA chips with both 5 µm and 10 µm diameter electrodes were performed. Successful dopamine exocytosis events

were recorded simultaneously on all the 54 UMEs with both dimensions and comparison of results using the two designs (5 µm and 10 µm UMEs) were discussed (Paper I).

Compartmentalized Microfluidics Chips (CMCs) with integrated MEAs were developed to re-construct neural pathways in in-vitro cell cultures, which may uncover the neural circuitry's primary mechanism. Three different MEA chip designs, each with a specific purpose, were fabricated and electrochemically characterised with similar high reproducibility of the fabrication process as reported for the UMEA design.

After a successful UMEA/MEA developments, cellular experiments were conducted with PC12 cells, using the Neurite guidance MEA – Design 1, integrated with a previously develop PDMS based CMC. Due to serious alignment problems between the small microchannels of the CMC and MEA chip, a new CMC device with larger microchannels needed to be fabricated. Due to the Covid-19 lockdown with no access to the cleanroom, a new micro-milling method for making the CMC mold was developed. PC12 differentiation was initiated on an integrated MEA-CMC device, but again due to the Covid-19 lockdown and my PhD time running out, the experiment had to be stopped and I was unable to conclude the study.

Enhanced 3D in vitro models are required to construct complex in vivo structures to develop advanced disease models to introduce more accurate therapeutic strategies. A hybrid technique was developed to form 3D-CSs that potentially could enable three-dimensional reconstruction of tissue with integrated sensing capability. The 3D-CS was fabricated using a modified soft lithography approach by implementing 3D printing of a sacrificial mold compartment (in poly vinyl alcohol (PVA)), in which a sugar cube could be placed (the scaffold template). This was followed by casting the template with SU-8 photoresist (replacing conventional PDMS casting), subsequent curing and dissolution of the PVA and sugar cube template. The resulting SU-8 scaffold was then pyrolyzed, resulting in a conductive 3D-CS, which also proved to be electrochemically active.

6.2 Outlook

This thesis presents tailor-made micro- and ultramicro electrode arrays with unique capabilities to fulfill specific requirements to study neural network activities. Compartmentalized microfluidic chips (CMC) device were constructed to re-create and

manipulate the neural circuitry pathway by integrating MEAs to specifically monitor neurotransmitter release. These devices provide proof-of-concept and multi-functional designs that could lead to a versatile approach for neuroscience applications. However, there exists much room for improvement.

Our initial cellular studies were performed using PC12 cells to record dopamine exocytosis events from single cells upon high K^+ chemical stimulation of the whole cell population. A future goal is to culture and differentiate human stem cell-derived neurons to study the intercommunication between individual neurons in a population. The idea is to stimulate single cells in a neural population, either by electrical stimulation or by light (optogenetically modified cells), studying the signal propagation in the cell population through electrochemical measurement of neurotransmitter release (dopamine) onto the individual UMEs. In the case of Parkinson´s disease, one could imagine studying the addition of various stimuli (drugs, toxins, alpha-synuclein etc.) to see how they affect the neural population, and this would be especially interesting when used in a two- or multi-compartment system with different neural population in each compartment. A multi-compartment CMC, representing various regions of the basal ganglia, containing different enzyme based (bio) sensors to enable detection of other neurotransmitters than dopamine (GABA, glutamate etc) would be an ultimate goal.

Regarding the microchip devices themselves, several improvements can be foreseen. The 54-channel UMEA chips can be improved by reducing the electrode dimension below 5 µm, which would ultimately enhance the spatial resolution to record dopamine exocytosis events. Another improvement could be to replace the gold electrodes with micro and/or nanostructured carbon, which has been reported to promote differentiation and maturity of neurons. The width and height of the CMC microchannels obtained using micromilling (200 µm and 50 µm, respectively) can be further reduced by optimizing the micromilling tool parameters.

In the case of 3D-CS design, the PVA mold can be replaced by omnidirectional 3D printing of microstructured SU-8 photoresist in granular gels, which after curing can be pyrolyzed to generate the microporous 3D-CS. Such microstructured 3D-CSs surrounded by a hydrogel environment would provide a 3D microenvironment for cell growth and differentiation closer to the in vivo architecture, as well as possibility to electrically stimulate cells and monitor neurotransmitter release.

In summary, this thesis provides different possibilities and directions towards creating novel brain-on-chip disease models by combining state of the art microfabrication techniques.

BIBLIOGRAPHY

1. Dawson, T. M., Golde, T. E. & Lagier-Tourenne, C. Animal models of neurodegenerative diseases. *Nat. Neurosci.* **21**, 1370–1379 (2018).

2. Misra, S. *et al.* Ex vivo organotypic culture system of precision-cut slices of human pancreatic ductal adenocarcinoma. *Sci. Rep.* **9**, 1–16 (2019).

3. Slanzi, A., Iannoto, G., Rossi, B., Zenaro, E. & Constantin, G. In vitro Models of Neurodegenerative Diseases. *Front. Cell Dev. Biol.* **8**, (2020).

4. Korkmaz, Ü. & Kaya, M. Experimental Models in Neurodegenerative Diseases. *Nucl. Med. Semin.* **5**, 69–77 (2019).

5. Gitler, A. D., Dhillon, P. & Shorter, J. Neurodegenerative disease: Models, mechanisms, and a new hope. *DMM Dis. Model. Mech.* **10**, 499–502 (2017).

6. Gladkov, A. *et al.* Design of Cultured Neuron Networks in vitro with Predefined Connectivity Using Asymmetric Microfluidic Channels. *Sci. Rep.* **7**, 1–14 (2017).

7. Toivanen, M. *et al.* Optimised PDMS tunnel devices on MEAs increase the probability of detecting electrical activity from human stem cell-derived neuronal networks. *Front. Neurosci.* **11**, 606 (2017).

8. Kajtez, J. *et al.* 3D-Printed Soft Lithography for Complex Compartmentalized Microfluidic Neural Devices. *Adv. Sci.* **2001150**, 1–14 (2020).

9. Osaki, T., Shin, Y., Sivathanu, V., Campisi, M. & Kamm, R. D. In Vitro Microfluidic Models for Neurodegenerative Disorders. *Adv. Healthc. Mater.* **7**, 1700489 (2018).

10. Dimaki, M. *et al.* A compact microelectrode array chip with multiple measuring sites for electrochemical applications. *Sensors (Switzerland)* **14**, 9505–9521 (2014).

11. Cui, H. F., Ye, J. S., Chen, Y., Chong, S. C. & Sheu, F. S. Microelectrode array biochip: Tool for in vitro drug screening based on the detection of a drug effect on dopamine release from PC12 cells. *Anal. Chem.* **78**, 6347–6355 (2006).

12. Li, S., Chen, X. & Han, F. Simulation of Cell Dielectric Properties Based on COMSOL. *J. Robot. Netw. Artif. Life* **4**, 330 (2018).

13. Olmo, A. & Yúfera, A. Computer simulation of microelectrode based bio-impedance measurements with COMSOL. in *BIODEVICES 2010 - 3rd International Conference on Biomedical Electronics and Devices, Proceedings* 178–182 (2010).

14. Dhall, A. *et al.* Simulating Fluid Flow through a Culture Chip for Cell Migration Studies in Microgravity. in *Proceedings of the 2016 COMSOL Conference in Boston* (2016).

15. Lifton, V. A., Lifton, G. & Simon, S. Options for additive rapid prototyping methods (3D printing) in MEMS technology. *Rapid Prototyp. J.* **20**, 403–412 (2014).

16. Abdelaal, O. A. M. & Darwish, S. M. H. Review of rapid prototyping techniques for tissue engineering scaffolds fabrication. *Adv. Struct. Mater.* **29**, 33–54 (2013).

17. Karakousis, P. C., Magill, S. S. & Gupta, A. Projected number of people with Parkinson disease in the most populous nations, 2005 through 2030. *Neurology* **69**, 223 (2007).

18. Roybon, L., Christophersen, N. S., Brundin, P. & Li, J. Y. Stem cell therapy for Parkinson's disease: Where do we stand? *Cell Tissue Res.* **318**, 261–273 (2004).

19. Durães, F., Pinto, M. & Sousa, E. Old drugs as new treatments for neurodegenerative diseases. *Pharmaceuticals* **11**, 1–21 (2018).

20. Gustavsson, A. *et al.* Cost of disorders of the brain in Europe 2010. *Eur. Neuropsychopharmacol.* **21**, 718–779 (2011).

21. James, P. An Essay on the Shaking Palsy. *J. Nerv. Ment. Dis.* **20**, 223–236 (2002).

22. Horowski, R. *et al.* An Essay on Wilhelm von Humboldt and the Shaking Palsy: First Comprehensive Description of Parkinson's Disease by a Patient. *Neurology* **45**, 565–568 (1995).

23. Foix, C., la, J. N.-A. cérébrale: les noyaux gris cenraux et & 1925, undefined. Anatomie cérébrale: les noyaux gris cenraux et la région mésencéphalo-sous-optique.

24. Graham, D. G. On the origin and significance of neuromelanin. *Arch. Pathol. & Lab. Med.* **103**, 359—362 (1979).

25. Hassler, R. Zur Pathologie Der Paralysis Agitains Und Des Postenzephalitischen

Parkinsonismus. *J. Psychiatr. Neurol.* **48**, 387–476 (1938).

26. Lloyd, K. & Hornykiewicz, O. Parkinson's disease: Activity of L-dopa decarboxylase in discrete brain regions. *Science (80-.).* **170**, 1212–1213 (1970).

27. Ozansoy, M. & Başak, A. N. The central theme of parkinson's disease: α-synuclein. *Mol. Neurobiol.* **47**, 460–465 (2013).

28. Tysnes, O. B. & Storstein, A. Epidemiology of Parkinson's disease. *J. Neural Transm.* **124**, 901–905 (2017).

29. Dauer, W. & Przedborski, S. Parkinson's disease: Mechanisms and models. *Neuron* vol. 39 889–909 (2003).

30. Politis, M. & Lindvall, O. Clinical application of stem cell therapy in Parkinson's disease. *BMC Medicine* vol. 10 1 (2012).

31. Jankovic, J. Parkinson's disease: Clinical features and diagnosis. *J. Neurol. Neurosurg. Psychiatry* **79**, 368–376 (2008).

32. Sanjay, P. & Prachaya, S. Levodopa-induced Dyskinesia: Clinical Features, Pathophysiology, and Medical Management. *Ann. Indian Acad. Neurol.* **20**, 190–198 (2017).

33. Menza, M. A., Sage, J., Marshall, E., Cody, R. & Duvoisin, R. Mood changes and "on-off" phenomena in Parkinson's disease. *Mov. Disord.* **5**, 148–151 (1990).

34. Alegret, M. *et al.* Obsessive-compulsive symptoms in Parkinson ' s disease. *J. Neurol. Neurosurg. Psychiatry* **70**, 394–396 (2001).

35. Codling, D., Shaw, P. & David, A. S. Hypersexuality in Parkinson's Disease: Systematic Review and Report of 7 New Cases. *Mov. Disord. Clin. Pract.* **2**, 116–126 (2015).

36. Tison, F., Mons, N., Geffard, M. & Henry, P. The metabolism of exogenous L-Dopa in the brain: An immunohistochemical study of its conversion to dopamine in non-catecholaminergic cells of the rat brain. *J. Neural Transm. - Park. Dis. Dement. Sect.* **3**, 27–39 (1991).

37. ANDRE, B. L-dopa therapy in Parkinson's disease. A Critical Review of Nine Years' Experience. *Can. Med. Assoc. J.* **101**, 59–68 (1969).

38. Hagan, J. J., Middlemiss, D. N., Sharpe, P. C. & Poste, G. H. Parkinson's disease: prospects for improved drug therapy. *Trends Pharmacol. Sci.* **18**, 156–163 (1997).

39. Cedarbaum, J. M., Gandy, S. E. & McDowell, F. H. "Early" initiation of levodopa treatment does not promote the development of motor response fluctuations, dyskinesias, or dementia in parkinson's disease. *Neurology* **41**, 622–629 (1991).

40. Blond, S. & Siegfried, J. Thalamic stimulation for the treatment of tremor and other movement disorders. *Acta Neurochir. Suppl. (Wien).* **52**, 109–111 (1991).

41. Neurosurg, S. F. Combined (Thalamotomy and Stimulation) Stereotactic Surgery of the VIM Thalamic Nucleus for Bilateral Parkinson Disease. **50**, 344–346 (1987).

42. Walter, B. L. & Vitek, J. L. Surgical treatment for Parkinson's disease. *Lancet Neurol.* **3**, 719–728 (2004).

43. Okun, M. S. Deep-brain stimulation for Parkinson's disease. *N. Engl. J. Med.* **367**, 1529–1538 (2012).

44. Moum, S. J. *et al.* Effects of STN and GPi deep brain stimulation on impulse control disorders and dopamine dysregulation syndrome. *PLoS One* **7**, e29768 (2012).

45. Parsons, T. D., Rogers, S. A., Braaten, A. J., Woods, S. P. & Tröster, A. I. Cognitive sequelae of subthalamic nucleus deep brain stimulation in Parkinson's disease: a meta-analysis. *Lancet Neurol.* **5**, 578–588 (2006).

46. Temel, Y. *Limbic effects of high-frequency stimulation of the subthalamic nucleus. Vitamins and hormones* vol. 82 (Elsevier Inc., 2010).

47. Lindvall, O. & Björklund, A. Cell Replacement Therapy: Helping the Brain to Repair Itself. *NeuroRx* **1**, 379–381 (2004).

48. Courtois, E. T. *et al.* In vitro and in vivo enhanced generation of human A9 dopamine neurons from neural stem cells by Bcl-XL. *J. Biol. Chem.* **285**, 9881–9897 (2010).

49. Seiz, E. G. *et al.* Human midbrain precursors activate the expected developmental genetic program and differentiate long-term to functional A9 dopamine neurons in vitro. Enhancement by Bcl-XL. *Exp. Cell Res.* **318**, 2446–2459 (2012).

50. Liste, I., García-García, E. & Martínez-Serrano, A. The generation of dopaminergic

neurons by human neural stem cells is enhanced by Bcl-XL, both in vitro and in vivo. *J. Neurosci.* **24**, 10786–10795 (2004).

51. Fan, Y., Winanto & Ng, S. Y. Replacing what's lost: A new era of stem cell therapy for Parkinson's disease. *Translational Neurodegeneration* vol. 9 2 (2020).

52. Ganz, J., Lev, N., Melamed, E. & Offen, D. Cell replacement therapy for Parkinson's disease: How close are we to the clinic? *Expert Review of Neurotherapeutics* vol. 11 1325–1339 (2011).

53. Jagmag, S. A., Tripathi, N., Shukla, S. D., Maiti, S. & Khurana, S. Evaluation of models of Parkinson's disease. *Front. Neurosci.* **9**, 1-13(503) (2016).

54. Foltynie, T., Brayne, C. & Barker, R. A. The heterogeneity of idiopathic Parkinson's disease. *J. Neurol.* **249**, 138–145 (2002).

55. Blandini, F. & Armentero, M. T. Animal models of Parkinson's disease. *FEBS J.* **279**, 1156–1166 (2012).

56. Blesa, J. & Przedborski, S. Parkinson's disease: Animal models and dopaminergic cell vulnerability. *Front. Neuroanat.* **8**, 1–12 (2014).

57. Vingill, S., Connor-Robson, N. & Wade-Martins, R. Are rodent models of Parkinson's disease behaving as they should? *Behav. Brain Res.* **352**, 133–141 (2018).

58. Dawson, T. M., Ko, H. S. & Dawson, V. L. Genetic Animal Models of Parkinson's Disease. *Neuron* **66**, 646–661 (2010).

59. Olanow, C. W., Kieburtz, K. & Schapira, A. H. V. Why have we failed to achieve neuroprotection in Parkinson's disease? *Ann. Neurol.* **64**, 101–110 (2008).

60. Cummings, J. L., Morstorf, T. & Zhong, K. Alzheimer's disease drug-development pipeline: few candidates, frequent failures. *Alzheimers. Res. Ther.* **4**, 6–37 (2014).

61. Schneider, L. S. *et al.* Clinical trials and late-stage drug development for Alzheimer's disease: An appraisal from 1984 to 2014. *J. Intern. Med.* **275**, 251–283 (2014).

62. Pfeuffer, S., Ruck, T., Kleinschnitz, C., Wiendl, H. & Meuth, S. G. Failed, interrupted and inconclusive trials on relapsing multiple sclerosis treatment: update 2010–2015. *Expert Rev. Neurother.* **16**, 689–700 (2016).

63. Anderson, R. M., Hadjichrysanthou, C., Evans, S. & Wong, M. M. Why do so many clinical trials of therapies for Alzheimer's disease fail? *Lancet* **390**, 2327–2329 (2017).

64. Genc, K., Durnaoglu, S. & Genc, S. Patient-specific pluripotent stem cells in neurological diseases. *Stem Cells Int.* **2011**, 17 (2011).

65. Marchetto, M. C. N., Winner, B. & Gage, F. H. Pluripotent stem cells in neurodegenerative and neurodevelopmental diseases. *Hum. Mol. Genet.* **19**, (2010).

66. Falkenburger, B. H., Saridaki, T. & Dinter, E. Cellular models for Parkinson's disease. *J. Neurochem.* **139**, 121–130 (2016).

67. Roberti, M. J., Bertoncini, C. W., Klement, R., Jares-Erijman, E. A. & Jovin, T. M. Fluorescence imaging of amyloid formation in living cells by a functional, tetracysteine-tagged α-synuclein. *Nat. Methods* **4**, 345–351 (2007).

68. Hasegawa, T. *et al.* Accelerated α-synuclein aggregation after differentiation of SH-SY5Y neuroblastoma cells. *Brain Res.* **1013**, 51–59 (2004).

69. Chutna, O. *et al.* The small GTPase Rab11 co-localizes with α-synuclein in intracellular inclusions and modulates its aggregation, secretion and toxicity. *Hum. Mol. Genet.* **23**, 6732–6745 (2014).

70. Jang, W. *et al.* The Neuroprotective Effect of Erythropoietin on Rotenone-Induced Neurotoxicity in SH-SY5Y Cells Through the Induction of Autophagy. *Mol. Neurobiol.* **53**, 3812–3821 (2016).

71. Kim, C. *et al.* Antagonizing Neuronal Toll-like Receptor 2 Prevents Synucleinopathy by Activating Autophagy. *Cell Rep.* **13**, 771–782 (2015).

72. Meka, D. P. *et al.* Parkin cooperates with GDNF/RET signaling to prevent dopaminergic neuron degeneration. *J. Clin. Invest.* **125**, 1873–1885 (2015).

73. Lotharius, J. *et al.* Progressive degeneration of human mesencephalic neuron-derived cells triggered by dopamine-dependent oxidative stress is dependent on the mixed-lineage kinase pathway. *J. Neurosci.* **25**, 6329–6342 (2005).

74. Takahashi, K. *et al.* Induction of Pluripotent Stem Cells from Adult Human Fibroblasts by Defined Factors. *Cell* **131**, 861–872 (2007).

75. Vagaska, B. & Ferretti, P. Toward modeling the human nervous system in a dish: Recent progress and outstanding challenges. *Regen. Med.* **12**, 15–23 (2017).

76. Karimi, M. *et al.* Nanotechnology in diagnosis and treatment of coronary artery disease. *Nanomedicine* vol. 11 513–530 (2016).

77. Malekzad, H. *et al.* Plant protein-based hydrophobic fine and ultrafine carrier particles in drug delivery systems. *Critical Reviews in Biotechnology* vol. 38 47–67 (2018).

78. Sambale, F. *et al.* Three dimensional spheroid cell culture for nanoparticle safety testing. *J. Biotechnol.* **205**, 120–129 (2015).

79. Jensen, C. & Teng, Y. Is It Time to Start Transitioning From 2D to 3D Cell Culture? *Frontiers in Molecular Biosciences* 33 (2020) doi:10.3389/fmolb.2020.00033.

80. Kapałczyńska, M. *et al.* 2D and 3D cell cultures – a comparison of different types of cancer cell cultures. *Arch. Med. Sci.* **14**, 910–919 (2018).

81. Hoarau-Véchot, J., Rafii, A., Touboul, C. & Pasquier, J. Halfway between 2D and animal models: Are 3D cultures the ideal tool to study cancer-microenvironment interactions? *International Journal of Molecular Sciences* vol. 19 181 (2018).

82. Farjadian, F. *et al.* Bacterial components as naturally inspired nano-carriers for drug/gene delivery and immunization: Set the bugs to work? *Biotechnology Advances* vol. 36 968–985 (2018).

83. Garreta, E. *et al.* Tissue engineering by decellularization and 3D bioprinting. *Materials Today* vol. 20 166–178 (2017).

84. Hong, N., Yang, G. H., Lee, J. H. & Kim, G. H. 3D bioprinting and its in vivo applications. *J. Biomed. Mater. Res. - Part B Appl. Biomater.* **106**, 444–459 (2018).

85. Tsutsui, K. I., Taira, M. & Sakata, H. Neural mechanisms of three-dimensional vision. *Neurosci. Res.* **51**, 221–229 (2005).

86. Karimi, M. *et al.* Redox-Sensitive Smart Nanosystems for Drug and Gene Delivery. *Curr. Org. Chem.* **20**, 2949–2959 (2016).

87. Aebersold, M. J. *et al.* 'Brains on a chip': Towards engineered neural networks. *TrAC - Trends in Analytical Chemistry* vol. 78 60–69 (2016).

88. Park, J., Wetzel, I., Dréau, D. & Cho, H. 3D Miniaturization of Human Organs for Drug Discovery. *Advanced Healthcare Materials* vol. 7 (2018).

89. Bhatia, S. N. & Ingber, D. E. Microfluidic organs-on-chips. *Nature Biotechnology* vol. 32 760–772 (2014).

90. Mofazzal Jahromi, M. A. *et al.* Nanomedicine and advanced technologies for burns: Preventing infection and facilitating wound healing. *Advanced Drug Delivery Reviews* vol. 123 33–64 (2018).

91. El-Ali, J., Sorger, P. K. & Jensen, K. F. Cells on chips. *Nature* vol. 442 403–411 (2006).

92. Meyvantsson, I. & Beebe, D. J. Cell culture models in microfluidic systems. *Annual Review of Analytical Chemistry* vol. 1 423–449 (2008).

93. Sosa-Hernández, J. E. *et al.* Organs-on-a-chip module: A review from the development and applications perspective. *Micromachines* vol. 9 536 (2018).

94. Yu, Y., Shang, L., Guo, J., Wang, J. & Zhao, Y. Design of capillary microfluidics for spinning cell-laden microfibers. *Nat. Protoc.* **13**, 2557–2579 (2018).

95. Van Midwoud, P. M., Janse, A., Merema, M. T., Groothuis, G. M. M. & Verpoorte, E. Comparison of biocompatibility and adsorption properties of different plastics for advanced microfluidic cell and tissue culture models. *Anal. Chem.* **84**, 3938–3944 (2012).

96. Zhou, J., Ellis, A. V. & Voelcker, N. H. Recent developments in PDMS surface modification for microfluidic devices. *Electrophoresis* vol. 31 2–16 (2010).

97. Whitesides, G. M. The origins and the future of microfluidics. *Nature* vol. 442 368–373 (2006).

98. Huh, D. *et al.* Microfabrication of human organs-on-chips. *Nat. Protoc.* **8**, 2135–2157 (2013).

99. Mancera-Andrade, E. I., Parsaeimehr, A., Arevalo-Gallegos, A., Ascencio-Favela, G. & Parra Saldivar, R. Microfluidics technology for drug delivery: A review. *Front. Biosci. (Elite Ed).* **10**, 74–91 (2018).

100. Jeon, N. L. *et al.* Generation of solution and surface gradients using microfluidic systems. *Langmuir* **16**, 8311–8316 (2000).

101. Dertinger, S. K. W., Chiu, D. T., Noo Li Jeon & Whitesides, G. M. Generation of gradients having complex shapes using microfluidic networks. *Anal. Chem.* **73**, 1240–1246 (2001).

102. Abhyankar, V. V., Lokuta, M. A., Huttenlocher, A. & Beebe, D. J. Characterization of a membrane-based gradient generator for use in cell-signaling studies. *Lab Chip* **6**, 389–393 (2006).

103. Tong, Z. Q. *et al.* Chemotaxis of cell populations through confined spaces at Single-Cell resolution. *PLoS One* **7**, e29211 (2012).

104. Chung, B. G. *et al.* Human neural stem cell growth and differentiation in a gradient-generating microfluidic device. *Lab Chip* **5**, 401–406 (2005).

105. Park, J. Y. *et al.* Differentiation of neural progenitor cells in a microfluidic chip-generated cytokine gradient. *Stem Cells* **27**, 2646–2654 (2009).

106. Millet, L. J., Stewart, M. E., Nuzzo, R. G. & Gillette, M. U. Guiding neuron development with planar surface gradients of substrate cues deposited using microfluidic devices. *Lab Chip* **10**, 1525–1535 (2010).

107. Park, J. W., Vahidi, B., Taylor, A. M., Rhee, S. W. & Jeon, N. L. Microfluidic culture platform for neuroscience research. *Nat. Protoc.* **1**, 2128–2136 (2006).

108. Taylor, A. M. *et al.* A microfluidic culture platform for CNS axonal injury, regeneration and transport. *Nat. Methods* **2**, 599–605 (2005).

109. Rao, S. M. N. *et al.* Demonstration of cancer cell Migration Using a Novel microfluidic device. *J. Nanotechnol. Eng. Med.* **1**, (2010).

110. Li, X., Valadez, A. V., Zuo, P. & Nie, Z. Microfluidic 3D cell culture: Potential application for tissue-based bioassays. *Bioanalysis* vol. 4 1509–1525 (2012).

111. Shin, Y. *et al.* Microfluidic assay for simultaneous culture of multiple cell types on surfaces or within hydrogels. *Nat. Protoc.* **7**, 1247–1259 (2012).

112. Temiz, Y., Lovchik, R. D., Kaigala, G. V. & Delamarche, E. Lab-on-a-chip devices: How to close and plug the lab? *Microelectronic Engineering* vol. 132 156–175 (2015).

113. Logun, M., Zhao, W., Mao, L. & Karumbaiah, L. Microfluidics in Malignant Glioma Research and Precision Medicine. *Advanced Biosystems* vol. 2 1700221 (2018).

114. Haring, A. P., Sontheimer, H. & Johnson, B. N. Microphysiological Human Brain and Neural Systems-on-a-Chip: Potential Alternatives to Small Animal Models and Emerging Platforms for Drug Discovery and Personalized Medicine. *Stem Cell Rev. Reports* **13**, 381–406 (2017).

115. Miccoli, B., Braeken, D. & Li, Y.-C. E. Brain-on-a-chip Devices for Drug Screening and Disease Modeling Applications. *Curr. Pharm. Des.* **24**, 5419–5436 (2019).

116. Mofazzal Jahromi, M. A. *et al.* Microfluidic Brain-on-a-Chip: Perspectives for Mimicking Neural System Disorders. *Mol. Neurobiol.* **56**, 8489–8512 (2019).

117. Bang, S., Jeong, S., Choi, N. & Kim, H. N. Brain-on-a-chip: A history of development and future perspective. *Biomicrofluidics* vol. 13 51301 (2019).

118. Lu, X., Kim-Han, J. S., O'Malley, K. L. & Sakiyama-Elbert, S. E. A microdevice platform for visualizing mitochondrial transport in aligned dopaminergic axons. *J. Neurosci. Methods* **209**, 35–39 (2012).

119. Moreno, E. L. *et al.* Differentiation of neuroepithelial stem cells into functional dopaminergic neurons in 3D microfluidic cell culture. *Lab Chip* **15**, 2419–2428 (2015).

120. Wang, Y. *et al.* Microfluidic engineering of neural stem cell niches for fate determination. *Biomicrofluidics* **11**, 014106 (2017).

121. Zór, K. *et al.* A compact multifunctional microfluidic platform for exploring cellular dynamics in real-time using electrochemical detection. *RSC Adv.* **4**, 63761–63771 (2014).

122. Achyuta, A. K. H. *et al.* A modular approach to create a neurovascular unit-on-a-chip. *Lab Chip* **13**, 542–553 (2013).

123. Park, J. *et al.* A microchip for quantitative analysis of CNS axon growth under localized biomolecular treatments. *J. Neurosci. Methods* **221**, 166–174 (2014).

124. Adriani, G., Ma, D., Pavesi, A., Kamm, R. D. & Goh, E. L. K. A 3D neurovascular microfluidic model consisting of neurons, astrocytes and cerebral endothelial cells as a blood-brain barrier. *Lab Chip* **17**, 448–459 (2017).

125. Wang, Y. I., Abaci, H. E. & Shuler, M. L. Microfluidic blood–brain barrier model provides in vivo-like barrier properties for drug permeability screening. *Biotechnol. Bioeng.* **114**,

184–194 (2017).

126. Brown, J. A. *et al.* Metabolic consequences of inflammatory disruption of the blood-brain barrier in an organ-on-chip model of the human neurovascular unit. *J. Neuroinflammation* **13**, 306 (2016).

127. Sellgren, K. L., Hawkins, B. T. & Grego, S. An optically transparent membrane supports shear stress studies in a three-dimensional microfluidic neurovascular unit model. *Biomicrofluidics* **9**, 061102 (2015).

128. Griep, L. M. *et al.* BBB on CHIP: Microfluidic platform to mechanically and biochemically modulate blood-brain barrier function. *Biomed. Microdevices* **15**, 145–150 (2013).

129. Herland, A. *et al.* Distinct contributions of astrocytes and pericytes to neuroinflammation identified in a 3D human blood-brain barrier on a chip. *PLoS One* **11**, e0150360 (2016).

130. Fan, Y., Nguyen, D. T., Akay, Y., Xu, F. & Akay, M. Engineering a Brain Cancer Chip for High-throughput Drug Screening. *Sci. Rep.* **6**, 1–12 (2016).

131. Sun, J. *et al.* A microfluidic platform for systems pathology: Multiparameter single-cell signaling measurements of clinical brain tumor specimens. *Cancer Res.* **70**, 6128–6138 (2010).

132. Park, J. *et al.* Three-dimensional brain-on-a-chip with an interstitial level of flow and its application as an in vitro model of Alzheimer's disease. *Lab Chip* **15**, 141–150 (2015).

133. Ruiz, A. *et al.* Testing Aβ toxicity on primary CNS cultures using drug-screening microfluidic chips. *Lab Chip* **14**, 2860–2866 (2014).

134. Sandlin, Z. D., Shou, M., Shackman, J. G. & Kennedy, R. T. Microfluidic electrophoresis chip coupled to microdialysis for in vivo monitoring of amino acid neurotransmitters. *Anal. Chem.* **77**, 7702–7708 (2005).

135. Kelava, I. & Lancaster, M. A. Stem Cell Models of Human Brain Development. *Cell Stem Cell* vol. 18 736–748 (2016).

136. Qian, T., Shusta, E. V. & Palecek, S. P. Advances in microfluidic platforms for analyzing and regulating human pluripotent stem cells. *Current Opinion in Genetics and Development* vol. 34 54–60 (2015).

137. Karimi, M. *et al.* Microfluidic systems for stem cell-based neural tissue engineering. *Lab on a Chip* vol. 16 2551–2571 (2016).

138. Pamies, D., Hartung, T. & Hogberg, H. T. Biological and medical applications of a brain-on-a-chip. *Exp. Biol. Med.* **239**, 1096–1107 (2014).

139. Prajumwongs, P., Weeranantanapan, O., Jaroonwitchawan, T. & Noisa, P. Human Embryonic Stem Cells: A Model for the Study of Neural Development and Neurological Diseases. *Stem Cells Int.* **2016**, (2016).

140. Takayama, Y. & Kida, Y. S. In vitro reconstruction of neuronal networks derived from human iPS cells using microfabricated devices. *PLoS One* **11**, (2016).

141. Hidalgo San Jose, L., Stephens, P., Song, B. & Barrow, D. Microfluidic Encapsulation Supports Stem Cell Viability, Proliferation, and Neuronal Differentiation. *Tissue Eng. - Part C Methods* **24**, 158–170 (2018).

142. Leslie, S. K., Kinney, R. C., Schwartz, Z. & Boyan, B. D. Microencapsulation of stem cells for therapy. in *Methods in Molecular Biology* vol. 1479 251–259 (2017).

143. Loessner, D. *et al.* Bioengineered 3D platform to explore cell-ECM interactions and drug resistance of epithelial ovarian cancer cells. *Biomaterials* **31**, 8494–8506 (2010).

144. Martinez-Rivas, A., González-Quijano, G. K., Proa-Coronado, S., Séverac, C. & Dague, E. Methods of micropatterning and manipulation of cells for biomedical applications. *Micromachines* vol. 8 (2017).

145. Campenot, R. B. Local control of neurite development by nerve growth factor. *Proc. Natl. Acad. Sci. U. S. A.* **74**, 4516–4519 (1977).

146. Taylor, A. M. *et al.* Microfluidic multicompartment device for neuroscience research. *Langmuir* **19**, 1551–1556 (2003).

147. Zweifel, L. S., Kuruvilla, R. & Ginty, D. D. Functions and mechanisms of retrograde neurotrophin signalling. *Nature Reviews Neuroscience* vol. 6 615–625 (2005).

148. Biffi, E. *Microfluidic and compartmentalized platforms for neurobiological research*. *Microfluidic and Compartmentalized Platforms for Neurobiological Research* vol. 103 (2015).

149. Taylor, A. M., Dieterich, D. C., Ito, H. T., Kim, S. A. & Schuman, E. M. Microfluidic Local Perfusion Chambers for the Visualization and Manipulation of Synapses. *Neuron* **66**, 57–68 (2010).

150. Robertson, G., Bushell, T. J. & Zagnoni, M. Chemically induced synaptic activity between mixed primary hippocampal co-cultures in a microfluidic system. *Integr. Biol. (United Kingdom)* **6**, 636–644 (2014).

151. Nagendran, T. *et al.* Distal axotomy enhances retrograde presynaptic excitability onto injured pyramidal neurons via trans-synaptic signaling. *Nat. Commun.* **8**, 1–16 (2017).

152. Kim, S., Park, J., Han, A. & Li, J. Microfluidic systems for axonal growth and regeneration research. *Neural Regen. Res.* **9**, 1703–1705 (2014).

153. Virlogeux, A. *et al.* Reconstituting Corticostriatal Network on-a-Chip Reveals the Contribution of the Presynaptic Compartment to Huntington's Disease. *Cell Rep.* **22**, 110–122 (2018).

154. Johnstone, A. F. M. *et al.* Microelectrode arrays: A physiologically based neurotoxicity testing platform for the 21st century. *NeuroToxicology* vol. 31 331–350 (2010).

155. Valdivia, P. *et al.* Multi-well microelectrode array recordings detect neuroactivity of ToxCast compounds. *Neurotoxicology* **44**, 204–217 (2014).

156. D. Jadhav, A., Wei, L. & Shi, P. Compartmentalized Platforms for Neuro-Pharmacological Research. *Curr. Neuropharmacol.* **14**, 72–86 (2015).

157. Jang, J. M., Lee, J., Kim, H., Jeon, N. L. & Jung, W. One-photon and two-photon stimulation of neurons in a microfluidic culture system. *Lab Chip* **16**, 1684–1690 (2016).

158. Neher, E. & Sakmann, B. Single-channel currents recorded from membrane of denervated frog muscle fibres. *Nature* **260**, 799–802 (1976).

159. Pan, L. *et al.* Large extracellular spikes recordable from axons in microtunnels. *IEEE Trans. Neural Syst. Rehabil. Eng.* **22**, 453–459 (2014).

160. Bakkum, D. J. *et al.* Tracking axonal action potential propagation on a high-density microelectrode array across hundreds of sites. *Nat. Commun.* **4**, 1–12 (2013).

161. Obien, M. E. J., Deligkaris, K., Bullmann, T., Bakkum, D. J. & Frey, U. Revealing neuronal

function through microelectrode array recordings. *Frontiers in Neuroscience* vol. 9 423 (2015).

162. Habibey, R. *et al.* A multielectrode array microchannel platform reveals both transient and slow changes in axonal conduction velocity. *Sci. Rep.* **7**, 8558 (2017).

163. Honegger, T., Scott, M. A., Yanik, M. F. & Voldman, J. Electrokinetic confinement of axonal growth for dynamically configurable neural networks. *Lab Chip* **13**, 589–598 (2013).

164. Honegger, T., Thielen, M. I., Feizi, S., Sanjana, N. E. & Voldman, J. Microfluidic neurite guidance to study structure-function relationships in topologically-complex population-based neural networks. *Sci. Rep.* **6**, 1–10 (2016).

165. Krukiewicz, K. Electrochemical impedance spectroscopy as a versatile tool for the characterization of neural tissue: A mini review. *Electrochemistry Communications* vol. 116 106742 (2020).

166. Jackowska, K. & Krysinski, P. New trends in the electrochemical sensing of dopamine. *Anal. Bioanal. Chem.* **405**, 3753–3771 (2013).

167. Wightman, R. M. *et al.* Temporally resolved catecholamine spikes correspond to single vesicle release from individual chromaffin cells. *Proc. Natl. Acad. Sci. U. S. A.* **88**, 10754–10758 (1991).

168. Venton, B. J. & Cao, Q. Fundamentals of fast-scan cyclic voltammetry for dopamine detection. *Analyst* **145**, 1158–1168 (2020).

169. Koehne, J. E. *et al.* Carbon nanofiber electrode array for electrochemical detection of dopamine using fast scan cyclic voltammetry. *Analyst* **136**, 1802–1805 (2011).

170. Stamford, J. A., Kruk, Z. L., Millar, J. & Wightman, R. M. Striatal dopamine uptake in the rat: In vivo analysis by fast cyclic voltammetry. *Neurosci. Lett.* **51**, 133–138 (1984).

171. Zhou, Z. & Misler, S. Amperometric detection of stimulus-induced quantal release of catecholamines from cultured superior cervical ganglion neurons. *Proc. Natl. Acad. Sci. U. S. A.* **92**, 6938–6942 (1995).

172. Bruns, D. & Jahn, R. Real-time measurement of transmitter release from single synaptic vesicles. *Nature* **377**, 62–65 (1995).

173. Pothos, E. N., Davila, V. & Sulzer, D. Presynaptic recording of quanta from midbrain dopamine neurons and modulation of the quantal size. *J. Neurosci.* **18**, 4106–4118 (1998).

174. Chen, G. & Ewing, A. G. Multiple classes of catecholamine vesicles observed during exocytosis from the Planorbis cell body. *Brain Res.* **701**, 167–174 (1995).

175. Chen, P. *et al.* Amperometric detection of quantal catecholamine secretion from individual cells on micromachined silicon chips. *Anal. Chem.* **75**, 518–524 (2003).

176. Cooper, J. M. Towards electronic Petri dishes and picolitre-scale single-cell technologies. *Trends in Biotechnology* vol. 17 226–230 (1999).

177. Kim, R., Joo, S., Jung, H., Hong, N. & Nam, Y. Recent trends in microelectrode array technology for in vitro neural interface platform. *Biomedical Engineering Letters* vol. 4 129–141 (2014).

178. Maher, M. P., Pine, J., Wright, J. & Tai, Y. C. The neurochip: A new multielectrode device for stimulating and recording from cultured neurons. *J. Neurosci. Methods* **87**, 45–56 (1999).

179. Berberian, K., Kisler, K., Qinghua, F. & Lindau, M. Improved surface-patterned platinum microelectrodes for the study of exocytotic events. *Anal. Chem.* **81**, 8734–8740 (2009).

180. Carabelli, V. *et al.* Nanocrystalline diamond microelectrode arrays fabricated on sapphire technology for high-time resolution of quantal catecholamine secretion from chromaffin cells. *Biosens. Bioelectron.* **26**, 92–98 (2010).

181. Chen, X., Gao, Y., Hossain, M., Gangopadhyay, S. & Gillis, K. D. Controlled on-chip stimulation of quantal catecholamine release from chromaffin cells using photolysis of caged Ca2+ on transparent indium-tin-oxide microchip electrodes. *Lab Chip* **8**, 161–169 (2007).

182. Dittami, G. M. & Rabbitt, R. D. Electrically evoking and electrochemically resolving quantal release on a microchip. *Lab Chip* **10**, 30–35 (2010).

183. Sun, X. & Gillis, K. D. On-chip amperometric measurement of quantal catecholamine release using transparent indium tin oxide electrodes. *Anal. Chem.* **78**, 2521–2525 (2006).

184. Tomagra, G. *et al.* Simultaneous multisite detection of quantal release from PC12 cells using micro graphitic-diamond multi electrode arrays. *Biophys. Chem.* **253**, 106241

(2019).

185. Cui, M. R. *et al.* Simultaneous monitoring of action potentials and neurotransmitter release from neuron-like PC12 cells. *Anal. Chim. Acta* **1105**, 74–81 (2020).

186. Tomagra, G. *et al.* Diamond-based multi electrode arrays for monitoring neurotransmitter release. in *Lecture Notes in Electrical Engineering* vol. 539 125–134 (2019).

187. Ching, S., Dudek, R. & Tabet, E. Cyclic voltammetry with ultramicroelectrodes. *J. Chem. Educ.* **71**, 602–605 (1994).

188. Heinze, J. Ultramicroelectrodes in Electrochemistry. *Angewandte Chemie International Edition in English* vol. 32 1268–1288 (1993).

189. Koudelka-Hep, M. & Van Der Wal, P. D. Microelectrode sensors for biomedical and environmental applications. *Electrochim. Acta* **45**, 2437–2441 (2000).

190. Wittstock, G., Gründig, B., Strehlitz, B. & Zimmer, K. Evaluation of Microelectrode Arrays for Amperometric Detection by Scanning Electrochemical Microscopy. *Electroanalysis* **10**, 526–531 (1998).

191. Feeney, R. & Kounaves, S. P. Microfabricated ultramicroelectrode arrays: Developments, advances, and applications in environmental analysis. *Electroanalysis* vol. 12 677–684 (2000).

192. Aqrawe, Z., Montgomery, J., Travas-Sejdic, J. & Svirskis, D. Conducting polymers for neuronal microelectrode array recording and stimulation. *Sensors and Actuators, B: Chemical* vol. 257 753–765 (2018).

193. Kim, R., Joo, S., Jung, H., Hong, N. & Nam, Y. Recent trends in microelectrode array technology for in vitro neural interface platform. *Biomed. Eng. Lett.* **4**, 129–141 (2014).

194. Gillis, W. F. *et al.* Carbon fiber on polyimide ultra-microelectrodes. *J. Neural Eng.* **15**, 016010 (2018).

195. Park, C. *et al.* Fast Cyclic Square-Wave Voltammetry to Enhance Neurotransmitter Selectivity and Sensitivity. *Anal. Chem.* **90**, 13348–13355 (2018).

196. Westbroek, P. Fundamentals of electrochemistry. in *Analytical Electrochemistry in*

Textiles 3–36 (Elsevier, 2005). doi:10.1533/9781845690878.1.1.

197. Sun, J. & Yang, W. Fringe effect of electrical capacitance and resistance tomography sensors. *Meas. Sci. Technol.* **24**, 074002 (2013).

198. Aligner, M. KARL SUSS MA6 OPERATING MANUAL. https://www.manualslib.com/manual/1265174/Karl-Suss-Ma6.html#manual.

199. HEIDELBERG. *HEIDELBERG MLA150 MASKLESS ALLIGNER MLA150 Maskless Aligner*. (2018).

200. MicroChemicals GmbH. AZ nLOF ™ 2000 Series. (2016).

201. Bordo, K. & Rubahn, H. G. Effect of deposition rate on structure and surface morphology of thin evaporated al films on Dielectrics and Semiconductors. *Medziagotyra* **18**, 313–317 (2012).

202. Friend, J. & Yeo, L. Fabrication of microfluidic devices using polydimethylsiloxane. *Biomicrofluidics* **4**, 026502 (2010).

203. McDonald, J. C. *et al.* Fabrication of microfluidic systems in poly(dimethylsiloxane). *Electrophoresis* vol. 21 27–40 (2000).

204. Alapan, Y., Hasan, M. N., Shen, R. & Gurkan, U. A. Three-Dimensional Printing Based Hybrid Manufacturing of Microfluidic Devices. *J. Nanotechnol. Eng. Med.* **6**, (2015).

205. Luo, L. W. *et al.* Rapid prototyping of microfluidic systems using a laser-patterned tape. *J. Micromechanics Microengineering* **17**, N107 (2007).

206. Yazdi, A. A. *et al.* 3D printing: an emerging tool for novel microfluidics and lab-on-a-chip applications. *Microfluid. Nanofluidics* **20**, 1–18 (2016).

207. Lee, J. W. 3D Nanoprinting Technologies for Tissue Engineering Applications. *J. Nanomater.* **2015**, 1–14 (2015).

208. Pilipchuk, S. P. *et al.* Integration of 3D Printed and Micropatterned Polycaprolactone Scaffolds for Guidance of Oriented Collagenous Tissue Formation In Vivo. *Adv. Healthc. Mater.* **5**, 676–687 (2016).

209. Chandrasekaran, A. *et al.* Thermal scribing to prototype plastic microfluidic devices, applied to study the formation of neutrophil extracellular traps. *Lab Chip* **17**, 2003–2012

(2017).

210. Strong, V. *et al.* Patterning and electronic tuning of laser scribed graphene for flexible all-carbon devices. *ACS Nano* **6**, 1395–1403 (2012).

211. Chandrasekaran, A. *et al.* Thermal scribing to prototype plastic microfluidic devices, applied to study the formation of neutrophil extracellular traps. *Lab Chip* **17**, 2003–2012 (2017).

212. Yen, D. P., Ando, Y. & Shen, K. A cost-effective micromilling platform for rapid prototyping of microdevices. *Technology* **04**, 234–239 (2016).

213. Carugo, D. *et al.* Facile and cost-effective production of microscale PDMS architectures using a combined micromilling-replica moulding (μMi-REM) technique. *Biomed. Microdevices* **18**, 1–10 (2016).

214. Lashkaripour, A., Silva, R. & Densmore, D. Desktop micromilled microfluidics. *Microfluid. Nanofluidics* **22**, 31 (2018).

215. Vergani, M. *et al.* Compact potentiostat for cellular electrochemical imaging with 54 parallel channels. *2012 IEEE Biomed. Circuits Syst. Conf. Intell. Biomed. Electron. Syst. Better Life Better Environ. BioCAS 2012 - Conf. Publ.* 136–139 (2012) doi:10.1109/BioCAS.2012.6418401.

216. Elgrishi, N. *et al.* A Practical Beginner's Guide to Cyclic Voltammetry. *J. Chem. Educ.* **95**, 197–206 (2018).

217. Foster, C. W., Kadara, R. O. & Banks, C. E. Quality control/quality assurance analysis of electrochemical screen-printed sensors. in *SpringerBriefs in Applied Sciences and Technology* 35–56 (Springer Verlag, 2016). doi:10.1007/978-3-319-25193-6_4.

218. Venton, B. J. & Wightman, R. M. Psychoanalytical Electrochemistry: Dopamine and Behavior. *Anal. Chem.* **75**, 414 A-421 A (2003).

219. Wang, Y., Li, Y., Tang, L., Lu, J. & Li, J. Application of graphene-modified electrode for selective detection of dopamine. *Electrochem. commun.* **11**, 889–892 (2009).

220. Atta, N. F., Galal, A., Ali, S. M. & Hassan, S. H. Electrochemistry and detection of dopamine at a poly(3,4-ethylenedioxythiophene) electrode modified with ferrocene and

cobaltocene. *Ionics (Kiel).* **21**, 2371–2382 (2015).

221. Lane, R. F. & Hubbard, A. T. Differential Double Pulse Voltammetry at Chemically Modified Platinum Electrodes for in vivo Determination of Catecholamines. *Anal. Chem.* **48**, 1287–1293 (1976).

222. Spégel, C. *et al.* On-chip determination of dopamine exocytosis using mercaptopropionic acid modified microelectrodes. in *Electroanalysis* vol. 19 263–271 (John Wiley & Sons, Ltd, 2007).

223. Amato, L. *et al.* Pyrolysed 3D-carbon scaffolds induce spontaneous differentiation of human neural stem cells and facilitate real-time dopamine detection. *Adv. Funct. Mater.* **24**, 7042–7052 (2014).

224. Trouillon, R., Lin, Y., Mellander, L. J., Keighron, J. D. & Ewing, A. G. Evaluating the diffusion coefficient of dopamine at the cell surface during amperometric detection: Disk vs ring microelectrodes. *Anal. Chem.* **85**, 6421–6428 (2013).

225. Kamande, J., Nagendran, T., Harris, J. & Taylor, A. M. Multi-compartment microfluidic device geometry and covalently bound poly-D-lysine influence neuronal maturation. *Front. Bioeng. Biotechnol.* **7**, 84 (2019).

226. Johnson, B. N. *et al.* 3D printed nervous system on a chip. *Lab Chip* **16**, 1393–1400 (2016).

227. Spégel, C. *et al.* On-chip determination of dopamine exocytosis using mercaptopropionic acid modified microelectrodes. *Electroanalysis* **19**, 263–271 (2007).

228. Vasudevan, S., Kajtez, J., Heiskanen, A., Emneus, J. & Keller, S. S. Leaky Opto-Electrical Neural Probe for Optical Stimulation and Electrochemical Detection of Dopamine Exocytosis. *Proc. IEEE Int. Conf. Micro Electro Mech. Syst.* **2020-Janua**, 388–391 (2020).

229. Canillas, M., Moreno, B., Chinarro, E. & Rajnicek, A. M. TiO2 surfaces support neuron growth during electric field stimulation. *Mater. Sci. Eng. C* **79**, 1–8 (2017).

230. Alexander, J. K., Fuss, B. & Colello, R. J. Electric field-induced astrocyte alignment directs neurite outgrowth. *Neuron Glia Biol.* **2**, 93–103 (2006).

231. Spira, M. E. & Hai, A. Multi-electrode array technologies for neuroscience and cardiology. *Nature Nanotechnology* vol. 8 83–94 (2013).

232. Obien, M. E. J., Deligkaris, K., Bullmann, T., Bakkum, D. J. & Frey, U. Revealing neuronal function through microelectrode array recordings. *Frontiers in Neuroscience* vol. 9 423 (2015).

233. Park, D. W. *et al.* Graphene-based carbon-layered electrode array technology for neural imaging and optogenetic applications. *Nat. Commun.* **5**, 1–11 (2014).

234. Koerbitzer, B. *et al.* Graphene electrodes for stimulation of neuronal cells. *2D Mater.* **3**, 024004 (2016).

235. Henderson, J. M., Carpenter, K., Cartwright, H. & Halliday, G. M. Degeneration of the centre median-parafascicular complex in Parkinson's disease. *Ann. Neurol.* **47**, 345–352 (2000).

236. Halliday, G. M., Macdonald, V. & Henderson, J. M. A comparison of degeneration in motor thalamus and cortex between progressive supranuclear palsy and Parkinson's disease. *Brain* **128**, 2272–2280 (2005).

237. Mistry, K. K., Sagarika Deepthy, T., Chaudhuri, C. R. & Saha, H. Electrochemical characterization of some commercial screen-printed electrodes in different redox substrates. *Curr. Sci.* **109**, 1427–1436 (2015).

238. Sever, M., Gunay, G., Guler, M. O. & Tekinay, A. B. Tenascin-C derived signaling induces neuronal differentiation in a three-dimensional peptide nanofiber gel. *Biomater. Sci.* **6**, 1859–1868 (2018).

239. Knight, E. & Przyborski, S. Advances in 3D cell culture technologies enabling tissue-like structures to be created in vitro. *Journal of Anatomy* vol. 227 746–756 (2015).

240. Murphy, A. R., Haynes, J. M., Laslett, A. L., Cameron, N. R. & O'Brien, C. M. Three-dimensional differentiation of human pluripotent stem cell-derived neural precursor cells using tailored porous polymer scaffolds. *Acta Biomater.* **101**, 102–116 (2020).

241. Vasita, R. & Katti, D. S. Nanofibers and their applications in tissue engineering. *International Journal of Nanomedicine* vol. 1 15–30 (2006).

242. Vijayavenkataraman, S. *et al.* 3D-Printed PCL/PPy Conductive Scaffolds as Three-Dimensional Porous Nerve Guide Conduits (NGCs) for Peripheral Nerve Injury Repair.

Front. Bioeng. Biotechnol. **7**, 266 (2019).

243. Li, N. *et al.* Three-dimensional graphene foam as a biocompatible and conductive scaffold for neural stem cells. *Sci. Rep.* **3**, 1–6 (2013).

244. Wang, S. *et al.* Hyaluronic acid doped-poly(3,4-ethylenedioxythiophene)/chitosan/gelatin (PEDOT-HA/Cs/Gel) porous conductive scaffold for nerve regeneration. *Mater. Sci. Eng. C* **71**, 308–316 (2017).

245. Sharma, A. D. *et al.* Oriented growth and transdifferentiation of mesenchymal stem cells towards a Schwann cell fate on micropatterned substrates. *J. Biosci. Bioeng.* **121**, 325–335 (2016).

246. Mohanty, S. *et al.* Fabrication of scalable and structured tissue engineering scaffolds using water dissolvable sacrificial 3D printed moulds. *Mater. Sci. Eng. C* **55**, 569–578 (2015).

247. Zhu, W., O'Brien, C., O'Brien, J. R. & Zhang, L. G. 3D nano/microfabrication techniques and nanobiomaterials for neural tissue regeneration. *Nanomedicine* vol. 9 859–875 (2014).

248. Mohanty, S. *et al.* Fabrication of scalable tissue engineering scaffolds with dual-pore microarchitecture by combining 3D printing and particle leaching. *Mater. Sci. Eng. C* **61**, 180–189 (2016).

249. Asif, A. *et al.* Pyrolytic Carbon Nanograss Enhances Neurogenesis and Dopaminergic Differentiation of Human Midbrain Neural Stem Cells. *Adv. Healthc. Mater.* (2020) doi:10.1002/adhm.202001108.

250. Wang, S. *et al.* 3D culture of neural stem cells within conductive PEDOT layer-assembled chitosan/gelatin scaffolds for neural tissue engineering. *Mater. Sci. Eng. C* **93**, 890–901 (2018).

251. Cao, Q., Puthongkham, P. & Venton, B. J. Review: New insights into optimizing chemical and 3D surface structures of carbon electrodes for neurotransmitter detection. *Analytical Methods* vol. 11 247–261 (2019).

252. Bilston, L. E. Brain Tissue Mechanical Properties. in 69–89 (Springer, New York, NY, 2011). doi:10.1007/978-1-4419-9997-9_4.

253. Budday, S. *et al.* Mechanical properties of gray and white matter brain tissue by indentation. *J. Mech. Behav. Biomed. Mater.* **46**, 318–330 (2015).

254. Barnes, J. M., Przybyla, L. & Weaver, V. M. Tissue mechanics regulate brain development, homeostasis and disease. *Journal of Cell Science* vol. 130 71–82 (2017).

255. Madhusudanan, P., Raju, G. & Shankarappa, S. Hydrogel systems and their role in neural tissue engineering. *Journal of the Royal Society Interface* vol. 17 (2020).

256. Tully-Dartez, S., Cardenas, H. E. & Sit, P. F. S. Pore characteristics of chitosan scaffolds studied by electrochemical impedance spectroscopy. *Tissue Eng. - Part C Methods* **16**, 339–345 (2010).

257. Miller, D. A. The ionic conductivity of p(2-Hydroxyethyl methacrylate Hydrogels. (1995).

258. Canali, C. *et al.* Impedance spectroscopic characterisation of porosity in 3D cell culture scaffolds with different channel networks. *Electroanalysis* **27**, 193–199 (2015).

APPENDIX

PAPER I

Ultramicroelectrode arrays for monitoring dopamine exocytosis form single cells in a cell population

Muhammad Salman Khan, Marco Giacometti, Arto Heiskanen, Afia Asif, Winnie Svendsen, Maria Dimaki, Marco Carminati, Giorgio Ferrari, Marco Sampietro, and Jenny Emnéus

Ultramicroelectrode arrays for monitoring dopamine exocytosis form single cells in a cell population

Muhammad Salman Khan[1(joint 1st)], Marco Giacometti[2(joint 1st)], Arto Heiskanen[1], Afia Asif[1], Winnie Svendsen[1], Maria Dimaki[1], Marco Carminati[2], Giorgio Ferrari[2], Marco Sampietro[2*], and Jenny Emnéus[1*]

[1] Technical University of Denmark, Department of Biotechnology and Biomedicine, Søltofts Plads, Building 221, 2800 Kgs. Lyngby, Denmark

[2] Politecnico di Milano, Dipartimento di Elettronica, Informazione e Bioingegneria - DEIB, P.za L. da Vinci 32, 20133 Milano, Italy

*Corresponding author

Phone: +4525473548

e-mail: jemn@dtu.dk and marco.sampietro@polimi.it

Abstract

Single-cell exocytosis measurements using carbon fiber microelectrodes have become a golden standard and provided a deep understanding of the mechanism of exocytosis. The emergence of silicon micromachining technology has opened possibilities to create planar microelectrode chips that may provide higher throughput for single-cell exocytosis measurements or allow population-based measurements. In this paper, we present fabrication, characterization, and single-cell exocytosis application of ultramicroelectrode arrays having 54 individually addressable gold ultramicroelectrodes (UMEs) covering a total area of 260 x 290 μm^2. Each UME is either 5 µm or 10 µm in diameter matching the dimension of a single rat pheochromocytoma (PC12) cell. PC12 cells were cultured for 24 h forming a dense cell population covering all the UMEs. To our best knowledge, this is the first demonstration of strictly single-cell exocytosis measurements in a population of adhering cells. Exocytosis was triggered by adding high-K^+ buffer after having recorded a stable baseline current. Simultaneous amperometric exocytosis measurement on each of the 54 UMEs of an array was facilitated by a tailor-made 54-channel potentiostat capable of current sampling every 60 µs. The average peak current and charge for an entire array of UMEs was approximately 5 times higher for the UMEs of 10 µm in diameter. This may be explained by the fact that a larger area of the basal cell membrane was in direct contact with an UME. Based on cyclic voltammetric characterization, the UMEs were highly reproducible (RSE ~ 0.5%), ensuring that variation in the exocytosis peak currents represented cellular heterogeneity.

1. Introduction

Neuronal connections and communication are among the most vital biological functions. The dominant mode of communication between neurons involves the release of neurotransmitters from nanometer sized vesicles, which serve as intracellular storage for neurotransmitters. During neural communication, the connection is established via neurotransmitters, released from vesicles that fuse with the cell membrane in a complex process known as exocytosis[1–3]. The mechanism of vesicular exocytosis has been extensively explored in the last few decades[4–6]. Neurodegerative diseases, such as Parkinson's disease, Alzheimer's disease and schizophrenia, are manifestations of serious failure in the neural communication networks[7,8].

Electrochemical detection and development of carbon fiber microelectrodes (CFME) have provided opportunities to directly record and quantify exocytosis events from single vesicles or groups of vesicles in different cell types[9,10]. The primary advantage of electrochemical monitoring lies in high sensitivity and temporal resolution that enable real-time detection of, for instance, dopamine exocytosis[11–14]. Wightman et al.[15] were among the first ones to perform real-time monitoring of dopamine exocytosis through electrochemical detection using CFMEs. Since then carbon fiber microelectrodes have been utilized by many researchers to record vesicular exocytosis from single cells with high spatial resolution[16–22]. Exocytosis measurements using CFMEs involves placement of an electrode in the close proximity of the cell membrane. A potential that allows oxidation of the released neurotransmitter is poised at the electrode, and the exocytosis is triggered by depolarizing the cell membrane using a buffer solution containing an elevated K^+ concentration. The neurotransmitter molecules released from a storage vesicle upon fusion with the cell membrane are immediately oxidized on the adjacently placed CFME. Detection of neurotransmitter release from each vesicle generates a current peak that allows calculation of, for instance, the number of released neurotransmitter molecules, frequency of the vesicular events, and the kinetics of the release events[23].

However, CFMEs do suffer from certain limitations: 1) To position the electrode in sufficiently close to the cell membrane using a micromanipulator under a microscope is challenging. 2) Exocytosis measurements can only be performed on a single cell at a time, while to determine the cell-to-cell variability in quantal release parameters requires a substantial number of cells to be tested[24]. 3) Only a small fraction of the cell membrane is targeted during detection due to the small dimension of CFMEs. Hence, vesicle-to-vesicle variation of release events in a single cell cannot easily be addressed[25]. These challenges can be circumvented through microfabrication of lithographically patterned microelectrode arrays (MEAs). Microfabrication not only allows flexible patterning of a wide range of different electrode arrays, but also provides an opportunity to select multiple materials along with the dimensions of choice[26], and incorporate them in cell culture chambers[23]. Recent advances in microfabrication techniques have resulted in MEA designs with several promising properties, which make them an ideal choice for cellular studies, e.g., sensing at multiple sites at a time[27–32]. However, most of the reported applications do not demonstrate individually addressable MEAs with dimensions that are of the same order as single cells[33–37].

The ability of neural stem cell to specialize into functional neurons has opened new strategies for treatment of neurodegenerative diseases and construction of disease models. Study of stem cell differentiation requires new tools and approaches. We have previously constructed conductive carbon-based cell culture substrates to study stem cell differentiation into dopamine (DA) releasing neurons, and determined *in situ* the development of dopaminergic phenotype by electrochemical detection of dopamine exocytosis from whole cell populations[38,39]. However, to understand better the heterogeneity of differentiating stem cells, it is desirable to study their differentiation and behavior at single cell level. Such investigations have to be performed, though, under the culture conditions where differentiating stem cells are involved in autocrine

and paracrine signaling[40]. Hence, new tools are need to be able to conduct *in situ* studies on the properties of single stem cells inside a population.

Here, we report fabrication and application of microfabricated ultramicroelectrode array (UMEA) chips, having UMEs with the order of dimension comparable to that of biological cells, to facilitate single-cell studies in a cell population. Two different designs having 54 individually addressable gold UMEs of 5 µm (design 1) or 10 µm (design 2) in diameter in a total array area of 260 µm × 290 µm were fabricated using maskless UV lithography. The functionality of the UMEs was characterized electrochemically to ensure that their performance would reproducible for 54 simultaneous measurements in cell-based experiments. To test the capability of the UMEAs for simultaneous detection of DA exocytosis from 54 cells, we used rat pheochromocytoma (PC12) cells, which were originally established and since then used as a model cell line to study the mechanism of exocytosis and release of catecholamines (DA, epinephrine, and norepinephrine)[41,42]. In PC12 cells, the exocytosis events are distributed along the entire cell membrane. However, they are spatially heterogeneous, i.e. the frequency of release events at a certain location is higher (hot spots) than at another location on the cell membrane (cold spots)[43–45]. Based on the experimental results, we evaluated how the two UMEA designs could detect DA exocytosis from single cells and resolve differences between individual cells.

2. Materials and Methods

2.1. Chemicals

Potassium hexacyanoferrate(II) ($K_4[Fe(CN)_6]$), potassium hexacyanoferrate(III) ($K_3[Fe(CN)_6]$), 2-(3,4-dihydroxy phenyl) ethylamine hydrochloride (Dopamine, DA), 3-mercaptopropionic acid, glucose (BioXtra grade), 4-(2-hydroxyethyl)piperazine-1 ethane sulfonic acid (HEPES; 1 M solution), potassium hydroxide (semiconductor grade), sodium hydroxide, potassium chloride, sodium chloride, magnesium chloride hexahydrate, calcium chloride dihydrate, hydrogen peroxide (30 % solution in water), horse serum (HS), fetal bovine serum (FBS), cell culture tested phosphate buffered saline (PBS) and cell culture tested water were purchased from Sigma Aldrich Corporation (St. Louis, MO, USA). Dulbecco's Modified Eagle Medium/Ham's Nutrient Mixture F12 with GlutaMAX (DMEM/F12), trypsin–EDTA (0.05 %), and 100x penicillin/streptomycin (P/S) were purchased from Life Technologies Ltd (Paisley, UK). Geltrex was from ThermoFisher Scientific. The aqueous solutions used in cell-based experiments were prepared in cell culture tested water. All other aqueous solutions were prepared in ultrapure water (resistivity 18.2 MΩ.cm) obtained from a Milli-Q® water purification system (Millipore Corporation, Billerica, MA, USA).

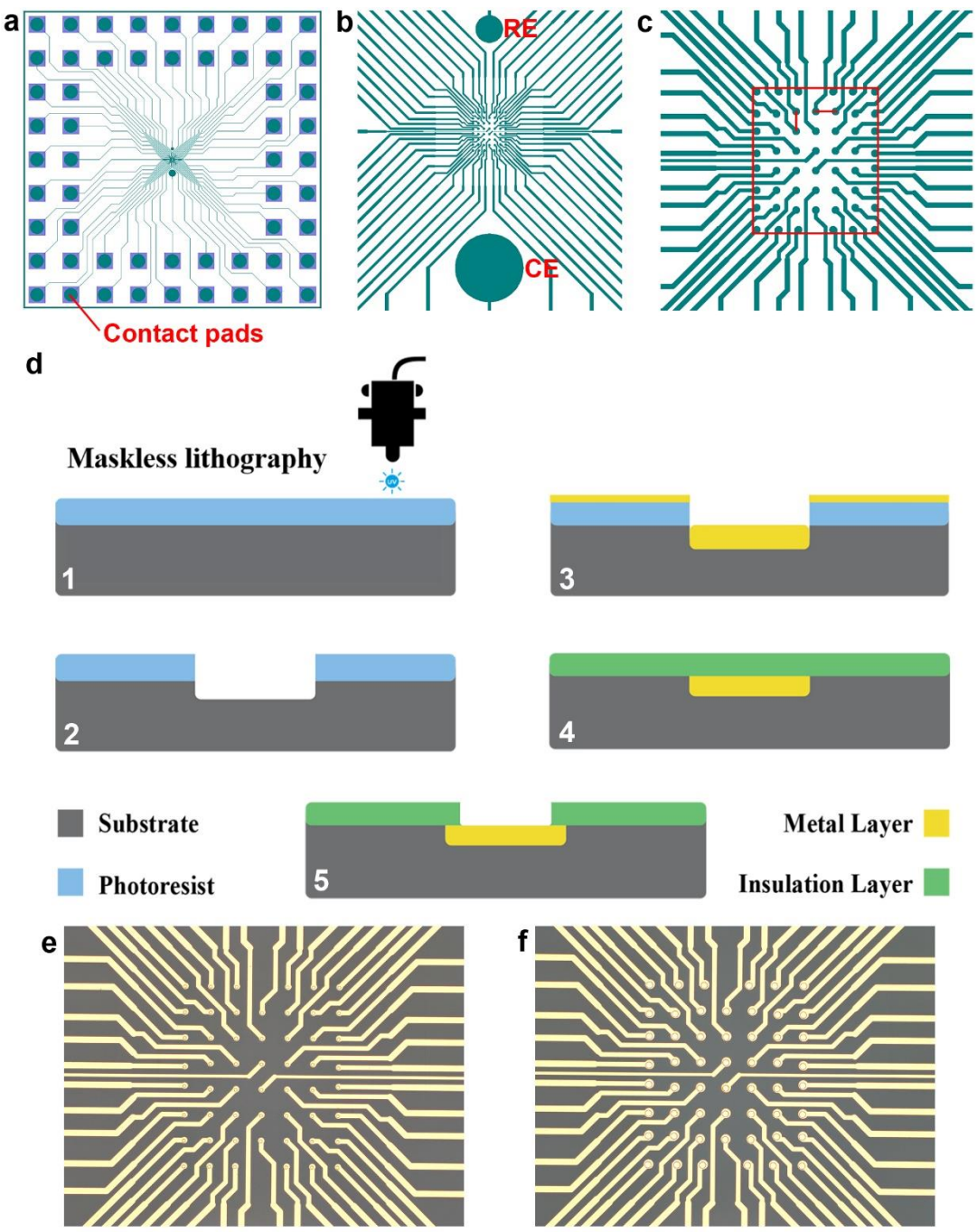

Figure 1. a) Schematic view of UMEA chip layout and Zoom-in view of b) the 54 UMEs (WEs), CE and RE, as well as c) the 260 µm x 290 µm area occupied UMEs and 40 µm interspacing between each of them. d) Schematic view of UMEA chip fabrication: 1) UV exposure of spin coated photoresist using maskless aligner; 2) BHF etching of glass wafer in areas exposed after development; 3) metal deposition by e-beam evaporation to pattern electrodes, leads, and contact pads; 4) deposition of photoresist for the insulation layer after the completed lift-off; 5) completed chip with patterned openings in the passivation layer to reveal the active electrode areas and contact pads. Zoom-in images of fabricated UMEA chips showing the 54 UME openings with diameter of e) 5 µm (design 1) and f) 10 µm (design 2).

2.2. Design and fabrication of ultramicroelectrode array chips

The ultramicroelectrode array (UMEA) chips (Figure 1a) comprise 54 individually addressable ultramicroelectrodes (used as working electrodes, WE), having a diameter of 5 µm (design 1) or 10 µm (design 2) along with an on-chip counter (CE; Ø 250 µm) and pseudo-reference electrode (RE; Ø 100 µm) in the proximity of the 54 WEs (Figure 1b). The electrode configuration and dimensions were designed to maximize the number of chips (9 chips with an area of 22 x 22 mm^2) patterned on a 4-inch wafer. Moreover, the number of WEs (recording sites), the size and pitch between each WE, the symmetry of the connecting leads from the WEs to the contact pads (Figure 1a), as well as the dimension of and pitch between each contact pad were considered. This design resulted in a symmetrical positioning of the 54 UMEs, covering an area of approximately 260 µm × 290 µm in the center of the chip (Figure 1c) along with the CE and RE in the format of an 8 x 7 array of electrodes. The pitch between each WE in the horizontal and vertical direction was 40 µm (Figure 1c). The distance from the UMEA to the RE and CE was 500 µm (Figure 1b).

The chips were fabricated on 4-inch glass wafers using traditional cleanroom-based techniques. The overall fabrication process comprised multiple steps, such as UV exposure, wet and dry etching, thin-film metal deposition, lift-off, and dicing. Figure 1d shows the stepwise fabrication of the UMEA chips. As a first step, the glass wafers went through an HDMS priming to enhance the adhesion of photoresist, followed by spin coating of 1.5 µm layer of the negative tone photoresist AZ nLOF 2020 (MicroChemicals GmbH) using GAMMA UV (SUSS MicroTec) spin coater. The first UV exposure (15 min), defining the areas where the electrodes, leads, and contact pads would be located, was done using a CAD design through an MLA150 maskless aligner from Heidelberg Instruments GmbH (Figure 1d, step 1). The exposed resist on the glass wafers were then developed using a negative developer AZ 726 MIF in an automated developer station (SUSS MicroTec) so that the uncrosslinked resist from the patterns was removed. Isotropic wet etching using buffered hydrofluoric acid (BHF, 12 % HF with ammonium fluoride) was performed at a rate of 80 nm per minute to make a 220 nm undercut cavity to allow the deposited metals to be leveled at the wafer surface[46] (Figure 1d, step 2). 20 nm of Ti (adhesion metal layer) and 200 nm of Au were deposited by electron-beam (e-beam) evaporation using a Temescal System (FerroTec, USA) at the deposition rate of 5 Å/sec (Figure 1d, step 3). The lift-off of the remaining photoresist with unwanted metal was performed in a fume hood with an ultrasonic bath using Remover 1165 (Shipley Co.) for 1 hour to reveal the patterned metal structures. The wafers were then rinsed with isopropyl alcohol in an ultrasonic bath for 5 mins followed by rinsing with deionized water to remove residual metal particles and the remover. After the lift-off, the wafers were prepared for the next lithography step to pattern the insulation layer that defines the active electrode areas and contact pads. HDMS priming was followed by spin coating a 500 nm thick layer of AZ nLOF 2020, diluted (1:1) with propylene glycol methyl ether acetate (Figure 1d, step 4). A second CAD pattern was used by the maskless aligner to define the active electrode areas and contact pads in the insulation layer. The alignment prior to the second UV exposure was a critical step in the overall chip fabrication, as minor misalignment could lead to complete failure of the fabricated UMEA chips. The exposed features, i.e., the 54 UMEs and the contact pads, were then developed using AZ 726 MIF (tetramethyl ammonium hydroxide, TMAH) in the automated developer station (SUSS MicroTec). The fabricated UMEAs were observed under an Olympus MX40 optical microscope to ensure correct alignment of the openings in the insulation layer (Figure 1d, step 5). Zoom-in views of the fabricated UMEs of design 1 and 2 are shown in Figure 1e and f, respectively.

2.3. Electrochemical characterization of UMEs

After fabrication, the glass wafers were diced using a Disco dicing saw (Disco HI-TEC Europe GmbH) to obtain individual 22 x 22 mm^2 UMEA chips. A chip holder was fabricated from poly(methyl methacrylate) (PMMA) to accommodate a UMEA chip and provide a vial to serve as an electrochemical cell. All the PMMA components of the chip holder system were designed using AutoCAD 2015 (Autodesk, Inc., San Rafael, CA, USA) and machined by micromilling using a Mini-Mill/3PRO system (Minitech Machinery Corporation, Norcross, GA, USA) executing G-code generated by EZ-CAM17 Express software (EZCAM Solutions, Inc., New York, NY, USA). The fabricated components were assembled using 2 mm screws. A fluid tight sealing between the vial of the chip holder and the UMEA chip was formed by a 1 mm thick gasket fabricated of RCT®-SH40 silicone rubber (RCT Reichelt Chemietechnik GmbH) using an Epilog Mini 18 CO_2 laser cutter (EpilogLaser, USA).

After fabrication, the UMEA chips were treated with O_2 plasma for 60 s (total O_2 pressure of 0.6 mbar and power of 50 W) in an Atto Plasma System (Diener Electronic GmbH, Ebhausen, Germany) equipped with a 13.56 MHz RF generator. The UMEs were first characterized by acquiring cyclic voltammograms (CV) in PBS containing 10 mM $[Fe(CN)_6]^{3-/4-}$ (scan rates ranging from 10 mV/s to 250 mV/s) followed by characterization in DA solution (concentrations ranging from 10 µM to 150 µM prepared in PBS purged with nitrogen for 20 min). Characterization with DA comprised acquisition of CVs (scan rate 50 mV/s) and amperometric recordings (at 600 mV; chosen based on acquired CVs). All the applied potentials were adjusted vs. the on-chip Au RE. Prior to characterization with DA, the UMEs were modified in 200 mM aqueous MPA solution[47]. Acquisition of CVs in $[Fe(CN)_6]^{3-/4-}$ solution and amperometric recordings in DA solution were performed using a tailor-made 54-channel multiplexing potentiostat[48]. This potentiostat represents the evolution of a previous design featuring 24 readout channels[49], also based on spring-contacts coupling to the UMEA chip placed in the microfluidic platform. In the same form factor, 54 channels (multiplexed in groups of 4) are here compacted. Data acquisition was performed through a portable computer-controlled NI-6259 USB system (National Instruments Corporation, Austin, TX, USA). However, due to the multiplexing function, the 54-channel potentiostat keeps all the electrodes biased at the applied potential although current mapping takes place on one electrode at a time. In the presence of DA, the continuously applied bias potential can cause electrode fouling despite protecting electrode modifications (see further details in section 3.1.2.). Hence, CVs in DA solutions were recorded using an 8-channel CHI 1010 potentiostat (CH Instruments, Austin TX).

2.4. Cellular studies using UMEA chips

Rat pheochromocytoma (PC12) cells were utilized as the cellular model to study DA exocytosis on the UMEs. PC12 cells were purchased from Sigma Aldrich Corporation (St. Louis, MO, USA). The passage number of the cells was below 10 in all the performed experiments. Subculturing was done in PLL-coated (50 µg/ml, 3 h) T25 culture flasks (Nunc A/S, Roskilde, Denmark) using a growth medium prepared in DMEM/F12 supplemented with 15 % HS, 2.5 % FBS, 1 % P/S, and 5 mM HEPES. Cells were cultured at 37 °C in a humidified incubator with an atmosphere of 5% CO_2/95 % air.

In preparation for cell-based experiments, UMEA chips were first O_2 plasma treated (details in section 2.3.) and immediately after that the UMEs were modified with MPA (solution prepared in cell culture tested water) for 2 hours[47]. Then the chips were assembled in the chip holder. The assembled setup was sterilized by keeping it under constant UV irradiation on the LAF bench for 30 min. To promote cell adhesion, the exposed surface of the UMEA chip in the 8.5 mm × 8.5 mm vial of the chip holder was coated with 200 µL

of Geltrex solution (1:200 dilution with PBS) for 1 h in the incubator. The UMEA chip surface and vial were then rinsed with PBS. PC12 cells were trypsinized using trypsin–EDTA for 1 min to harvest the cells from the culture flask followed by addition of culture medium to quench the effect of trypsin. The cells were centrifuged for 5 min at 2000 rpm. The cells in the pellet were counted using a NucleoCounter® NC-200™ and suspended in culture medium to obtain the desired cell density. Cells were seeded onto the coated chip surface at the density of 10^6 cells/cm^2 in a total volume of 600 µL. Cells were cultured for 24 h prior to performing exocytosis measurements.

DA exocytosis from PC12 cells cultured on UMEA chips was triggered using an elevated K^+ concentration[47] and measured amperometrically at 600 mV vs. on-chip Au RE. Before recording exocytosis measurements, the culture medium was replaced by 100 µL of a sterile filtered low-K^+ buf fer (10 mM HEPES, 5 mM glucose, 1.2 mM $MgCl_2$, 2 mM $CaCl_2$, 150 mM NaCl and 5 mM KCl) and a baseline current was recorded. After recording a stable baseline, exocytosis was triggered by pipetting 50 µL of a sterile filtered high-K^+ buffer (the same composition as in the low-K^+ buffer except for 450 mM KCl and 5 mM NaCl) directly into the vial corner to elevate the K^+ concentration to about 150 mM. The current-time traces on all of the 54 electrodes corresponding to the released dopamine were recorded simultaneously after triggering exocytosis. All the cell-based electrochemical real-time measurements were performed under room temperature using the tailor-made 54-channel multiplexing potentiostat[48] (described in section 2.3). The low noise design of the current front-ends of the potentiostat offers 4pA resolution with an analog bandwidth of 5kHz. The current sampling rate at each of the 54 UMEs was set to the maximum rate of 60 µs. Each of the 54 UMEs functioned as an individually addressable measurement site while the on-chip CE and RE were common.

2.5. Data analysis and statistics

The file for the data points of the CVs and amperometric current-time traces recorded for each UME through the Microsoft Visual Studio based software of the tailor-made 54-channel potentiostat were stored in the computer controlling the system. A MATLAB script (MATLAB ver. R2019b) was initially used to plot and analyze the recordings. Then Origin 2018, (OriginLab Corp., Northampton, MA) was used to generate final plots of all the recorded traces and these were statistically analyzed in terms of the electrochemical measurements at each of the 54 WEs. The data from electrochemical measurements was presented as average ± standard deviation. Additionally, OriginPro 2018 was used to generate a heatmap-based graphical visualization of the exocytosis event on individual UMEs to provide a color matrix representing the measured current magnitude. Dark red represents high current and light red low current.

3. Results and discussion

The fabricated UMEA chips had 54 WEs with two different diameters, i.e. 5 µm (design 1) and 10 µm (design 2), to address individual cells in a cell population. In order to monitor dopamine release on 54 individually addressable WEs, each of them has to have reliable and reproducible electrochemical behavior. The first step toward reliability and reproducibility is successful fabrication of the UMEA chips. We have previously demonstrated that lithographic definition of metalic microelectrodes results in formation of “lift-off ears”, which are manifested as rough edges of the metallized patterns, often having sharp vertical outshoots that reach even hundreds of nanometers from the metal surface[46]. Lift-off ears compromise the stability of the insulation layer that defines the active electrode area and ultimately the electrochemical behavior of the microelectrodes. We demonstrated that when using positive photoresist for patterning

electrode structures, two fabrication steps are required in order to eliminate formation of lift-off ears: 1) Image reversal process of the photoresist, which creates an undercut at the edges of the developed photoresist, eliminating metal coverage on the side walls during e-beam metal deposition; and 2) an additional HF etching step to create recessions in the wafer substrate to allow metallization of the lithographically patterned regions without contact with the photoresist that serves as the metallization mask. In the present work, the metallized structures, including the WEs of both designs, were lithographically patterned using negative photoresist, which naturally renders the cross-sections of the developed photoresist with the desired undercut (Figure 1d, step 2). To form the recessions for metal evaporation (Figure 1d, step 2), BHF etching of the glass wafer substrate was optimized to reach the depth of 220 nm, corresponding to the total thickness of the deposited metal layers (20 nm of Ti and 200 nm of Au), which allowed the electrodes to be leveled at the surface of the wafer (Figure 1d, steps 3-5). The final lithographic definition of the 5 µm and 10 µm diameter UMEs, CE, pseudo-RE, and contact pads was done by spin coating 500 nm of negative photoresist that insulates the surrounding areas (Figure 1d, step 4). As a consequence of the thickness of the insulation layer, the UMEs were recessed 500 nm below the chip surface (Figure 1d, step 5). Figures 1e and f show a microscope image of the UME designs 1 and 2, respectively.

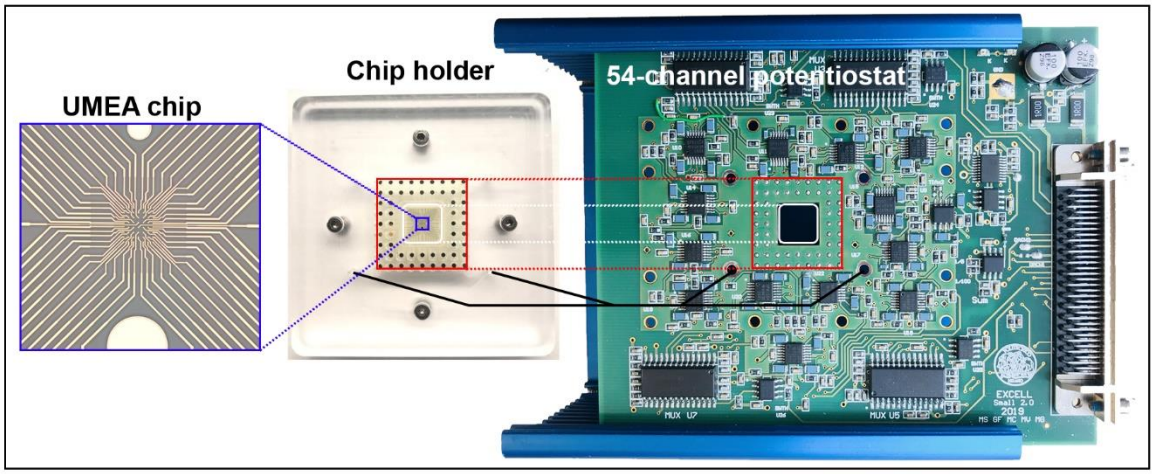

Figure 2. Electrochemical setup for exocytosis measurements: 54-channel potentiostat with an opening for liquid handling (right panel) inside the vial of the UMEA chip holder (middle panel) which is attached under the potentiostat PCB during experiments, allowing access to the UMEs of the chip (left panel).

3.1. Electrochemical characterization of UMEs

Electrochemical characterization of the UMEs with 5 µm and 10 µm diameter, corresponding to an electrode area of 19.6 μm^2 and 78.5 μm^2, respectively, addressed i) reproducibility of all the 54 electrodes in each UMEA design, ii) behavior of the two electrode areas in comparison with each other, iii) influence of electrode preparation on electrochemical behavior, and iv) amperometric response to transient addition of electroactive species. Figure 2 shows the electrochemical setup, comprising the tailor-made potentiostat (capable of performing multiplexed cyclic voltammetric and amperometric recordings on 54 electrodes)[48] and PMMA holder to accommodate an UMEA chip. During experiments, the printed circuit board (PCB) of the potentiostat was kept in a metal casing (Figure 2, right) that also served as a Faraday cage, facilitating additional noise reduction. The chip holder (Figure 2, middle), defining an electrochemical cell that covers the central part of the employed UMEA chip (Figure 2, left), was attached under the PCB, which has an opening for liquid handling during experiments. The on-chip CE and pseudo-RE were used during the electrochemical measurements.

3.1.1. Response to potassium hexacyanoferrate ($[Fe(CN)_6]^{3-/4-}$)

Due to the reversible electrochemical behavior, the redox couple potassium hexacyanoferrate(II/III) ($[Fe(CN)6]^{3-/4-}$) has been widely used to characterize the performance of microfabricated metal electrodes [50,51]. Based on preliminary tests, the electrochemical behavior of the fabricated UMEs, especially those of design 1 having 5 µm diameter, was highly irreproducible if the UMEA chips were mounted in the chip holder directly after fabrication. Need for electrode cleaning has been widely addressed in literature. After cleanroom fabrication gold electrodes may have residual photoresist left on the electrode surfaces and even short-term storage of electrodes may render them contaminated in a way that influences their electrochemical performance. Different cleaning protocols have been published in the electrochemical literature, such as the dual-step cleaning using chemical oxidation in a solution containing H_2O_2 and KOH followed by electrochemical reduction in KOH solution, which we have successfully used especially for MEA chips with silicon nitride insulation layer[52]. However, in the case of the UMEA chips presented here, this cleaning protocol was not suitable since it could compromise the integrity of the photoresist insulation layer. We optimized a cleaning procedure using O_2 plasma instead. Upon evaluating the influence of plasma treatment, we also observed that the reason for the initial unreliable electrochemical behavior was also caused by lack of proper wetting of the UMEs that were recessed under the hydrophobic photoresist.

Figures 3a and b show a typical set of 54 CVs acquired in 10 mM $[Fe(CN)6]^{3-/4-}$ solution (scan rate 50 mV/s) for a UMEA chip of design 1 (5 µm UMEs) and design 2 (10 µm UMEs), respectively. For both electrode dimensions, the recorded CVs have sigmoidal shape with diffusion-limited steady-state current (i_{ss}) characteristic of UME behavior. In each figure, the inset shows a single CV as a representative example of the details. Figure S1 in the Supporting Information shows sets of 54 CVs acquired on two other UMEA chips of both designs. For each CV, the anodic ($i_{ss,a}$) and cathodic ($i_{ss,c}$) steady-state current (for 5 µm: $i_{ss,a}$ = 9.1 ± 0.5 nA, $i_{ss,c}$ = -8.4 ± 0.5 nA and for 10 µm: $i_{ss,a}$ = 20.8 ± 1.4 nA, $i_{ss,c}$ = -19.5 ± 1.4 nA) was determined at 400 mV and -400 mV, respectively. Evaluation of the steady-state current values for all the 3 tested chips, the following average values were obtained: 5 µm UMEs: $i_{ss,a}$ = 9.46 ± 0.05 nA, $i_{ss,c}$ = -8.66 ± 0.04 nA and for 10 µm UMEs: $i_{ss,a}$ = 21.4 ± 0.1 nA, $i_{ss,c}$ = -20.1 ± 0.1 nA (the average values are reported here ± standard error of mean, n = 162). The relative standard error for all the UMEs of the 3 chips was only about 0.5 %. Figure 3c shows the average $i_{ss,a}$ and $i_{ss,c}$ for both UME designs (the inset shows variations between individual UMEs). The obtained results indicate that the UMEs of each design have highly reproducible electrochemical behavior. This leads to the conclusion that results obtained in cell-based experiments during electrochemical monitoring of DA exocytosis would primarily reflect differences in the biological behavior of the cell residing on each UME as well as how the individual cells are adhering on each UME, rather than differences between individual UMEs.

As mentioned above, the UMEs of both designs were recessed below the chip surface by 500 nm, i.e. the thickness of the insulation layer. The recessed location of UMEs influences the diffusion pattern, diminishing the purely radial diffusion that is typical for inlaid UMEs[53]. The consequence of the changed diffusion pattern is a slight decrease in the recorded diffusion-limited i_{ss}. According to the model presented by Bond et al., the i_{ss} decreases by a factor of $\pi/(4L/a + \pi)$, where L is the depth of the recess and a is the radius of the UME[54]. For the UMEs of design 1 and 2, the i_{ss} would be lowered by the factor of 0.7970 and 0.8871, respectively, in comparison with inlaid UMEs having the same diameter. The calculated factors for the two UME designs are so close to each other, though, that when comparing the electrochemical performance of 5 µm and 10 µm UMEs, the primary scaling factor was expected to be the geometric area that increases 4-fold in relation to the increase of the diameter from 5 µm to 10 µm. Based on the average diffusion-limited i_{ss} values for the UMEA chips presented as examples in Figure 3a-c, the average increase in i_{ss} for the 10 µm diameter UMEs was, however, only about 2-fold in comparison with the 5 µm UMEs.

Both UMEA designs were further characterized by acquiring CVs at different scan rates ranging from 10 mV/s to 250 mV/s. Figure 3d shows the linear relationship between the square root of scan rate and the diffusion-limited steady-state currents, $i_{ss,a}$ and $i_{ss,c}$ for 3 UMEs of each design, which indicates that the recessed location of the UMEs does not influence the diffusion-limited current in the applied range of scan rates.

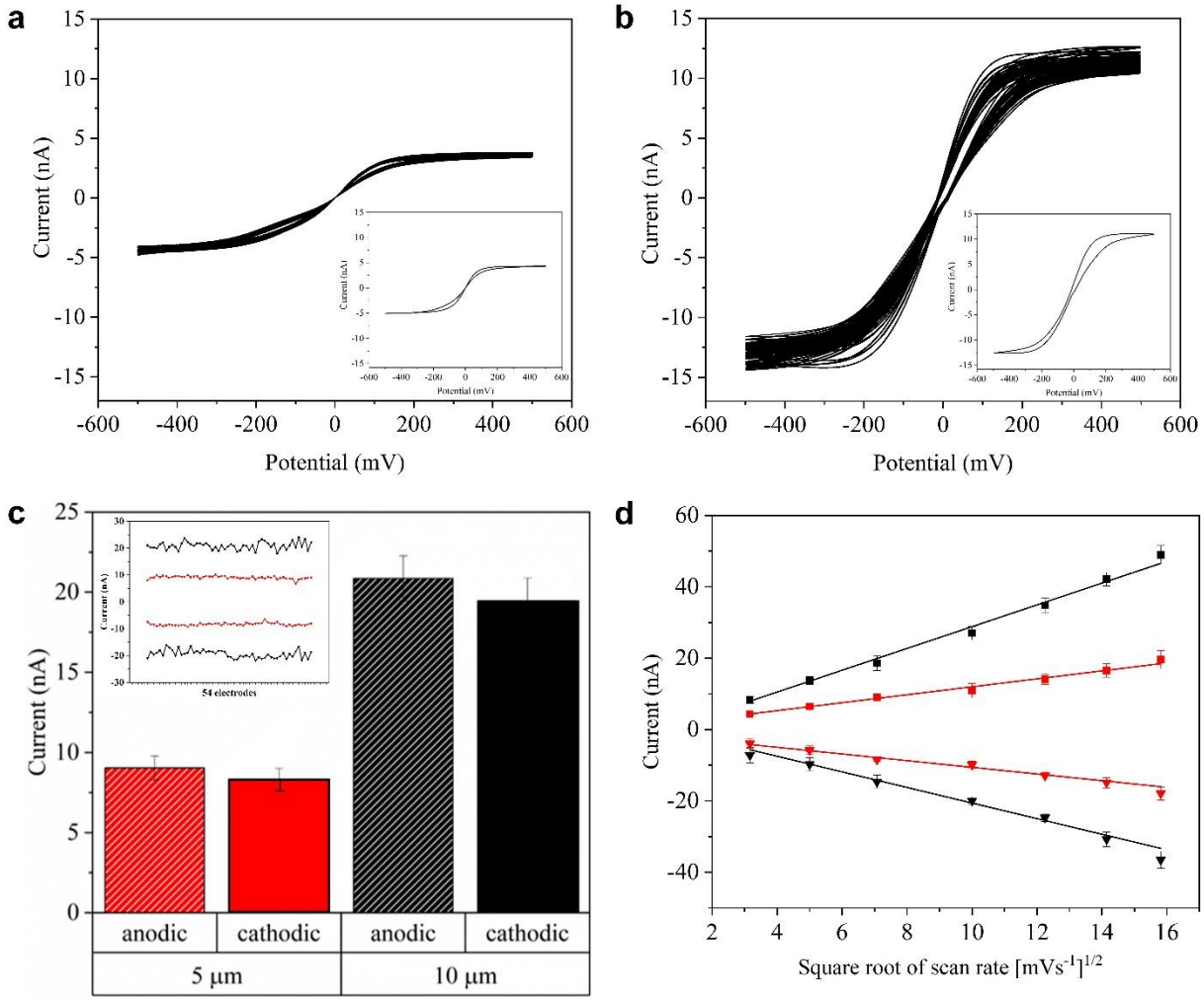

Figure 3. A set of 54 CVs for UMEs of a) design 1 and b) design 2; the inset of a and b shows a typical individual CV. c) Average anodic and cathodic steady-state currents (i_{ss}) extracted from the CVs shown in a and b (the error bars represent standard deviation, n = 54); the inset shows the variation of the i_{ss} for each of the 54 UMEs). d) Peak current vs. square root of scan rate for UMEs of design 1 (red) and design 2 (black) (the error bars represent standard deviation, n = 3). (All the CVs were acquired in PBS containing 10 mM $[Fe(CN)_6]^{3-/4-}$; scan rate 50 mV/s. The $i_{ss,a}$ and $i_{ss,c}$ values were evaluated at 400 mV and -400 mV vs. on-chip RE.)

3.1.2. Response to dopamine (DA)

Electrochemical detection of DA has gained wide interest in research due to its dualistic role in human physiology as both hormone and neurotransmitter. Detection applications have ranged from analysis of blood samples[55,56] to *in vitro* monitoring of DA exocytosis from single dopaminergic cells[5,15,47] and cell

populations [38,50,51] as well as *in vivo* monitoring of DA levels in the brain[9,10]. A great deal of research has focused on electrode modifications and other measures that minimize either the influence of interfering substances[55,56], such as ascorbic acid and uric acid, or electrode fouling due to DA dimerization and polymerization under an applied potential[57]. During electrochemical detection, oxidation of DA at an electrode surface involves donation of two electrons and removal of two protons, yielding dopamine o-quinone (DAOQ). DAOQ may readily undergo intracyclization to leucodopaminechrome (LDAC). LDAC is then converted to dopaminechrome (DAC) upon further oxidation by DAOQ. DAC is the intermediate that is readily polymerized to melanin derivatives, generally known as polydopamine, which strongly passivates the electrode surface hampering reproducible detection. Overoxidized polypyrrole[50] and MPA[47] are examples of electrode modifications that have been used to minimize fouling of gold electrodes during DA detection. In order to prepare the UMEA chips for characterization with DA, the O_2 plasma treated chips were modified using aqueous MPA solution.

Figures 4a and b show 54 typical CVs acquired in 150 µM DA solution (scan rate 50 mV/s) on a UMEA chip of each design with 5 µm and 10 µm UMEs, respectively. As in the case of $[Fe(CN)6]^{3-/4-}$, the CVs acquired in DA solution show sigmoidal shape, albeit a week indication of a cathodic peak can be observed. Moreover, the CVs are strongly overlapping, demonstrating high reproducibility between the individual UMEs. The $i_{ss,a}$ for CVs acquired on the 5 µm and 10 µm UMEs was evaluated at 450 mV vs. on-chip RE. The calculated average value for the two designs was 0.81 ± 0.06 nA and 1.6 ± 0.1 nA (the uncertainties represent standard deviation, n = 54), respectively. For comparison, Figure S2 in the Supporting Information shows sets of 54 CVs acquired on two other UMEA chips of both designs. In order to evaluate the sensitivity and limit of detection (LOD) of the UMEs, CVs were also recorded in DA solutions in the concentration range from 10 µM to 150 µM (scan rate 50 mV/s) for each UMEA design. Figures 4c and d show a set of typical CVs for one 5 µm and 10 µm UME, respectively. Figure 4e shows calibration curves ($i_{ss,a}$ vs. DA concentration; $i_{ss,a}$ was evaluated at 300 mV vs. on-chip RE) based on CVs acquired on three UMEs of each design. The calculated slope (m) that represents the detection sensitivity was 5.8 ± 0.1 pA/µM and 10.4 ± 0.3 pA/µM for the 5 µm and 10 µm UMEs, respectively. The LOD was evaluated as $3\times s_{y/x}/m$, where $s_{y/x}$ is the standard error of the y-intercept. The calculated values of LOD were 3.9 µM and 2.9 µM for the 5 µm and 10 µm UMEs, respectively.

Aside from O_2 plasma treatment and MPA modification described above, cell culture experiments on UMEA chips require that they be coated to ensure that the seeded PC12 cells adhere well on the chip surface and especially on the electrodes. PC12 cells require an extra cellular matrix (ECM) protein coating of, for instance, collagen[35] or laminin[51], in order to adhere and spread on a culture substrate. Collagen-coating of electrodes has been shown to decrease the sensitivity to DA detection[35], while laminin showed slight enhancement of sensitivity[51]. We have recently used ECM extracts like Geltrex, which promotes well PC12 cell adhesion and spreading. Since previous studies have indicated that ECM protein coatings can influence the sensitivity to DA detection, the response of UMEs was evaluated after Geltrex coating to ensure that single-cell monitoring on the coated UMEs would not be hindered. Prior to Geltrex coating of the UMEA chips to be used for characterization underwent the complete treatment that would be used in preparation for cell-based experiments, i.e. O_2 plasma treatment, assembly in the chip holder, MPA modification, and UV sterilization. However, prior to performing the complete preparation, each chip was tested using $[Fe(CN)6]^{3-/4-}$. Usually, the commercial Geltrex is diluted 1:100 in order to achieve a thin coating of cell culture substrate. As can be seen in Figure 4f, the UME that was coated with Geltrex based on 1:100 dilution showed a drastic decrease of sensitivity to DA in comparison with a UME without Geltrex coating. Due to that, we performed a preliminary PC12 cell culture test to ensure that 1:200 dilution would sufficiently promote cell adhesion. Electrochemical characterization of one UMEA chip using that dilution also showed decreased sensitivity (Figure 4f). However, further dilution of Geltrex was expected to compromise the

ability to promote cell adhesion. Hence, based on the obtained results, 1:200 was chosen as the appropriate dilution for further experiments.

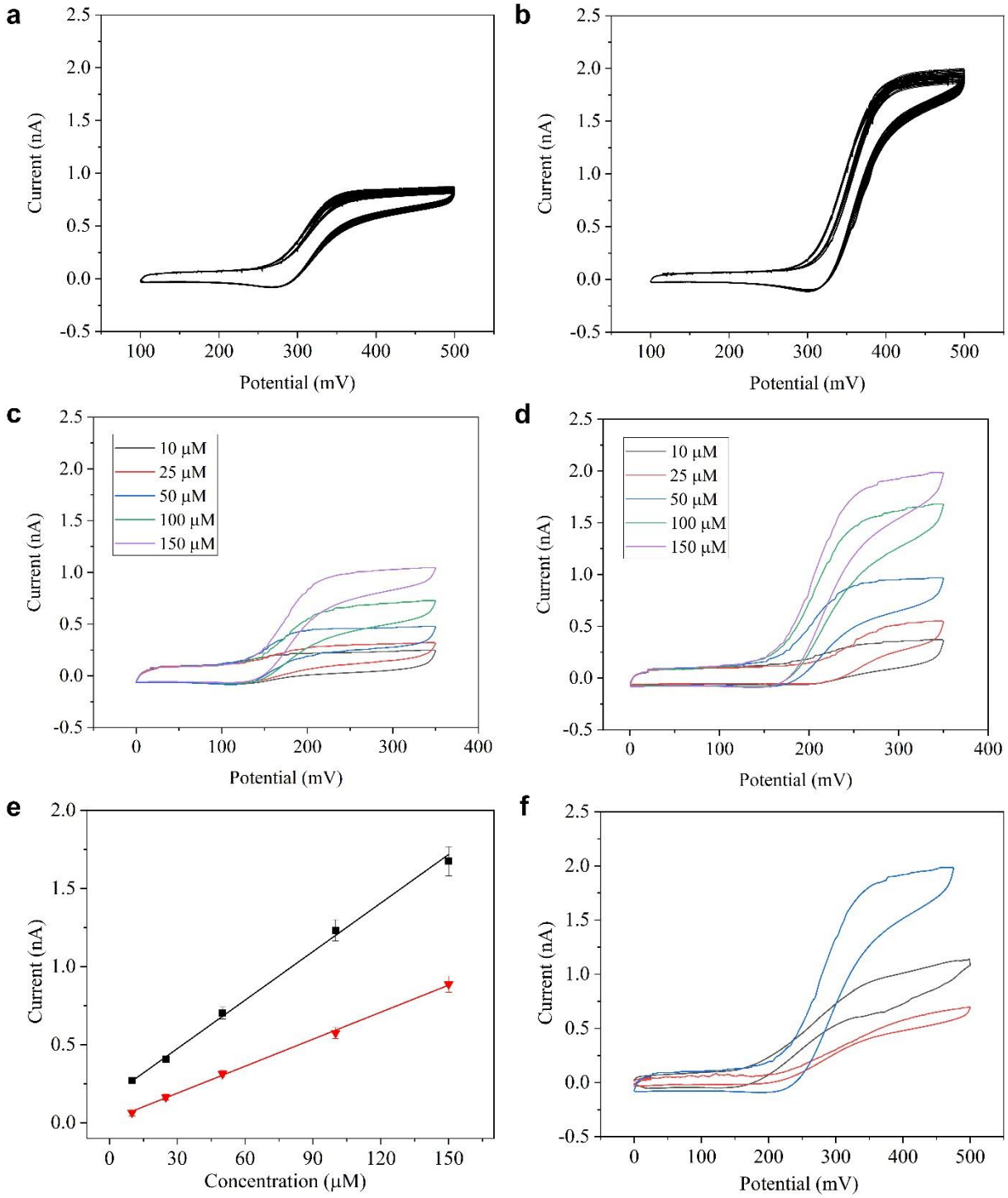

Figure 4. A set of 54 CVs for UMEs of a) design 1 and b) design 2 acquired in PBS containing 150 μM DA. A set of CVs for one UME of c) design 1 and d) design 2 acquired in solutions having varying DA concentration. e) A typical calibration curve for UMEs of design 1 (red) and design 2 (black) (the error bars represent standard deviation, n = 3). f) A set of CVs for UMEs of design 2 acquired in PBS containing 150 μM DA after only MPA modification (blue), as well as after MPA modification followed

by coating with Geltrex diluted 1:100 (red) and 1:200 (black). (All the CVs were acquired at the scan rate of 50 mV/s. The $i_{ss,a}$ and $i_{ss,c}$ values in e were evaluated at 300 mV vs. on-chip RE.)

Aside from characterization using cyclic voltammetry, to ensure that the UMAs would respond to a transient introduction of DA, the previously characterized Geltrex coated UMEA chips (one of each design) were characterized using amperometry, which is the electrochemical technique to be employed in monitoring of DA exocytosis. Based on the results shown in Figure 4f, 600 mV vs. the on-chip RE was chosen as the applied potential during amperometry to provide sufficient overpotential to drive DA oxidation. Upon recording a stable baseline current, DA was introduced to the center of the tested UMEA chip by fast pipetting 200 µl of 150 µM DA solution. Figure 5 shows a representative current-time trace for one UME of each design. Figure S3 in the Supporting Information shows the simultaneous response of all the 54 UMEs of each design. The calculated average peak current for all the 54 UMEs with 5 µm and 10 µm diameter was (154 ± 13 pA) and (489 ± 48 pA). (the uncertainties represent standard deviation, n = 54). The obtained results clearly show that all the UMEs of a chip can promptly respond to transiently introduced DA and that the average peak current scales with the electrode area, the value for the 10 µm UMEs being 4 times higher than that for the 5 µm UMEs. Moreover, the result also demonstrates that the 54-channel potentiostat is able to record a transient current peak simultaneously on all electrodes.

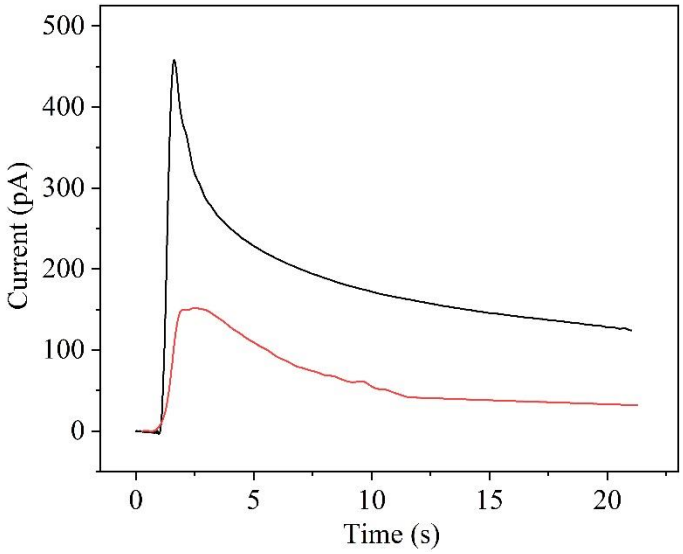

Figure 5. A characteristic amperometric current-time trace for an MPA modified and Geltrex coated (1:200 dilution) UME of design 1 (red) and design 2 (black) acquired by pipetting PBS containing 150 µM DA. (The recordings were made at 600 mV vs. on-chip RE)

3.2. Real-time detection of DA release from PC12 cells

The UMEA chips were designed to have electrodes that accommodate only one PC12 cell (diameter ca. 10 µm) in the recess formed by the photoresist insulation layer. The distance between each UME (vertically and horizontally) was 40 µm and the entire area occupied by the UMEA was 260 µm × 290 µm (Figure 1c). The chip holder defined a vial of 0.85 cm × 0.85 cm with rounded corners, providing a total area of ca. 0.7 cm^2. The cell seeding density 10^6 cells/cm^2 was chosen to maximize the chance to have a cell on each UME of the chip. In this study, PC12 cells were allowed to adhere and spread for 24 h prior to exocytosis measurements. As a consequence of this, the cells that were able to settle on an UME after seeding could

fully cover the surface during adhesion and spreading. Moreover, the contact between a cell and an UME would be sufficiently close to allow the contents of the neurotransmitter vesicles to be emptied directly on the electrode surface.

Current-time trace recordings during exocytosis measurements on single cells are customarily performed using a current sampling frequency ranging from 5 kHz to 10 kHz, which correspond to current sampling every 100 to 200 µs. This rate allows recording of fully resolved current peaks corresponding to DA release from individual storage vesicles. Duration of such exocytotic events, defined as baseline width of the recorded peaks, may vary in the range from a few ms to over 20 ms depending on the cell type (e.g. PC12 cells or chromaffin cells from adrenal gland) and the type electrode that was employed in the measurements [20,32,34]. The functional principle of the 54-channel multiplexing potentiostat[48] that was used to record current-time traces upon oxidation of released DA was such that all the WEs of an UMEA were biased simultaneously at the desired potential, while the multiplexing function switched from one WE to another to read the current. The used setting allowed current mapping from each UME at the rate of ca. 60 µs.

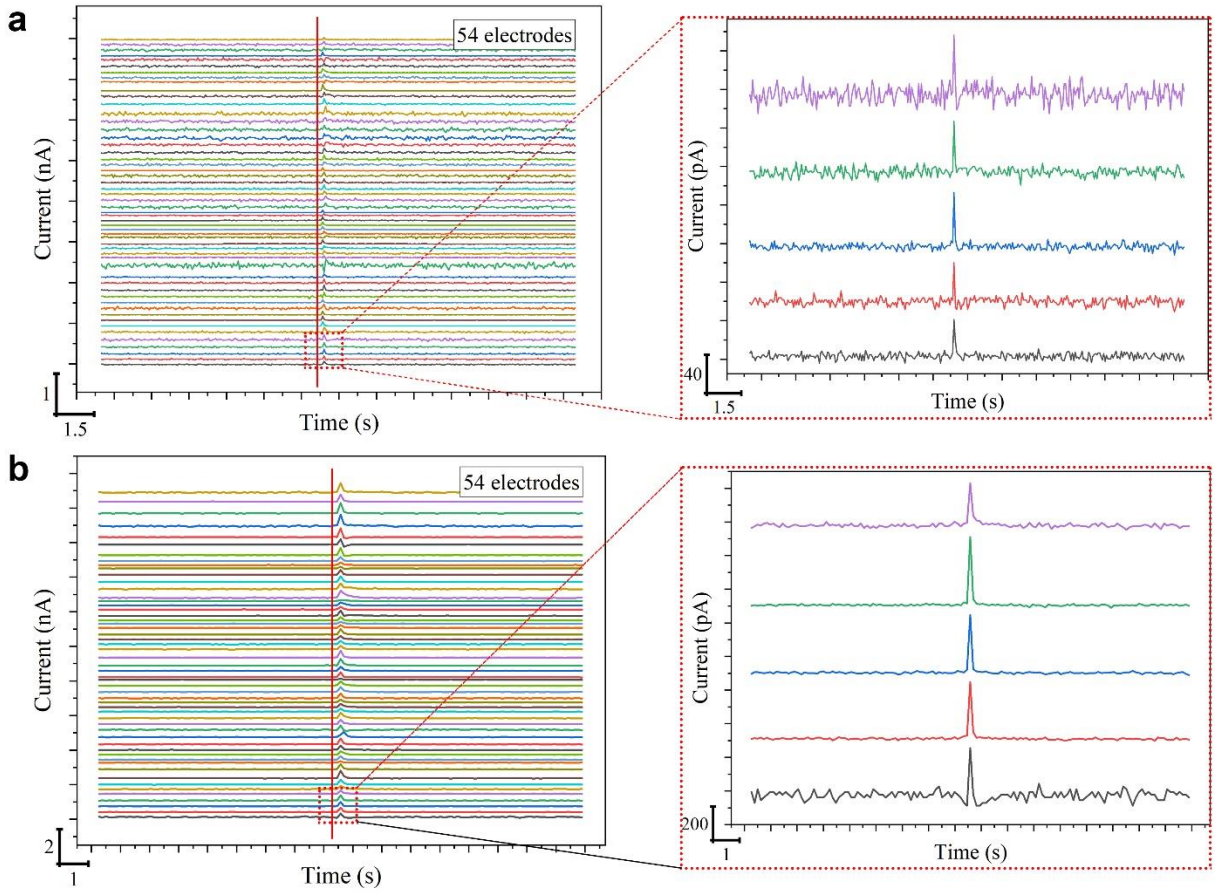

Figure 6. (Left panels) Simultaneous current-time trace recording on 54 UMEs during measurement of K^+-induced dopamine exocytosis (time of K^+ addition indicated by the solid red line) from PC12 cells: UMEA chip of a) design 1 and b) design 2. The inset (right panel) of a) and b) shows a zoom-in of the current-time trace for five UMEs. (The recordings were made at 600 mV vs. on-chip RE)

During the amperometric measurements performed in this work, the cell population was initially incubated in 100 µl of a low-K^+ buffer to record a stable baseline current. Exocytosis was triggered by pipetting 50

µl of a high-K^+ buffer in one of the corners of the cell culture vial. As soon as the K^+ concentration in the central area of the UMEA chip reached sufficiently high level to facilitate membrane depolarization of each cell residing on an UME, a current peak could be recorded. Figures 6a and b (left panels) show 54 recorded current-time traces on each of the UMEA designs. A zoom-in view of five current-time traces is shown in the right panel of each figure. The presented recordings show that the current peaks occurred nearly simultaneously, which indicates that the pipetted high-K^+ buffer reached all the cells residing on an UME roughly at the same time. This can be attributed to the small area occupied by an entire UMEA. Figures 7a and b show a heatmap plot as an alternative way of visualizing the current amplitude of each recorded peak. A control experiment was performed to rule out that the recorded peaks were not caused by hydrodynamic perturbations due to pipetting of the high-K^+ buffer. Figure S4 in the Supporting Information shows a current recording on 54 UMEs without any cells. Pipetting of buffer on the chip with bare UMEs clearly generated a perturbation, whereas the current-time traces recorded in the presence of adhering cells (Figure 6a and b) do not show such a perturbation.

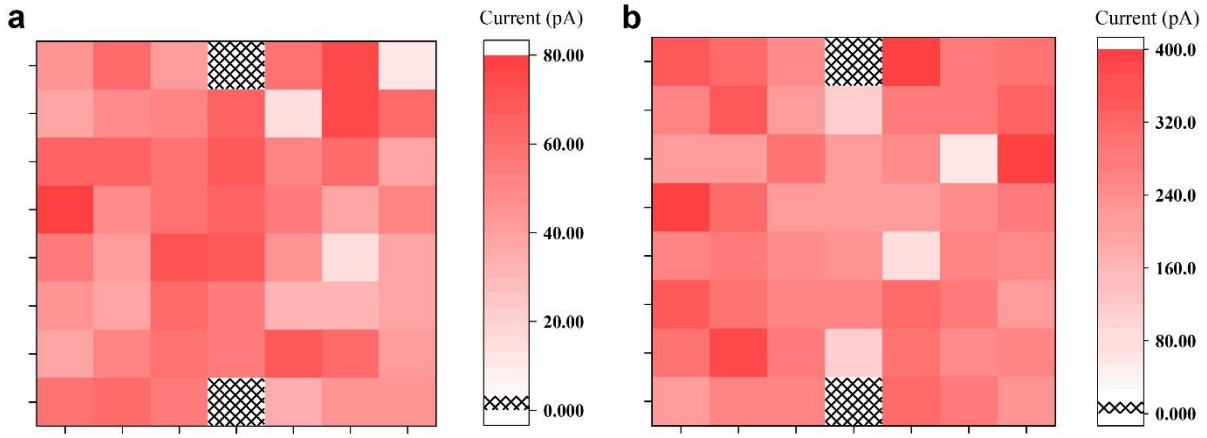

Figure 7. Heatmap presentation of the peak current amplitude for each of the 54 UMEs based on current-time trance recordings of Figure 6a and b: UMEA chip of a) design 1 and b) design 2. (The hatched cells represent the CE and RE)

The recorded current peaks were analyzed to calculate the average current amplitude for the 54 UMEs of each design. The calculated average values were 51 pA ± 14 pA and 263 pA ± 69 pA (the uncertainties represent standard deviation, n = 54) for the 5 µm and 10 µm UMEs, respectively, indicating that the average current amplitude recorded on the 10 µm UMEs was roughly 5-fold in comparison with that of the 5 µm UMEs. Aside from the detailed results presented above, exocytosis measurements were conducted on two additional UMEA chips of each design. Average current amplitude recorded on the 54 UMEs of all the three chips of each design were 53 pA ± 1 pA and 280 pA ± 7 pA (the uncertainties represent standard error of mean, n = 162) Electrochemical characterization of several UMEA chips demonstrated their reproducible performance. Based on that, we can be confident that the variation of current amplitude between individual UMEs was caused by differences in the cellular response to K^+-induced depolarization. Each current peak was also integrated in order to determine the charge (Q) generated during DA oxidation and the total duration of each peak. Figure 8a shows the variation in the generated charge for each UME of design 1 and 2. The corresponding average for the UMEs of each design (Figure 8b) was 35 pC ± 10 pC and 182 pC ± 50 pC (the uncertainties represent standard deviation, n = 54), respectively, which indicates that the average charge for the 10 µm UMEs was more than 5-fold in comparison with the average charge generated during DA oxidation at the 5 µm UMEs. The number of oxidized molecules (N) can be calculated based on

Faraday's law of electrolysis $N = N_A \times Q/nF$, where N_A is the Avogadro's number (6.022×10^{23} molecules/mol), n is the number of electrons involved in the oxidation (2 for DA), and F is the Faraday constant (96485 C/mol). For the 5 µm and 10 µm UMEs, the calculated average charge values were equivalent to $1.1\times10^8 \pm 3.1\times10^7$ and $5.7\times10^8 \pm 1.6\times10^8$ (the uncertainties represent standard deviation, n = 54), respectively, oxidized molecules. Finally, the duration of the current peaks, defined as the baseline width for each peak, was determined for each UME of the two designs (Figure 8c) and the average duration was calculated to be 605 ms ± 67 ms and 863 ms ± 135 ms (the uncertainties represent standard deviation, n = 54) (Figure 8d).

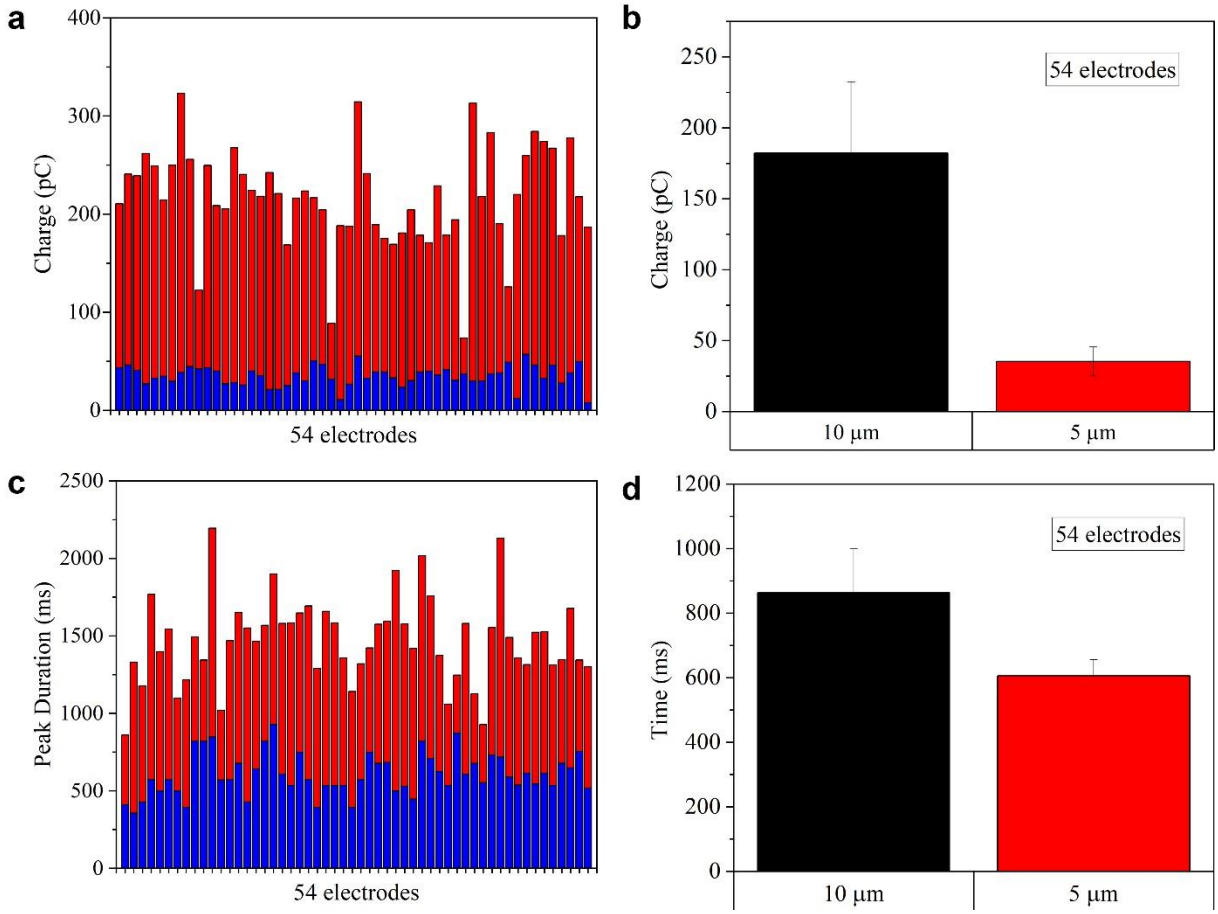

Figure 8. Parameters calculated based on the current peaks recorded during measurement of K^+-induced dopamine exocytosis shown in Figure 6a and b: (a,b) Generated charge and (c,d) duration of current peaks on 54 individual UMEs (a,c; blue – design 1, red – design 2) and averaged for each design (b,d). (The error bars in b and d represent standard deviation, n = 54.)

As mentioned above, the average length of a single-vesicle exocytotic event (peak duration) may be even over 20 ms. For PC12 cells, estimates of average current amplitude have been ca. 20 pA[20,47] and the average charge has been slightly below 0.2 pC[47]. Based on all the average values presented above, the recorded current peaks, generated charge, and peak duration were significantly higher than what could be expected for a single-vesicle exocytotic event. Furthermore, variation of the individual values represented by the standard deviation was also significantly higher than what has been reported in literature in relation to single-vesicle measurements. Moreover, customarily in single-cell exocytosis measurements the recorded current-time traces comprise a large number of current peaks, each representing a single-vesicle exocytotic

event, whereas the recordings presented here only give one current peak for each UME. On the other hand, the peak shape and parameters presented here are also clearly different from those presented elsewhere for cell population-based measurements[38,50,51]. The conclusion is that the recorded single current peaks represent single-cell exocytosis measurements composed of several superimposed single-vesicle exocytotic events.

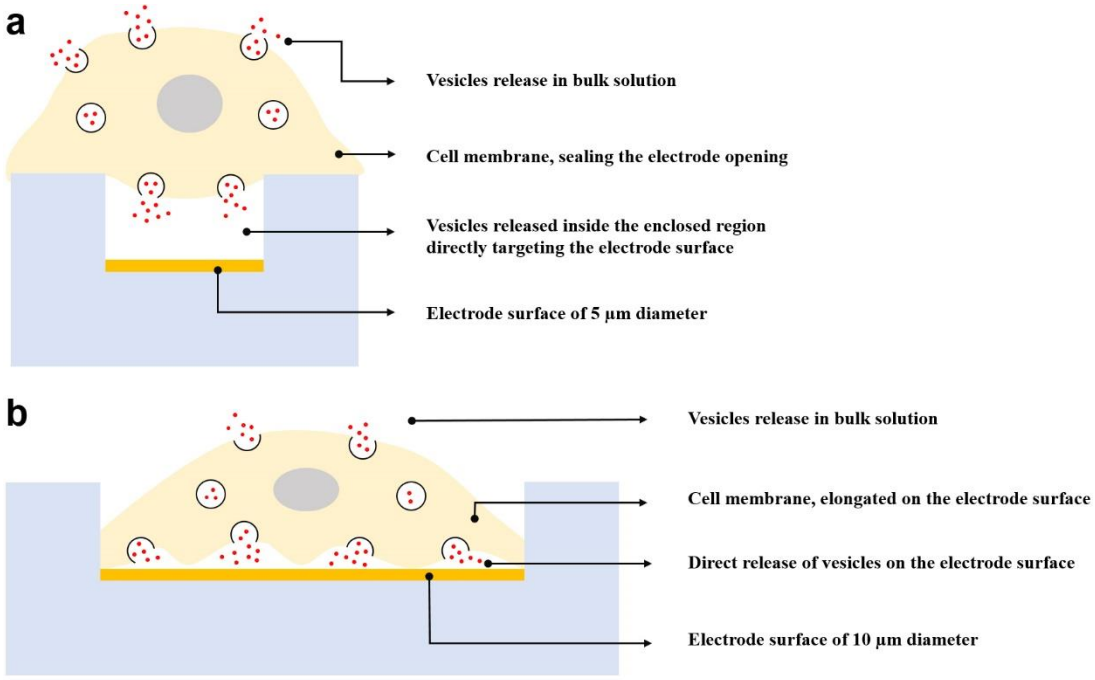

Figure 9. Schematic view a cell sealing the opening of a recessed electrode: a) An UME of 5 µm in diameter has an area that is smaller than an adhering cell. The adhering cell may be partially elevated from the electrode surface and have only a limited number of focal adhesion points, which concomitantly limits the number of vesicles able to release DA directly to the electrode surface. a) An UME of 10 µm in diameter has an area that is closely of the same order of dimension as an adhering cell. The adhering cell may spread on the electrode surface and form focal adhesion points, allowing a great portion of the vesicles fusing with the basal cell membrane to be able to release DA directly onto the electrode surface.

One plausible explanation for the appearance of only one single peak is related to the way how a PC12 cell resides on a recessed UME. Considering that when a cell immediately after seeding has sedimented on an UME, it has spherical shape. During the following adhesion and spreading, it becomes widened and flattened. Although the shape of an adhering PC12 cell is close to oval, based on AFM scans of multiple cells an average area and height could be approximated by 10×10 µm^2 and 1.5 – 2 µm[58]. Figure 9a and b show a schematic view how an adherent and flattened PC12 cell can form a 'lid' on a recessed UME with 5 µm and 10 µm diameter, respectively. Such an intimate contact between a cell and an UME has three main consequences: 1) The released DA molecules cannot readily diffuse out from the 'vial' closed by the 'lid', 2) the basal cell membrane is in intimate contact, i.e. forming focal adhesion points, with practically the entire UME area, and 3) all the vesicles that are able to release their contents to the UME have roughly the same distance from the electrode surface. Hence, all of the multiple single-vesicle exocytotic events are 'fast' as previously described[59]. On the other hand, DA molecules released from vesicles that are not in close contact with the UME surface, i.e. they are outside the 'vial' formed around the recessed UME, cannot be oxidized and contribute to the measurements. The roughly 5-fold higher peak currents obtained for the

10 µm UMEs is a consequence of a significantly larger number of vesicles in direct contact with the electrodes. Furthermore, observed variations between the recorded current peaks can plausible be explained as a combination of two factors: 1) Heterogeneity of the vesicular distribution in the cell membrane portion that is in contact with an UME[43–45] and 2) the general variation in the behavior of individual vesicles that has been demonstrated in scientific literature dealing with single-vesicle exocytosis measurements.

4. Conclusion

This work presents, to our best knowledge, the first single-cell dopamine (DA) exocytosis measurements in a population of cells. We have fabricated on glass substrate ultramicroelectrode arrays (UMEAs) using maskless photolithography. The UMEAs, having a footprint of approximately 260 µm x 290 µm, comprised 54 individually addressable recessed ultramicroelectrodes (UMEs) of two designs, 5 µm and 10 µm in diameter, defined by lithographically patterned 500 nm thick insulating photoresist layer on the chip surface. Simultaneous amperometric real-time detection of DA exocytosis on all of the 54 UMEs of each design was performed using a tailor-made 54-channel potentiostat, having current sampling time of about 60 µs, and demonstrated using adherently growing rat pheochromocytoma (PC12) cells. Both UME designs had a dimension comparable to that of PC12 cells, i.e. on average 10 µm in diameter, securing that only one cell was able to release dopamine on each UME. Based on thorough electrochemical characterization, the UMEs proved to be highly reproducible in their electrochemical behavior, which formed the basis for reliable DA detection from single cells. On virtue of the reproducible behavior of the fabricated UMEs, we can confidently conclude that the variation in peak current amplitude during exocytosis measurements between individual UMEs was due to differences in the behavior of individual cells. On each UME, only one current peak was recorded during exocytosis measurements. The average amplitude and peak duration were significantly higher compared to traditional single-cell measurements, where each peak corresponds to a single vesicle being emptied. The conclusion is that the recorded peaks represent a sum of single-vesicular exocytotic events from a cell that releases the DA into a confined space defined by the cell covering an entire recessed UME. In comparison between the two UME designs, the determined average current amplitude and charge was roughly five times higher on the 10 µm UMEs. This is also plausible considering that a larger area of the basal cell membrane was adhering on the UME surface, and hence, a larger number of vesicles could release the contents directly on the electrode surface.

The presented approach to perform single-cell exocytosis measurements on cells belonging to a cell population is different from the traditional single-cell measurements. However, it provides a new paradigm in terms of a fast summation of how effective the exocytotic function is on single-cell level, while, at the same time, allowing to obtain a significant view of the variations of neurotransmitter release on population level. It is useful for diverse purposes, such as for characterizing the maturity of single differentiating neural stem cells, assessing the response of individual optogenetically modified stem cells and neurons in a population, and screening on single-cell level for the potency of therapeutic substances that modulate the exocytotic functions.

Acknowledgements

The authors are thankful for the funding support from Marie-Skłodowska-Curie Horizon-2020 Innovative Training Network (H2020-MSCA-ITN-2016) with grant agreement number: 722779.

References

1. Südhof, T. C. The synaptic vesicle cycle. *Annual Review of Neuroscience* vol. 27 509–547 (2004).
2. Valtorta, F. *et al.* Neurotransmitter release and synaptic vesicle recycling. *Neuroscience* **35**, 477–489 (1990).
3. Edwards, R. H. The Neurotransmitter Cycle and Quantal Size. *Neuron* vol. 55 835–858 (2007).
4. Burgoyne, R. D. & Morgan, A. Secretory granule exocytosis. *Physiological Reviews* vol. 83 581–632 (2003).
5. Amatore, C., Arbault, S., Guille, M. & Lemaître, F. Electrochemical monitoring of single cell secretion: Vesicular exocytosis and oxidative stress. *Chemical Reviews* vol. 108 2585–2621 (2008).
6. Holz, R. W. Control of exocytosis from adrenal chromaffin cells. *Cellular and Molecular Neurobiology* vol. 8 259–268 (1988).
7. Ballatore, C., Lee, V. M. Y. & Trojanowski, J. Q. Tau-mediated neurodegeneration in Alzheimer's disease and related disorders. *Nature Reviews Neuroscience* vol. 8 663–672 (2007).
8. Shintani, T. & Klionsky, D. J. Autophagy in health and disease: A double-edged sword. *Science* vol. 306 990–995 (2004).
9. Wightman, R. M. Probing cellular chemistry in biological systems with microelectrodes. *Science* vol. 311 1570–1574 (2006).
10. Kissinger, P. T., Hart, J. B. & Adams, R. N. Voltammetry in brain tissue - a new neurophysiological measurement. *Brain Res.* **55**, 209–213 (1973).
11. Li, X., Dunevall, J., Ren, L. & Ewing, A. G. Mechanistic Aspects of Vesicle Opening during Analysis with Vesicle Impact Electrochemical Cytometry. *Anal. Chem.* **89**, 9416–9423 (2017).
12. Trouillon, R. & Ewing, A. G. Actin controls the vesicular fraction of dopamine released during extended kiss and run exocytosis. *ACS Chem. Biol.* **9**, 812–820 (2014).
13. Ganesana, M., Lee, S. T., Wang, Y. & Venton, B. J. Analytical Techniques in Neuroscience: Recent Advances in Imaging, Separation, and Electrochemical Methods. *Analytical Chemistry* vol. 89 314–341 (2017).
14. Mosharov, E. V. & Sulzer, D. Analysis of exocytotic events recorded by amperometry. *Nature Methods* vol. 2 651–658 (2005).
15. Wightman, R. M. *et al.* Temporally resolved catecholamine spikes correspond to single vesicle release from individual chromaffin cells. *Proc. Natl. Acad. Sci. U. S. A.* **88**, 10754–10758 (1991).
16. Leszczyszyn, D. J. *et al.* Secretion of Catecholamines from Individual Adrenal Medullary Chromaffin Cells. *J. Neurochem.* **56**, 1855–1863 (1991).
17. De Toledo, G. A., Fernández-Chacón, R. & Fernández, J. M. Release of secretory products during transient vesicle fusion. *Nature* **363**, 554–558 (1993).
18. Zhou, Z. & Misler, S. Amperometric detection of stimulus-induced quantal release of catecholamines from cultured superior cervical ganglion neurons. *Proc. Natl. Acad. Sci. U. S. A.*

92, 6938–6942 (1995).

19. Bruns, D. & Jahn, R. Real-time measurement of transmitter release from single synaptic vesicles. *Nature* **377**, 62–65 (1995).

20. Chen, T. K., Luo, G. & Ewing, A. G. Amperometric Monitoring of Stimulated Catecholamine Release from Rat Pheochromocytoma (PC12) Cells at the Zeptomole Level. *Anal. Chem.* **66**, 3031–3035 (1994).

21. Pothos, E. N., Davila, V. & Sulzer, D. Presynaptic recording of quanta from midbrain dopamine neurons and modulation of the quantal size. *J. Neurosci.* **18**, 4106–4118 (1998).

22. Chen, G. & Ewing, A. G. Multiple classes of catecholamine vesicles observed during exocytosis from the Planorbis cell body. *Brain Res.* **701**, 167–174 (1995).

23. Barlow, S. T., Louie, M., Hao, R., Defnet, P. A. & Zhang, B. Electrodeposited Gold on Carbon-Fiber Microelectrodes for Enhancing Amperometric Detection of Dopamine Release from Pheochromocytoma Cells. *Anal. Chem.* **90**, 10049–10055 (2018).

24. Colliver, T. L., Hess, E. J., Pothos, E. N., Sulzer, D. & Ewing, A. G. Quantitative and statistical analysis of the shape of amperometric spikes recorded from two populations of cells. *J. Neurochem.* **74**, 1086–1097 (2000).

25. Chen, P. *et al.* Amperometric detection of quantal catecholamine secretion from individual cells on micromachined silicon chips. *Anal. Chem.* **75**, 518–524 (2003).

26. Amatore, C., Oleinick, A., Klymenko, O. V. & Svir, I. In situ and online monitoring of hydrodynamic flow profiles in microfluidic channels based upon microelectrochemistry: Concept, theory, and validation. *ChemPhysChem* **6**, 1581–1589 (2005).

27. Maher, M. P., Pine, J., Wright, J. & Tai, Y. C. The neurochip: A new multielectrode device for stimulating and recording from cultured neurons. *J. Neurosci. Methods* **87**, 45–56 (1999).

28. Berberian, K., Kisler, K., Qinghua, F. & Lindau, M. Improved surface-patterned platinum microelectrodes for the study of exocytotic events. *Anal. Chem.* **81**, 8734–8740 (2009).

29. Carabelli, V. *et al.* Nanocrystalline diamond microelectrode arrays fabricated on sapphire technology for high-time resolution of quantal catecholamine secretion from chromaffin cells. *Biosens. Bioelectron.* **26**, 92–98 (2010).

30. Chen, X., Gao, Y., Hossain, M., Gangopadhyay, S. & Gillis, K. D. Controlled on-chip stimulation of quantal catecholamine release from chromaffin cells using photolysis of caged Ca2+ on transparent indium-tin-oxide microchip electrodes. *Lab Chip* **8**, 161–169 (2007).

31. Dittami, G. M. & Rabbitt, R. D. Electrically evoking and electrochemically resolving quantal release on a microchip. *Lab Chip* **10**, 30–35 (2010).

32. Sun, X. & Gillis, K. D. On-chip amperometric measurement of quantal catecholamine release using transparent indium tin oxide electrodes. *Anal. Chem.* **78**, 2521–2525 (2006).

33. Hafez, I. *et al.* Electrochemical imaging of fusion pore openings by electrochemical detector arrays. *Proc. Natl. Acad. Sci. U. S. A.* **102**, 13879–13884 (2005).

34. Yakushenko, A., Kätelhön, E. & Wolfrum, B. Parallel on-chip analysis of single vesicle neurotransmitter release. *Anal. Chem.* **85**, 5483–5490 (2013).

35. Cui, H. F., Ye, J. S., Chen, Y., Chong, S. C. & Sheu, F. S. Microelectrode array biochip: Tool for

in vitro drug screening based on the detection of a drug effect on dopamine release from PC12 cells. *Anal. Chem.* **78**, 6347–6355 (2006).

36. Tomagra, G. *et al.* Simultaneous multisite detection of quantal release from PC12 cells using micro graphitic-diamond multi electrode arrays. *Biophys. Chem.* **253**, 106241 (2019).

37. Tomagra, G. *et al.* Diamond-based multi electrode arrays for monitoring neurotransmitter release. in *Lecture Notes in Electrical Engineering* vol. 539 125–134 (Springer Verlag, 2019).

38. Amato, L. *et al.* Pyrolysed 3D-carbon scaffolds induce spontaneous differentiation of human neural stem cells and facilitate real-time dopamine detection. *Adv. Funct. Mater.* **24**, 7042–7052 (2014).

39. Vasudevan, S. *et al.* Leaky Optoelectrical Fiber for Optogenetic Stimulation and Electrochemical Detection of Dopamine Exocytosis from Human Dopaminergic Neurons. *Adv. Sci.* **6**, 1902011 (2019).

40. Eftekhari, B. S., Eskandari, M., Janmey, P. A., Samadikuchaksaraei, A. & Gholipourmalekabadi, M. Surface Topography and Electrical Signaling: Single and Synergistic Effects on Neural Differentiation of Stem Cells. *Advanced Functional Materials* vol. 30 1907792 (2020).

41. Greene, L. A. & Tischler, A. S. Establishment of a noradrenergic clonal line of rat adrenal pheochromocytoma cells which respond to nerve growth factor. *Proc. Natl. Acad. Sci. U. S. A.* **73**, 2424–2428 (1976).

42. Westerink, R. H. S. & Ewing, A. G. The PC12 cell as model for neurosecretion. in *Acta Physiologica* vol. 192 273–285 (John Wiley & Sons, Ltd, 2008).

43. Kozminski, K. D., Gutman, D. A., Davila, V., Sulzer, D. & Ewing, A. G. Voltammetric and pharmacological characterization of dopamine release from single exocytotic events at rat pheochromocytoma (PC12) cells. *Anal. Chem.* **70**, 3123–3130 (1998).

44. Zhang, B. *et al.* Spatially and temporally resolved single-cell exocytosis utilizing individually addressable carbon microelectrode arrays. *Anal. Chem.* **80**, 1394–1400 (2008).

45. Lin, Y. *et al.* Carbon-ring microelectrode arrays for electrochemical imaging of single cell exocytosis: Fabrication and characterization. *Anal. Chem.* **84**, 2949–2954 (2012).

46. Dimaki, M. *et al.* A compact microelectrode array chip with multiple measuring sites for electrochemical applications. *Sensors (Switzerland)* **14**, 9505–9521 (2014).

47. Spégel, C. *et al.* On-chip determination of dopamine exocytosis using mercaptopropionic acid modified microelectrodes. in *Electroanalysis* vol. 19 263–271 (John Wiley & Sons, Ltd, 2007).

48. Vergani, M. *et al.* Compact potentiostat for cellular electrochemical imaging with 54 parallel channels. in *2012 IEEE Biomedical Circuits and Systems Conference: Intelligent Biomedical Electronics and Systems for Better Life and Better Environment, BioCAS 2012 - Conference Publications* 136–139 (2012). doi:10.1109/BioCAS.2012.6418401.

49. Vergani, M. *et al.* Multichannel Bipotentiostat Integrated With a Microfluidic Platform for Electrochemical Real-Time Monitoring of Cell Cultures. *IEEE Trans. Biomed. Circuits Syst.* **6**, 498–507 (2012).

50. Sasso, L. *et al.* Doped overoxidized polypyrrole microelectrodes as sensors for the detection of dopamine released from cell populations. *Analyst* **138**, 3651–3659 (2013).

51. Zór, K. *et al.* A compact multifunctional microfluidic platform for exploring cellular dynamics in

real-time using electrochemical detection. *RSC Adv.* **4**, 63761–63771 (2014).

52. Fischer, L. M. *et al.* Gold cleaning methods for electrochemical detection applications. *Microelectron. Eng.* **86**, 1282–1285 (2009).

53. Orozco, J., Fernández-Sánchez, C. & Jiménez-Jorquera, C. Ultramicroelectrode array based sensors: A promising analytical tool for environmental monitoring. *Sensors* vol. 10 475–490 (2010).

54. Bond, A. M., Luscombe, D., Oldham, K. B. & Zoski, C. G. A comparison of the chronoamperometric response at inlaid and recessed disc microelectrodes. *J. Electroanal. Chem.* **249**, 1–14 (1988).

55. Veera Manohara Reddy, Y. *et al.* Ultrafine Pt-Ni bimetallic nanoparticles anchored on reduced graphene oxide nanocomposites for boosting electrochemical detection of dopamine in biological samples. *New J. Chem.* **42**, 16891–16901 (2018).

56. Manbohi, A. & Ahmadi, S. H. Sensitive and selective detection of dopamine using electrochemical microfluidic paper-based analytical nanosensor. *Sens. Bio-Sensing Res.* **23**, 100270 (2019).

57. Lane, R. F. & Hubbard, A. T. Differential Double Pulse Voltammetry at Chemically Modified Platinum Electrodes for in vivo Determination of Catecholamines. *Anal. Chem.* **48**, 1287–1293 (1976).

58. Reddy, C. V. G., Malinowska, K., Menhart, N. & Wang, R. Identification of TrkA on living PC12 cells by atomic force microscopy. *Biochim. Biophys. Acta - Biomembr.* **1667**, 15–25 (2004).

59. Trouillon, R., Lin, Y., Mellander, L. J., Keighron, J. D. & Ewing, A. G. Evaluating the diffusion coefficient of dopamine at the cell surface during amperometric detection: Disk vs ring microelectrodes. *Anal. Chem.* **85**, 6421–6428 (2013).

Supporting Information:

Ultramicroelectrode arrays for monitoring dopamine exocytosis form single cells in a cell population

Muhammad Salman Khan[1(joint 1st)], Marco Giacometti[2(joint 1st)], Arto Heiskanen[1], Afia Asif[1], Winnie Svendsen[1], Maria Dimaki[1], Marco Carminati[2], Giorgio Ferrari[2], Marco Sampietro[2*], and Jenny Emnéus[1*]

[1] Technical University of Denmark, Department of Biotechnology and Biomedicine, Søltofts Plads, Building 221, 2800 Kgs. Lyngby, Denmark

[2] Politecnico di Milano, Dipartimento di Elettronica, Informazione e Bioingegneria - DEIB, P.za L. da Vinci 32, 20133 Milano, Italy

*Corresponding author

Phone: +4525473548

e-mail: jemn@dtu.dk and marco.sampietro@polimi.it

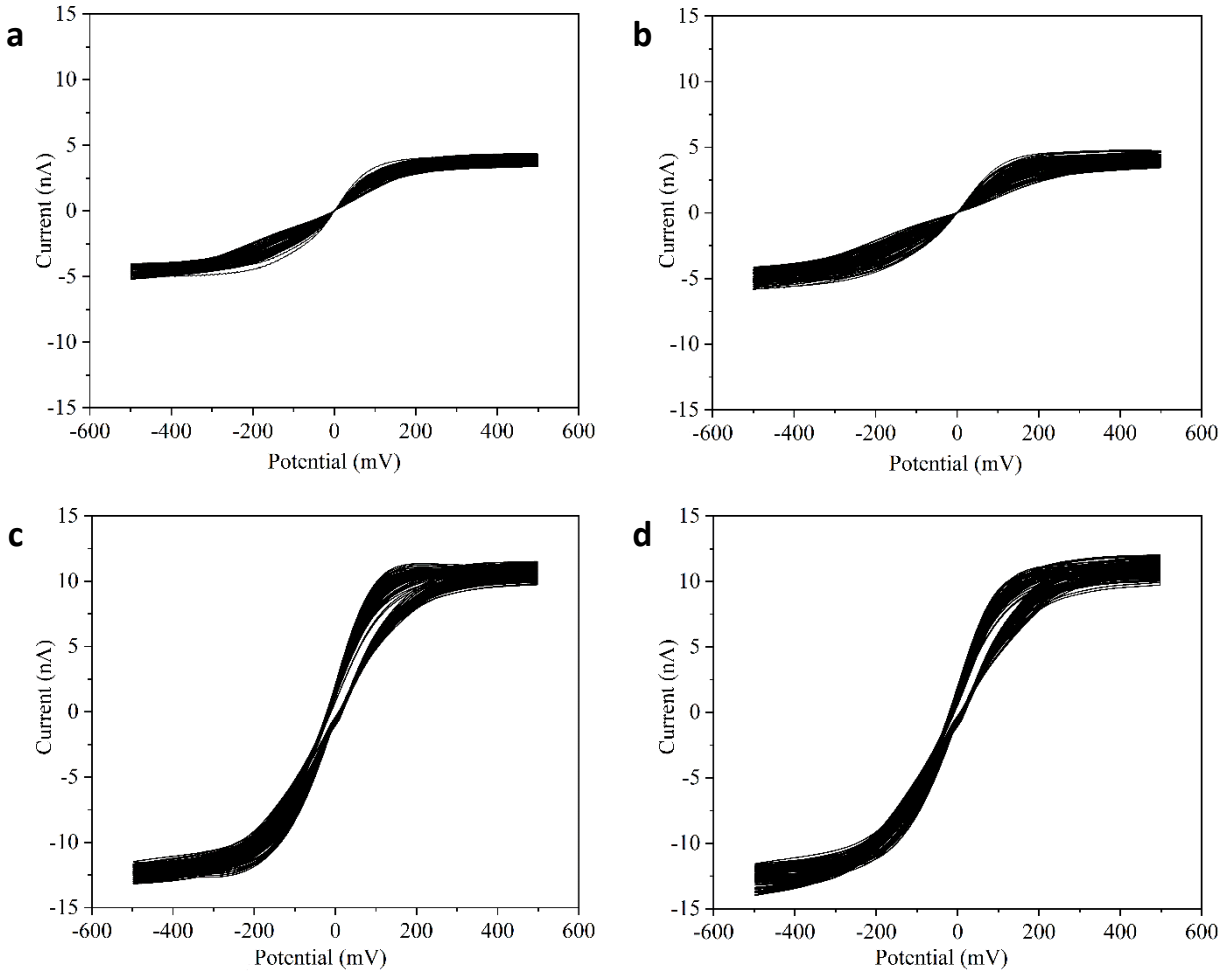

Figure S1. A set of 54 CVs for UMEs of a,b) design 1 and c,d) design 2. (All the CVs were acquired in PBS containing 10 mM $[Fe(CN)_6]^{3-/4-}$; the applied potentials were vs. the on-chip RE, scan rate 50 mV/s)

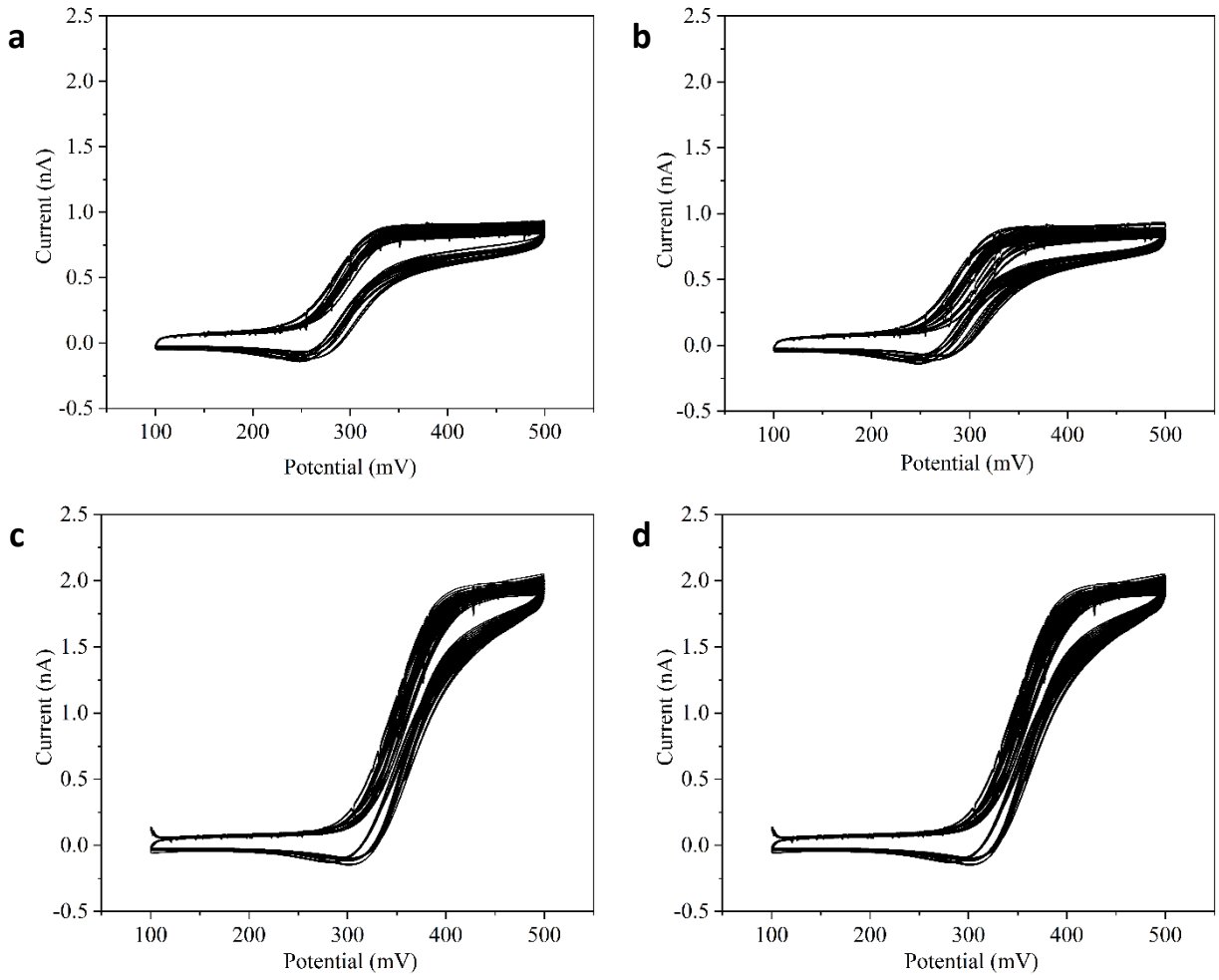

Figure S2. A set of 54 CVs for UMEs of a,b) design 1 and c,d) design 2. (All the CVs were acquired in PBS containing 150 µM DA; the applied potentials were vs. the on-chip RE, scan rate 50 mV/s)

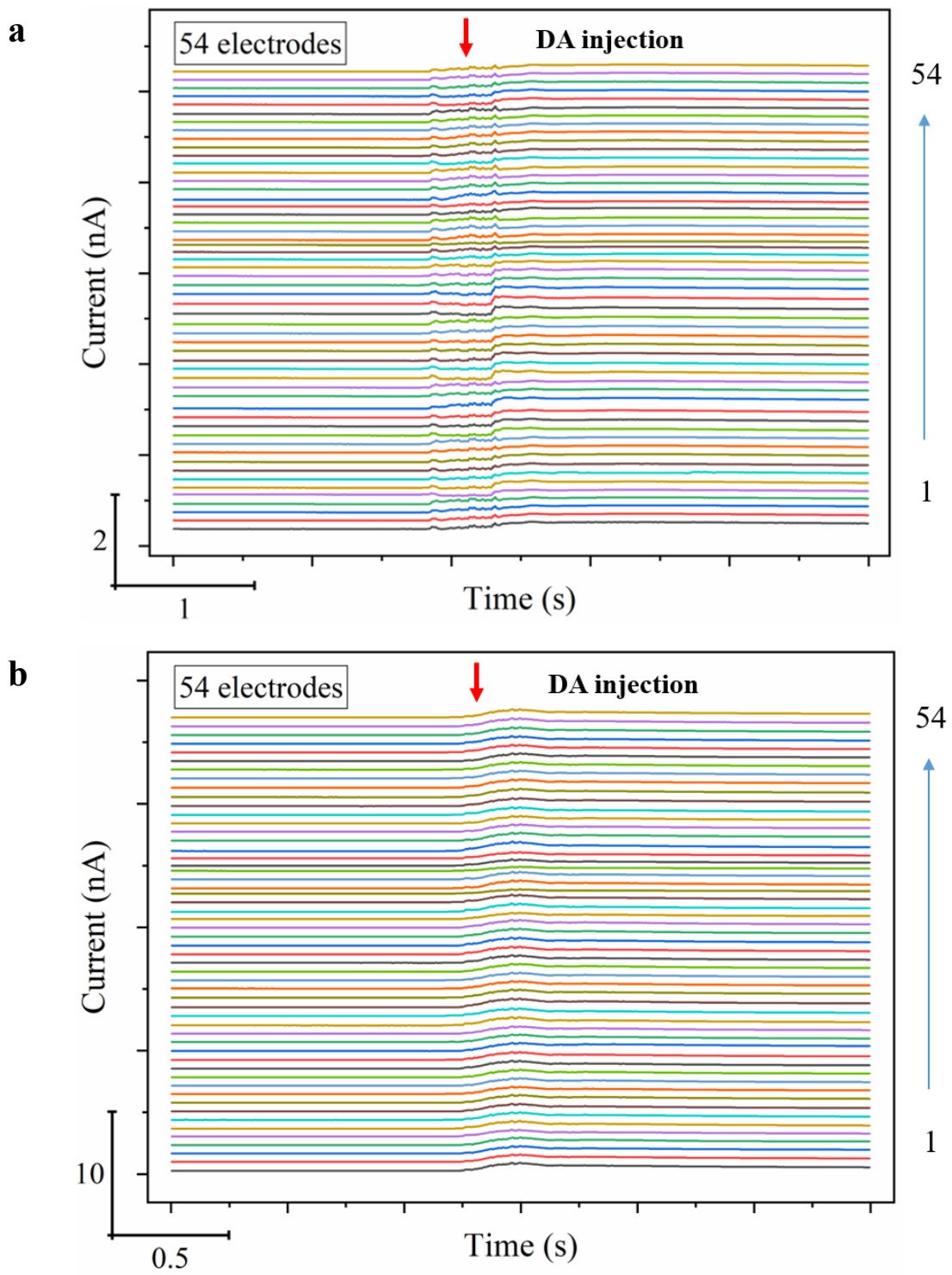

Figure S3. Simultaneous amperometric recordings on 54 UMEs of a) design 1 (5 µm in diameter) and b) design 2 (10 µm in diameter). 200 µl of PBS containing 150 mM DA was pipetted in the vial of the UMEA chip holder. All the electrodes were continuously biased at 0.6 V vs. the on-chip RE. The red arrows indicate the time of pipetting.

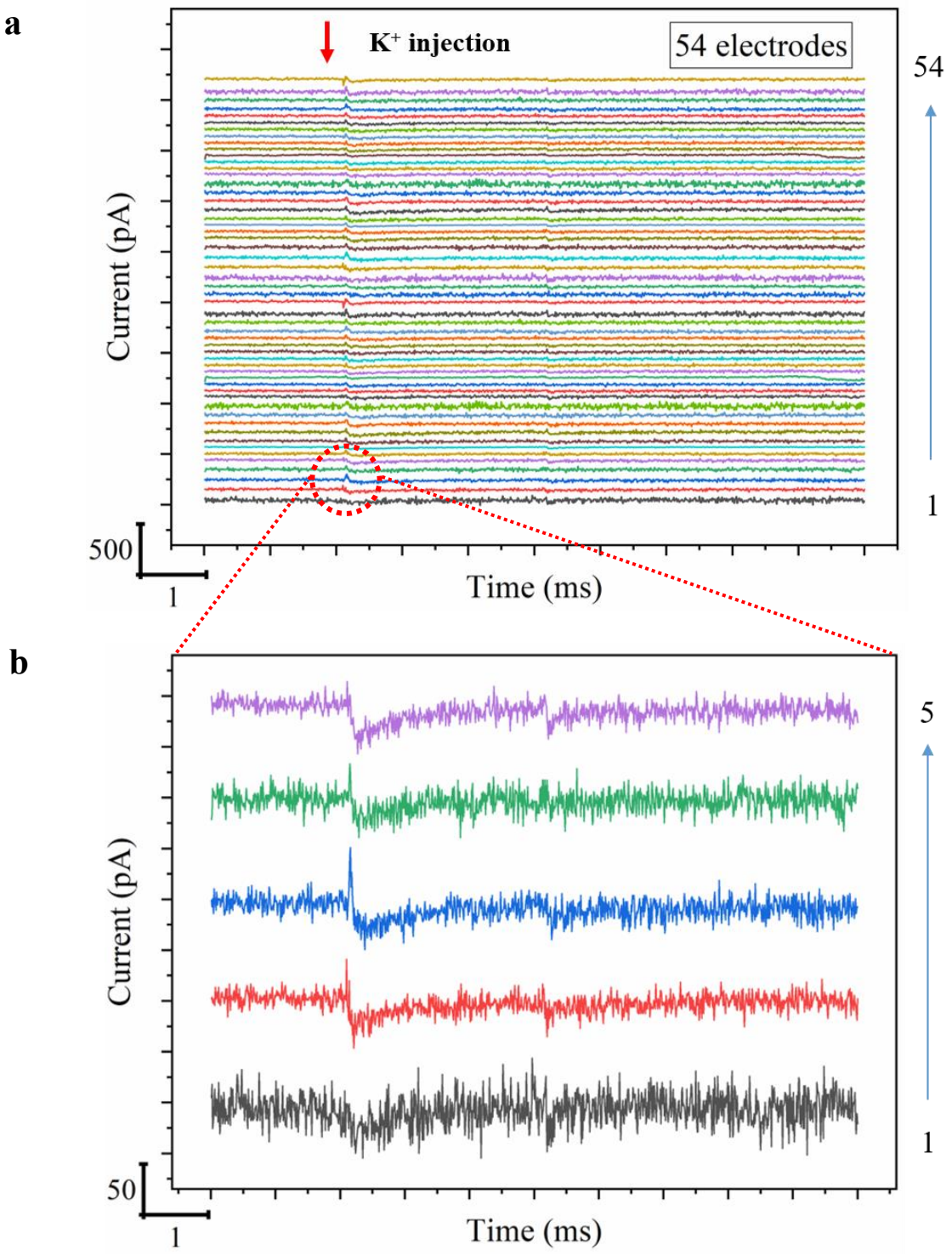

Figure S4. a) Simultaneous amperometric recordings on 54 UMEs of design 1 (5 µm in diameter) in the absence of cells. Hydrodynamic perturbation caused by pipetting of high-K^+ buffer into the vial of the UMEA chip holder. All the electrodes were continuously biased at 0.6 V vs. the on-chip RE. The red arrow indicates the time of pipetting.

PAPER II

Impedance characterization of biocompatible hydrogel suitable for biomimetic lipid membrane applications

Agnieszka Mech-Dorosz, M Salman Khan, Ramona Valentina Mateiu, Claus Hélix-Nielsen, Jenny Emnéus, Arto Heiskanen

Impedance characterization of biocompatible hydrogel suitable for biomimetic lipid membrane applications

Agnieszka Mech-Dorosz[1,2], Muhammad Salman Khan[1], Ramona Valentina Mateiu[3], Claus Hélix-Nielsen[4,5], Jenny Emnéus[1], Arto Heiskanen[1,*]

[1]Technical University of Denmark, Department of Biotechnology and Biomedicine, Produktionstorvet, Building 423, DK-2800 Kgs. Lyngby, Denmark

[2]Present address: Novo Nordisk A/S, Brennum Park 24 K, 3400 Hillerød, Denmark

[3]Technical University of Denmark, Center for Electron Nanoscopy, Fysikvej, Building 307, 2800 Kgs. Lyngby, Denmark

[4]Technical University of Denmark, Department of Environmental Engineering, Bygningstorvet, Building 115, DK-2800 Kgs. Lyngby, Denmark

[5]Aquaporin A/S, Nymøllevej 78, DK-2800 Kgs. Lyngby, Denmark

*Corresponding Author

Phone: +45-45-256839

e-mail: arhe@dtu.dk

Abstract

Hydrogels, biocompatible and hydrophilic polymeric networks, have been widely applied in, e.g., pharmaceutical and biomedical research. Their physico-chemical properties can be fine-tuned by changing the fraction and molecular structure of cross-linkers. Hydrogel layers with varying thickness have also been used to support biomimetic lipid bilayers studied using electrochemical impedance spectroscopy (EIS). To provide deeper understanding of the impedimetric behavior of thick covalently tethered hydrogels on an electrode and the influence of cross-linking, we present here a thorough EIS characterization of poly(2-hydroxyethyl methacrylate) hydrogels cross-linked with poly(ethylene glycol)-dimethacrylate in ratios 1:100, 1:200, and 1:400. We propose an equivalent circuit model comprising an open-boundary finite-length Warburg element and constant phase element in series to describe the mass transfer differences between the bulk hydrogel and covalently tethered domain at the electrode-hydrogel interface. The results indicated that an increased fraction of the hydrophilic high-molecular weight cross-linker significantly decreased the charge transfer resistance for $[Fe(CN)_6]^{3-/4-}$, which could be attributed to increased permeability and decreased electrode passivation due to lower degree of tethering on the acrylate modified electrodes. Cryo-SEM visualization of the structural differences caused by cross-linking showed good agreement with the EIS results, whereas the degree of hydration of the hydrogels did not show any statistically significant differences.

Keywords: Impedance spectroscopy; Poly(2-hydroxyethyl methacrylate) hydrogel; Poly(ethylene glycol)-dimethacrylate cross-linking; Covalent hydrogel tethering; Cryo-SEM

1. INTRODUCTION

Since the pioneering work of Wichterle and Lim in 1960 [1], hydrogels, i.e. three dimensional cross-linked polymeric structures with an ability to imbibe large amounts of water, have attracted great attention due to their excellent biocompatibility. Hydrogels have been increasingly recognized as materials in a wide spectrum of biomedical applications ranging from tissue engineering [2] and drug delivery systems [3–9] to construction of contact lenses [10,11], biosensor devices [12–14] and biomimetic systems, where they can function as porous supports for lipid membranes [15–20] and lipo-polymersomes [21], as well as substrates mimicking cellular cytoskeleton [22] or extracellular matrix (ECM) [23,24].

Sensitivity of hydrogels to different physical and chemical factors, e.g., temperature, potential, electrolyte concentration, pH, and degree of hydration, make them excellent ”stimuli responsive” or ”smart” materials for construction of chemical sensors and biosensors [25]. Aside from utilization as a passive immobilization matrix, their swelling capacity can facilitate construction of responsive matrices dependent on environmental changes. Elastic modulus of different hydrogels is similar to that of living tissues, which in combination with their hydrophilicity makes them suitable for *in vivo* and *in vitro* applications [4]. Among the wide diversity of hydrogels, poly(2-hydroxyethyl methacrylate) (PHEMA) has emerged as one of the most widely researched, patented, and successfully commercialized materials [26]. Similarly, poly(ethylene glycol) (PEG) and its acrylate derivatives are widely utilized in biomedical applications due to their good biocompatibility and non-immunogenicity. Flexibility in PEG hydrogel formulation makes it a primary choice for constructing porous scaffolds similar to certain type of soft tissues [25]. Modified PEG macromers have been successfully utilized as mimic of ECM [23,24] for constructing biodegradable scaffolds for controlled drug release [3,4,7].

The performance of a hydrogel in a particular application is dependent on its molecular network structure usually characterized by several parameters, including polymer volume fraction in the swollen state, molecular weight of the polymer chain between two cross-linking points (cross-linking density) and the corresponding mesh size, which determines the maximum diameter of the molecules and ions that can pass through the hydrogel network [4]. Polymer volume fraction in the swollen state determines the amount of fluids that may be absorbed and retained by the hydrogel, which reaches equilibrium with its surroundings after polymerization. Swelling capacity of hydrogels is also exceptionally important since it determines *in vivo* and *in vitro* biocompatibility of hydrogel structures [4]. 2-hydroxyethyl methacrylate (HEMA) monomers may be readily copolymerized with other acrylate, methacrylate and acrylamide monomers including PEG derivatives [26], which may serve as cross-linkers. Copolymerized HEMA and poly(ethylene glycol)-dimethacrylate (PEG-DMA) monomers have found use in drug delivery systems [8,9], biosensor devices [12–14], and as solid support for stabilizing biomimetic lipid membranes [18–20] and lipo-polymersomes [21].

For electrochemical bioapplications of hydrogels, the passage of ions through the hydrogel layer as well as the hydrogel thickness and electrode geometry are key factors when designing an application [13]. Thorough electrochemical characterization of hydrogel coated electrodes is necessary for deep understanding of the hydrogel behavior in different applications. Electrochemical impedance spectroscopy (EIS) is widely applied to probe both resistive and capacitive properties of modified electrodes, applications ranging from characterization of porous [27] and hydrogel coated [13,17,20,28] electrodes to detection with a variety of biosensors [29]. Justin et al. reported on the EIS behavior of 6 μm thick PHEMA/PEGMA hydrogel films covalently immobilized on gold microdisc electrodes [13]. Yang et al. characterized complex 5 μm hydrogel covalently immobilized on various designs of interdigitated electrodes [28]. Kibrom et al. applied EIS to characterize 60 nm thick hydrogel

supported protein-tethered lipid bilayer membrane suitable for functional protein studies [17]. In our previous work, PHEMA hydrogel has been used as a support for black lipid membranes (thickness 500 μm) [18,20] and lipo-polymersomes (in combination with a polyethersulfone membrane) [21]. For such applications, the hydrogel was composed of 1:200 molar ratio of PEG-DMA/HEMA monomers. EIS was applied to characterize the influence of the covalently immobilized hydrogel on the electrode interface impedance [20,21].

EIS is a widely used technique in applications of biomimetic lipid membranes either directly on an electrode surface or on a supporting cushion layer (e.g. a hydrogel). Hence, a deeper understanding of the impedimetric behavior of hydrogels is important. Since many applications rely on usage of electrode microchips modified with a hydrogel, we present here a detailed EIS characterization of thick PHEMA hydrogels that were covalently tethered on the working electrodes. The study evaluated the influence of PEG-DMA cross-linking ratio (1:100, 1:200, 1:400) on mass and charge transfer behavior of electroactive species. To provide a simple and fast analysis of EIS results in hydrogel applications requiring a wide frequency range, we developed an equivalent circuit model that highlights the structural difference between the covalently tethered domain close to the electrode surface and the bulk hydrogel. The presented EIS characterization was correlated to the structural properties of hydrogels with different cross-linking ratios visualized using cryo-SEM as well as to their swelling capacity based on dry and wet weight determination.

2. EXPERIMENTAL

2.1 Chemicals

Poly(ethylene glycol)-dimethacrylate (PEG-DMA, Mw 1000 g/mol) was purchased from Polysciences, Inc. (Warrinngton, PA, USA). 2-hydroxyethyl methacrylate (HEMA), 1,4-butanedioldiacrylate (BDDA), ammonium persulfate (APS), N,N,N',N'-

tetramethylethylenediamine (TEMED), β-mertcaptoethanol, 3-(trimethoxysilyl propyl) methacrylate (TMS-PMA), 30% hydrogen peroxide, potassium hydroxide, acetic acid, potassium hexacyanoferrate(III) ($[Fe(CN)_6]^{3-}$), potassium hexacyanoferrate(II) ($[Fe(CN)_6]^{4-}$), and phosphate buffered saline (PBS; pH 7.4) were from Sigma-Aldrich Corporation (St. Louis, MO, USA). All aqueous solutions were prepared using ultrapure water (resistivity 18.2 MΩcm) from a Mili-Q® water purification system (Milipore Corporation, Bedford, MA, USA).

2.2 Fabrication and surface modification of electrode microchips

Electrode microchips (Fig. 1A), comprising three working electrodes (WE), one counter electrode (CE), one reference electrode (RE), leads and contact pads, were fabricated according to a previously published protocol through standard lithographic process using wet-oxidized 500 µm thick 4-inch silicon wafers (one side polished) [20]. The active electrode areas and contact pads on the patterned metal structures (10 nm Ti adhesion layer and 150 nm Au) were opened by reactive ion etching of the 500 nm thick silicon nitride passivation layer deposited through plasma-enhanced chemical vapor deposition. Prior to use, the microchips were cleaned for 10 min in a mixture of H_2O_2 (25% v/v) and KOH (50 mM) followed by a potential sweep from -200 mV to -1200 mV in 50 mM KOH [30] using the on-chip three electrode set-up. To obtain a proper adhesion between the hydrogel and the gold electrode microchips, these were chemically modified: To form a uniform layer of hydroxyl groups on the silicon nitride and exposed gold surfaces, the chips were treated with 3% (v/v) H_2O_2 (1 h) followed by β-mercaptoethanol modification (1 h in 200 mM aqueous solution). The hydroxyl groups were further functionalized by 1-h incubation in a 2 % (v/v) aqueous solution of TMS-PMA at pH 4 (adjusted using 1 M acetic acid) [20]. After each modification step, the microchips were rinsed thoroughly with water.

2.3 *In situ* hydrogel polymerization

Each silanized gold electrode microchip was placed in a Teflon mold (schematically shown in Fig. 1B) for *in situ* polymerization of hydrogel. The mold diameter (6 mm) defined the *in situ* polymerized hydrogel in such a way that the WEs were fully covered, whereas the CE and RE remained outside the hydrogel. The polymerization solution (diluted with water) contained PEG-DMA (30, 15, or 7.5 mM) and HEMA monomers (3 M) to obtain the molar ratios 1:100, 1:200, or 1:400, respectively, as well as BDDA (17 mM). Polymerization was induced by adding an aliquot of an aqueous solution containing the initiator (APS) and radical source (TEMED) to obtain the final concentrations of 27 mM and 33 mM, respectively. The resulting solution was thoroughly vortexed for 10 s, after which 28.3 µl were introduced on the microchip assembled in the mold to obtain 1 mm thick hydrogel disc covering the WEs (Fig. 1C).

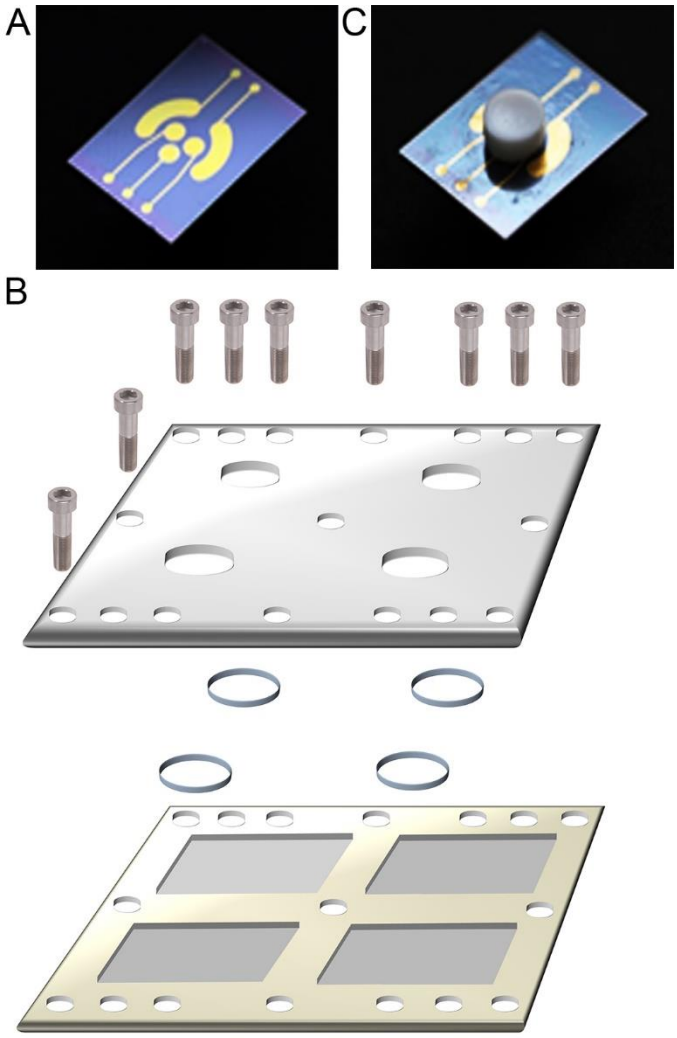

Figure 1. Electrode microchip and hydrogel polymerization setup: A) A photo of a gold electrode microchip comprising three circular working electrodes (WE, Ø 1.5 mm) placed in the center, and two larger electrodes used as counter (CE) and reference electrode (RE) during electrochemical characterization. The electrode structures, leads and contact pads were defined using a UV lithographic process followed by reactive ion etching to define the active electrode and contact pad areas in the 500 nm thick silicon nitride layer deposited through the plasma enhanced chemical vapor deposition. B) A schematic view of the Teflon mold used for hydrogel polymerization: a bottom plate with four recessions for placement the electrode chips; an upper plate with four openings (diameter: 6 mm; sealed using polydimethylsiloxane (PDMS) O-rings, blue) that define the structure of the polymerized hydrogels. The plates were assembled together using screws. C) A photo of an *in situ* polymerized covalently tethered hydrogel disk (thickness: 1 mm, diameter: 6 mm) on a gold electrode microchip. The hydrogel covered the three WEs and the surrounding silicon nitride passivation layer.

2.4 EIS characterization

The electrochemical cell for EIS characterization (Supplementary Material, Fig. S1) was filled with 300 µl of PBS containing 10 mM $([Fe(CN)_6]^{3-/4-}$ (1:1). The microchips were characterized after each step of chemical modification and hydrogel polymerization using the on-chip CE. The sinusoidal perturbation potential (10 mV_{rms}) was applied with respect to the open circuit potential in the frequency range between 100 mHz and 1 MHz. EIS analysis was performed using a computer controlled Reference 600 potentiostat from Gamry Instruments (Warminster, PA, USA) operated by EIS300 software (v. 6.10). Data analysis was done using EchemAnalyst software (v. 6.10) from Gamry Instruments by fitting the data to equivalent circuit models using nonlinear least-squares (NLLS) regression.

2.5 Cryo-SEM imaging

Cryo-SEM imaging was performed using an extended low-vacuum Quanta 200F FEG SEM (FEI Company, Hillsboro, OR, USA) with a Quorum PP2200 cryo-attachment (Quorum Technologies Ltd., East Sussex, UK). The samples were first cut into small pieces with a pair of scissors followed by mechanical fixing on an aluminum cryo-stub. Then, the samples were frozen by plunging them into nitrogen slush on the Quorum preparation bench and transferred to the cryo-preparation chamber, where they were freeze-fractured. The samples were not

coated. For imaging, each sample was transferred onto the cold stage in the SEM chamber and sublimated at -90 °C for 15 min prior to imaging. The imaging was performed at -140 °C using an Everhart-Thornley (ETD) detector with an electron beam accelerated to 2 keV and a spot size of 2 nm with a 30 μm mechanical aperture. Quantification of sample morphology was done by manual size measurements using Image J software.

2.6 Determination of the degree of hydration

The swelling capacity of the hydrogels with different molar ratios of PEG-DMA/HEMA monomers was determined as the degree of hydration based on the approach of Brahim et al. [31] using the equation Hydration% = $[(w_{wet} - w_{dry})/w_{wet}] \times 100\%$. The results are presented as average ± standard deviation, n = 4. The used hydrogel discs were polymerized on unmodified silicon nitride surfaces, from which they could be easily removed after polymerization. The dry weight determination was performed after overnight drying of the hydrogels in a convection oven at 50 °C, while the wet weight determination was done after overnight soaking in PBS. Prior to the wet weight determination, the excess of PBS was removed from the hydrogel discs by quick blotting with tissue paper.

3. RESULTS AND DISCUSION

Successful hydrogel modification of the microchips requires that the electrolyte, and hence, the electroactive species have access to the surface of the WEs only through the *in situ* polymerized hydrogel, i.e. no electrolyte flux should take place directly to the electrodes. We have previously demonstrated that this is achieved by covalent tethering of the hydrogel (primarily composed of PEG-DMA cross-linked PHEMA) on both gold WEs and the surrounding silicon nitride that have been chemically modified [20,21]. EIS characterization of the chemical modification steps is shown in the Supplementary Material Fig. S2.

3.1 Characterization of 1:200 cross-linked hydrogel (PEG-DMA/HEMA)

In our previous studies, cross-linking ratio (PEG-DMA/HEMA) 1:200 was used for applications with biomimetic lipid membranes [20] and and lipo-polymersomes (in combination with a polyethersulfone membrane) [21]. Hence, it is presented here as the standard hydrogel to compare the behavior of unconditioned and differently cross-linked hydrogels (PEG-DMA/HEMA – 1:100 and 1:400).

In the abovementioned hydrogel applications, EIS characterization was performed from 1 MHz down to 1 Hz and 100 mHz, respectively. When performing EIS characterization in such a wide frequency window using electrodes covered by a complex hydrogel matrix, it is crucial that the electric field generated by the applied sinusoidal potential fully penetrates the hydrogel at each of the frequencies. Otherwise, the recorded spectral features, requiring a detailed equivalent circuit model, may not be a representative description of the tethered hydrogel. We used COMSOL Multiphysics finite element (FE) simulations to evaluate the penetration of the electric field through a hydrogel matrix at different frequencies from 100 mHz to 1 MHz. Two different cases were modeled in COMSOL Multiphysics: 1) The hydrogel only covered the WE while the CE was outside the hydrogel (Fig. 2A-1; the case experimentally characterized in the presented work); 2) the hydrogel covered both the WE and CE (Fig. 2A-2). Fig. 2B and C show electric field line representation of the FE simulations for two frequencies, 100 mHz and 1 MHz, respectively. More detailed presentation of the electric field behavior is presented in the Supplementary Material Fig. S3. The obtained FE simulation results clearly indicate that in case 1 (only WE covered) majority of the electric field lines fully penetrated the hydrogel construct prior to reaching the CE. Incase 2, on the other hand, a significant portion of the electric filed lines passed from the WE to the CE inside the hydrogel construct never penetrating it. In conclusion, based on the performed FE simulations, the entire frequency range (from 1 MHz

down to 100 mHz) used in the experimental work presented here provides spectral information that is characteristic of the hydrogel behavior.

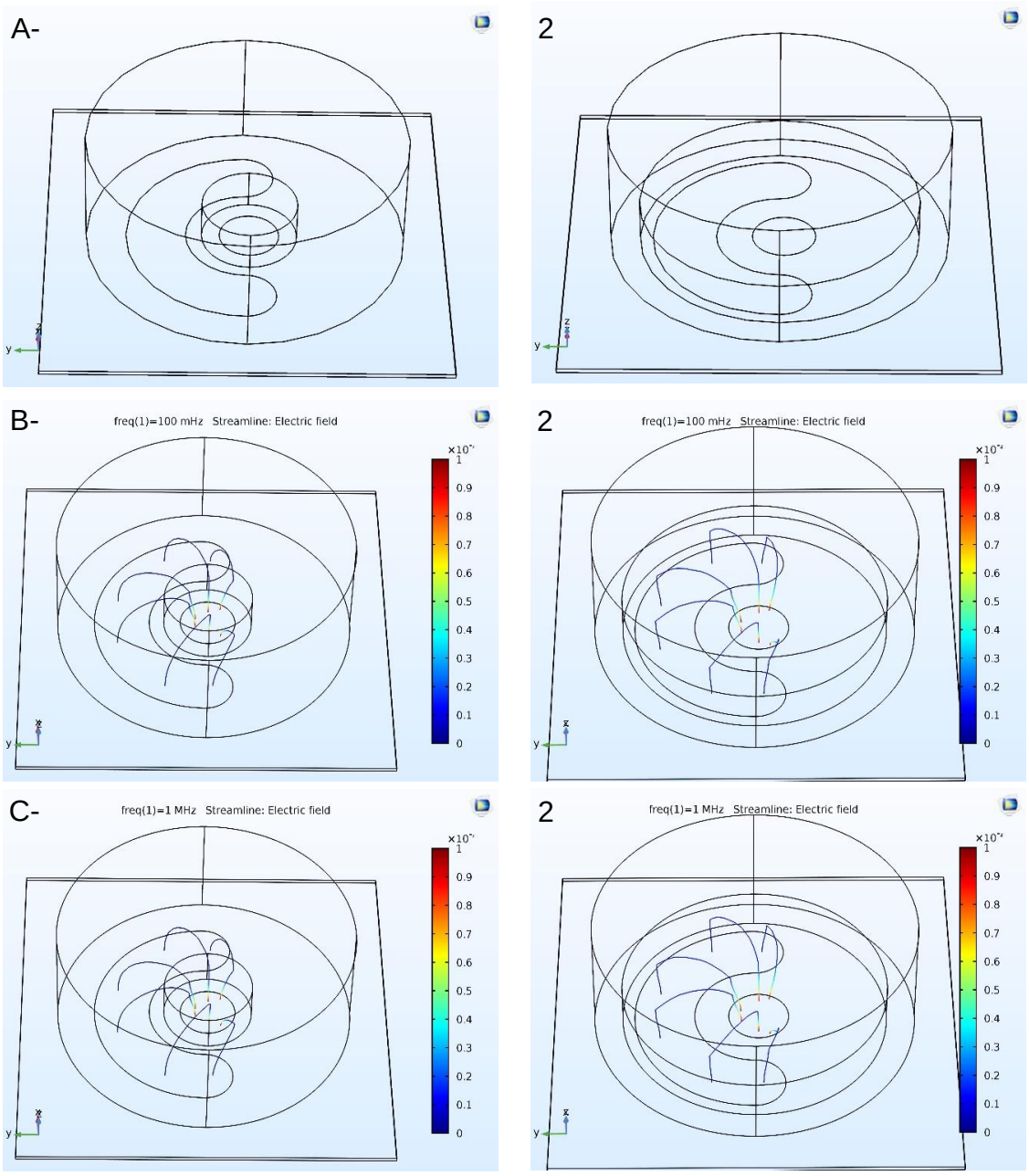

Figure 2. Finite element simulations using COMSOL Multiphysics: A) Schematic view of the used models (case 1 – hydrogel covers only the WE; case 2 – hydrogel covers both the WE and CE). Electric field streamline propagation between the WE and CE for B) 100 mHz and C) 1 MHz.

3.1.1 Behavior after electrolyte conditioning

Usually after polymerization, a hydrogel is conditioned in an electrolyte solution prior to electrochemical analysis in order to equilibrate the electrolyte composition in the bulk hydrogel [20,28]. During conditioning, a hydrogel reaches its maximal inherent swelling capacity, which contributes to its permeability to low molecular compounds [26]. Our preliminary tests indicated that at least 16-h conditioning was required to reach constant EIS behavior. Hence, EIS characterization of conditioned hydrogels was performed after 24 h.

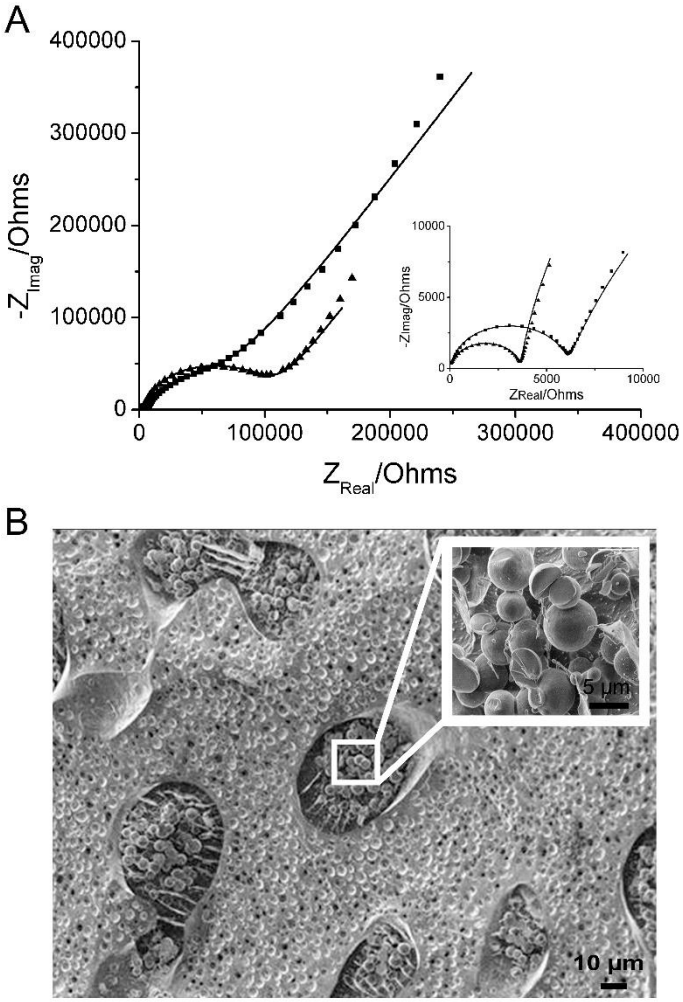

Figure 3. Characterization of 1:200 cross-linked hydrogels after conditioning: A) Two characteristic Nyquist plots (24-h conditioning in PBS containing 10 mM $[Fe(CN)_6]^{3-/4-}$). The EIS analysis was performed using the same electrolyte solution. The inset shows a magnified view of the high-frequency range of the Nyquist plots. The solid lines represent NLLS fit of the data to equivalent circuit model in Scheme 1. B) A characteristic cryo-SEM image. The hydrogel forms a compact porous matrix (round pores, 2 – 3 µm in diameter) engulfing large irregular pores (dimensions from less than 30 µm to almost 200 µm). The inset shows a magnified view of the interior of a large pore.

Fig. 3A shows two typical impedance spectra (presented as Nyquist plots) for 1 mm thick hydrogel. Each Nyquist plot consists of three characteristic parts: two semicircles (one in the high-frequency range and another in the intermediary frequency range) and a line in the low-frequency range. The semicircle in the high-frequency range is shown in the zoom-in view of the inset. Although the polymerization conditions were kept constant, the spectral features of several characterized hydrogel coated electrodes varied. These observed differences may result from the complexity of the formed porosity during the polymerization process shown in the cryo-SEM image of Fig 3B. The phenomenon is analogous to the behavior of porous electrodes, where varying pore geometry significantly influences the acquired impedance spectra [32]. Although these hydrogels are not conductive like porous electrodes, the covalent tethering makes them an integral part of the electrode interface impedance. Hence, a variety of randomly structured pores with different dimensions and distribution may contribute to the characteristic impedimetric behavior. In our previous application on PHEMA supported BLMs [20], we observed variation in the specific membrane capacitance and resistance of the BLMs. This could partially be attributed to the structural variation of polymerized PHEMA.

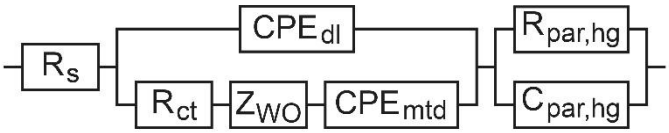

Scheme 1. Equivalent circuit model: R_S – solution resistance, CPE_{dl} – constant phase element (accounting for the double layer capacitance and electrode surface inhomogeneity), R_{ct} – charge transfer resistance, Z_{WO} – open boundary finite-length Warburg impedance, CPE_{mtd} – constant phase element (accounting for mass transfer deviation at low frequencies), $R_{par,hg}$ and $C_{par,hg}$ – the resistance and capacitance of the bulk hydrogel, respectively.

The solid lines in Fig. 3A indicate NLLS fitting of the data to the equivalent circuit model shown in Scheme 1. The semicircle in the high-frequency range is represented by the additional time constant (parallel element $R_{par,hg}$ and $C_{par,hg}$). Based on the observation of such a semicircle in previous studies on hydrogel coated electrodes and ultrafiltration membranes, it has been assigned to the capacitive and resistive properties of the bulk material, allowing modelling as a

parallel RC element [17,20,28,33]. A high-frequency semicircle has also been modelled using a capacitor in parallel with the rest of the equivalent circuit, described as a geometric capacitance (C_g) [34]. It has been attributed to different system/material properties depending on the scope of the presented application, e.g., membrane capacitance [35], coating capacitance for conducting polymer tube modification [36], and capacitance of interdigitated electrodes [37]. However, based on our evaluation, the high-frequency semicircle in spectra for thick hydrogels on WEs could not be described by C_g. Performed EIS simulations using C_g in the equivalent circuit generated spectra with an incomplete semicircle.

The semicircle and line in the intermediary and low-frequency range are characteristic of the behavior described by Randles equivalent circuit [38]. The slightly recessed semicircle could be represented by a resistor and constant phase element (CPE) in parallel. This corresponds to the interface impedance of the underlying gold electrode, accounting for faradaic processes of the electroactive probe (charge transfer resistance, R_{ct}) as well as double layer capacitance and surface inhomogeneity (CPE_{dl}). The slope of the low-frequency line is clearly greater than 45°, which is known as the characteristic feature of the semi-infinite diffusion impedance (Warburg impedance element, Z_W, see Supplementary material S4 for the mathematical description) describing the behavior of an electrode-electrolyte interface where the diffusion layer thickness is not limited. Using Z_W complete fitting was obtained only down to frequencies between 1 and 10 Hz (Supplementary material Fig. S5A). Although the presented frequency range may be narrowed in many applications in order to facilitate fitting using a simple equivalent circuit model, it would not be plausible in the case of the spectra acquired for thick hydrogels since truncation of the spectra would eliminate the entire line corresponding to the diffusion impedance. Moreover, considering applications relying on EIS detection, such as monitoring of valinomycin in hydrogel supported lipid bilayers requiring spectral analysis down to 1 Hz

[20], it is necessary to achieve a detailed understanding of the impedimetric behavior of hydrogels down to low frequencies.

Studies on, e.g., polymer-coated electrodes and ion exchange or ion-selective membranes, have warranted description of the low-frequency impedimetric behavior using finite diffusion layer models [39,40]. The two known cases are the open-boundary (O element, Z_{WO}) and blocked-boundary (T element, Z_{WT}) finite-length Warburg impedance (see Supplementary material S4 for the mathematical description). In both cases, the initial slope of the Warburg line is 45°. At a low-frequency inflection point, Z_{WO} bends toward the Z_{Real} axis, whereas Z_{WT} turns into a 90° capacitive line (see schematic illustration in Supplementary material S4). The low-frequency behavior of the Nyquist plots in Fig. 3A is intermediary between that of W_O and W_T. Similar spectral behavior has been theoretically analyzed by Bisquert et al. [39], indicating the need of a CPE to describe the impedimetric behavior in the lowest end of the frequency range. As shown by the NLLS fitting in Fig. 3A, the series combination of Z_{WO} and CPE_{mtd}, accounting for very low-frequency mass transfer deviation from the pure Z_{WO} behavior, provides a good description of the impedimetric behavior down to the lowest frequency end (the range for different parameter values obtained by analyzing several hydrogel samples is shown in Table 1). Fitting of the Nyquist plots using an equivalent circuit having Z_{WO} alone (Supplementary material Fig. S5B) only gives a marginally better result than using Z_W alone (Fig. S5A). Although Z_{WO} could not alone describe the behavior of the data, its significance as the Warburg element for finite diffusion layer behavior was demonstrated by using an equivalent circuit with Z_{WT} (instead of Z_{WO}) in combination with CPE_{mtd}. The result indicated that in the lowest end of the frequency range the slope of the generated Warburg line was consistently higher than shown by the data (Fig. S5C).

Table 1. Typical ranges for the EIS parameters obtained based on NLLS fit of impedance spectra acquired for several 1 mm thick HEMA hydrogels cross-linked with PEG-DMA in ratios 1:100, 1:200, and 1:400. (Details of the used EIS parameters can be found in the text and Supporting material S3.)

EIS parameters	**Cross-linking ratio - (PEG-DMA:HEMA)**			
	After polymerization	**24 h after conditioning in PBS containing electro-active probe $[Fe(CN)_6]^{3-/4-}$**		
	1:200 [(a)]		**1:400** [(a)]	**1:100** [(a)]
R_s/Ω [(b)]	225	225	225	225
Q_{dl}/nSs^{α} [(c)]	180 - 270	270 - 475	235 - 280	340 - 1125
α_{dl} [(c)]	0.920 - 0.945	0.820 - 0.920	0.880 - 0.910	0.740 - 0.820
$R_{ct}/k\Omega$	nd[e]	85 - 105	435 - 470	0.9 - 16
$Y_{WO}/\mu Ss^{½}$ [(d)]	nd[e]	8.3 – 11.6	0.9 - 2	16 - 49
$B_{WO}/s^{½}$ [(d)]	nd[e]	0.03 – 0.2	0.9 - 1.6	0.06 - 2.4
$R_{par,hg}/k\Omega$	3.4 - 3.5	3.5 - 5.8	1 - 1.7	0.20 - 0.23
$C_{par,hg}/pF$	520 - 535	430 - 500	580 - 600	720 - 880
$Q_{mtd}/\mu Ss^{\alpha}$ [(c)]	n/a[f]	2.9 - 11	n/a[f]	245 - 430
α_{mtd} [(c)]	n/a[f]	0.66 - 0.68	n/a[f]	0.31 - 0.54

[(a)] Equivalent circuits for NLLS analysis: conditioned 1:200 and 1:100 cross-linked hydrogels (Scheme 1); 1:200 cross-linked hydrogels after polymerization and 1:400 cross-linked conditioned hydrogels (the same as in Scheme 1 without CPE_{mtd})
[(b)] The average value of R_s (also comprising possible contact resistance) obtained in several tests
[(c)] Q – magnitude of CPE impedance expressed as admittance (Supplementary material S4); α – exponent acquiring values between 0 and 1 (Q_{dl} and Q_{mtd} correspond to CPE_{dl} and CPE_{mtd} in the equivalent circuit model of Scheme 1)
[(d)] Y_{WO} – magnitude of Z_{WO} impedance expressed as admittance (Supplementary material S4); B_{WO} – characteristic time constant
[(e)] nd - not defined during NLLS regression analysis
[(f)] n/a - not applicable due to the choice of equivalent circuit model

The requirement of two components to describe the mass transfer behavior of thick covalently tethered hydrogels can be plausibly explained by considering a hydrogel as a porous membrane of two structural domains with different mobility of ions. The upper domain, i.e. the bulk of the hydrogel, is interfaced on one side to the bulk electrolyte and on the other side to a more densely packed hydrogel (the lower domain) covalently tethered to the microchip. The denser structure

of the covalently tethered domain originates from the HEMA monomers coupled to the acrylate functionalities on the chip surfaces making the hydrogel less flexible to swell than the bulk hydrogel. The membrane potential of porous membranes comprises Donnan potentials, arising from separation of ions according to their charges, and a diffusion potential due to differences in ion mobility [33]. Considering ionic dimensions, cross-linked PHEMA hydrogels are highly porous, only causing a partial Donnan exclusion due to the increased electron density of the oxygen functionalities. Hence, the diffusion potential may be the predominating as the contribution to mass transfer impedance. In the case presented here, the diffusion potential originates from the two structurally different domains, clearly requiring the combination of two components in the equivalent circuit model, which is analogous to two-layer polymer films on electrodes presented by Freger [40]. To test the validity of these conclusions, further studies using both functionalized hydrogels and electroactive probes both having different charges are required. The assumption that covalent tethering creates a dense hydrogel domain on an electrode has to be confirmed using hydrogel disks that are interfaced as a partition between two aqueous compartments [18,41].

3.1.2 Behavior immediately after polymerization

Fig. 4 shows a typical Nyquist plot for a hydrogel immediately after polymerization. The semicircle in the high-frequency range (inset of Fig. 4) is indicative of the resistive and capacitive behavior of the bulk hydrogel. No semicircle is observed in the intermediary frequency range. The NLLS analysis of the data was done using an equivalent circuit without CPE_{mtd}. The determined parameters are summarized in Table 1. The results indicate that the impedimetric behavior of hydrogels immediately after polymerization is primarily capacitive. The magnitude of CPE_{dl} was on average lower than for hydrogels after conditioning in electrolyte and the exponent of CPE_{dl} (α) approached 1, which is similar to the behavior of a chemical modification leading to decreased double layer capacitance [30]. R_{ct} and Z_{WO} could

not be determined at all. The fact that CPE_{mtd} was not required for curve fitting may be explained by the fact that the covalently tethered hydrogel domain was structurally similar to the bulk when hydration was not complete. Although after polymerization the hydrogels show significantly retarded permeability to electroactive species, the resistance of the bulk hydrogel ($R_{par,hg}$) was comparable to the one obtained after conditioning.

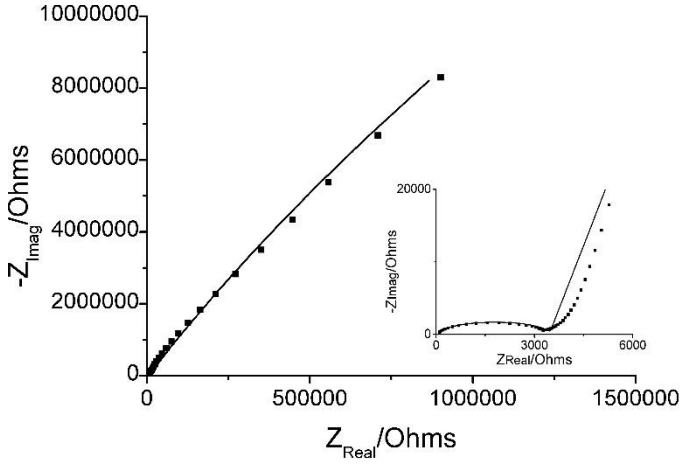

Figure 4. Characterization of 1:200 cross-linked hydrogel after polymerization: A characteristic Nyquist plot (immediately after polymerization). The EIS analysis was performed using PBS containing 10 mM $[Fe(CN)_6]^{3-/4-}$. The inset shows a magnified view of the high-frequency range of the Nyquist plot. The solid line represents NLLS fit of the data. The used equivalent circuit model was otherwise the same as in Scheme 1 except without CPE_{mtd}.

3.2 Characterization of conditioned hydrogels – effect of cross-linking

Usually higher cross-linking ratio in a hydrogel creates a more compact structure, i.e. lower swelling capacity. However, hydrophilic high-molecular weight cross-linkers, such as PEG, may introduce an opposite effect, increasing the swelling capacity due to the longer cross-links that make the polymer network more flexible [7]. To provide a clear comparison with the properties of the standard hydrogel described in section 3.1, we characterized polymers having a cross-linking ratio that was one half of (1:400) and twice as high (1:100) as the standard hydrogel.

Fig. 5A shows a characteristic Nyquist plot acquired for a hydrogel with cross-linking ratio 1:400. The inset shows a magnification of the high-frequency range. As in the case of the

standard hydrogel, two semicircles can be seen, one in the high-frequency range (capacitive and resistive properties of the hydrogel) and another weakly defined one at the intermediate frequencies (R_{ct} and double layer capacitance). A cryo-SEM image of the same hydrogel is shown in Fig. 5B. The shown curve fitting was based on an equivalent circuit without CPE_{mtd} (summary in Table 1). Generally, the observed ranges based on characterization of several hydrogels were clearly narrower than in the case of the standard hydrogel. This can be attributed to the uniformity of the microscopic features and compactness of the formed hydrogels as seen in Fig. 5B.

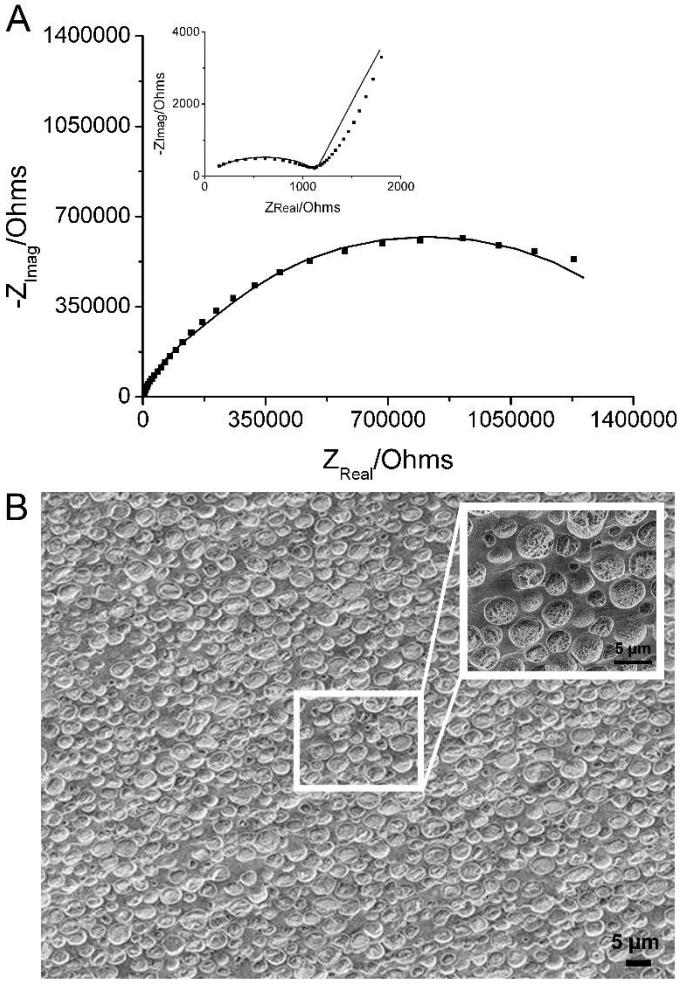

Figure 5. Characterization of 1:400 cross-linked hydrogel after conditioning: A characteristic Nyquist plot (24-h conditioning in PBS containing 10 mM $[Fe(CN)_6]^{3-/4-}$). The EIS analysis was performed using the same electrolyte solution. The solid line represents NLLS fit of the data. The equivalent circuit model was otherwise the same as in Scheme 1 except without CPE_{mtd}. B) A cryo-SEM image of the hydrogel. The inset shows a magnified view of the uniformly spread oval-shaped pores (minor axis: 1.5 – 3.5 µm; major axis: 2 – 4.5 µm).

The seen compactness and structural uniformity can also plausibly explain the fact that CPE_{mtd} was not needed. The compact bulk and covalently tethered domain may be structurally comparable. This entails that due to the decreased fraction of the long-chained highly hydrophilic PEG-DMA cross-linker the HEMA monomers determine the resulting structure, making the hydrogel more uniform and compact. Consequently, it leads to more limited (increased W_O impedance) but uniform (no CPE_{mtd}) mass transfer in the bulk hydrogel to the electrode-hydrogel interface. R_{ct} increased significantly in comparison with the standard hydrogel. A major contribution to this increase may be attributed to hydrogel tethering on the electrode surface, which upon decreasing the PEG-DMA fraction increases the density of covalently immobilized HEMA monomers on the acrylate functionalized electrode. This, on the other hand, decreases the active electrode area and the apparent standard rate constant of the redox process of the electroactive probe [30], which are inversely proportional to R_{ct}.

Fig. 6A shows a characteristic Nyquist plot for a hydrogel with cross-linking ratio 1:100. As shown in the inset, even in this case a second semicircle, albeit only partially formed, can be seen in the high-frequency range. The shown NLLS analysis required the equivalent circuit shown in Scheme 1 including CPE_{mtd} (summarized in Table 1). The fact that the analysis of 1:100 and 1:200 cross-linked hydrogels required CPE_{mtd}, whereas in the case of 1:400 cross-linked hydrogels it was not necessary, leads to the conclusion that the covalent tethering on the microchip surface causes more significant mass transfer difference when the permeability of the bulk hydrogel increases. In comparison with the standard hydrogel, the impedimetric behavior indicates increased mass transfer to the electrode-hydrogel interface (decreased Z_{WO} impedance), decreased bulk resistance ($R_{par,hg}$), and decreased R_{ct}. This is in accordance with the expected behavior due to the increased fraction of the high-molecular weight cross-linker. A cryo-SEM image of the same hydrogel is shown in Fig. 6B. Considering the size distribution of the pores, the impedimetric behavior is apparently contradictory. The pore dimensions are

smaller than in the less cross-linked hydrogels while the mass transfer is increased. On the other hand, comparison between this hydrogel and the one in Fig. 5B points out one significant difference aside from the determined pore size distributions. The pores of the hydrogel in Fig. 6B appear to be deeper than the ones in Fig 5B, which may be an indication of greater interconnectivity of the pores throughout the bulk hydrogel.

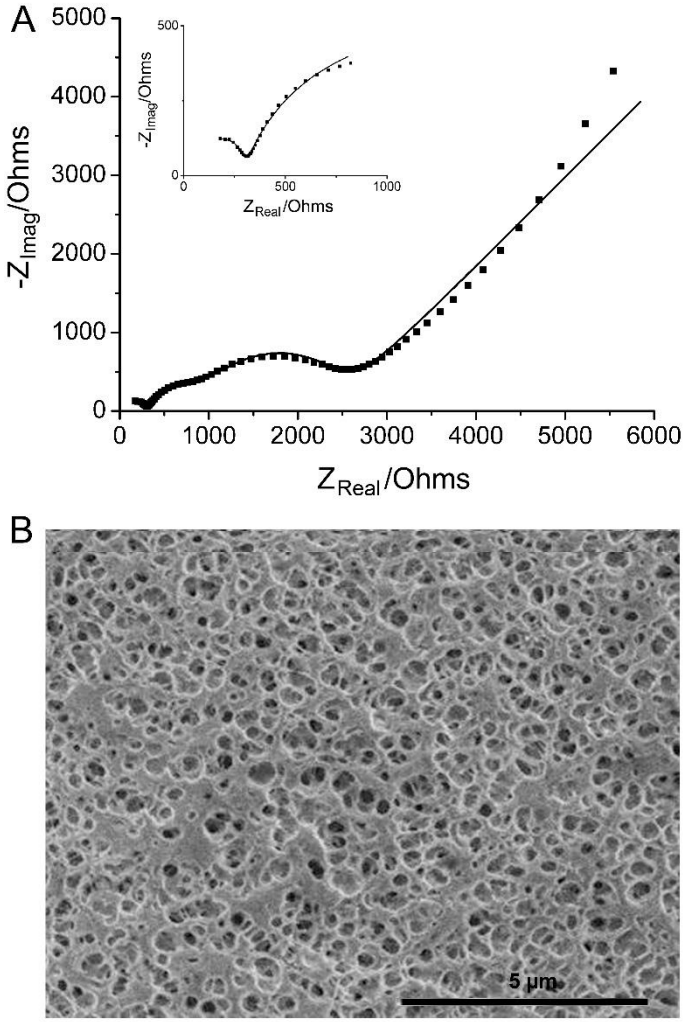

Figure 6. Characterization of 1:100 cross-linked hydrogel after conditioning: A characteristic Nyquist plot acquired after 24-h conditioning in PBS containing $[Fe(CN)_6]^{3-/4-}$ (10 mM). The EIS analysis was performed using the same electrolyte solution. The inset shows a magnified view of the high-frequency range of the Nyquist plot. The solid line represents NLLS fit of the data to equivalent circuit model in Scheme 1. B) A cryo-SEM image of the hydrogel. The pores are nearly circular (diameters: 200 – 500 nm).

Although cryo-SEM does not show the structure of hydrated hydrogels, it provides a qualitative understanding of the structural differences. To confirm the presented findings, pore

interconnectivity in cross-linked hydrogels will be studied using a two-chamber system with dividing hydrogel membrane [18,41] and the EIS method proposed by Canali et al. [42] that relies on the effect of porosity on the apparent solution resistance. Such a study, using externally placed electrodes, will also allow further evaluation of electric field penetration, which may cause a limitation in sensitivity when using coplanar on-chip electrodes.

The degree of hydration (calculated as described in section 2.6) of hydrogels with 1:100, 1:200 and 1:400 molar ratio of PEG-DMA and HEMA monomers was 50 ± 1 %, 49 ± 2 % and 50 ± 6 % (average ± standard deviation, n = 4), respectively, after 24-h hydration that was comparable to the conditioning performed prior to EIS measurements. Based on two-tailed student's t-test, the degree of hydration of the hydrogels was not significantly different (5 % level; details in the Supplementary Material S6). Considering this result and the impedimetric behavior of the differently cross-linked covalently tethered hydrogels, as presented above, it is clear that although the varying cross-linking ratio does not significantly change the swelling capacity, it drastically influences mass transfer, active electrode area, and electrode performance due to changes in the micro- and nanoenvironment at the electrode-hydrogel interface. Further studies on the state of bound water in hydrated hydrogels using, for instance differential scanning calorimetry [43], may provide possibility for more detailed correlation with EIS characterization.

4. CONCLUSION

To provide a deeper understanding on how cross-linking influences the impedimetric behavior of thick hydrogels in a wide frequency range, we performed a thorough EIS characterization of biocompatible hydrogels composed of poly(2-hydroxyethyl methacrylate) (PHEMA) cross-linked with hydrophilic high molecular weight poly(ethylene glycol)dimethacrylate (PEG-DMA). The studied hydrogels were covalently tethered on working electrode surfaces. The

obtained results demonstrated that an increased PEG-DMA/HEMA ratio (1:400 – 1:200 – 1:100) enhanced permeability. When using $[Fe(CN)_6]^{3-/4-}$ as the electroactive probe, the increased cross-linking ratio significantly decreased the charge transfer resistance due to both increased mass transfer and less dense tethering on the electrode surface modified with methacrylate moieties. Equivalent circuit modeling showed that covalently tethered thick hydrogels required an open-boundary finite-length Warburg element (Z_{WO}) to describe the mass transfer behavior. Increased cross-linking ratio was also shown to cause a difference in mass transfer at the electrode-hydrogel interface in comparison with the bulk hydrogel, requiring an additional constant phase element in series with Z_{WO} to describe the mass transfer deviation in the lowest frequency range. Cryo-SEM imaging indicated that the formed porosity was highly dependent on the cross-linking ratio and provided a good correlation with the EIS results. On the other hand, degree of hydration of the differently cross-linked hydrogels did not show any statistically significant differences. The presented study and the proposed equivalent circuit model provide a possibility for fast data analysis in applications relying on hydrogel modified electrodes. The results can serve as a basis for further studies of diverse functionalized hydrogel systems using, e.g., transmission line modeling as well as finite element simulations to determine detection sensitivity in on-chip applications using, for instance, membrane protein carrying lipid bilayers.

5. ACKNOWLEDGMENTS

This work was financially supported by the Copenhagen Research School of Nanotechnology (CONT) from Denmark, Department of Micro- and Nanotechnology at Technical University of Denmark and a cleantech company Aquaporin A/S in Copenhagen, Denmark.

References

[1] O. Wichterle, D. Lim, Hydrophilic Gels for Biological Use, Nature. 185 (1960) 117–118.

[2] J.L. Drury, D.J. Mooney, Hydrogels for tissue engineering: scaffold design variables and applications, Biomaterials. 24 (2003) 4337–4351. https://doi.org/10.1016/S0142-9612(03)00340-5.

[3] X. Zhao, M.J. Harris, Novel Degradable Poly(ethylene glycol) Hydrogels for Controlled Release of Protein, J. Pharm. Sci. 87 (1998) 1450–1458.

[4] N.A. Peppas, P. Bures, W. Leobandung, H. Ichikawa, Hydrogels in pharmaceutical formulations, Eur. J. Pharm. Biopharm. 50 (2000) 27–46.

[5] K. Nam, J. Watanabe, K. Ishihara, Modeling of swelling and drug release behavior of spontaneously forming hydrogels composed of phospholipid polymers., Int. J. Pharm. 275 (2004) 259–69. https://doi.org/10.1016/j.ijpharm.2004.02.009.

[6] G.W. Bos, J.J.L. Jacobs, J.W. Koten, S. Van Tomme, T. Veldhuis, C.F. van Nostrum, W. Den Otter, W.E. Hennink, In situ crosslinked biodegradable hydrogels loaded with IL-2 are effective tools for local IL-2 therapy., Eur. J. Pharm. Sci. 21 (2004) 561–7. https://doi.org/10.1016/j.ejps.2003.12.007.

[7] J.A. DiRamio, W.S. Kisaalita, G.F. Majetich, J.M. Shimkus, Poly(ethylene glycol) methacrylate/dimethacrylate hydrogels for controlled release of hydrophobic drugs., Biotechnol. Prog. 21 (2005) 1281–1288. https://doi.org/10.1021/bp0495670.

[8] J. Bako, M. Szepesi, A.J. Veres, C. Cserhati, Z.M. Borbely, C. Hegedus, J. Borbely, Synthesis of biocompatible nanocomposite hydrogels as a local drug delivery system, Colloid Polym. Sci. 286 (2007) 357–363. https://doi.org/10.1007/s00396-007-1793-7.

[9] S.N. Dobić, J.M. Filipović, S.L. Tomić, Synthesis and characterization of poly(2-hydroxyethyl methacrylate/itaconic acid/poly(ethylene glycol) dimethacrylate) hydrogels, Chem. Eng. J. 179 (2012) 372–380.

https://doi.org/10.1016/j.cej.2011.10.083.

[10] C.C.S. Karlgard, N.S. Wong, L.W. Jones, C. Moresoli, In vitro uptake and release studies of ocular pharmaceutical agents by silicon-containing and p-HEMA hydrogel contact lens materials, Int. J. Pharm. 257 (2003) 141–151. https://doi.org/10.1016/S0378-5173(03)00124-8.

[11] X. Hu, L. Hao, H. Wang, X. Yang, G. Zhang, G. Wang, X. Zhang, Hydrogel Contact Lens for Extended Delivery of Ophthalmic Drugs, Int. J. Polym. Sci. 2011 (2011) 814163 (9 pages). https://doi.org/10.1155/2011/814163.

[12] O. Andersson, A. Larsson, T. Ekblad, B. Liedberg, Gradient hydrogel matrix for microarray and biosensor applications: an imaging SPR study., Biomacromolecules. 10 (2009) 142–8. https://doi.org/10.1021/bm801029b.

[13] G. Justin, S. Finley, A.R. Abdur Rahman, A. Guiseppi-Elie, Biomimetic hydrogels for biosensor implant biocompatibility: electrochemical characterization using micro-disc electrode arrays (MDEAs)., Biomed. Microdevices. 11 (2009) 103–115. https://doi.org/10.1007/s10544-008-9214-3.

[14] A. Mateescu, Y. Wang, J. Dostalek, U. Jonas, Thin hydrogel films for optical biosensor applications., Membranes (Basel). 2 (2012) 40–69. https://doi.org/10.3390/membranes2010040.

[15] T.-J. Jeon, N. Malmstadt, J.J. Schmidt, Hydrogel-encapsulated lipid membranes., J. Am. Chem. Soc. 128 (2006) 42–43. https://doi.org/10.1021/ja056901v.

[16] T.-J. Jeon, N. Malmstadt, J.L. Poulos, J.J. Schmidt, Black lipid membranes stabilized through substrate conjugation to a hydrogel, Biointerphases. 3 (2008) FA96–FA100. https://doi.org/10.1116/1.2948314.

[17] A. Kibrom, R.F. Roskamp, U. Jonas, B. Menges, W. Knoll, H. Paulsen, R.L.C. Naumann, Hydrogel-supported protein-tethered bilayer lipid membranes: a new approach toward polymer-supported lipid membranes, Soft Matter. 7 (2011) 237–246.

https://doi.org/10.1039/c0sm00618a.

[18] M. Roerdink Lander, S. Ibragimova, C. Rein, J. Vogel, K. Stibius, O. Geschke, M. Perry, C. Hélix-Nielsen, Biomimetic membrane arrays on cast hydrogel supports., Langmuir. 27 (2011) 7002–7007. https://doi.org/10.1021/la1050699.

[19] S. Ibragimova, K. Stibius, P. Szewczykowski, M. Perry, H. Bohr, C. Hélix-Nielsen, Hydrogels for in situ encapsulation of biomimetic membrane arrays, Polym. Adv. Technol. 23 (2012) 182–189. https://doi.org/10.1002/pat.1850.

[20] A. Mech-Dorosz, A. Heiskanen, S. Bäckström, M. Perry, H.B. Muhammad, C. Hélix-Nielsen, J. Emnéus, A reusable device for electrochemical applications of hydrogel supported black lipid membranes, Biomed. Microdevices. 17 (2014) DOI 10.1007/s10544-015-9936-y.

[21] A. Mech-Dorosz, N. Bajraktari, C. Hélix-Nielsen, J. Emnéus, A. Heiskanen, Stationary photocurrent generation from bacteriorhodopsin-loaded lipo-polymersomes in polyelectrolyte multilayer assembly on polyethersulfone membrane, Anal. Bioanal. Chem. doi.org/10 (2020). https://doi.org/10.1007/s00216-020-02533-8.

[22] M. Kühner, R. Tampé, E. Sackmann, Lipid mono- and bilayer supported on polymer films: composite polymer-lipid films on solid substrates., Biophys. J. 67 (1994) 217–26. https://doi.org/10.1016/S0006-3495(94)80472-2.

[23] G.P. Raeber, M.P. Lutolf, J.A. Hubbell, Molecularly engineered PEG hydrogels: a novel model system for proteolytically mediated cell migration., Biophys. J. 89 (2005) 1374–1388. https://doi.org/10.1529/biophysj.104.050682.

[24] J. Zhu, Bioactive modification of poly(ethylene glycol) hydrogels for tissue engineering., Biomaterials. 31 (2010) 4639–4656. https://doi.org/10.1016/j.biomaterials.2010.02.044.

[25] G.A. Urban, T. Weiss, Hydrogels for Biosensors, in: G. Gerlach, K.-F. Arndt (Eds.), Hydrogel Sensors and Actuators, Springer, Heidelberg, 2009.

[26] A. Guiseppi-Elie, Electroconductive hydrogels: synthesis, characterization and biomedical applications., Biomaterials. 31 (2010) 2701–2716. https://doi.org/10.1016/j.biomaterials.2009.12.052.

[27] J. Bisquert, G. Garcia-Belmonte, F. Fabregat-Santiago, A. Compte, Anomalous transport effects in the impedance of porous film electrodes, Electrochem. Commun. 1 (1999) 429–435.

[28] L. Yang, A. Guiseppi-Wilson, A. Guiseppi-Elie, Design considerations in the use of interdigitated microsensor electrode arrays (IMEs) for impedimetric characterization of biomimetic hydrogels., Biomed. Microdevices. 13 (2011) 279–89. https://doi.org/10.1007/s10544-010-9492-4.

[29] J.-G. Guan, Y.-Q. Miao, Q.-J. Zhang, Impedimetric Biosensors, J. Biosci. Bioeng. 97 (2004) 219–226. https://doi.org/10.1263/jbb.97.219.

[30] A.R. Heiskanen, C.F. Spégel, N. Kostesha, T. Ruzgas, J. Emnéus, Monitoring of Saccharomyces cereviisiae cell proliferation on thiol-modified planar gold microelectrodes using impedance spectroscopy, Langmuir. 24 (2008) 9066–9073.

[31] S. Brahim, D. Narinesingh, A. Guiseppi-Elie, Synthesis and hydration properties of pH-sensitive p(HEMA)-based hydrogels containing 3-(trimethoxysilyl)propyl methacrylate, Biomacromolecules. 4 (2003) 497–503. https://doi.org/10.1021/bm020080u.

[32] H. Keiser, K.D. Beccu, M.A. Gutjahr, Abschätzung der porenstruktur poröser elektroden aus impedanzmessungen, Electrochim. Acta. 21 (1976) 539–543. https://doi.org/10.1016/0013-4686(76)85147-X.

[33] J. Benavente, Electrical Characterization of Membranes, in: C. Güell, M. Ferrando, F. López (Eds.), Monit. Vis. Membr. Process., 2nd ed., WILEY-VCH Verlag GmbH & Co. KGaA, Weinheim, 2009: pp. 177–207.

[34] J.R. MacDonald, W.B. Johnson, Fundamental impedance spectroscopy, in: E.B.

Barsoukov, J.R. MacDonald (Eds.), Impedance Spectrosc. Theory, Exp. Appl., 2nd ed., John Wiley & Sons, Inc., Hoboken, 2005: pp. 1–26.

[35] R. de Levie, D. Vukadin, Dipicrylamine transport across an ultrathin phosphatidylethanolamine membrane, J. Electroanal. Chem. 62 (1975) 95–109. https://doi.org/10.1016/0022-0728(75)80029-5.

[36] M.R. Abidian, D.C. Martin, Experimental and theoretical characterization of implantable neural microelectrodes modified with conducting polymer nanotubes, Biomaterials. 29 (2008) 1273–1283. https://doi.org/10.1016/j.biomaterials.2007.11.022.

[37] Á. Rodríguez, E. Valera, J. Ramón-Azcón, F.J. Sanchez, M.P. Marco, L.M. Castañer, Single frequency impedimetric immunosensor for atrazine detection, Sensors Actuators, B Chem. 129 (2008) 921–928. https://doi.org/10.1016/j.snb.2007.10.003.

[38] J.E.B. Randles, Kinetics of rapid electrode reactions, Discuss. Faraday Soc. 1 (1947) 11–19.

[39] J. Bisquert, G. Garcia-Belmonte, F. Fabregat-Santiago, P.R. Bueno, Theoretical models for ac impedance of finite diffusion layers exhibiting low frequency dispersion, J. Electroanal. Chem. 475 (1999) 152–163. https://doi.org/10.1016/S0022-0728(99)00346-0.

[40] V. Freger, Diffusion impedance and equivalent circuit of a multilayer film, Electrochem. Commun. 7 (2005) 957–961. https://doi.org/10.1016/j.elecom.2005.06.020.

[41] L. Peláez, V. Romero, S. Escalera, S. Ibragimova, K. Stibius, J. Benavente, C. Hélix-Nielsen, Electrochemical characterization of hydrogels for biomimetic applications, Polym. Adv. Technol. 22 (2011) 1381–1388. https://doi.org/10.1002/pat.2028.

[42] C. Canali, S. Mohanty, A. Heiskanen, H.B. Muhammad, Ø.G. Martinsen, M. Dufva, A. Wolff, J. Emnéus, Impedance spectroscopic characterisation of porosity in 3D cell

culture scaffolds with different channel networks, Electroanalysis. 27 (2015) 193–199. https://doi.org/10.1002/elan.201400413.

[43] C.N. Kotanen, D.R. Janagam, R. Idziak, L. Rhym, R. Sullivan, A.M. Wilson, T.L. Lowe, A. Guiseppi-Elie, Partitioning of coomassie brilliant blue into DMAEMA containing poly(HEMA)-based hydrogels, Eur. Polym. J. 72 (2015) 438–450. https://doi.org/10.1016/j.eurpolymj.2015.07.035.

SUPPLEMENTARY MATERIAL

Impedance characterization of biocompatible hydrogel suitable for biomimetic lipid membrane applications

Agnieszka Mech-Dorosz[1,2], Muhammad Salman Khan[1], Ramona Valentina Mateiu[3], Claus Hélix-Nielsen[4,5], Jenny Emnéus[1], Arto Heiskanen[1,*]

[1]Technical University of Denmark, Department of Biotechnology and Biomedicine, Produktionstorvet, Building 423, DK-2800 Kgs. Lyngby, Denmark

[2]Present address: Novo Nordisk A/S, Brennum Park 24 K, 3400 Hillerød, Denmark

[3]Technical University of Denmark, Center for Electron Nanoscopy, Fysikvej, Building 307, 2800 Kgs. Lyngby, Denmark

[4]Technical University of Denmark, Department of Environmental Engineering, Bygningstorvet, Building 115, DK-2800 Kgs. Lyngby, Denmark

[5]Aquaporin A/S, Nymøllevej 78, DK-2800 Kgs. Lyngby, Denmark

*Corresponding Author

Phone: +45-45-256839

e-mail: arhe@dtu.dk

Content

S1 Electrochemical cell for characterization of electrode modifications

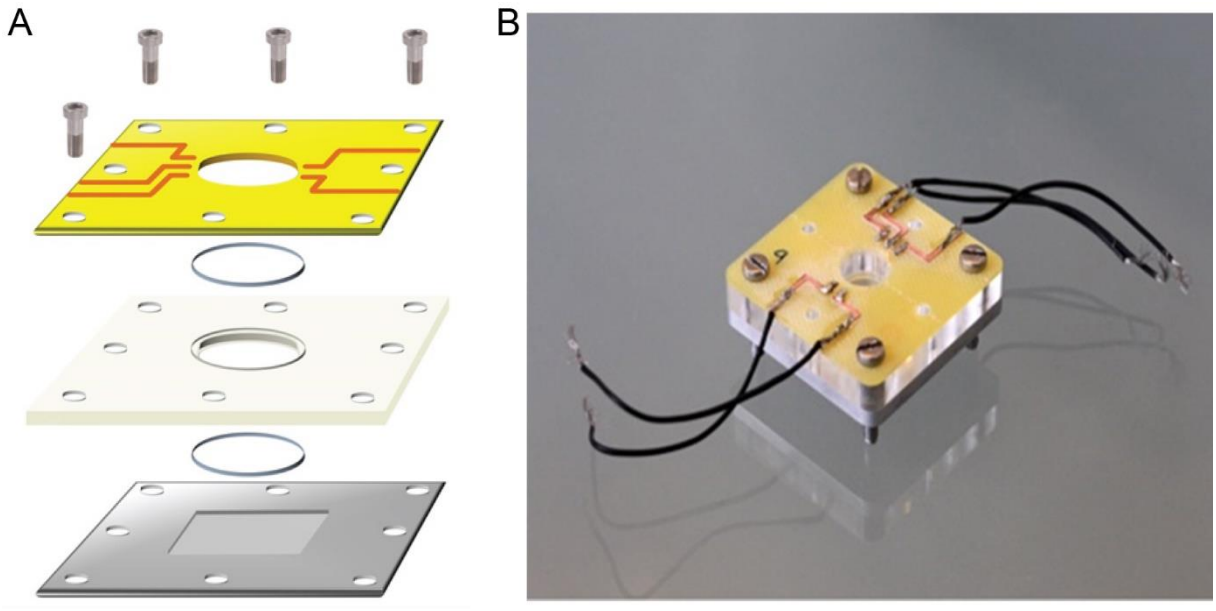

Figure S1. Electrochemical cell for characterization of chemical electrode modifications. A) The system comprises two micromilled plates: 1) the bottom metal plate (grey) with a recession for electrode microchip placement and 2) poly(methyl methacrylate) (PMMA) plate (white) which defines the electrochemical cell (height 5 mm), and a micromilled printed circuit board (PCB, yellow) with spring loaded pins for electric connections to the inserted electrode microchip. The diameter of the electrochemical cells is 10 mm facilitating access to the three working electrodes (in the middle) and the two larger electrodes used as on-chip counter and reference electrode. Fluid tight connection between the electrode microchip and the PMMA plate is achieved by using a polydimethylsiloxane (PDMS) O-ring (blue), prepared by casting PDMS into a micromilled mold. Another PDMS O-ring was placed between the PMMA plate and PCB to avoid that the electrolyte in the electrochemical cell creeps between the PMMA plate and PCB. B) A photo of an assembled setup.

S2 EIS characterization of chemical modifications of a gold electrode microchip

The performed chemical modifications of electrode microchips comprised three steps aiming at formation of hydroxyl functionalities followed by silanization to introduce methacrylate moieties on both electrode surfaces (gold) and the surrounding silicon nitride passivation layer. The influence of each modification step was characterized by electrochemical impedance spectroscopy (EIS) using the on-chip counter and reference electrode (frequency range: 100 mHz – 1 MHz; 10 data points per decade; 10 mV_{rms} sinusoidal potential) in the presence of equimolar $[Fe(CN)_6]^{3-/4-}$ (10 mM) in PBS. Figure S2 shows characteristic Nyquist plots acquired for one working electrode. Data were fitted to the modified Randles circuit (shown schematically in the inset of Figure S2) that represents the solution resistance in series with a parallel circuit composed of a constant phase element (CPE), accounting for double layer capacitance and surface inhomogeneity, parallel with charge transfer resistance (R_{ct}) and Warburg impedance (W). Hydroxylation of silicon nitride surface using H_2O_2 strongly oxidizes gold, increasing the charge transfer resistance. A further increase in R_{ct} was observed after β-mercaptoethanol SAM formation on gold (introduces hydroxyl functionalities for silanization) and silanization by 3-(trimethoxysilyl propyl) methacrylate of both the nitride and gold surfaces, indicating formation of a "physical barrier" for electroactive species. The oxidation of the gold surface as a consequence of the hydroxylation step resulted in a significant increase in CPE corresponding to increased capacitance analogously to what was shown in our previous work using PBS without any electroactive species [1]. The further chemical modifications decreased the CPE as an indication of decreased capacitance since such capacitive contributions to the overall impedance behave as series capacitors [2]. The value of W was only negligibly influenced by the modification steps.

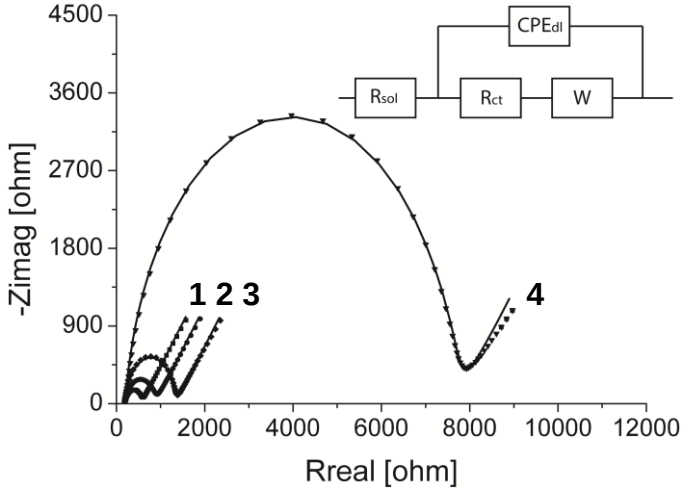

Figure S2. Nyquist plots acquired on 1) a cleaned electrode (▲), as well as the same electrode after 2) hydroxylation (H_2O_2 treatment) of the gold electrode microchip (●), 3) β-mercaptoethanol SAM formation on the H_2O_2 treated electrode (◆), and 4) silanization of β-mercaptoethanol SAM with 3-(trimethoxysilyl propyl) methacrylate (▼). Solid lines represent the nonlinear least square fitting of the data to the Randles equivalent circuit model (including a constant phase element, CPE_{dl}, to describe the double layer capacitance and surface inhomogeneity of the electrode) shown in the inset.

S3 Finite element simulations

A hydrogel scaffold tethered on an electrode surface develops corrugated voids due to the random scaffold structure. These voids promote currents leakage, such that electric fields avoid the scaffold structure and bypass through the electrolyte, which is not desirable when characterizing hydrogel scaffolds. Tully-Dartez et al. has described this anomaly while performing a similar study between chitosan scaffolds with embedded cylindrical electrodes [3]. In our study, the electric field, originating from the applied sinusoidal potential across the complex 3D hydrogel scaffold, which was covalently tethered on the electrode surface and the surrounding silicon nitride passivation layer, must essentially penetrate through the hydrogel during the entire frequency range.

3D space dimension model along with frequency domain and time dependent study was selected, and model was constructed as shown in Figure S3-1A and Figure S3-2A, for Case 1 and Case 2, respectively. The AC/DC physics interface was selected to model electric field lines at various frequencies for both cases. Figure S3-1B-G shows the simulation results for Case 1 at the frequencies of 100 mHz, 10 Hz, 1 kHz, 10 kHz, 100 kHz and 1 MHz as side (left panels) and top (right panels) view, respectively. Similarly Figure S3-2B-G shows the results at the abovementioned frequencies as side (left panels) and top (right panels) view for Case 2. The conductivity of PBS and pHEMA were defined based on previously published values as 1.6 S/m [4] and 3.5 mS/m [5], respectively. The mesh consisted of tetrahedral elements and for Case 1 and Case 2 the element values are shown in Table S3 below.

Table S3. Mesh quantity of each element and mesh quality for both cases.

Elements	Case1	Case2
Domain elements	109519	187687
Boundary elements	26402	38952
Edge elements	1491	1895
Mesh quality	0.91	0.92

Case 1 – Hydrogel covers only the WE

Side view **Top view**

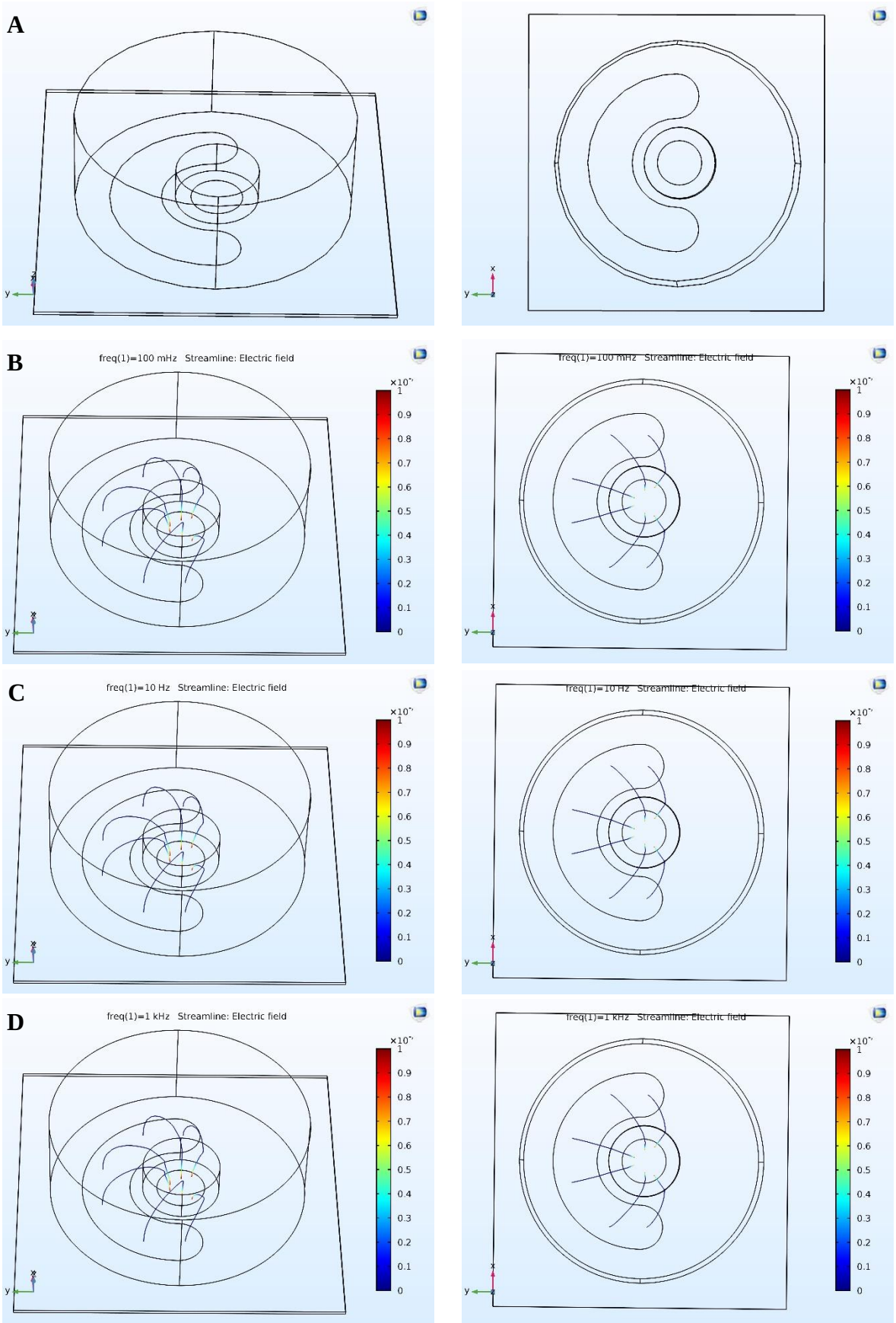

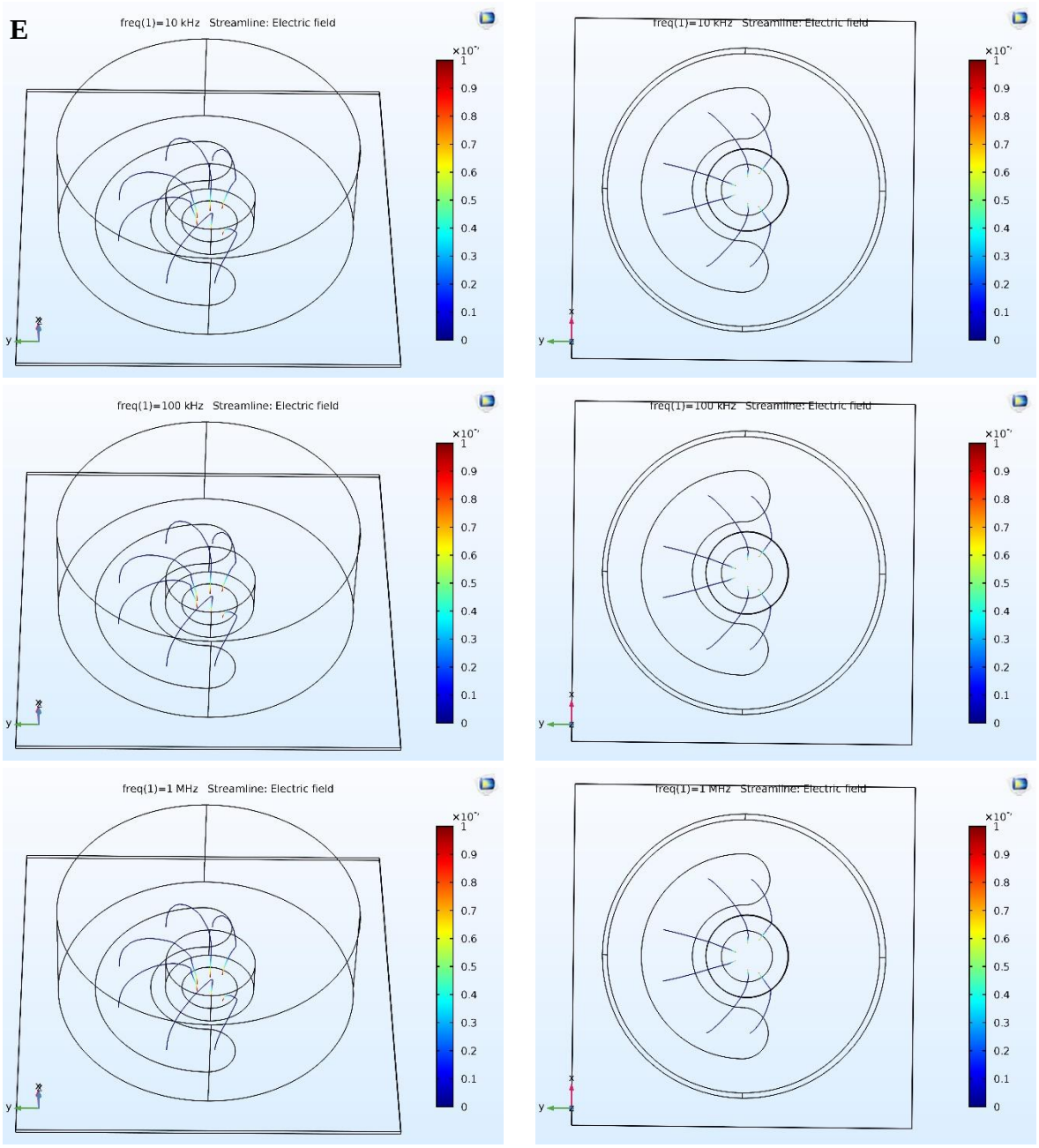

Figure S3-1. Finite element simulations using COMSOL Multiphysics for case 1:
A) Schematic view of the used model (Left column – side view; right column – top view). Electric field streamline propagation between the WE and CE for B) 100 mHz; C) 10 Hz; D) 1 kHz; E) 10 kHz; F) 100 kHz; G) 1 MHz.

Case 2 – Hydrogel covers both the WE and CE

Side view **Top view**

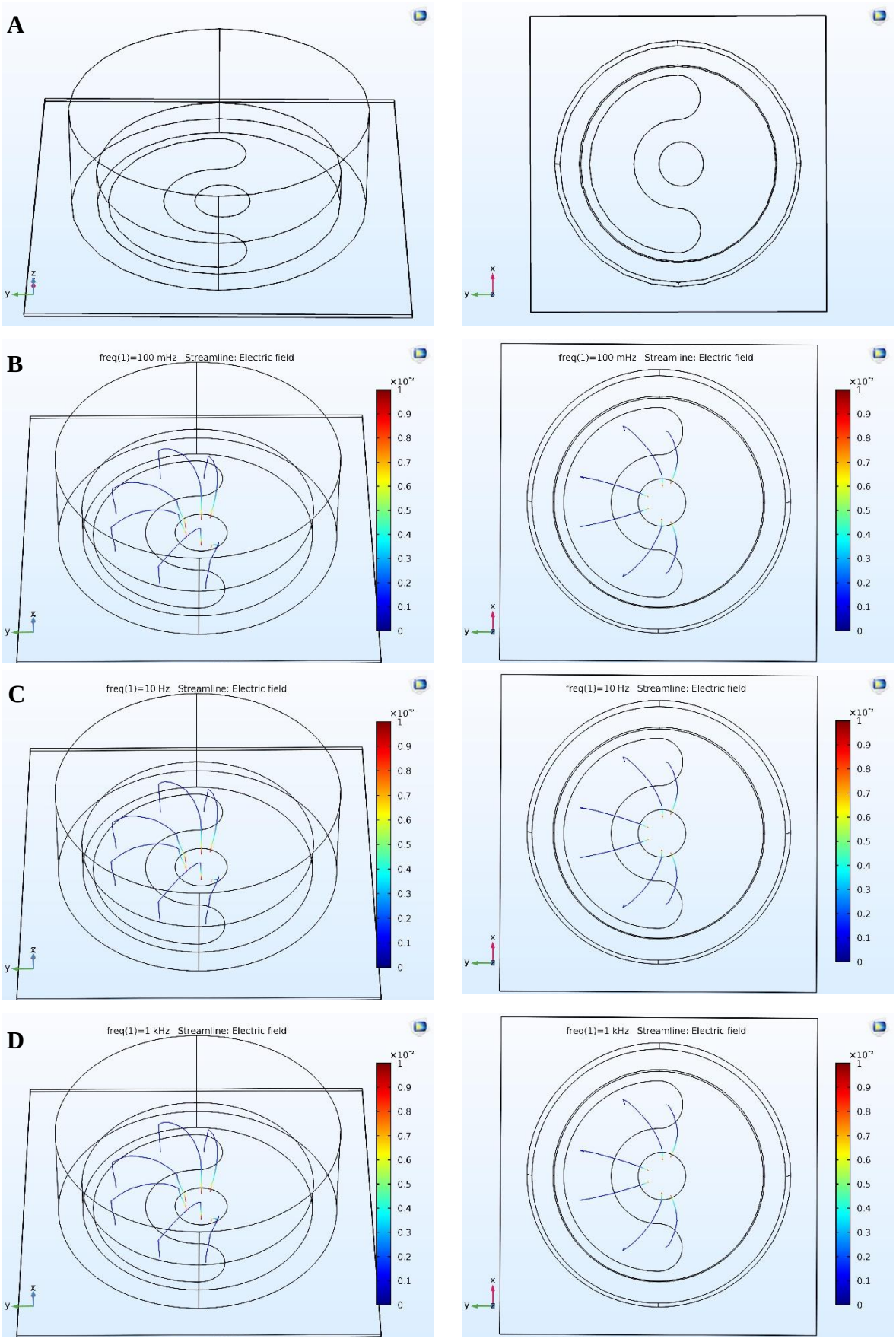

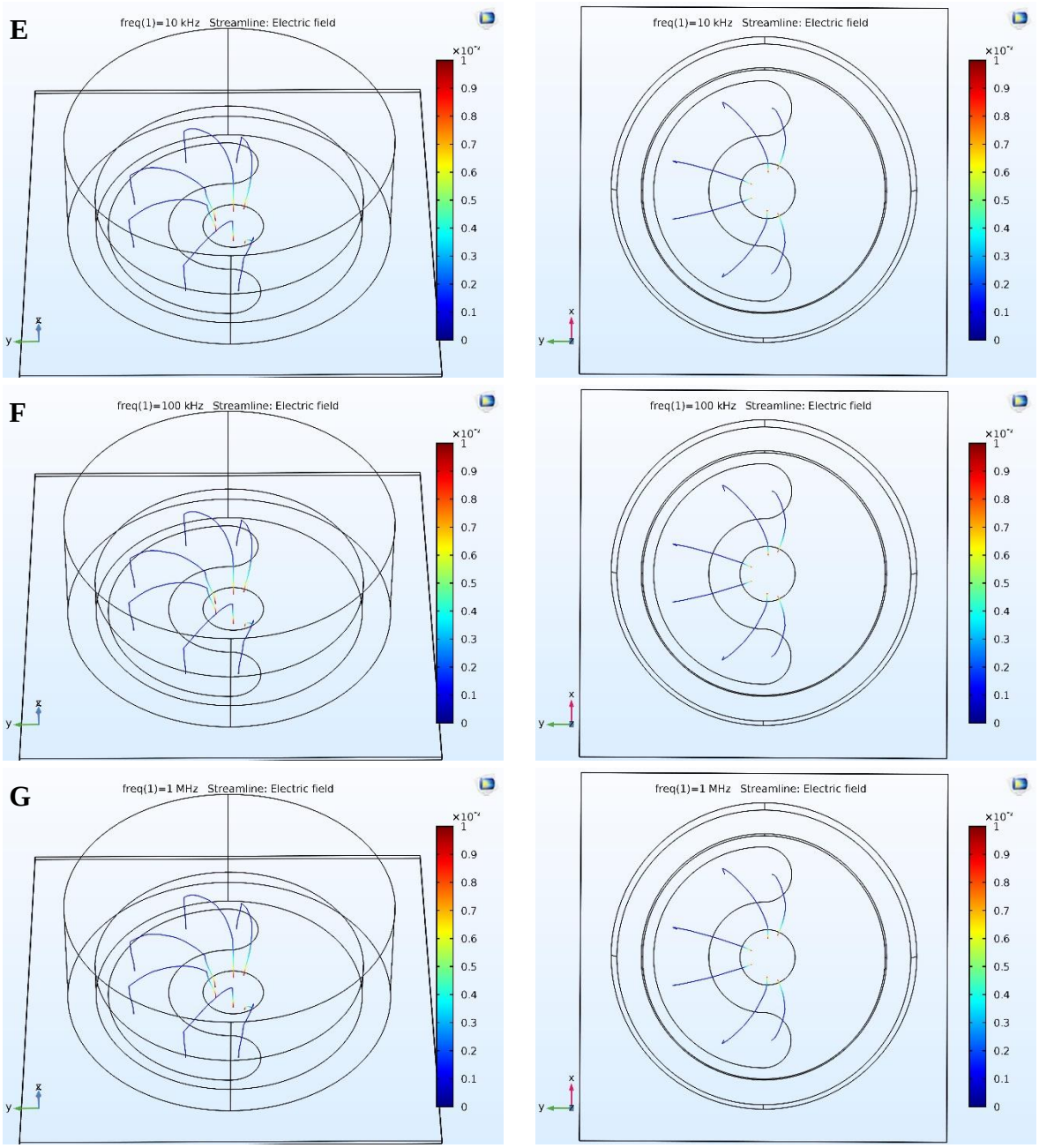

Figure S3-2. Finite element simulations using COMSOL Multiphysics for case 2: A) Schematic view of the used model (Left column – side view; right column – top view). Electric field streamline propagation between the WE and CE for B) 100 mHz; C) 10 Hz; D) 1 kHz; E) 10 kHz; F) 100 kHz; G) 1 MHz.

S4 Description of impedance elements

Constant phase element (CPE)

Constant phase element (CPE) has been used to characterize the interface behavior of solid electrodes when the behavior is not purely capacitive (i.e. due to phenomena that could be attributed to, e.g., surface roughness, a certain degree of dispersion is observed instead of pure double layer capacitance behavior) [6]. It has also found applications in modeling of finite diffusion layer behavior at electrodes with a porous coating [7]. Mathematically, its impedance is expressed as shown in Eq. 1

$$\vec{Z}_{CPE} = \frac{1}{Q_0(j\omega)^{\alpha}} \qquad \text{Eq. 1}$$

where ω is the angular frequency, $j = (-1)^{½}$, Q_0 the magnitude of $1/Z_{CPE}$ (Y_{CPE}) at $\omega = 1$ rad/s, α obtains values between 0 and 1. When $\alpha = 1$, Z_{CPE} represents pure capacitance ($Q_0 = C$). At the opposite limit, $\alpha = 0$, Z_{CPE} represents pure resistor. The value of α determines the constant phase angle (θ_{CPE}) according to $\theta_{CPE} = -(\pi/2)\alpha$. The unit of $|Z_{CPE}|$ is Ω, and hence, since ω^{α} has unit $s^{-\alpha}$, Q_0 has unit Ss^{α}. Q_0 is the value given by many equivalent circuit modeling programs (e.g. Gamry Echem Analyst).

In the complex impedance plane (Nyquist plot), Z_{CPE} in parallel with a resistance (e.g. charge transfer resistance) generates the well-known recessive semicircle. Fig. S4-1A illustrates a Nyquist plot generated using the equivalent circuit in Fig. S4-1B (analogous to the equivalent circuit of Scheme 1 in the article with the exception that no diffusion impedance is included).

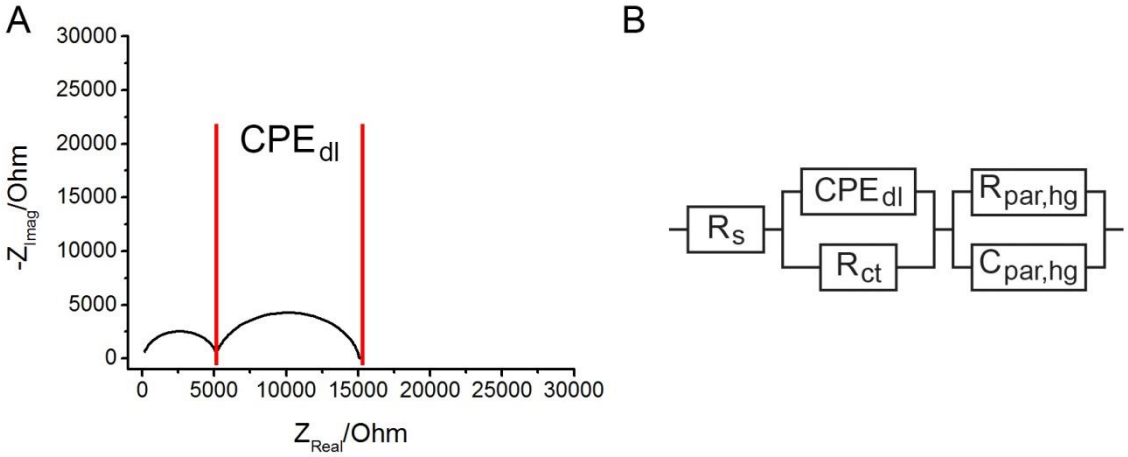

Figure S4-1. A) Complex impedance plane representation (Nyquist plot) of impedance generated based on the equivalent circuit in B). (CPE_{dl} – Z_{CPE} related to the interface impedance comprising the double layer capacitance; other components as described in the article; generated by EIS simulation script of Gamry Echem Analyst v. 6.10 – R_s = 100 Ω, $Q_{0,dl}$ = 500 nSs^{α} (Q_0 of CPE_{dl}), α = 0.900, R_{ct} = 10 kΩ, $R_{par,hg}$ = 5 kΩ, $C_{par,\,hg}$ = 800 pF)

Warburg impedance for semi-infinite diffusion (Z_W)

The Warburg impedance (Z_W) has been commonly used as diffusion impedance element suitable for characterizing diffusion of electroactive species to an electrode-electrolyte interface with semi-infinite thickness of the Nernst diffusion layer (δ) [8]. Mathematically, it is expressed as shown in Eq. 2 [9]

$$\vec{Z}_W(\omega) = \sigma\omega^{-½} - j\sigma\omega^{-½} \qquad |Z_W| = \sqrt{2}\,\sigma\omega^{-½} \qquad \text{Eq. 2a}$$

$$\sigma = \frac{RT}{n^2F^2A\sqrt{2}}\left(\frac{1}{D_O^{½}C_O^*} + \frac{1}{D_R^{½}C_R^*}\right) \qquad \text{Eq. 2b}$$

where ω is the angular frequency, $j = (-1)^{½}$, R the molar gas constant (8.314 J mol^{-1} K^{-1}), T the absolute temperature, n the number of electrons involved, F the Faraday constant (96485 C mol^{-1}), D_O and D_R the diffusion coefficient of the oxidized and reduced species, respectively, C^*_O and C^*_R the bulk concentration of the oxidized and reduced species, respectively. The magnitude of Z_W ($|Z_W|$) has unit Ω, and hence, since $\omega^{-½}$ has unit s^{½}, σ has unit Ωs$^{-½}$. As admittance notation, $|Z_W|$ can be expressed as shown in Eq. 3

$$\frac{1}{|Z_W|} = \frac{1}{\sqrt{2}\,\sigma}\,\omega^{½} \qquad \text{Eq. 3}$$

where $1/\sigma$ can be denoted by Y_W. Hence, using this notation $|Z_W|$ can be expressed as shown in Eq. 4

$$|Z_W| = \sqrt{2}\frac{1}{Y_W}\omega^{-½} \qquad \text{Eq. 4}$$

Y_W having unit Ω^{-1}s^{½} (Ss^{½}) is the value given by many equivalent circuit modeling programs (e.g. Gamry Echem Analyst). This approach facilitates an easy comparison of obtained values. The smaller the value of Y_W is the more limited is diffusion based mass transfer (i.e. the higher is $|Z_W|$).

In the complex impedance plane (Nyquist plot), Z_W generates the well-known Warburg line with 45° slope. Fig. S4-2A illustrates a Nyquist plot generated using the equivalent circuit in Fig. S4-2B (analogous to the equivalent circuit of Scheme 1 in the article with the exception that Z_W is solely representing the diffusion impedance).

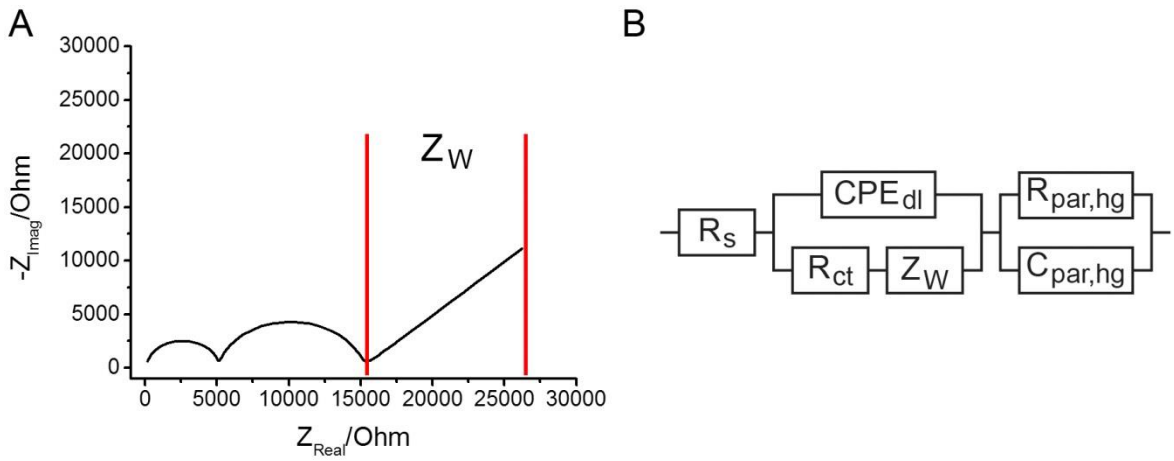

Figure S4-2. A) Complex impedance plane representation (Nyquist plot) of impedance generated based on the equivalent circuit in B). (Z_W – semi-infinite Warburg impedance; all the other components of the equivalent circuit are the same as described in Fig. S4-1 and the article; generated by EIS simulation script of Gamry Echem Analyst v. 6.10 – Y_W = 800 $\mu Ss^{½}$; the other components have the same values as in Fig. S4-1)

Open-boundary Warburg impedance for finite diffusion (Z_{WO})

Modeling of, for instance, porous electrode modifications with an open (unperturbed) outer boundary, leading to a finite thickness of δ, has employed open-boundary finite-length Warburg impedance (Z_{WO}, O element) [10]. Z_{WO} is a modified version of Z_W and can be expressed as shown in Eq. 5 when following the notation in Eq. 4 above.

$$\vec{Z}_{WO}(\omega) = \left(\frac{1}{Y_{WO}\sqrt{j\omega}}\right) \tanh\left(B\sqrt{j\omega}\right) \qquad \text{Eq. 5a}$$

$$B = \delta/\sqrt{D} \qquad \text{Eq. 5b}$$

As above, the unit of Y_{WO} is $Ss^{½}$. The unit of B (characteristic time constant describing diffusion through δ) is $s^{½}$.

In the complex impedance plane (Nyquist plot), Z_{WO} generates a Warburg line with 45° slope at frequencies, $f > 2/B^2$, while at lower frequencies the curve bends toward the Z_{Real} axis. Fig. S4-3A illustrates a Nyquist plot generated using the equivalent circuit in Fig. S4-3B (analogous to the equivalent circuit of Scheme 1 in the article with the exception that Z_{WO} is solely representing the diffusion impedance).

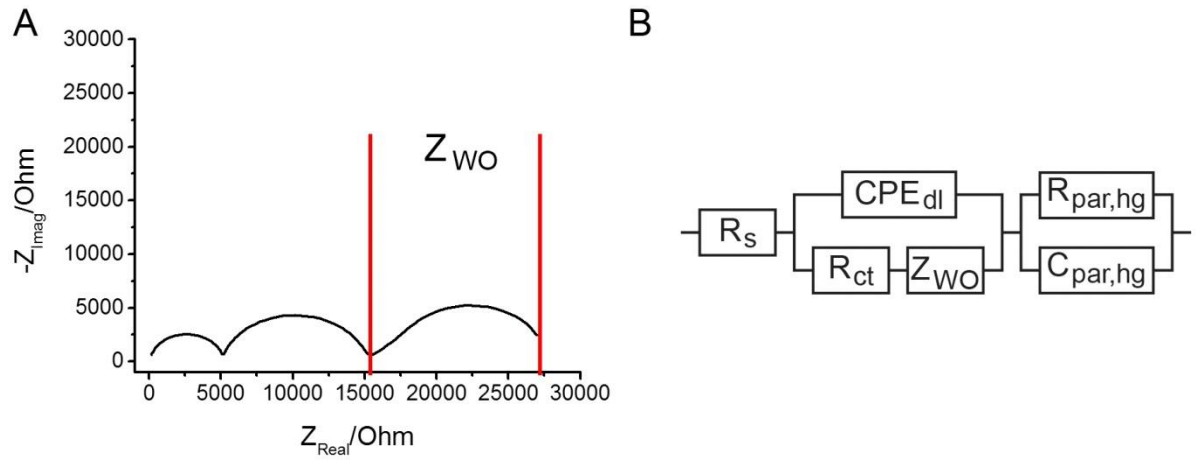

Figure S4-3. A) Complex impedance plane representation (Nyquist plot) of impedance generated based on the equivalent circuit in B). (Z_{WO} – open-boundary finite-length Warburg impedance; all the other components of the equivalent circuit are the same as described in Fig. S4-1 and the article; generated by EIS simulation script of Gamry Echem Analyst v. 6.10 – Y_{WO} = 800 µSs^{½}, B = 10 s^{½})

Blocked-boundary Warburg impedance for finite diffusion (Z_{WT})

Modeling of, for instance, porous electrode modifications with a blocked outer boundary, leading to a finite thickness of δ, has employed blocked-boundary finite-length Warburg impedance (Z_{WT}, T element) [10]. Z_{WT} is a modified version of Z_W and can be expressed as shown in Eq. 6 when following the notation in Eq. 4 analogously as in the case of Eq. 5.

$$\vec{Z}_{WO}(\omega) = \left(\frac{1}{Y_{WT}\sqrt{j\omega}}\right) \coth\left(B\sqrt{j\omega}\right) \qquad \text{Eq. 6}$$

The unit of Y_{WT} is the same as for Y_{WO}. B is defined as shown above (Eq. 5b).

In the complex impedance plane (Nyquist plot), Z_{WT} generates a Warburg line with 45° slope at frequencies, $f > 2/B^2$, while at lower frequencies the curve turns into a 90° capacitive line. Fig. S4-4A illustrates a Nyquist plot generated using the equivalent circuit in Fig. S4-4B (analogous to the equivalent circuit of Scheme 1 in the article with the exception that Z_{WT} is solely representing the diffusion impedance).

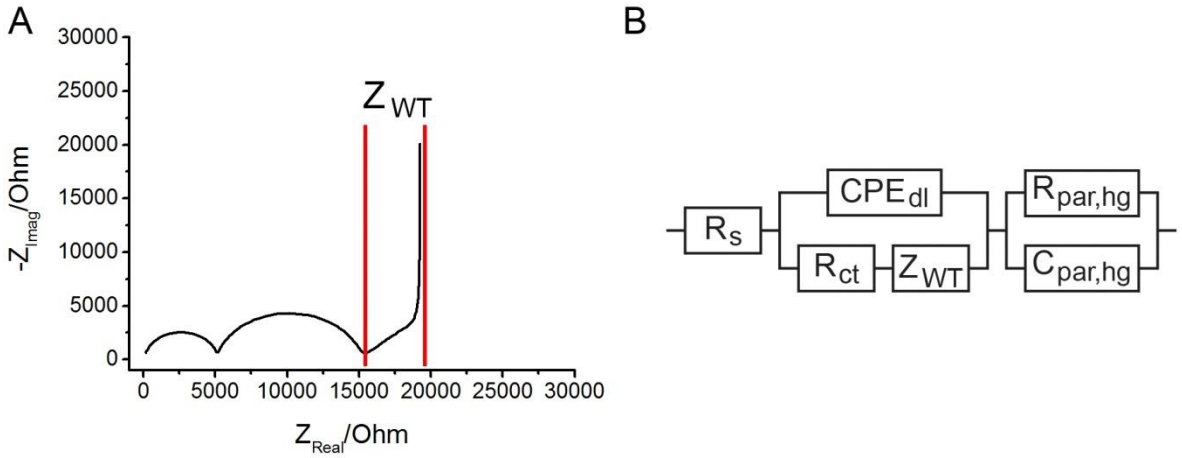

Figure S4-4. A) Complex impedance plane representation (Nyquist plot) of impedance generated based on the equivalent circuit in B). (Z_{WT} – blocked-boundary finite-length Warburg impedance; all the other components of the equivalent circuit are the same as described in Fig. S4-1 and the article; generated by EIS simulation script of Gamry Echem Analyst v. 6.10 – Y_{WT} = 800 µSs^{½}, B = 10 s^{½})

S5 NLLS regression analysis using alternative equivalent circuit models

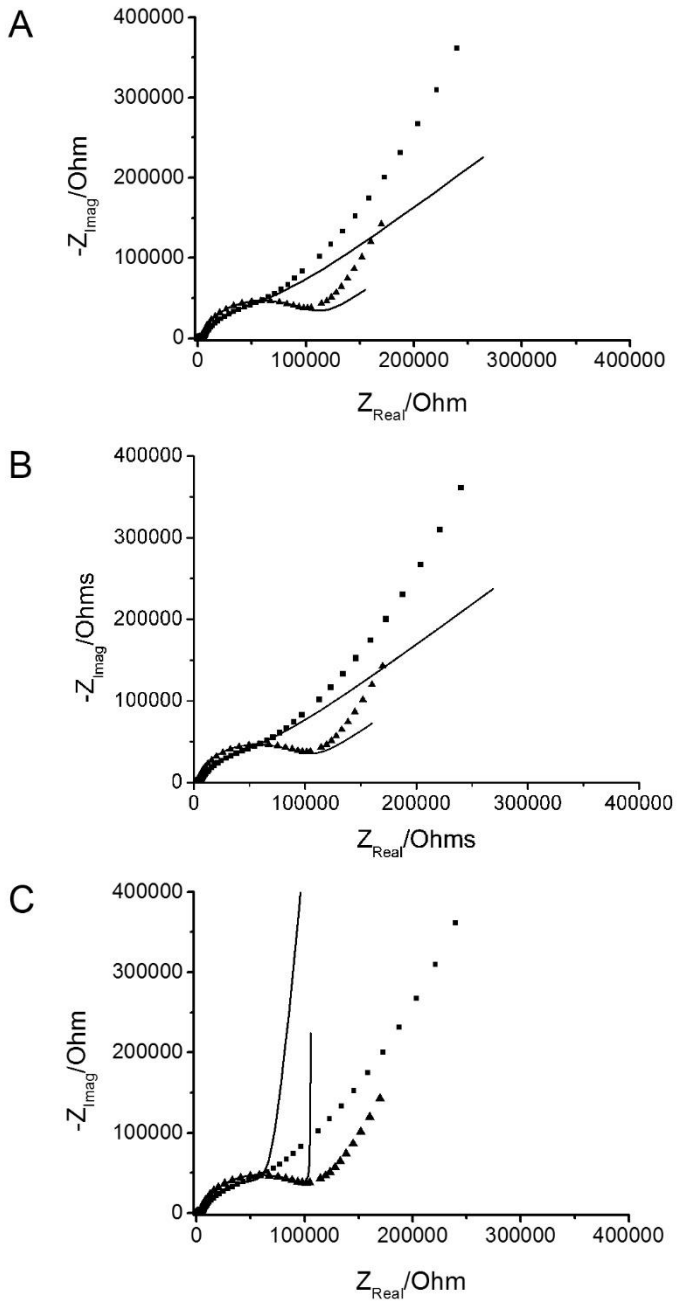

Figure S5. NLLS regression analysis of Nyquist plots (Fig. 2A in the article) acquired for 1:200 cross-linked conditioned hydrogel using the equivalent circuit model shown in A) S4-2B, B) Scheme 1 of the article without CPE_{mtd}, and C) Scheme 1 of the article except that Z_{WO} was replaced by Z_{WT}.

S6 Degree of hydration for cross-linked hydrogels

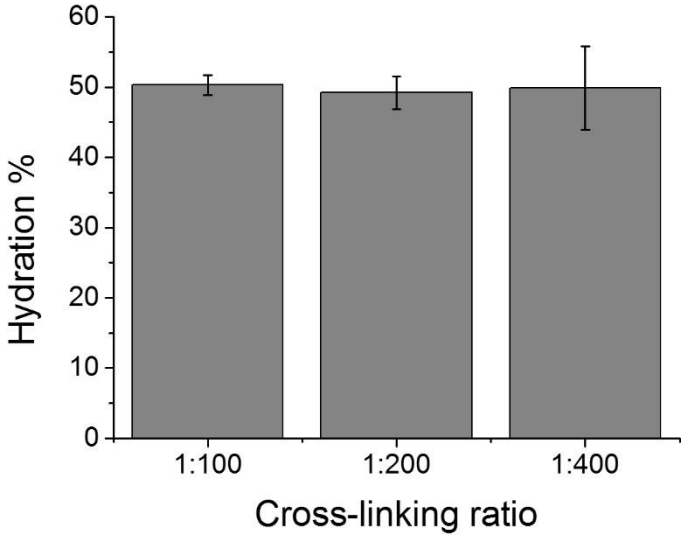

Figure S6. Degree of hydration presented as Hydration % = $[(w_{wet} - w_{dry})/w_{wet}] \times 100\%$ [11]; Average ± standard deviation (n = 4).

Table S6. Statistical analysis of hydration % (cross-linking ratio PEG-DMA[1]:HEMA[2])

Two-sample tests (5% level)	**1:100** Normal distribution[3] p = 0.9885	**1:200** Normal distribution[3] p = 0.2376	**1:400** Normal distribution[3] p = 0.4540
1:100		Equal variance[4] p = 0.4462 t-test[5] p = 0.4519	Unequal variance[4] p = 0.0440 t-test[5] p = 0.8973
1:200			Equal variance[4] p = 0.1613 t-test[5] p = 0.8379

[1] PEG-DMA – Poly(ethylene glycol)-dimethacrylate
[2] HEMA – 2-hydroxyethyl methacrylate
[3] Normality test: Shapiro-Wilk (OriginPro 9.0)
[4] Two-tailed F-test (OriginPro 9.0)
[5] Two-tailed t-test (OriginPro 9.0)

References

[1] Mech-Dorosz, A. Heiskanen, S. Bäckström, M. Perry, H. B. Muhammad, C. Hélix-Nielsen, J. Emnéus, A reusable device for electrochemical applications of hydrogel supported black lipid membranes, Biomed. Microdevices 17:21 (2015). doi:10.1007/s10544-015-9936-y

[2] R. Heiskanen, C. F. Spégel, N. Kostesha, T. Ruzgas, J. Emnéus, Monitoring of *Saccharomyces cerevisiae* cell proliferation on thiol-modified planar gold microelectrodes using impedance spectroscopy, Langmuir. 24 (2008) 9066. doi:10.1021/la800580f

[3] S. Tully-Dartez, H. E. Cardenas, P. F. S. Sit, Pore characteristics of chitosan scaffolds studied by electrochemical impedance spectroscopy. Tissue Eng. - Part C Methods 16 (2010) 339.

[4] D. A. Miller, The ionic conductivity of p(2-Hydroxyethyl methacrylate Hydrogels, PhD thesis, The University of Adelaide, 1995.

[5] C. Canali, S. Mohanty, A. Heiskanen, H. B. Muhammad, Ø. G. Martinsen, M. Dufva, A. Wolff, J. Emnéus, Impedance spectroscopic characterization of porosity in 3D cell culture scaffolds with different channel networks. Electroanalysis 27 (2015), 193.

[6] G. J. Brug, A. L. G. Van den Eeden, M. Sluyters-Rehbach, J. H. Sluyters, The analysis of electrode impedances complicated by the presence of a constant phase element, J. Electroanal. Chem. 176 (1984) 275. doi:10.1016/S0022-0728(84)80324-1

[7] J. Bisquert, G. Garcia-Belmonte, F. Fabregat-Santiago, P. R. Bueno, Theoretical models for ac impedance of finite diffusion layers exhibiting low frequency dispersion, J. Electroanal. Chem. 475 (1999) 152. doi:10.1016/S0022-0728(99)00346-0

[8] E. Warburg, Ueber das Verhalten sogenannter unpolarisirbarer Elektroden gegen Wechselstrom, Ann. Physik 303 (1899) 493. doi: 10.1002/andp.18993030302

[9] A. J. Bard, L. R. Faulkner, Electrochemical Methods: Fundamentals and Applications, 2nd Ed., John Wiley & Sons, Inc., Hoboken, 2001.

[10] V. Freger, Diffusion impedance and equivalent circuit of a multilayer film, Electrochem. Commun. 7 (2005) 957. doi:10.1016/j.elecom.2005.06.020

[11] S. Brahim, D. Narinesingh, A. Guiseppi-Elie, Synthesis and hydration properties of pH-sensitive p(HEMA)-based hydrogels containing 3-(trimethoxysilyl)propyl methacrylate, Biomacromolecules 4 (2003) 497. doi:10.1021/bm020080u